NORTHWESTERN UNIVERSITY

Atomic-Scale Structural Investigations of the
Low-Temperature Phase Transitions for the
1/3 ML Sn/Ge(111) and 1/3 ML Pb/Ge(111) Surfaces

A DISSERTATION

SUBMITTED TO THE GRADUATE SCHOOL
IN PARTIAL FULLFILLMENT OF THE REQUIREMENTS

for the degree

DOCTOR OF PHILOSOPHY

Field of Materials Science and Engineering

By

John Scott Okasinski

EVANSTON, ILLINOIS

JUNE 2004

ABSTRACT

Atomic-Scale Structural Investigations of the Low-Temperature Phase Transitions
for the 1/3 ML Sn/Ge(111) and 1/3 ML Pb/Ge(111) Surfaces

John Scott Okasinski

Insight into the two-dimensional physics of surface phase transitions, dynamics, and kinetics often requires an accurate atomic-scale description. Submonolayer thin films of tin or lead on surfaces of germanium provide material systems that enable gaining a fundamental understanding of metal on semiconductor surfaces. Measuring the atomic structure of the metal-semiconductor interface will provide a basis for further development and growth of related thin film systems.

At room temperature, the 1/3 ML Sn on Ge(111) surface forms a $(\sqrt{3} \times \sqrt{3})R30°$ reconstruction and is typically modeled with a single Sn atom occupying one of the three T_4–adsorption sites within the $(\sqrt{3} \times \sqrt{3})R30°$ unit cell. A similar structure is also observed for 1/3 ML Pb/Ge(111). When cooling from the critical temperature (T_C ~210 K) to near 100 K, the surface reconstruction completes a gradual and reversible transition to a (3 x 3) phase. Scanning tunneling microscopy images show one of the Sn (or Pb) atomic protrusions in the (3 x 3) unit cell appearing different than the other two. The main controversies for the structures are whether the Sn atoms have a corrugated distribution at room temperature, and whether the Sn distribution is "one up and two down" or "two up and one down".

To study this apparent broken symmetry in the atomic distribution, we have developed a new method for three-dimensional imaging of adsorbate atoms on crystalline surfaces that is based on the direct Fourier inversion of x-ray standing

wave (XSW) data. The XSW technique is well suited to measure the time-averaged Sn distribution, and we address these structural questions using a model and high-resolution XSW measurements in the [111] direction.

At room temperature, the Sn atoms are found to occupy T_4–adsorption sites with one-third of these Sn atoms 0.45 Å higher than the remaining two-thirds. The (3 x 3) phase has no significant change in the XSW-measured structural parameters and is consistent with an order-disorder type phase transition. Additionally, for both Sn/Ge(111) and Pb/Ge(111) systems, a fraction of the Sn and Pb are found to substitute into the bottom position of the Ge atomic bilayer.

Approved:

_____

Professor Michael J. Bedzyk
Department of Materials Science and Engineering
Northwestern University
Evanston, IL

ACKNOWLEDGEMENTS

I would like to acknowledge the numerous people who have influenced and helped me throughout my years at Northwestern. I am indebted to Prof. Jerry Cohen for launching me into the x-ray diffraction field and sharing his enthusiasm of applying x-ray scattering techniques to a wide-array of materials science problems. I am grateful to Prof. Mike Bedzyk who accepted me into his group, after Prof. Cohen passed away, and shared with me the resources needed for me to change my thesis topic.

My thesis committee, Dr. Denis Keane, Prof. Mark Asta, and Prof. Laurie Marks, are appreciated for participating in my thesis defense and for sharing their thoughts on this research problem.

Fellow members (both former and present) in Professors Cohen's and Bedzyk's research groups are valued for their help (whether directly or indirectly to me), in chronological order from Prof. Cohen's group: Jon Almer, Kevin Peters, Jerry Carsello, Gabriela González Avilés, Kristine Kupiecki (Witkowski), and Wen-Jih Lin, and later in Mike's group: Paul Lyman, Likwan Cheng, William Rodrigues, Tien-Lin Lee, Don Walko, Chang-Yong Kim, Zhan Zhang, David Marasco, Duane Goodner, Anthony Escuadro, and Joe Libera. In the physics department, Oliver Warschkow also contributed with discussions and computational efforts. I hope to continue both professional and personal relationships with them in the future.

During the initial experiments at 5ID-C, Chang-Yong and Don were fundamental in familiarizing me with UHV methods and the particulars of the 5ID-C station at the

TABLE OF CONTENTS

LIST OF TABLES

LIST OF FIGURES

Chapter 1: Introduction

Insight into the two-dimensional physics of surface phase transitions, dynamics, and kinetics often requires an accurate atomic-scale description. Surface science provides many tools that enable scientists to investigate the structure of materials at surfaces and interfaces. By determining the local and long-range ordering at the atomic level, we increase our understanding of these materials so that we can continue to improve them and create new functionality from them.

The development of surface science has contributed to the growth of the semiconductor industry, which relies, in part, on careful manipulation of Si surfaces. As feature sizes of devices decrease, the structure of the surface becomes increasingly important because the surface to volume ratio increases. Additionally, as the number of atoms in the device decreases, the effects of defects, whether detrimental or beneficial, play an increasing role in devices.

Because Ge is quite similar to Si, it may provide one avenue for the continued development in semiconductor materials. Incorporating Ge into Si structures

permits tailoring of the materials properties. Also, because Si and Ge are so much alike, subtle effects can be investigated using this pair of materials as an experimental variable. Applying the same processing and characterization to both Si and Ge creates a larger understanding of both of them than just independently examining them.

Investigating the atomic-scale structure during the growth of thin metal films on semiconductor surfaces will expand the understanding of Schottky barrier formation. Submonolayer thin films of tin or lead on surfaces of germanium provide material systems that enable gaining fundamental understanding of a metal on a semiconductor surface. Measuring the atomic structure of this metal-semiconductor interface will provide a basis for further development and growth of related thin film systems. One example, is the role both Pb and Sn can play in surfactant mediated hetero- and homoepitaxy for the Si/Ge system. [1 - 2]

While Al alloys are no longer the dominant material used for interconnects in the semiconductor field, metal alloys will continue to be required for some applications. The addition of dilute amounts of Cu to Al, improves its mechanical properties, increasing both the strength and resistance to electron migration. While the bulk structure for Al-Cu alloys is well-understood, not as much is known on the structure at the surfaces.

In the work described here, the surface structures are investigated for three materials systems: 1/3 monolayer (ML) of Sn on the Ge(111) surface, 1/3 ML of Pb on the Ge(111) surface, and the low-index surfaces of an Al-1.7at% Cu alloy. The Sn/Ge(111) and Pb/Ge(111) surface were examined primarily using the x-ray standing wave (XSW) technique and low-energy electron diffraction (LEED). The

surfaces of the Al-Cu alloy were characterized using LEED and Auger electron spectroscopy (AES).

An overview of the Sn/Ge(111) and Pb/Ge(111) surfaces is presented in Chapter 2. These systems have recently attracted much interest due to the presence of a surface phase transition. Both the structures and the mechanism for this phase transition are disputed. Because the surface can be investigated with numerous experimental and theoretical tools, controversy has arisen due to conflicting results. To investigate this problem, the XSW technique is used to directly measure the atomic distribution for the Sn and Pb atoms at the surface.

Chapter 3 contains a description of the XSW method, as well as, the newly developed XSW direct space imaging technique. Because XSW results provide the Fourier coefficients of the atomic distribution, the atomic density distribution in real space can be directly mapped out.

The design, function, and performance of the key equipment used to prepare samples and perform experiments are described in Chapter 4. In particular, the x-ray optics and the ultra-high vacuum chamber located in the 5ID-C experimental station at the Advanced Photon Source are discussed.

The experimental results for the XSW measurements on 1/3 ML Sn/Ge(111) are discussed in Chapter 5. XSW direct space images are created for two samples prepared under different annealing conditions and reveal different atomic distribution for the Sn at the surface. The experimental results for 1/3 ML Pb/Ge(111) are included in Chapter 6. For both of these systems, the XSW results provide information to address the phase transition determination.

Chapter 7 contains information on the structural and chemical composition measurements for the surfaces of a dilute Al–1.7at% Cu alloy for three low-index orientations: [001], [011], and [111]. Results are summarized in Chapter 8, and an outlook for potential research related to these material systems is offered.

Chapter 2: Background on the Sn/Ge(111) and Pb/Ge(111) surfaces

2.1 Introduction

In this chapter, the bulk-terminated (1 x 1) and the reconstructed c(2 x 8) surfaces for Ge in the [111] direction is first described. This is the surface from which the 1/3 ML Sn/Ge(111) and 1/3 ML Pb/Ge(111) structures are prepared on. Background information for the Sn/Ge(111) and Pb/Ge(111) surfaces is then reviewed. The description for both the Sn and Pb systems will be grouped together because they exhibit similar structures. The controversy over the structures of the ($\sqrt{3}$ x $\sqrt{3}$)R30° to (3 x 3) phase transition is discussed. Finally, the short-range ordering on the Pb/Ge(111) surface with a coverage between 1/6 ML and 1/3 ML is presented.

2.2 The Ge(111) surface

When viewed from above, the top two atomic layers for the Ge(111) surface appear as an array of hexagons, as shown in Figure 2.1. If the surface has the

same structure as the underlying 3D crystal, it is considered to be a bulk-terminated surface. The unit cell is denoted as (1 x 1) and is outlined in green. For the diamond cubic crystal structure along the [111] direction, the sequence of atomic layers can be referred to as bilayers. The atomic planes are grouped into two planes of atoms separated by 1/4 of a d_{111} spacing. Subsequent bilayers are offset along the [110] direction and can be seen in Figure 2.2.

The bulk-terminated Ge(111) surface has three high-symmetry sites (T_1, H_3, and T_4) that are defined by their lateral positions. The subscripts 1, 3, and 4 refer to the coordination number of each site. The (blue) T_1-site sits atop a Ge atom in the top of the bilayer. The (yellow) H_3-site is located in the hollow position that appears in the middle of each hexagon. The (red) T_4-site is above the atom in the bottom of the bilayer and is also coordinated to three atoms in the top of the bilayer. The point symmetry for all three of these sites is 3m.

Ge adatoms on the Ge(111) surface are located in T_4-sites and are shown with purple circles in Figure 2.1. The surface reconstruction is a c(2 x 8) unit cell that is composed of an ordered arrangement of Ge adatoms in a (2 x 2) subunit and a c(4 x 2) subunit [3 - 5]. This larger c(2 x 8) reconstruction is shown with purple, dashed lines.
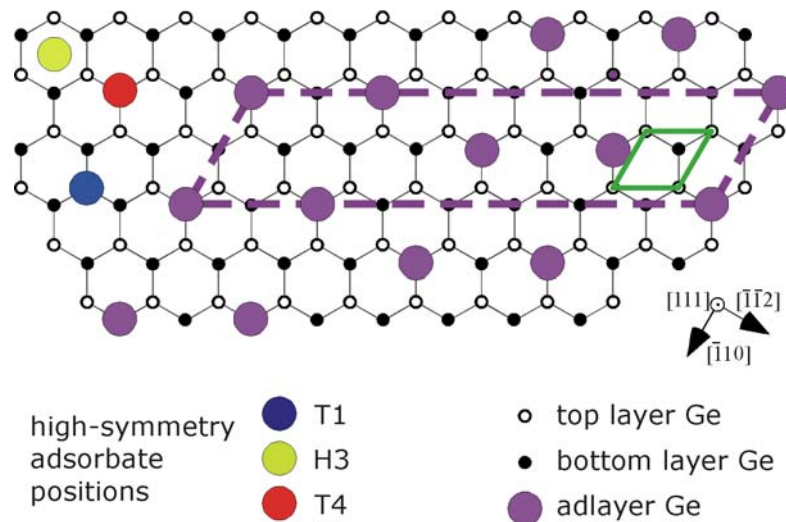
Figure 2.1: Top view of the Ge(111) surface depicting the lateral positions for the three high-symmetry adsorption sites (T_1, H_3, and T_4) and the c(2 x 8) reconstruction for the clean surface. The (blue) T_1-site sits atop a Ge atom in the top of the bilayer. The (yellow) H_3-site is located in the middle of the hollow position that appears as a hexagon from above. The (red) T_4-site is above the lower atom in the bilayer and is surrounded by three atoms that are in the top of the bilayer. Ge, Pb, and Sn adsorbate atoms occupy the T_4-site at low coverage. The Ge atoms in the adlayer are shown in purple. The Ge (1 x 1) unit cell is outlined in green, and the larger c(2 x 8) reconstruction is shown with purple, dashed lines.
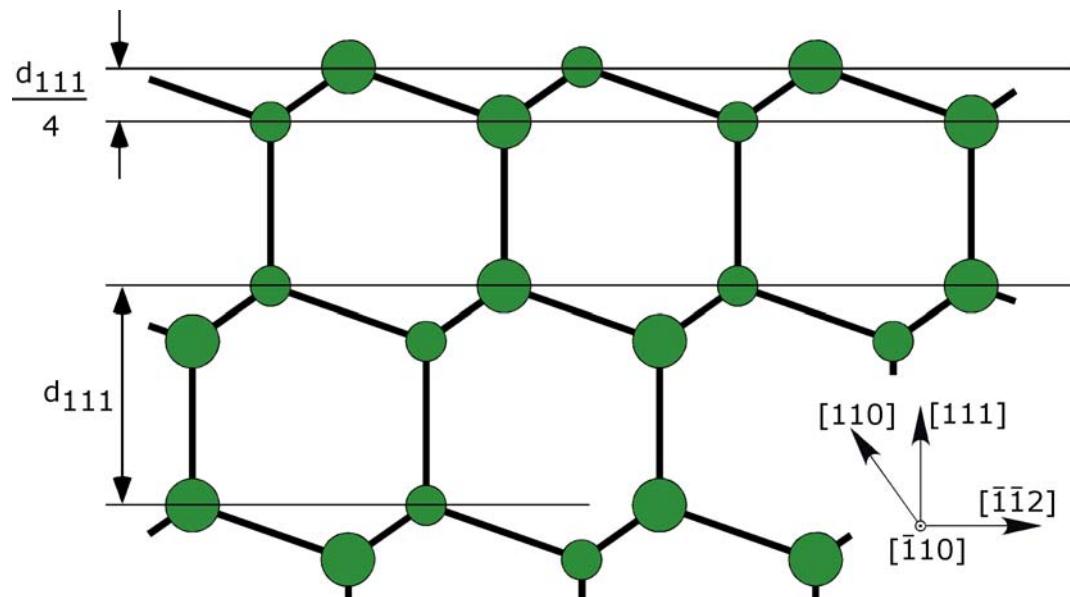
Figure 2.2: Side view of the Ge(111) surface along the $[1\bar{1}0]$ direction and depicting the Ge atoms stacked in a sequence of bilayers that are offset from the previous layer in the [110] direction.

2.3 Sn/Ge(111) and Pb/Ge(111) surfaces

2.3.1 Background

The interfacial structure of Sn (or Pb) on Ge(111) provides an interesting metal/semiconductor system. The two elements Sn and Pb are both in the Group IVA column of the periodic chart, therefore, it is not surprising that they exhibit similar behavior in their relationship to Ge. Looking at the bulk phase diagrams for Sn-Ge and Pb-Ge in Figures 2.3 and 2.4, neither system forms an intermediate phase [6]. Additionally, while Sn shows some susceptibility for intermixing into the bulk Ge structure, Pb and Ge are mutually insoluble in each other over a substantial temperature range. This bulk insolubility makes the Pb-Ge binary system a good candidate for two-dimensional, surface structure [7]. The low solubility also makes Sn-Ge a good system for surface studies. Additionally, Sn and Pb are metals, so the submonolayer structures of Sn (or Pb) on Ge are interesting systems for metal/semiconductor interface studies.

Surface phase diagrams depict the surface reconstructions present as a function of atomic layer coverage Θ and temperature. In Figure 2.5, the Sn/Ge(111) phase diagram was determined using RHEED [8] and was focussed on the high temperature region where the (7 x 7) and (5 x 5) phases exist. At lower temperatures, it does not fully describe the complexity of the phases.

More descriptive surface phase diagrams for Sn/Ge(111) and Pb/(111) are shown in Figure 2.6 [9 - 10]. In part A, increasing amounts of Pb on the surface changes the reconstruction from c(2 x 8) for the clean Ge surface to a (1 x 1) phase. At 1/3 ML the α-phase forms with a $(\sqrt{3} \times \sqrt{3})R30°$ unit cell (to be referred
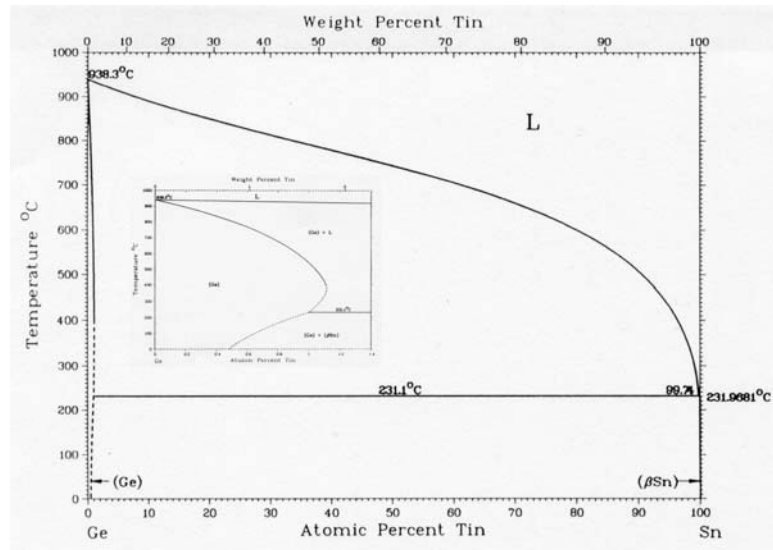
Figure 2.3: Bulk phase diagram for Sn-Ge. Inset shows the Sn solubility is nearly 1.0 atomic percent at 325 °C. Figure taken from reference [6].
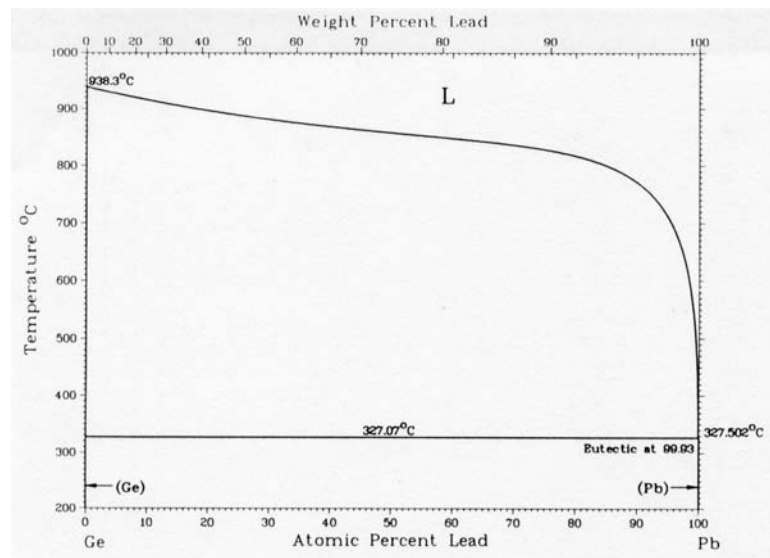
Figure 2.4: Bulk phase diagram for Pb-Ge. Pb solubility in Ge is virtually zero over a wide temperature range. Figure taken from reference [6].
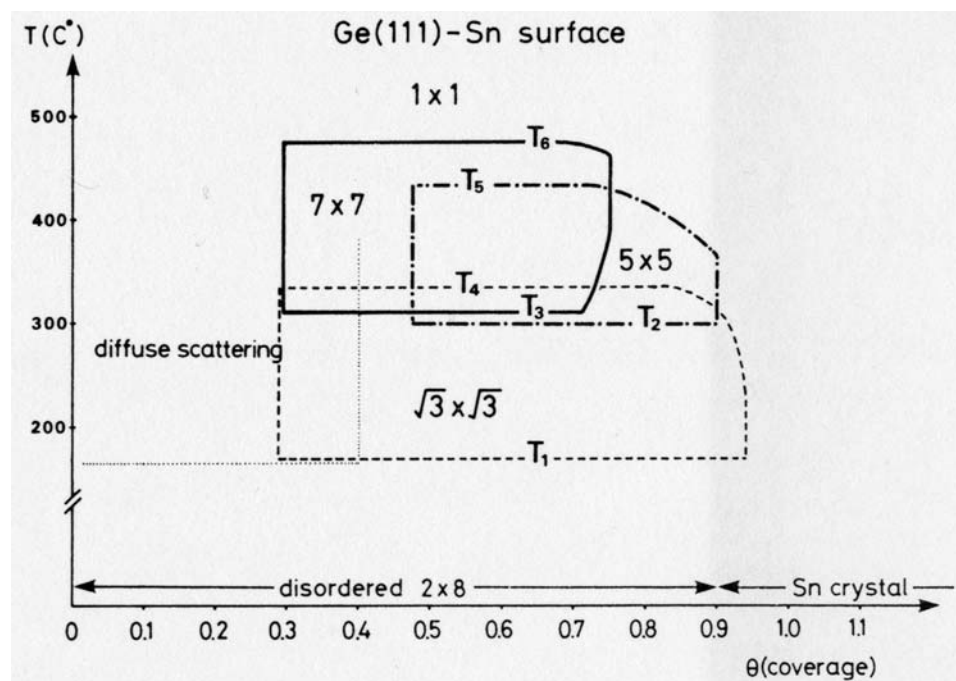
Figure 2.5: Surface phase diagram for Sn on Ge(111) depicts the surface reconstructions present as a function of atomic layer coverage Θ and temperature. This Sn/Ge(111) phase diagram was determined using RHEED and does not fully describe the complexity of the phases at lower temperatures. Figure taken from reference [8].
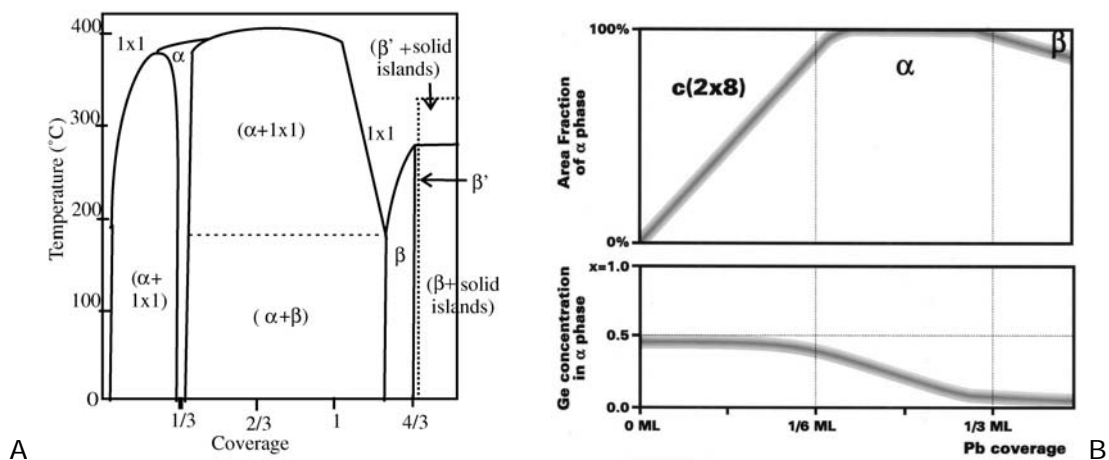
Figure 2.6: Surface phase diagrams for Pb on Ge(111) based on SXRD and STM. A) The addition of the Pb (or Sn) adatoms at low coverage onto the clean Ge(111) causes the surface to form a (1 x 1) reconstruction that is also present at high temperatures. The α-phase is centered at 1/3 ML and the β-phase forms near 4/3 ML. While the $\alpha-$ and β-phases both have $\sqrt{3}$ reconstructions, they have different densities, 1 and 4 atoms/unit cell, respectively. When the amount of Pb (or Sn) exceeds 4/3 ML, islands begin to form. The two-phase regions between these single-phase fields are a combination of adjacent phases. B) A more detailed phase diagram near 1/3 ML Pb on Ge(111) that also shows the solubility of Ge in the γ-phase between 1/6 and 1/3 ML. Figures taken from references [9] and [10].

to as √3). A more dense β-phase also has a √3 unit cell at 4/3 ML. While the α–
and β-phases both have √3 reconstructions, they have different densities, 1 and 4
atoms/unit cell, respectively. When the amount of Pb (or Sn) exceeds 4/3 ML,
islands begin to form. The two-phase regions between the single-phase fields are a
mixture of adjacent phases.

There are also reports of a "mosaic" γ-phase at 1/6 ML with a (2 x 2) structure
[11]. The description of this phase varies among different groups, but the idea can
be seen in Figure 2.6B. In the region between 1/6 to 1/3 ML, the adlayer is
composed of a mixture of Pb and Ge atoms. Due to ordering of the Pb and Ge
atoms, the structure appears more like a (2 x 2) phase. The atomic ordering in this
Ge_{1-x}-Pb_x phase is discussed in section 2.4.

2.3.2 (√3 x √3)*R*30° to (3 x 3) phase transition for the 1/3 ML
Sn/Ge(111) and 1/3 ML Pb/Ge(111) systems

The two material systems of 1/3 ML Sn/Ge(111) and 1/3 ML of Pb/Ge(111)
form similar atomic-scale structures and have similar phase transitions. The
background description for this section will focus primarily on the 1/3 ML
Sn/Ge(111) system because more research exists for this in the literature. When
the published results for the structure and behavior of 1/3 ML Pb/Ge(111) differ
from Sn, they will be addressed.

Figure 2.7 contains a top view of the α-phase with a √3 reconstruction for 1/3
ML Sn on the Ge(111) surface. The Sn adatoms are located at T_4-adsorption sites
and are represented with red circles; the top Ge bilayer is shown with black circles.
The Sn adatoms occupy 1/3 of the T_4-sites [12 - 13]. The (1 x 1), √3, and
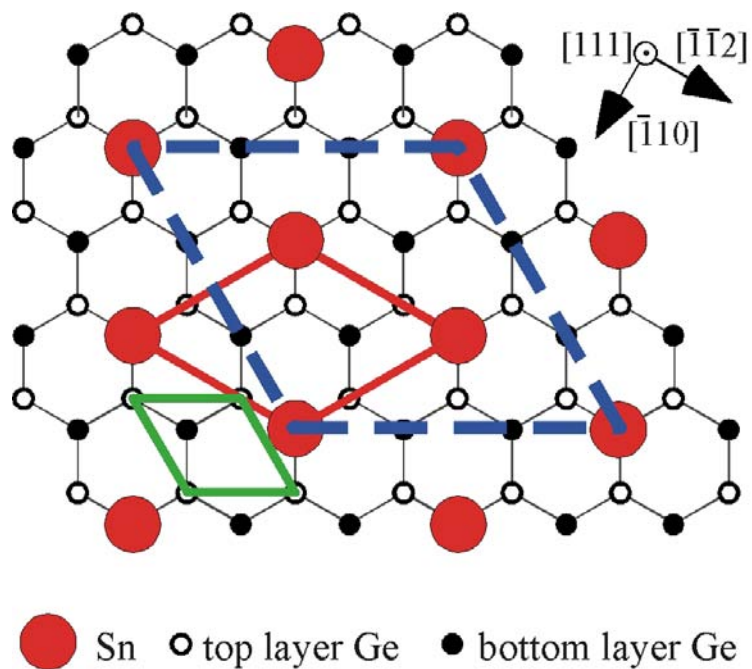
Figure 2.7: Top view of the α-phase with a (√3 x √3)R30° reconstruction for 1/3 ML Sn on the Ge(111) surface. The Sn adatoms at T_4-adsorption sites are represented with red circles, and the top Ge bilayer (two layers separated by $d_{111}/4$) are shown with black circles. The (1 x 1), (√3 x √3)R30°, and (3 x 3) surface unit cells are outlined in green, red, and dashed blue lines, respectively.

(3 x 3) surface unit cells are outlined in green, red, and dashed blue lines, respectively.

The 1/3 ML Sn phase has attracted interest due to the presence of a gradual and reversible phase transition from √3 to (3 x 3) when it is cooled. The onset has been reported near 210 K (253 K for Pb) with completion near 100 K [14 - 15]. This phase transition was first reported for Pb on Ge(111) based on experiments using STM and LEED [14]. The STM images show the Sn atoms occupying one-third of the T_4 sites as shown in Fig. 2.8. At room temperature (RT) all of the Sn adatoms appear equivalent. However, at low temperature (LT) the STM image of the atomic protrusions in the electron density of states shows that one of the three atoms per (3 x 3) unit cell appears different than the other two. In the registry aligned STM images (60 Å x 105 Å in size) for Sn on Ge(111), there appears two types of Sn atoms at LT with a 1:2 occupation ratio [15]. Ge substitutional defects appear as black points in the filled state images.

Initially, the authors attributed this difference in appearance at LT to a redistribution of valence charge for the Pb atoms and not to atomic displacements [14, 16]. Despite numerous investigations into this system, the structure and nature of this transition are still unresolved [17 - 26].

2.3.3 Electronic structure measurements

Counting the electrons for the 1/3 ML Sn on Ge(111) surface in the top view of Figure 2.7, the Sn atoms on the surface are expected to have half-filled, dangling bonds oriented normal to the surface. Contrary to expectations that these dangling bonds would have a half-filled dispersive surface state, experiments measured two
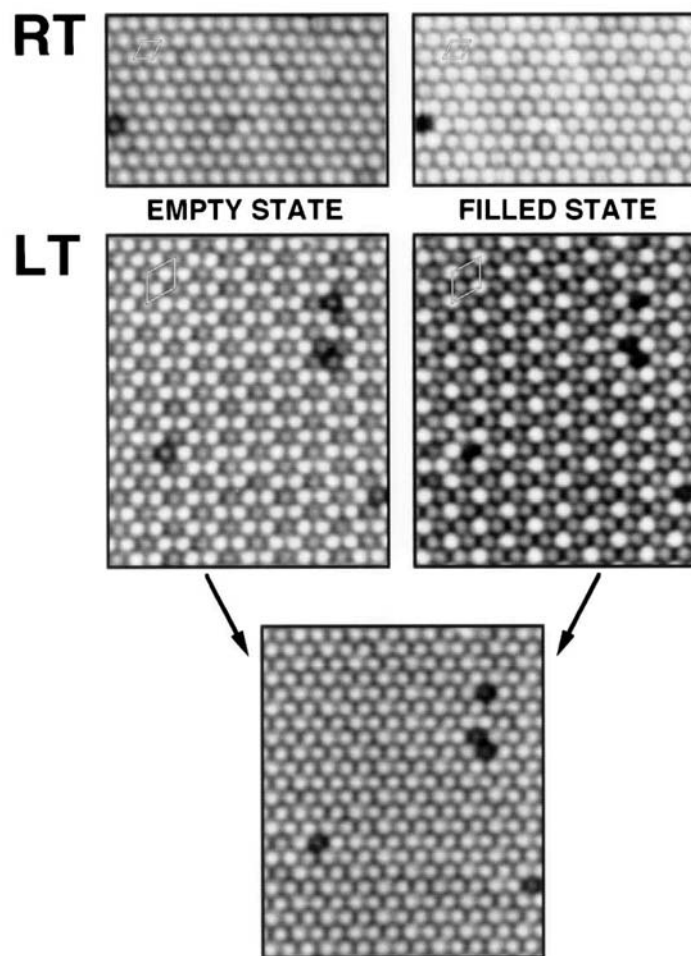
Figure 2.8: Registry aligned STM images (60 Å x 105 Å in size) for Sn on Ge(111). The empty state (V_{sample}=+1.0 V) images on the left and the filled state (V_{sample}=-1.0 V) images show the density of states for the surface at RT and LT (60 K). The Sn atoms at RT appear equivalent. Two types of Sn atoms appear at LT with a 1:2 occupation ratio. Ge substitutional defects appear as black points in the filled state images. Figures taken from reference [15].

components in the Sn $4d$ core-level spectra for the $\sqrt{3}$, which is inconsistent with a single type of Sn at the T_4-site [27].

Later, core level spectroscopy measurements were also made for the (3 x 3) surface reconstruction and was found to have similar features as the $\sqrt{3}$ phase [17]. As shown in Figure 2.9, the Sn $4d$ emission data for both structures are similar to each other [17]. While the existence of these two components may agree with the STM images at LT, showing two types of Sn adatoms, the spectra did not agree with a single T_4-adsorption site. When the surface structure changes from $\sqrt{3}$ to (3 x 3), the Sn atoms do not appear to undergo a significant change in their electronic structure.

2.3.4 Diffraction measurements on the RT ($\sqrt{3}$ x $\sqrt{3}$)R30° and LT (3 x 3) phases

To better understand this phase transition, the atomic-scale structures for the two phases need to be accurately quantified. Several SXRD experiments have been completed for this system but have come to somewhat different conclusions [20 - 21, 23]. The initial SXRD measurements were focussed on measuring the atomic-scale structure for both of the RT $\sqrt{3}$ and LT (3 x 3) phases. The main controversies are whether the Sn atoms (and underlying Ge atoms) possess a rippled topography at both RT and LT, and whether the topography is "one up and two down" or "two up and one down".

In their structural models for the 1/3 ML Sn/Ge(111) surface, Bunk *et al.* concluded the Sn atoms in the $\sqrt{3}$ phase were in the T_4-site and had a single height of 1.84 Å above the surface [20]. For the (3 x 3) phase, their model had three
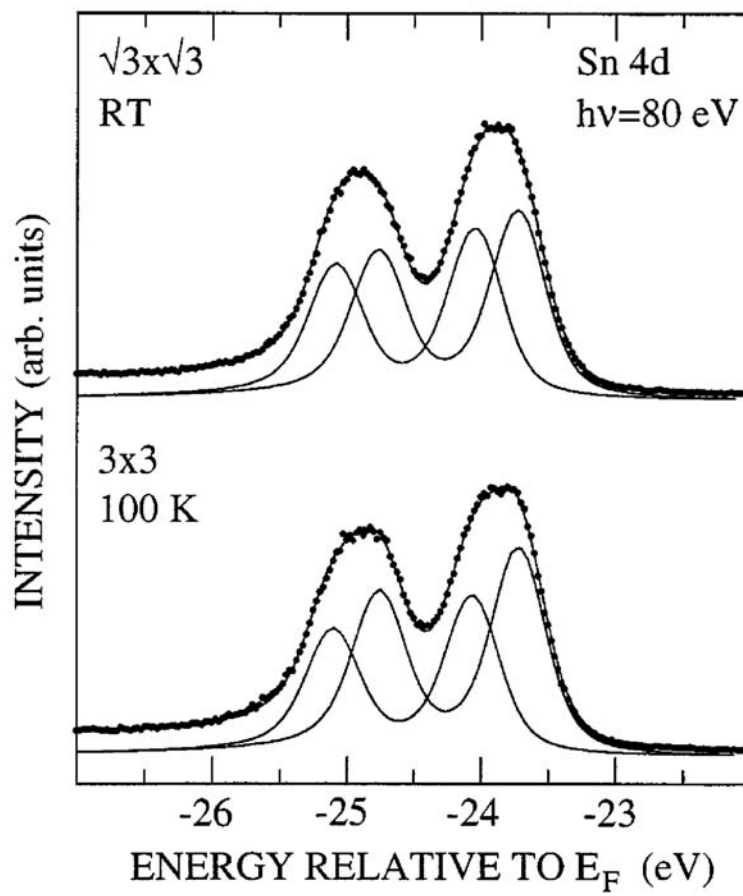
Figure 2.9: Sn 4*d* core-level spectra for the √3 and the (3 x 3) surface reconstructions. The Sn 4*d* emission data for both structures are very similar to each other. The existence of the two components in the spectra is inconsistent with a single T_4-adsorption site. Figures taken from reference [17].

different Sn atoms per unit cell (two of them with comparable heights) that had a vertical separation of 0.26 Å in a "one up and two down" geometry. These structures can be seen in Figure 2.10 with side views for the √3 phase at RT (in A) and the (3 x 3) phase at LT (in B) [20]. The distortions from their bulk-like positions for the Ge atoms are listed near the atoms. In the model for the (3 x 3) phase, the displacements are relative to the RT √3 structure. In both cases, the distortions in the Ge atom positions extend down to the third bilayer. At LT, the (3 x 3) diffraction peaks are ~4X wider than the √3 diffraction spots and correspond to a 120 Å domain size for the (3 x 3) phase [20].

In the SXRD measurements by Avila *et al.*, they measured the structure at LT [23]. Their results for the LT (3 x 3) phase differed from others; their model had a "two up and one down" configuration. Also, they measured some of the fractional order rods for the (3 x 3) phase as a function of temperature. They concluded that the size of the (3 x 3) domains decreased in area as the temperature increased towards the transition temperature; the (3 x 3) diffraction spots are not observed at RT because the (3 x 3) domain size approaches zero.

The only reported SXRD measurements on the LT (3 x 3) phase for 1/3 ML Pb on Ge(111) are by Mascaraque *et al.* [28]. Their structural model is "one up and two down" and similar to the one in Figure 2.10B, except the vertical separation in the Pb heights is ~0.4 Å.

A

B

Figure 2.10: Side views of atomic structural models from SXRD measurement for A) the √3 phase at RT and for B) the (3 x 3) phase at LT. In the √3 model, there is a single Sn atom in the T_4-adsportion site and is 1.84 Å above the bulk-like surface. The model for the (3 x 3) phase has three different Sn atoms per unit cell, although two have similar heights. The distortion of the Ge atom positions are listed in Å and extend down to the third bilayer. Figures taken from reference [20].

2.3.5 (√3 x √3)*R*30° to (3 x 3) phase transition

The leading models for this phase transition generally fall into either a displacive or an order-disorder transition type. This difference in the phase transitions can be considered in the contexts of a double well potential [26], shown in Figure 2.11. In this simplified picture, the configurations for the Sn atoms are represented by the two minima of the double well potential. Below the transition temperature, the Sn atoms are locked into a long-range ordered up/down structure and do not have enough thermal energy to pass over the barrier height between the two positions. In a displacive phase transition, the free energy curve with a double-well potential is related to the entropy ($\Delta G = \Delta H - T\Delta S$). As the temperature increases, the double-well potential gives rise to a curve with a single minimum. Therefore, the atoms have an average position in the center of the potential well. In an order-disorder phase transition, the barrier height is of comparable magnitude to the thermal energy above the transition temperature. In the RT phase, the atoms primarily occupy the two positions in the double potential well, but can move between them.

2.3.5.1 Displacive phase transition

In STM images, it has been observed that Ge atoms can replace Sn atoms in the adlayer [15, 29, 30] and can be considered substitutional point defects. At RT the Sn atoms nearest to the Ge defects appear as a small patch with (3 x 3) structure. As the temperature is lowered past the transition point, these little
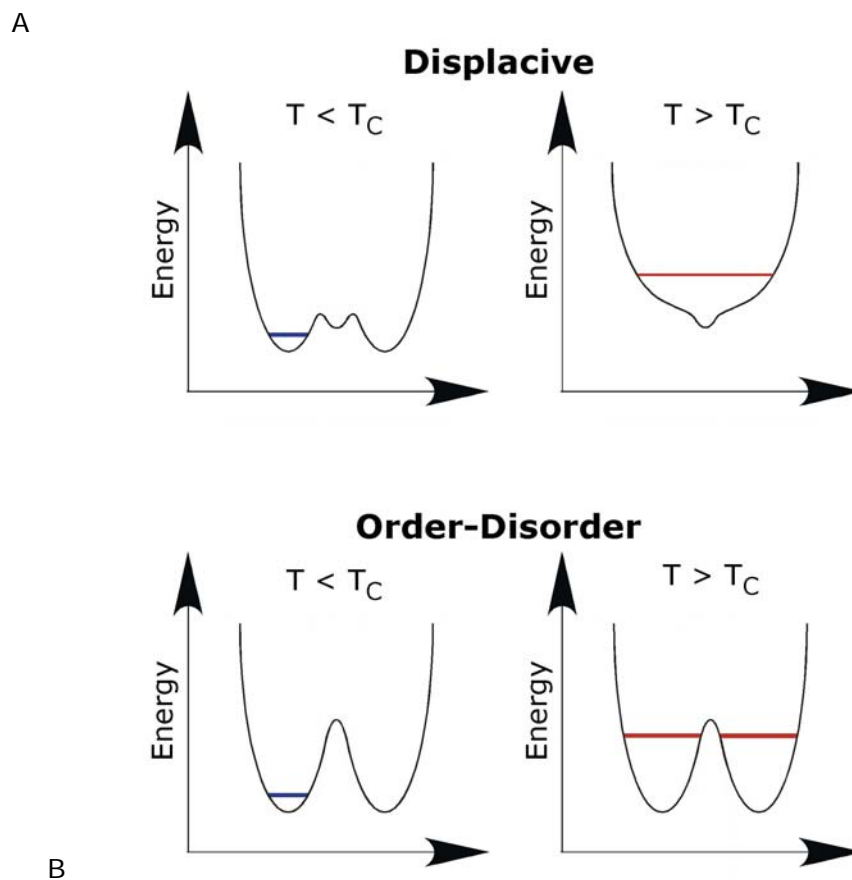
Figure 2.11: Displacive and order-disorder phase transitions can be considered in the contexts of a double well potential. A) In a displacive phase transition, the free energy is dominated by the entropy term, $\Delta G = \Delta H - T\Delta S$. As the temperature increases, the double-well potential transforms to a curve with a single minimum, therefore, the atoms have an average position in the center of the potential well. B) In an order-disorder phase transition, the barrier height is of comparable magnitude to the thermal energy above the critical temperature T_C. Below the T_C, the structure has the ground state structure. Above the transition temperature, the atoms primarily occupy the two end positions but can move between them.
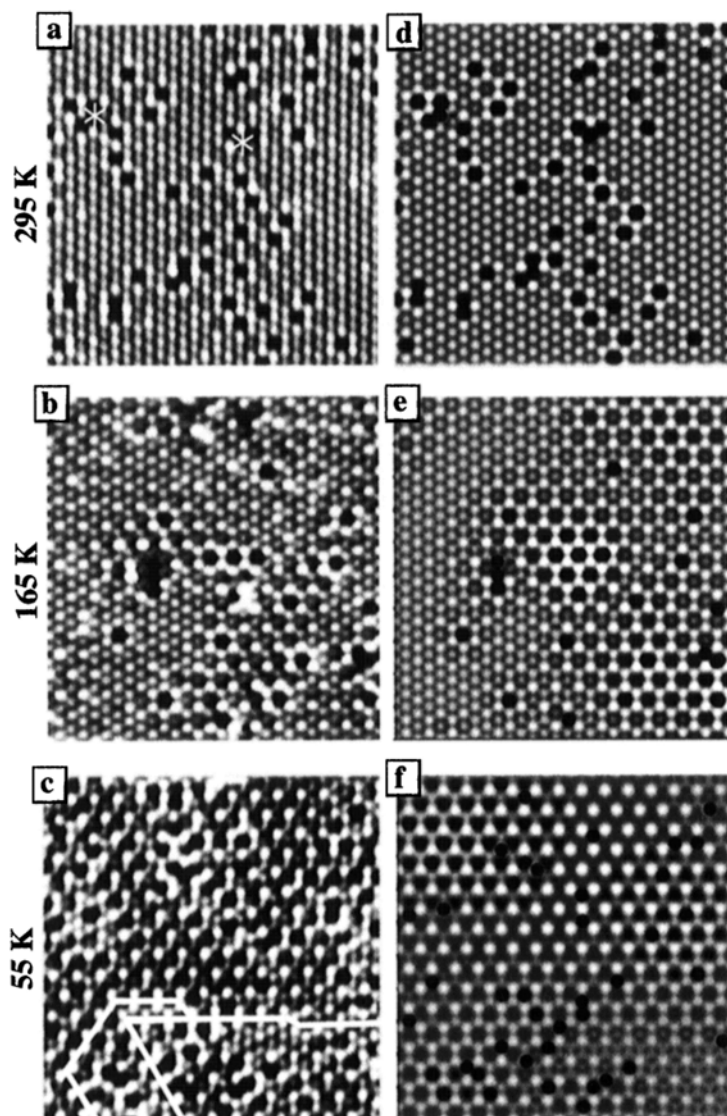
Figure 2.12: STM filled state images for Sn on Ge(111) at three temperature (a – c) and simulated images (d – f). Two Ge substitutional defects are labeled with asterisks in a. The (3 x 3) domain size increases as the temperature decreases. The decay lengths in the simulations in images d–f correspond to 11, 25, and 100 Å. Figures taken from reference [31].

regions of (3 x 3) phase increase in area. This can be seen in Figure 2.12 in the STM filled state images for Sn on Ge(111) at three temperature (A: 295, B: 165, C: 55 K) and their simulated images (D – F) from [31]. Two Ge substitutional defects are labeled with asterisks in A. The (3 x 3) domain size increases as the temperature decreases. The decay length in the simulations in images D – F correspond to 11, 25, and 100 Å.

2.3.5.2 Order-Disorder Phase Transition

In an order-disorder model for the transition, Avila *et al.* used molecular dynamics to show that the vertical distribution of Sn atoms is attributed to dynamical fluctuations [19]. In this model, the distribution of Sn is correlated and varies in time for the three Sn atoms in the (3 x 3) unit cell. As shown in Figure 2.14 [19], below the transition temperature (125 K) the Sn atom are locked into either an up position (blue) or the down position (black and red). The long-range order of the Sn heights gives rise to the (3 x 3) unit cell. As the temperature increases above the transition temperature, the Sn atoms undergo rapid, correlated interchanging in their heights. On average, one Sn is in the up position and two Sn atoms are in the down position. At RT structural probes, like STM and diffraction, observe the smaller $\sqrt{3}$ unit cell with higher symmetry because all of the Sn atoms appear equivalent due to time averaging of the rapid interchanging of their heights.

In density functional theory calculations on the 1/3 ML Sn on Ge(111) surface, Pérez *et al.* demonstrated the presence of a soft phonon at the surface that is stabilized by rehybridization of the Sn dangling bond [24]. In this lattice vibration, the motion of one Sn atom moving upwards is coupled to the motion of the
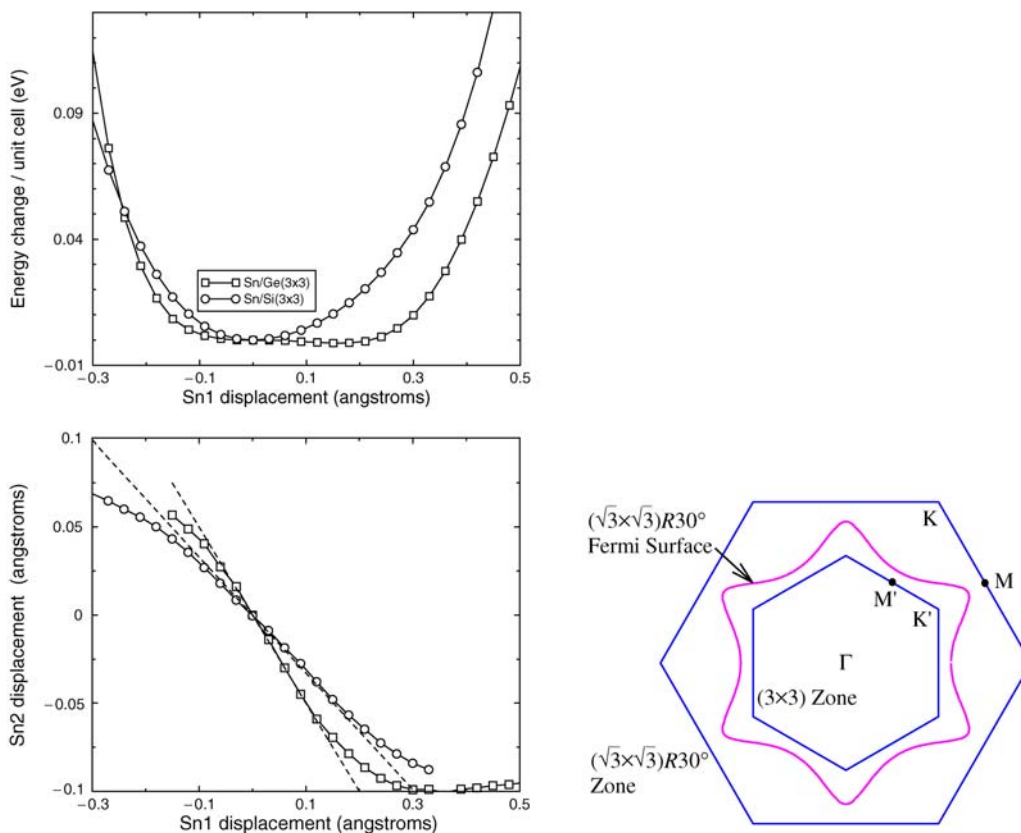
Figure 2.13: Calculations for the soft phonon model of Sn on the Ge (and Si) surface. A) The total energy as function of Sn vertical displacement on Ge shows a flat region where the location of the Sn adatoms has little variation in energy. B) The displacement of one Sn atoms is coupled to the displacement of the other two Sn atoms in the (3 x 3) unit cell. C) The larger hexagon shows the outer boundary of the first Brillouin zone for the √3 phase. The smaller hexagon represents the boundary for the first Brillouin zone for the (3 x 3) phase. Figures taken from references [24] and [11].
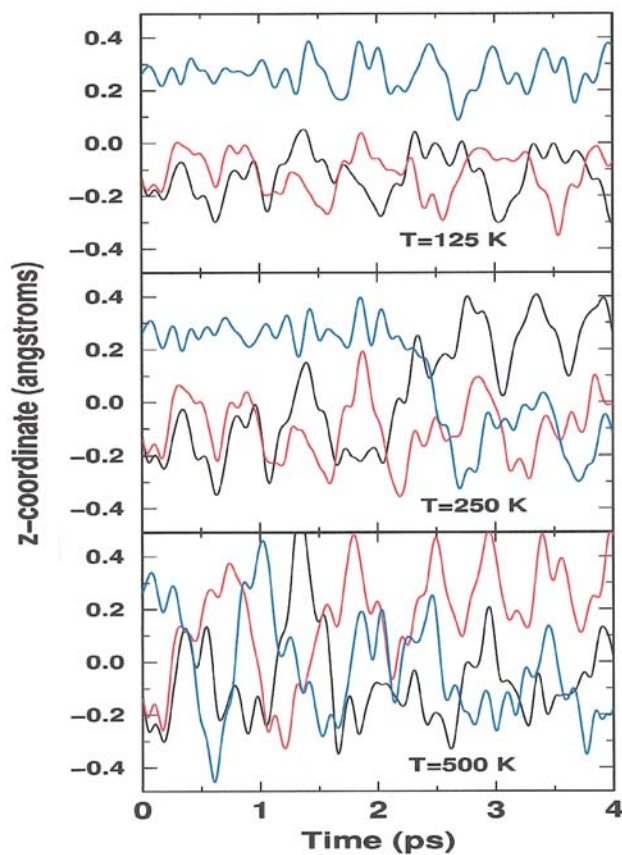
Figure 2.14: In the dynamical fluctuations model, the distribution of Sn is correlated and varies in time for the three Sn atoms in the (3 x 3) unit cell. Below the transition temperature (125 K) the Sn atom are locked into either an up position (blue) or the down position (black and red). The long range order of the Sn heights gives rise to the (3 x 3) unit cell. As the temperature increases above the transition temperature, the Sn atoms undergo rapid, correlated interchanging in their heights. On average, one Sn is in the up position and two Sn atoms are in the down position. The rapid interchanging of the Sn heights makes the Sn atoms appear equivalent, giving rise to the $\sqrt{3}$ phase. Figures taken from reference [19].

remaining two Sn atoms, in the (3 x 3) unit cell, moving downwards. In Figure 2.13 [24], the graph shows that the lattice vibration energy is low for the Sn atoms moving in the range of −0.1 to 0.2 Å in height. A zero frequency mode for the soft phonon is found in a position corresponding to the $\overline{K}'$ point (see bottom of Figure 2.13) and matches the (3 x 3) periodicity. When the frequency goes to zero, the phonon becomes static and is considered to be frozen. Petersen *et al.* later proposed that the Ge defects locally freeze in a soft phonon mode for the (3 x 3) phase [26].

2.4 Short-range order at low-coverage for the Pb-Ge

In the Pb/Ge(111) phase diagram shown in Figure 2.6B [10], the Pb and Ge adatoms are shown to be soluble for the α-phase over the range of 1/6 ML to 1/3 ML. For this √3 structure, the surface can be considered to be a mixture of Pb and Ge atoms with a composition of $Pb_{1-x}Ge_x$, where $0 \leq x \leq 0.5$. STM images for this $Pb_{1-x}Ge_x$ α-phase at two different coverages of Pb on Ge(111) are shown in Figure 2.15 [10]. Using images in both empty and filled states, the vacancies (arrow 1), Pb atoms (arrow 2), and Ge atoms (arrow 3) can be distinguished.

In Figure 2.15A, the filled state image shows some ordering of the Ge and Pb atoms. There appears some coordination preference in the 1st and 2nd nearest neighbor shells. In Figure 2.15B, the filled state image shows a very high degree of ordering of the Ge and Pb atoms along three axes. This ordering in the surface plane can be quantified using the Warren-Cowley short-range order parameter α_{lm} that is defined as [32],

$$\alpha_{lm} = 1 - \left(\frac{P_{lm}^{AB}}{c_B} \right) \equiv 1 - \left(\frac{P_{lm}^{BA}}{c_A} \right) \quad . \tag{2.1}$$

P_{lm}^{AB} is the conditional probability of finding an atom B at the end of a vector $\mathbf{r}_{lm}$ originating from an atom A, P_{lm}^{BA} is the conditional probability of finding an atom B at the end of a vector $\mathbf{r}_{lm}$ originating from an atom B, c_A is the fractional composition of component A, and c_B is the fractional composition of component B. If there is a preference for unlike neighbors, $\alpha_{lm} < 0$. If there is a preference for like neighbors, $\alpha_{lm} > 0$. For a random arrangement of atoms, $\alpha_{lm} = 0$.

By superimposing a grid onto the STM images of $Pb_{1-x}Ge_x$ in Figure 2.15, the composition at the sites can be determined, and the short-range order parameter can be calculated. The images in Figure 2.15A and B have a composition of $Pb_{0.8}Ge_{0.2}$ and $Pb_{0.6}Ge_{0.4}$, respectively, and the values for α_{lm} are listed in Table 2.1. The error values for α_{lm} were determined by taking the standard deviation between the three directions. As apparent with visual inspection of the STM image in Figure 2.15B, the $Pb_{0.6}Ge_{0.4}$ surface has a high degree of ordering. A value of -0.21 for α_{10} shows a strong preference for unlike neighbors in the first coordination shell. The positive value of 0.12 for α_{11} indicates there is fairly high preference for the second nearest neighbor to be the same as at the origin the $\mathbf{r}_{lm}$. (While this short-range ordering is not further explored here, it does offer an interesting system for future work.)
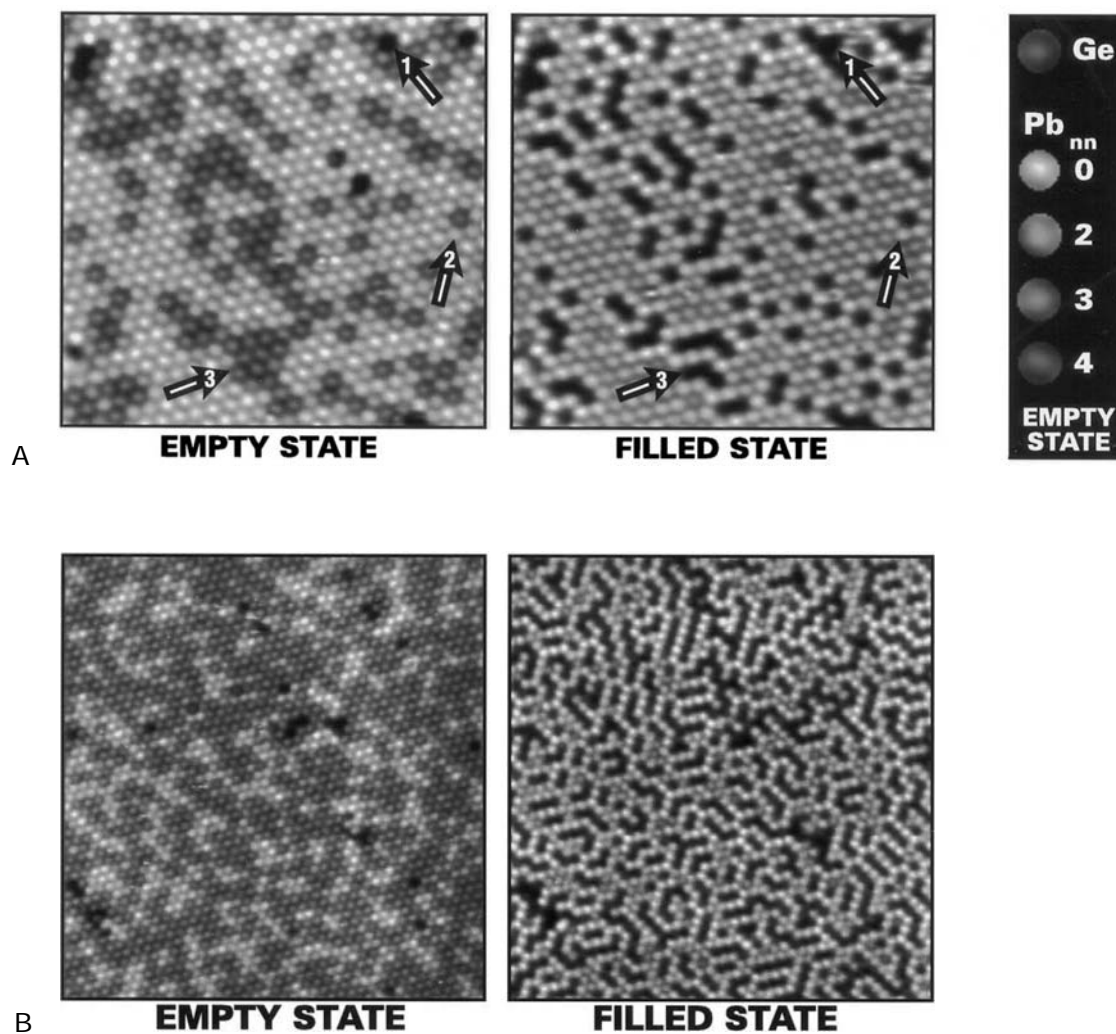
Figure 2.15: STM images of the γ-phase $Pb_{1-x}Ge_x$ alloy for different coverages of Pb on Ge(111). Using images in both empty and filled states, the vacancies (arrow 1), Pb (arrow 2), and Ge (arrow 3) can be distinguished. A) Filled state image for $Pb_{0.8}Ge_{0.2}$ shows some ordering of the Ge atoms. B) Filled state image for $Pb_{0.6}Ge_{0.4}$ shows a high degree of ordering of the Ge and Pb atoms along three directions. Figures taken from reference [10].

Table 2.1: Measured Warren-Cowley short range ordering parameter for Pb-Ge from STM images in Figures 2.15A and 2.15B.

l	m	r/a	Figure 2.15A	Figure 2.15B
1	0	1.00	-0.05 (3)	-0.21 (3)
1	1	1.73	0.05 (2)	0.12 (1)
2	0	2.00	0.02 (2)	0.02 (1)
2	1	2.65	-0.02 (2)	-0.06 (3)
3	0	3.00	-0.02 (4)	0.02 (2)
2	2	3.46	-0.02 (2)	0.04 (5)
3	1	3.61	0.01 (3)	-0.01 (2)
4	0	4.00	-0.01 (6)	0.00 (3)
total # of atoms			701	2081
% Pb			79.7	59.9
% Ge			19.4	39.0
% vacancies			0.9	1.1

Chapter 3: X-ray Standing Wave Technique

3.1 Introduction

The x-ray standing wave (XSW) method is an established technique and can directly determine the atomic distribution of atoms within bulk crystals, in thin films, and at interfaces. The interference of two, superimposed x-ray beams creates an XSW field. Some of the geometries used to generate an XSW are: Bragg diffraction from bulk crystal or from thin films, total external reflection of x-rays from an interface, and diffraction from layered synthetic multilayers (with periods larger than typical interatomic planes). While many XSW experiments are made using nearly perfect single crystals of Si or Ge, the technique can also be applied to less than perfect crystals, such as natural minerals. In the following discussion, the focus is on an XSW created from Bragg diffraction with a superposition of an incident and diffracted x-ray beams on the "front" side of a single crystal.

The schematic in Figure 3.1 depicts how an XSW is generated from an x-ray
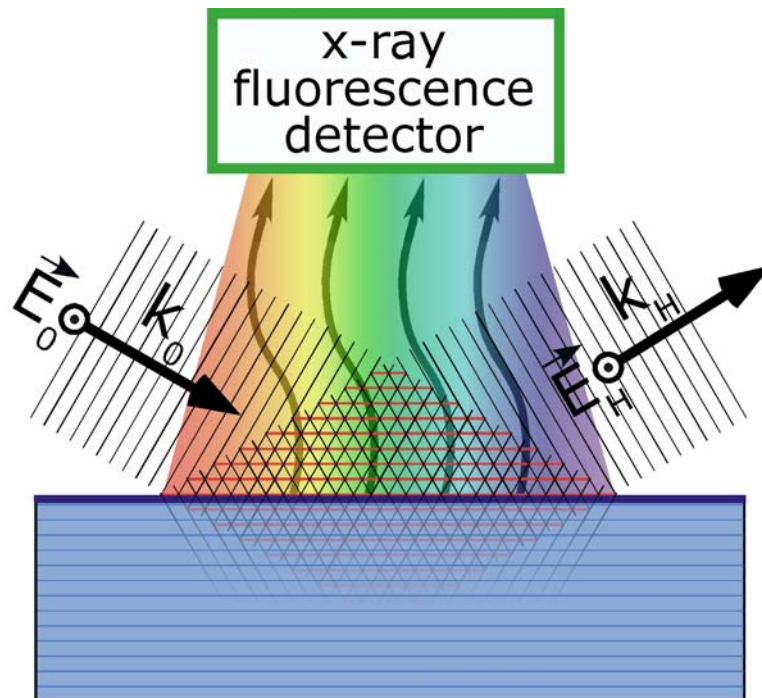
Figure 3.1: Schematic of the generation of an XSW and the x-ray fluorescence created by the electric fields. An incident wave vector $\mathbf{K}_0$ diffracts from a single crystal and creates the second electric field $\mathbf{K}_H$. Constructive interference fringes (shown in red) from these two plane waves are called the nodes of the XSW and exist inside the crystal, at the interface, and above the crystal surface. The modulated x-ray fluorescence is collected with an energy dispersive x-ray detector.

plane-wave undergoing Bragg diffraction from a bulk crystal. The incident plane-wave has a wave vector $\mathbf{k}_0$ and amplitude $\vec{E}_0$. The diffracted traveling plane-wave has a wave vector $\mathbf{k}_H$ and amplitude $\vec{E}_H$. The superposition of these two electric fields creates antinodes (shown in red) of constructive interference that have a period equal to the spacing of the interatomic planes of the Bragg reflection (depicted with horizontal, blue lines in the sample). The intensity of the electric field and the position of these antinodes will be described in the following section. When the sample is scanned through the Bragg reflection, the antinode of the XSW shifts in position and induces a modulation in the signal from the atoms within the XSW field. In this instance, the signal is the x-ray fluorescence and is measured using an energy dispersive detector. It should also be noted that because x-rays have a relatively low interaction cross-section with matter, x–rays (on the order of 10 keV) penetrate inside of the crystal in the μm range. The incident and diffracted plane waves generate the XSW; therefore the XSW exists inside of the crystal, at the interface, and above the surface.

Batterman first observed XSW fields inside of a Ge single crystal [33]. He later demonstrated the XSW technique by measuring the position of substitutional, arsenic atoms inside of a single crystal of silicon [34]. Golovchenko and others later expanded XSW use for atoms absorbed on surfaces [35 - 36]. Further utilization came with combining XSW measurements from normal and off-normal reflections to the surface to triangulate the adsorption site for adsorbate atoms [36]. Several reviews on the XSW method have been prepared by Afanas'ev *et al* [37], Takahashi and Kikuta [38], Hertel *et al* [39], Bedzyk and Materlik [40],

Zegenhagen [41], and Bedzyk and Cheng [42]. In this chapter, the XSW method will be explained using classical dynamical diffraction theory. The traditional method of using XSW to measure and triangulate the positions of adsorbate atoms on surface will be explained, as well as one potential problem of this method. Later in this chapter, a new method for direct space imaging of atoms based on the information determined from XSW measurements is introduced and demonstrated.

3.2   Dynamical diffraction theory for x-rays

In a kinematical approach, Bragg's Law can be used to describe the diffraction condition,

$$\lambda = 2\mathrm{d}\sin\left(\theta_\mathrm{B}\right) \quad . \tag{3.1}$$

Here λ is the x-ray wavelength, d is the interatomic planar spacing ($d = 1/|\mathbf{H}|$), and θ_B is the Bragg angle. The real diffraction vector $\mathbf{H}$ is equal to $h\mathbf{a}^* + k\mathbf{b}^* + l\mathbf{c}^*$. However, to consider how the XSW is generated from a Bragg reflection from a nearly perfect single crystal, a dynamical diffraction theory of x-rays is needed. The approach presented here follows from the work of von Laue and Ewald [43] and has been reviewed Batterman and Cole [44], and Authier [45]. The real, external wave vectors $\mathbf{k}_0$ and $\mathbf{k}_H$ are related to the complex, internal wave vectors $\mathbf{K}_0$ and $\mathbf{K}_H$ through boundary conditions at the crystal surface. For dynamical

diffraction theory of x-rays, the incident $\mathbf{K}_0$ and diffracted $\mathbf{K}_H$ internal wave vectors are related using the Laue condition, as shown in Equation 3.2,

$$\mathbf{K}_H = \mathbf{K}_0 + \mathbf{H} \quad . \tag{3.2}$$

The internal incident and diffracted x-rays (with a frequency ν) can be described as complex, electromagnetic plane waves with the form of

$$\vec{\mathcal{E}}_0(\mathbf{r}, t) = \vec{E}_0 \exp\left[2\pi i(\nu t - \mathbf{K}_0 \cdot \mathbf{r})\right] \tag{3.3}$$

and

$$\vec{\mathcal{E}}_H(\mathbf{r}, t) = \vec{E}_H \exp\left[2\pi i(\nu t - \mathbf{K}_H \cdot \mathbf{r})\right] \quad . \tag{3.4}$$

While the electric field can be divided into two polarization states (σ and π), only the σ-polarization state is considered here because all of the experiments used this geometry. Additionally, the synchrotron radiation at the Advanced Photon Source can be considered as linearly polarized. The total electric field $\vec{\mathcal{E}}_T$ is the summation of the incident and diffracted plane waves,

$$\vec{\mathcal{E}}_T = \vec{\mathcal{E}}_0 + \vec{\mathcal{E}}_H$$

$$= \vec{E}_0 \exp\left[2\pi i\left(\nu t - \mathbf{K}_0 \cdot \mathbf{r}\right)\right] + \vec{E}_H \exp\left[2\pi i\left(\nu t - \mathbf{K}_H \cdot \mathbf{r}\right)\right]$$

$$= \vec{E}_0 \exp\left(2\pi i\nu t\right)\left[\exp\left(-2\pi i\mathbf{K}_0 \cdot \mathbf{r}\right) + \frac{E_H}{E_0}\exp\left(-2\pi i\mathbf{K}_H \cdot \mathbf{r}\right)\right] \quad . \tag{3.5}$$

$$= \vec{E}_0 \exp\left(2\pi i\nu t\right)\exp\left(-2\pi i\mathbf{K}_0 \cdot \mathbf{r}\right)\left[1 + \frac{E_H}{E_0}\exp\left(-2\pi i\mathbf{H} \cdot \mathbf{r}\right)\right]$$

The complex electric field amplitude ratio E_H/E_0 can be determined using dynamical diffraction theory to give the following,

$$\frac{E_H}{E_0} = -|b|^{1/2}\left(\frac{F_H}{F_{\overline{H}}}\right)^{1/2}\left(\eta \pm \left(\eta^2 - 1\right)^{1/2}\right) \quad . \tag{3.6}$$

The asymmetry factor b is determined by the following equation,

$$b = -\frac{\sin\left(\theta_B - \phi_m\right)}{\sin\left(\theta_B + \phi_m\right)} \quad . \tag{3.7}$$

The misalignment angle ϕ_m is the angle between the diffraction plane normal and the surface normal.   A positive value for ϕ_m represents a diffraction vector inclined towards the incident x-ray beam.   For symmetric reflections, $\phi_m = 0$ and

$|b| = 1$. The reduced angle parameter η is related to $\Delta\theta$ (the difference from the Bragg angle, $\theta - \theta_B$) by

$$\eta = \frac{b \sin(2\theta_B)\Delta\theta + \frac{1}{2}(1-b)F_0\Gamma}{|b|(F_H F_{\overline{H}})^{1/2}\Gamma} \quad . \tag{3.8}$$

The constant Γ is defined as

$$\Gamma = \frac{r_e \lambda^2}{\pi V_{uc}} \quad , \tag{3.9}$$

where r_e is the value for the classical electron radius ($r_e = e^2/mc^2 = 2.82 \times 10^{-5}$ Å) and V_{uc} is the volume of the unit cell of the crystal. The structure factor F_H for the **H** Bragg reflection can be determined from the summation

$$F_H = \sum_j^N (f_0 + \Delta f' + i\,\Delta f'')_j^H \exp\left[2\pi i(\mathbf{H}\cdot\mathbf{r_j})\right] \quad , \tag{3.10}$$

where f_0 is the form factor of the atoms in the unit cell. Including $\Delta f'$ and $\Delta f''$ corrects for anomalous dispersion. The position (in fractional coordinates) of the jth atom in the unit cell is represented by r_j. F_H is the Hth Fourier coefficient of the electron density of the lattice and is properly described as a complex value,

$$F_H = F_H' + iF_H'' \quad , \tag{3.11}$$

where F_H' and F_H'' are the real and imaginary components of F_H. The ratio of the electric fields can also be expressed in a complex-plane form as

$$\frac{E_H}{E_0} = \left| \frac{E_H}{E_0} \right| \exp(i\varphi) \quad , \tag{3.12}$$

where φ is the phase difference between the incident and scattered waves. The reflectivity R can be expressed as

$$R = \left| \frac{E_H}{E_0} \right|^2 \quad . \tag{3.13}$$

The plot of reflectivity as a function of θ is often called the rocking curve or the Darwin reflectivity curve. The Darwin width (of the curve) can be calculated with

$$\omega = \frac{2\Gamma \sqrt{(F_H' F_H' + F_0''^2 - F_H'' F_H'')}}{\sin(2\theta_B) |b|^{1/2}} \quad . \tag{3.14}$$

Using a complex-plane form of the ratio of electric field shown in Equation 3.11, the total electric field can be expressed as

$$\vec{\mathcal{E}}_T = \vec{E}_0 \exp(2\pi i \nu t)\exp(-2\pi i \mathbf{K}_0 \cdot \mathbf{r})\left[1 + \left|\frac{E_H}{E_0}\right|\exp(i\varphi - 2\pi i \mathbf{H} \cdot \mathbf{r})\right]. \quad (3.15)$$

The normalized intensity of the total electric field,

$$I(\theta, z) = \frac{\vec{\mathcal{E}}_T \cdot \vec{\mathcal{E}}_T^*}{|E_0|^2}, \quad (3.16)$$

can be expressed as a function of the angle θ and the depth z,

$$I(\theta, z) = \left[1 + R(\theta) + 2\sqrt{R(\theta)}\cos(\varphi(\theta) - 2\pi \mathbf{H} \cdot \mathbf{r})\right] \times \begin{cases} 1; \text{ above the surface} \\ e^{-\mu_z(\theta)z}; \text{ z below surface} \end{cases}. \quad (3.17)$$

The effective thickness factor for atoms at the surface equals unity. The correction for the extinction effect varies with θ and z. The effective absorption coefficient μ_z varies with θ and can be expressed as

$$\mu_Z(\theta) = \mu_0 \frac{1 + \dfrac{F'_{\overline{H}}}{F''_0}\left(\dfrac{E_H}{E_0}\right)'' + \dfrac{F''_{\overline{H}}}{F''_0}\left(\dfrac{E_H}{E_0}\right)'}{\sin(\theta - \phi_m)}. \quad (3.18)$$

The linear absorption coefficient μ_0 is determined from

$$\mu_0 = \frac{2\pi F_0'' \, \Gamma}{\lambda} \quad .$$

(3.19)

In Figure 3.2 the reflectivity curves for the Ge (111) reflection is shown for two energies, 7.00 keV (blue) and 16.35 keV (red) [46]. The centers of both peaks are offset from the Bragg angle θ_B because of the change in the index of refraction at the Ge crystal surface. The full width at half maximum (fwhm) of the 7.00 keV and 16.35 keV are 101 μrad and 42.5 μrad, respectively. The curve for 7.00 keV is wider than the 16.35 keV curve because it has a larger Bragg angle and longer wavelength (see Equations 3.1, 3.9, and 3.14). As can be observed in Figure 3.2B, there is a π phase shift in the position of the antinodes as the angle is scanned through the rocking curves. For both energies, the penetration depth of x-rays ranges from about 0.3 μm to about 5 μm. The antinodes of the XSW are located on the (111) diffraction planes on the high-angle side of the rocking curve. The unit cell origin chosen for $\mathbf{r}_i$ is directly linked to the phases of the structure factor F_H, E_H/E_0, and the phase of the Fourier coefficient P_H. Unless noted otherwise for this work, the eight atoms in the diamond cubic lattice are located at the positions listed in Table 3.1. This choice places the origin on the atom located in the top position of the (111) bilayer, as shown in Figures 2.1 and D.1. The location of the origin
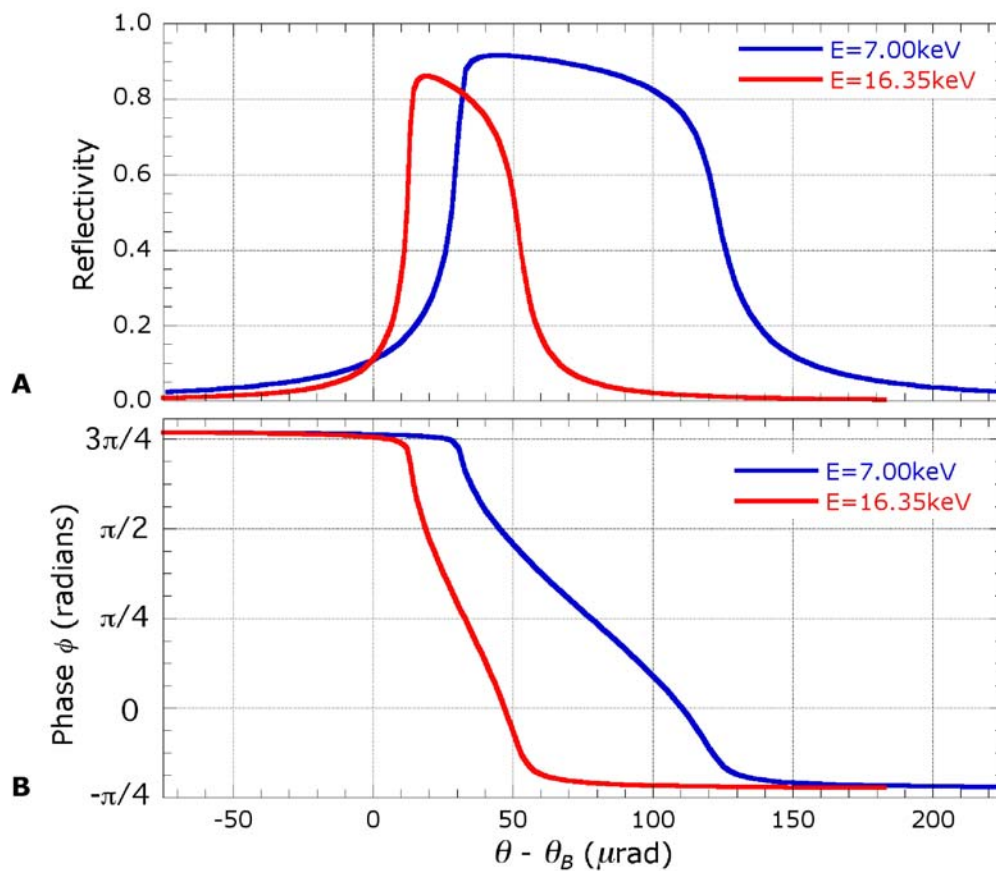
Figure 3.2: A) The angular dependence for the Ge(111) reflectivity at 7.00 keV (blue) and 16.35 keV (red). B) The phase of the XSW antinodes relative to the origin which is chosen to be located on the top atom in the (111) bilayer (as shown in Figure 2.2 and D.1).

chosen by some other researchers is shifted by a value (1/8, 1/8, 1/8) in orthogonal xyz-coordinates. The fractional coordinate values for other origins are listed in Appendix D and shown in Figure D.1.

Table 3.1: Fractional coordinates of the eight atoms in the diamond cubic crystal structure used in this work. The atom located at (0, 0, 0) is at the top position in the (111) bilayer.

x	y	z
0	0	0
1/2	1/2	0
1/2	0	1/2
0	1/2	1/2
1/4	1/4	1/4
3/4	3/4	1/4
3/4	1/4	3/4
1/4	3/4	3/4

3.3 XSW analysis

3.3.1 Determining the atomic distribution using the XSW technique

The XSW technique uses the modulated electric field intensity to probe the atomic distributions via the photoelectric effect. The phase of the XSW is determined relative to the bulk crystalline atomic lattice and is shifted by scanning

through a reflection. The period of these antinodes (constructive interference fringes) of the XSW are equal to the interplanar lattice spacing (diffraction plane spacing d). These antinodes of the XSW lie in planes parallel to the diffraction planes. As the angle θ is scanned through the Bragg condition, the positions of these antinodes translate in a direction normal to the atomic planes. A signal from the atoms within the XSW is generated because the x-rays cause the atoms to emit characteristic electrons and radiation by means of the photoelectric effect. As the XSW antinodes shift, the electron and photon yields will have a modulation unique to the atomic distribution. The determination of this distribution uses the dipole approximation for the photoelectric effect, which assumes the signal (photoelectrons, Auger electrons, or x-ray fluorescence) is proportional to the electric field intensity at the center of the atom [47].

In the photoelectric effect, an atom absorbs a photon, and a photoelectron is ejected with a kinetic energy of

$$E = h\nu - E_b \quad , \tag{3.20}$$

where $h\nu$ is the photon energy and E_b is the binding energy for the electron. The yield signal for an XSW measurement can be the primary emission (photoelectrons) and can also come from the secondary emission (fluorescent x-rays and Auger electrons), which are created when an outer level electron fills in an inner shell hole. The photoelectrons, Auger electrons, and x-ray fluorescence are element-specific signals with characteristic energies.

The periodic lattice, used to create the XSW, is also the basis for defining the atomic distributions for the atoms by using a normalized distribution function,

$$\int_{\substack{\text{unit}\\\text{cell}}} \rho(\mathbf{r})\, d\mathbf{r} = 1 \quad . \tag{3.21}$$

The distribution function for atoms $\rho(r)$ with a position r into the lattice is element specific and can differ for the atomic species. If the signal from the atom is proportional to the strength of the electric field intensity, then the total yield for the atomic distribution is

$$Y(\theta) = \int \rho(\mathbf{r})\, I(\theta, \mathbf{r}) \exp\left(-\mu_f(\alpha) z\right) d\mathbf{r} \quad . \tag{3.22}$$

The effective thickness absorption coefficient $\mu_f(\alpha)$ for the x-ray fluorescence emitted from the sample will depend on their take-off angle α.

The Hth Fourier component $\mathcal{F}_H[\rho(\mathbf{r})]$ has an amplitude f_H and phase P_H that are referred to as the coherent fraction and the coherent position, respectively, in XSW terminology. The off-Bragg yield corresponds to the 0th order Fourier component $\mathcal{F}_0$. From Equation 3.21, it can be seen that

$$\mathcal{F}_0[\rho(\mathbf{r})] = 1 \quad . \tag{3.23}$$

Using these coefficients, the terms inside the integral

$$\mathcal{F}_H\left[\rho(\mathbf{r})\right] = \int_{\substack{\text{unit}\\\text{cell}}} \rho(\mathbf{r})\exp(2\pi i\mathbf{H}\cdot\mathbf{r})\,d\mathbf{r} \quad , \tag{3.25}$$

can be expressed as

$$\mathcal{F}_H\left[\rho(\mathbf{r})\right] = f_H \exp(2\pi i P_H) \quad . \tag{3.26}$$

The normalized yield for an atom is expressed in Equation 3.27 in terms of the x–ray reflectivity $R(\theta)$, the coherent fraction f_H, the phase of the XSW $\varphi(\theta)$, the coherent position P_H, and the effective thickness factor $Z(\theta)$,

$$Y(\theta) = \left[1 + R(\theta) + 2f_H\sqrt{R(\theta)}\cos(\varphi(\theta) - 2\pi P_H)\right]Z(\theta) \quad . \tag{3.27}$$

Using dynamical diffraction theory to fit the rocking curve, the angular scale is determined and the measured XSW yield is fit with three parameters: Y_{OB}, f_H, and P_H. The value of P_H is typically listed between 0 and 1. The Hth order Fourier component of the atomic distribution is a time-averaged distribution that is projected into the unit cell.

The coherent fraction is composed of three terms: the degree of ordering of the atoms C, the geometric distribution a_H, and the vibrational amplitude of the atoms D_H. This can be expressed as

$$f_H = C\, a_H\, D_H \quad,$$

<div align="right">(3.28)</div>

where C, a_H, and D_H each have values between zero and unity. The ordered fraction is a measure of the randomness of the atoms, where zero means completely random and one means totally ordered in preferred lattice positions. The geometric factor is a term with consequence if there is more than one preferred atomic site in the primitive unit cell. If there is a single atom in the unit cell, a_H will equal one. If there are two or more atoms in the unit cell, the value of a_H will depend on the distribution. This can occur in surface structures with multiple adsorption sites, epitaxial films strained in the surface normal direction, and in non-commensurate structures. In XSW analysis, the mean square sum of the vibrational amplitude $\langle u_H^2 \rangle$ is lower than for conventional x-ray diffraction by a factor of 2 in the exponent because the atom is at the level of field. The Debye-Waller factor is expressed as

$$D_H = \exp\left(\frac{-2\pi^2 \langle u_H^2 \rangle}{d_H^2} \right) \quad.$$

<div align="right">(3.29)</div>

Figure 3.3 shows how the XSW yield varies with the coherent position. In this figure the coherent fraction is set to unity. As this figure demonstrates, the shape of the yield curve is sensitive to the atomic distribution. Because the spacing between interatomic planes is the gauge length used to measure the atomic
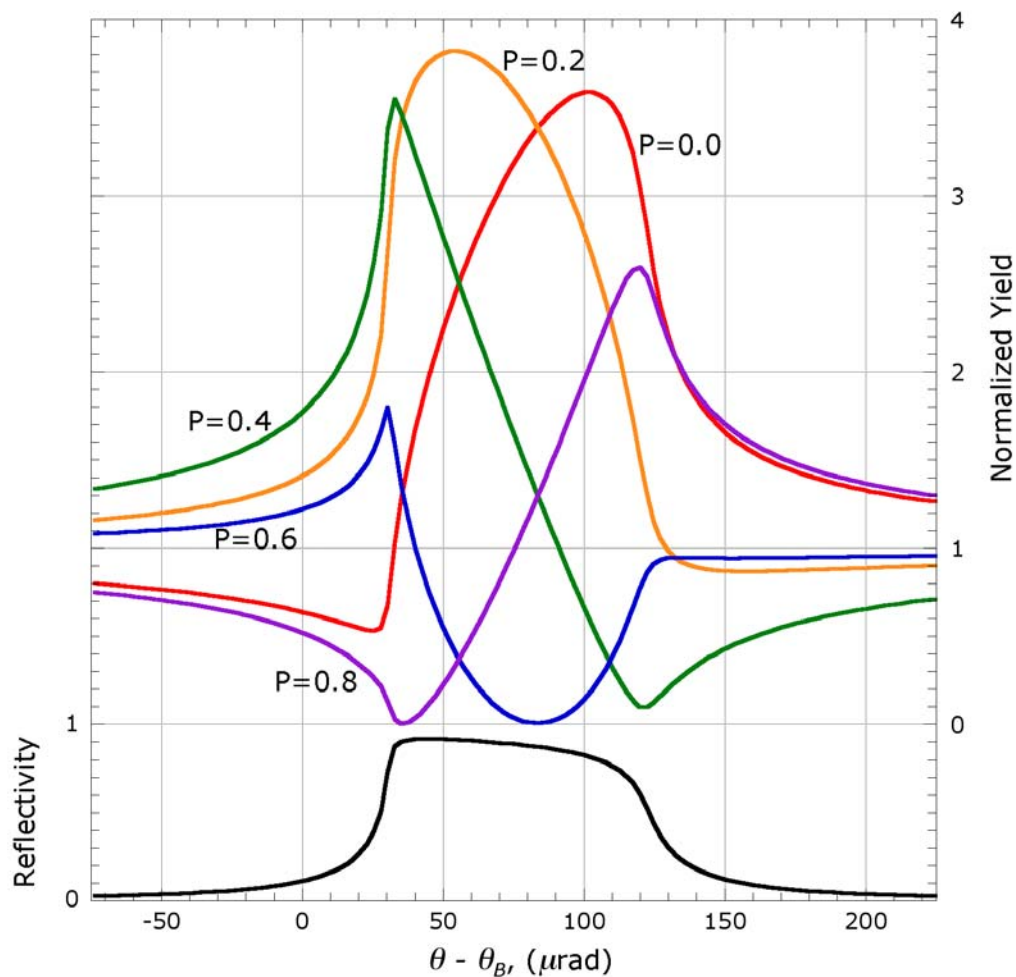
Figure 3.3: The calculated reflectivity and yield curves for the Ge(111) reflection at 7.00 keV with different coherent position values. The yield curves show that when the atoms are located at different positions (relative to the Bragg planes), there are distinctly different responses. In this figure, the coherent fraction is set to one, and the origin is located on the top atom in the (111) bilayer (corresponding to $P_H=0$).
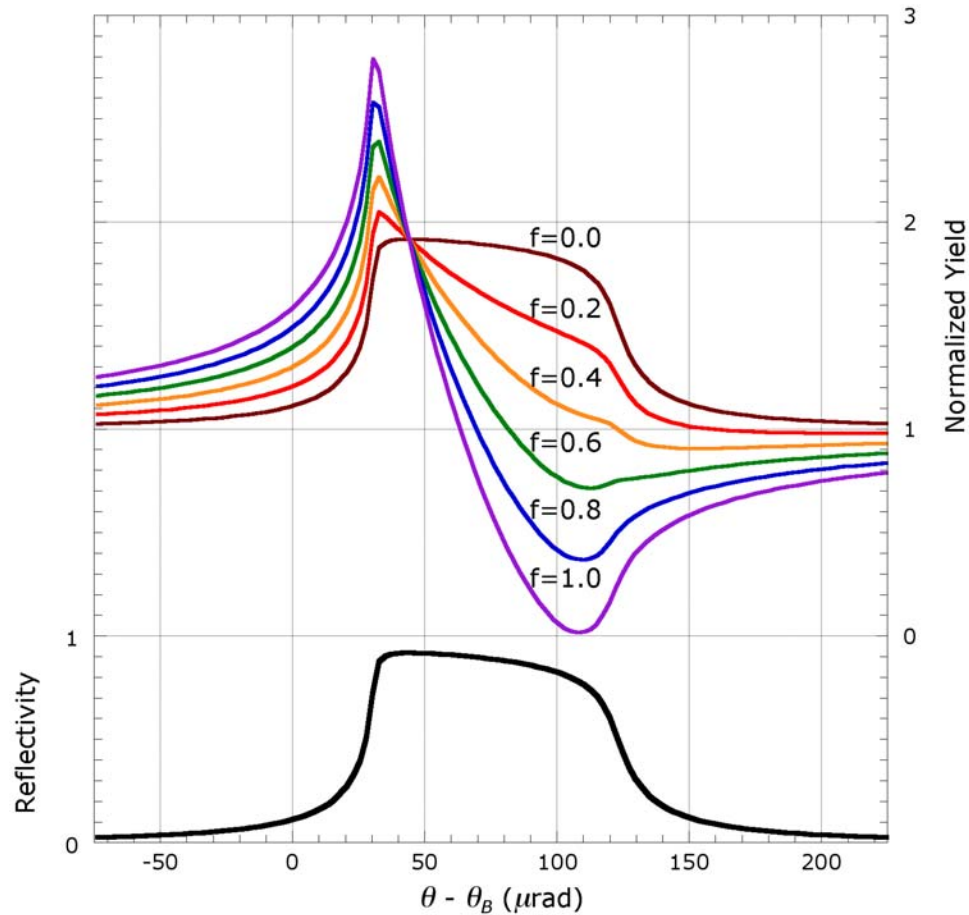
Figure 3.4: The calculated reflectivity and yield curves for the Ge(111) reflection at 7.00 keV with different values for coherent fraction, from zero to unity. The range in value for coherent fraction could be attributed to the degree of ordering of the atoms, where $f_H=1$ represents complete ordering of the atoms and $f_H=0$ represents a random distribution of the atoms. The coherent position is set to 0.5 for the yield curves in this figure, and the origin is located on the top atom in the (111) bilayer (corresponding to $P_H=0$).

distribution, very high spatial resolution can be achieved. This sensitivity gives the XSW techniques the capability to measure atomic positions with an accuracy of hundredths of angstroms.

In Figure 3.4 the yield varies with coherent fraction and the coherent position equals 0.5. Referring to Equation 3.27, the effect of the coherent fraction on the shape of the yield is evident. As the coherent fraction decreases, the contribution of the R component increases. In the extreme case where the coherent fraction is equal to zero, the yield is modulated with the form of $1 + R$.

3.3.2 Atomic distribution in the complex plane

The atomic distribution, perhaps, can be best considered in the contexts of the complex plane. The coherent position for an ensemble of n atoms with unit cell positions $\mathbf{r}_j$ is described as

$$P_H = \frac{1}{2\pi} \text{Arg}\left[\sum_{j=1}^{n} D_j \exp\left(2\pi i \mathbf{H} \cdot \mathbf{r}_j\right)\right] \quad , \qquad (3.30)$$

where D_j is the Debye-Waller factor for the individual atom. The coherent fraction can be expressed as

$$f_H = \frac{C}{n} \left|\sum_{j=1}^{n} D_j \exp\left(2\pi i \mathbf{H} \cdot \mathbf{r}_j\right)\right| \quad . \qquad (3.31)$$
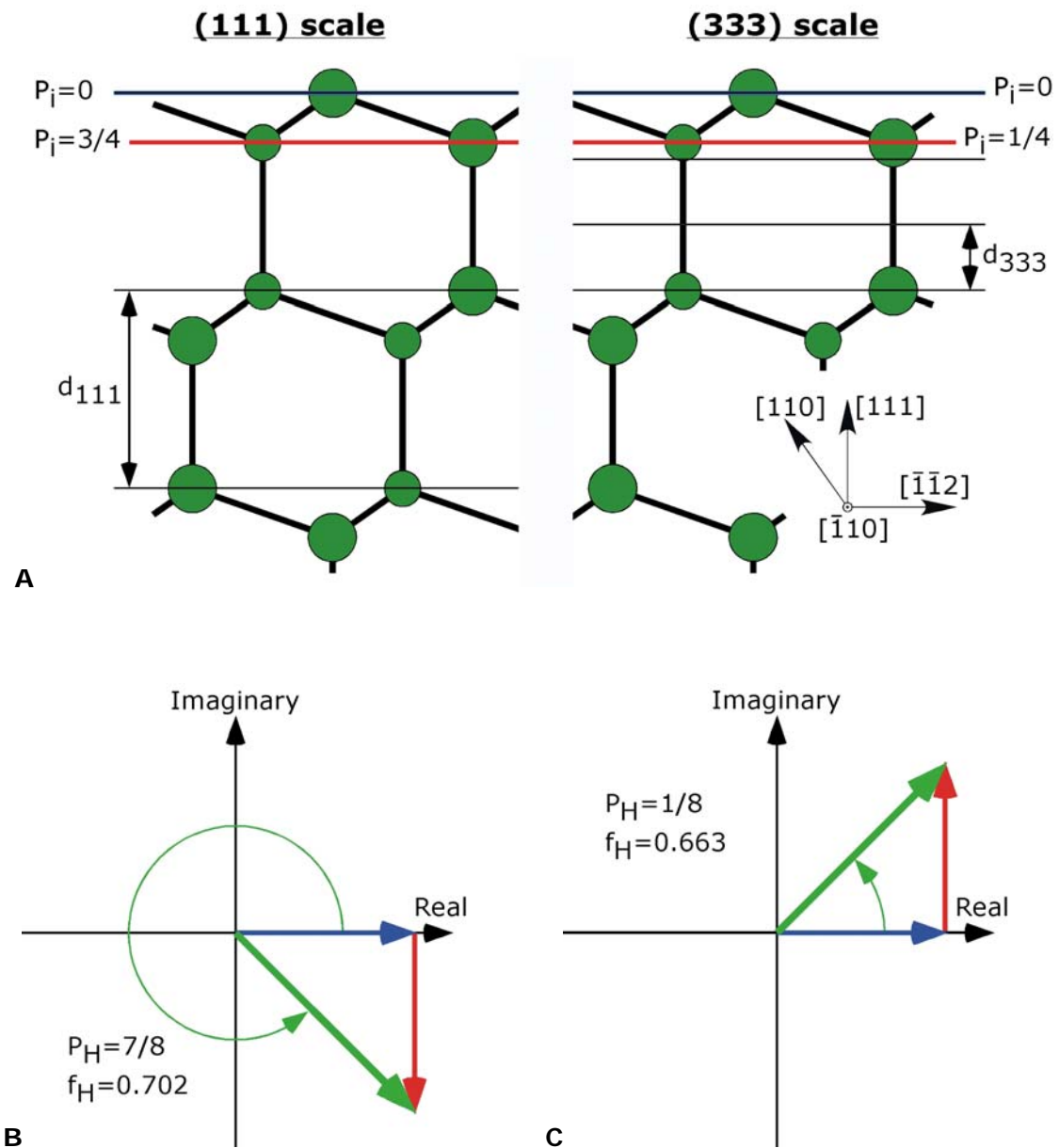
Figure 3.5: A demonstration of how the atomic distribution can be represented using the complex plane. A) This example is for a diamond cubic crystal structure with a surface normal in the [111] direction and viewed along the [1$\bar{1}$0] direction.

(Caption for Figure 3.5 continued)

There are two atoms in the primitive unit cell. Two measuring scales are shown, the (111) on the left side and the (333) on the right side. B) Using the (111) basis and the complex plane, the two atoms are represented by the blue and red vectors. The coherent position is represented by the phase of the (green) resultant vector. The coherent fraction is equal to the magnitude of the resultant vector relative to the total length of the component vectors. C) With a (333) basis, the coherent position and coherent fraction appear differently than the (111) case in the complex plane. In this figure, the origin is located on the top atom in the (111) bilayer (corresponding to $P_H=0$).

As a demonstration of this complex plane representation, consider the atomic distribution along the [111] direction in the diamond cubic crystal structure. In this structure, there are two atoms in the primitive unit cell. The atoms are arranged in bilayers composed of atoms separated by 1/4 of a (111) d-spacing. In a side view along the [1$\bar{1}$0] direction, Figure 3.5a shows a direct space representation of the atomic stacking sequence. A blue line passes through one of the atom positions and represents the position of the origin for the unit cell. On the left side, the positions of the atoms are shown using a (111) scale, whereas, the right side uses a (333) spatial length.

By representing the atomic positions in the complex plane, as in listed in Equations 3.30 and 3.31, Figure 3.5B shows how the two atoms per unit cell would appear using the (111) reference frame. Because the origin of the unit cell is centered on one of the atoms, the position (or phase) of that atom is 0. The second atom would have a position of 3/4 (or −1/4). To determine the coherent position and coherent fraction, the component (red and blue) vectors representing these two atom positions are added head to tail to create the overall (green) vector. The coherent position is the phase of the resultant vector and equals 7/8 (or −1/8). The magnitude of this resultant vector represents the coherent fraction. If all atoms are in the crystalline lattice, $C = 1$. For Ge atoms at room temperature, the vibrational amplitude for the atoms reduces the relative length of each component vector from 1/2 to 0.993*1/2. The value of the geometric factor can be seen in Figure 3.5B to equal $1/\sqrt{2}$. Using the XSW technique to measure the atomic distribution of Ge atoms in the diamond cubic structure along the [111]

direction, the measured values for coherent position would be 0.875 and the coherent fraction would be 0.702.

To further demonstrate this method, Figure 3.5C shows how the atomic distribution would appear using the (333) Bragg reflection. Due to the shorter length scale, the component atoms would have phases of 0 and +1/4. While the geometric factor turns out to be the same as in the (111) case, the vibrational amplitude would reduce the vector's relative magnitude from 1/2 to 0.938*1/2. Using the XSW technique to measure the atomic distribution of Ge atoms in the diamond cubic structure with the (333) reflection, the measured values for coherent position would be +0.125 and the coherent fraction would be 0.663.

3.3.3 Determining atomic position with triangulation of XSW measurements

One of the practical uses of the XSW technique is to combine the results from multiple reflections to triangulate the position of atoms at interfaces. Using the values of coherent positions normal and off-normal to the surface, the registry of the adsorbate atoms can be determined relative to the underlying bulk crystal structure. This concept was first applied to Br on the Si surface [36] and has been extensively applied to many material systems. A side view representation of the Ge(111) surface is shown in Figure 3.6; the Ge atoms are shown in green and are organized in bilayers. On the surface of the crystal are three distinct positions for the adsorbate atoms; the atoms colored in red, yellow, and blue represent the three high-symmetry sites on the surface.
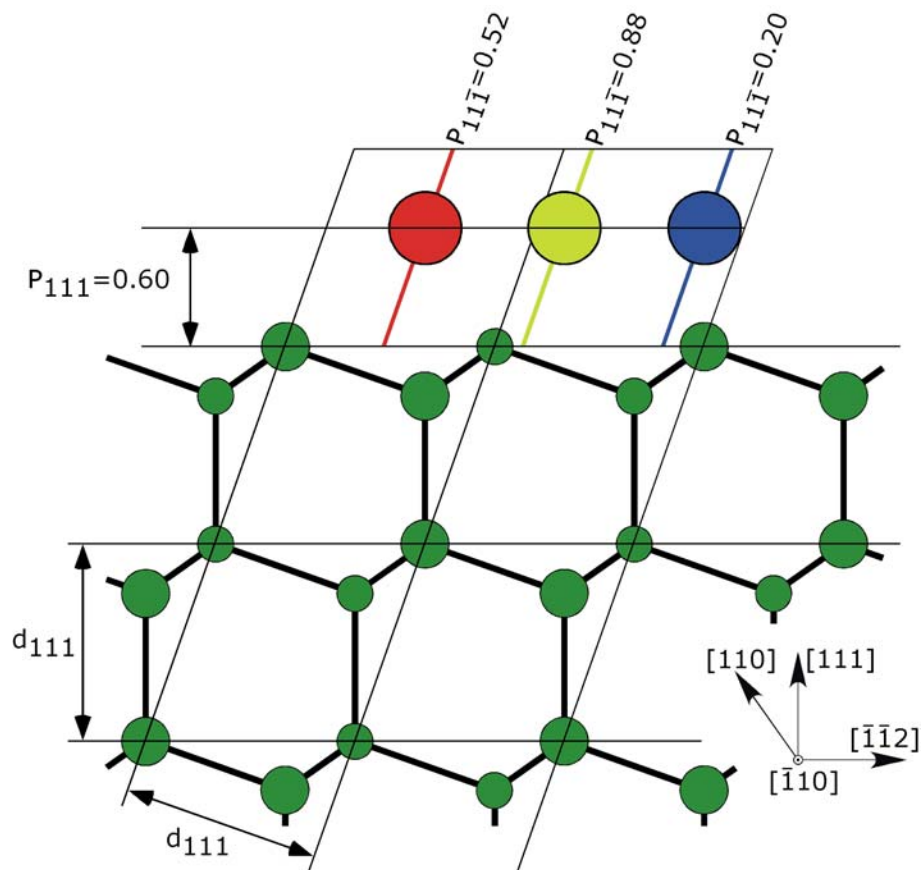
Figure 3.6: To determine the position of an adsorbate atom on the surface, the intersection of coherent positions for two XSW measurements can triangulate the atom. On the Ge(111) surface three, high-symmetry positions are distinguished by the combination of the surface normal and off-normal XSW measurements. Although the vertical positions for the blue, red, and yellow atoms are the same, the coherent position value in the off-normal direction distinguishes them. In this figure, the origin is located on the top atom in the (111) bilayer (corresponding to $P_H=0$).

If the coherent position for the (111) reflection were measured to be 0.60(1) for the adsorbate, it could be said the atom was 1.96 ± 0.03 Å above the bulk-like surface atomic plane. Using the radii for the substrate and adsorbate atoms to estimate the bond length, one could guess at the adsorption site. However, the lateral position for the adsorbate atom is better determined by also making an off-normal XSW measurement. If there is only one preferred position, the intersection of the coherent positions for both measurements will triangulate the position. As shown in the figure, the off-normal $(11\bar{1})$ XSW measurements distinguishes between the sites.

3.3.4 Coherent position versus average position in direct space

When there is more than one atomic site in the unit cell, associating the coherent position with the average position for the atoms in the unit cell can be misleading and can lead to an inaccurate description of the atomic distribution. Consider the distribution along the x-direction for the two dimensional lattice shown Figure 3.7A. Here, one atom is located at the origin of the unit cell, and two more of the same atom are located at the fractional coordinate of x = 1/3. The average position (center of mass) in the lattice along the x-direction is 2/9, and the atoms are completely ordered. If only a single XSW measurement were made for the (10) reflection, the values would be $P_{10} = 1/4$ and $f_{10} = 1/\sqrt{3}$ (ignoring thermal vibrations). The vector summation leading to these XSW results can been seen in Figure 3.7B.

$P_H=1/4$ $P_H=1/4$ $P_H=1/4$

X | 0 $\frac{2}{9}$ $\frac{1}{3}$ 1 $\frac{11}{9}$ $\frac{4}{3}$ 2 $\frac{20}{9}$ $\frac{7}{3}$ real space

A

Imaginary

$P_H=1/4$
$f_H=1/\sqrt{3}$

Real

B
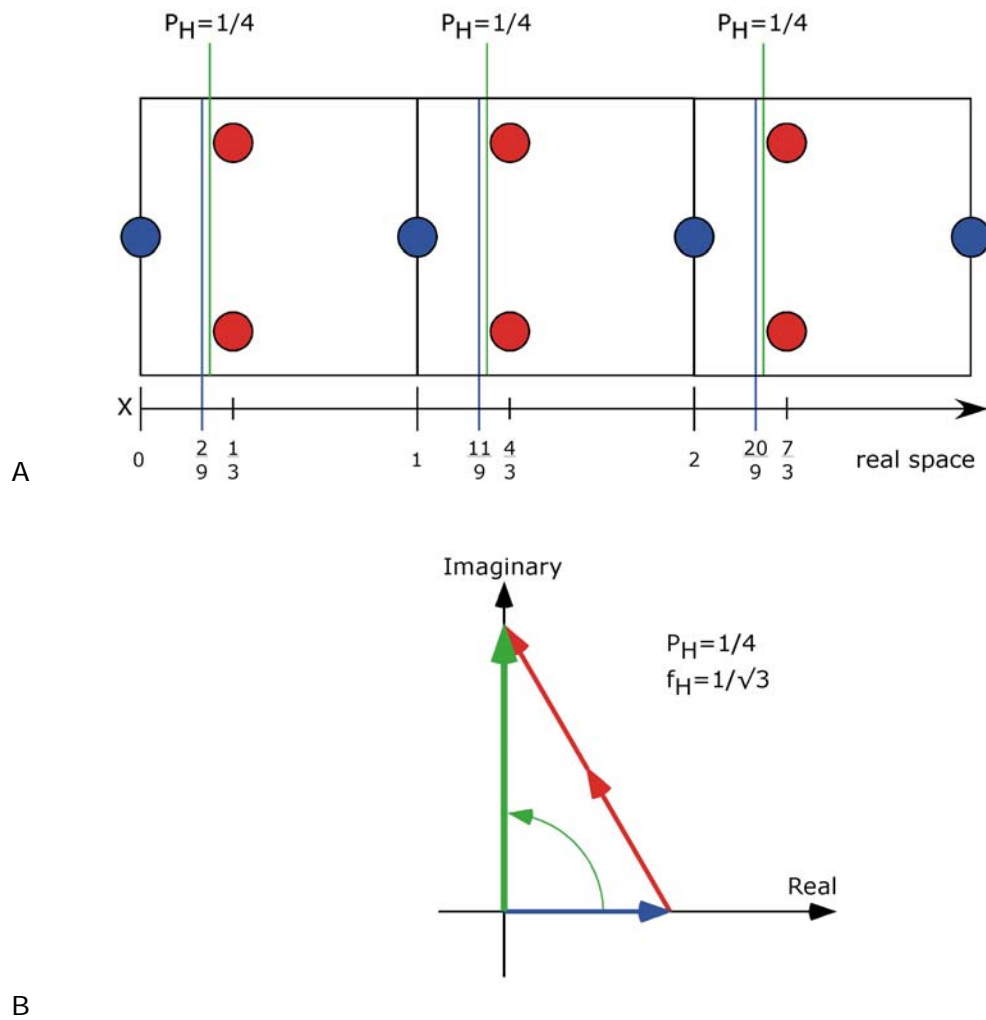
Figure 3.7: An example of how the average spatial position can differ from the coherent position. A) For a two-dimensional lattice in real space, consider the atomic distribution along the x-direction. In the unit cell, one (blue) atom is located at $x=0$ and two more (red) of the same atom are located at $x=1/3$. The average position in fractional coordinates is $x_{avg}=2/9$ B) Using vectors in the complex plane to represent the atomic positions the coherent position is 1/4 and the coherent fraction in $1/\sqrt{3}$.

It is the geometric factor that creates this difference between the coherent position and average position. When there is more than one atom in the primitive unit cell, the atoms can counteract one another from the XSW point of view. If the pair of atoms in Figure 3.7A were at $x = 1/2$ instead of 1/3, the atom at $x = 0$ and one of the atoms at $x = 1/2$ would cancel each other out because they have opposite phases with respect to each other. This is synonymous to calculating the structure factor in x-ray diffraction, where multiple atoms in the unit cell can lead to forbidden reflections.

Without additional measurements, an incorrect conclusion would be that the atomic position is at 1/4 and that the atoms were not well ordered. While this is a relatively simple scenario, it illustrates a potential problem with interpreting XSW results. Making multiple XSW measurements and combining other techniques are helpful to avoid a misinterpretation such as this.

3.4 XSW direct space imaging

3.4.1 Direct space atomic density distribution from XSW measurements

A direct approach to solving the atomic scale distribution is a powerful technique for structural determination because it does not require a model prior to the analysis. When experimental data is used to refine a model, it is subject to settling into local minima rather than the correct solution. By directly imaging the atomic structure with the XSW technique, the atomic structure can be determined *apriori*. One needs only to accurately measure a set of Fourier coefficients over a

sufficient range of reciprocal space, apply certain symmetry rules, and sum up the Fourier terms.

Conventional x-ray diffraction methods suffer from the so-called "phase problem" because only the amplitude of the diffracted plane wave is detected. In the XSW technique, the "detector" is the atom, located within the interference field, and senses both the phase and amplitude of the diffracted plane wave. In the formalism of crystallography, these are the geometrical structure factors (including the Debye-Waller factor) for the individual sublattices of each fluorescent atomic species. Because the XSW method measures both the amplitude and the phase of the Fourier coefficient for an atomic distribution, these quantities can be used to reconstruct the atomic density in direct space. As was developed in section 3.3.1, the Fourier coefficient can be related to the coherent fraction and coherent phase,

$$\mathcal{F}_H\left[\rho(\mathbf{r})\right] = f_H \exp\left(2\pi i P_H\right) \quad . \tag{3.32}$$

Generating a direct-space, atomic density map from XSW-measured Fourier coefficients is simple and straightforward. The normalized atomic distribution function $\rho(r)$ for the atom can be expressed as a summation of Fourier coefficients,

$$\begin{aligned}\rho(\mathbf{r}) &= \sum_H \mathcal{F}_H\left[\rho(\mathbf{r})\right]\exp\left[-2\pi i(\mathbf{H}\cdot\mathbf{r})\right] \\ &= \sum_H f_H \exp\left[2\pi i\left(P_H - \mathbf{H}\cdot\mathbf{r}\right)\right]\end{aligned} \quad . \tag{3.33}$$

The expression in Equation 3.33 can be further simplified because for a normalized distribution, the 0th order Fourier term is equal to 1. Using Euler's formula,

$$\exp(i\theta) = \cos(\theta) + i\sin(\theta), \tag{3.34}$$

the normalized distribution function expressed in Equation 3.33 can be written as

$$\rho(\mathbf{r}) = 1 + \sum_{H \neq 0} f_H \left(\cos\left[2\pi\left(P_H - \mathbf{H}\cdot\mathbf{r}\right)\right] - i\sin\left[2\pi\left(P_H - \mathbf{H}\cdot\mathbf{r}\right)\right] \right) \quad . \tag{3.35}$$

Crystallographic symmetry will reduce the number of coefficients that need to be measured. The coherent position values for $\mathbf{H}$ and $\overline{\mathbf{H}}$ are related by inversion through the origin and have an opposite sign of its inverse reflection,

$$P_H = -P_{\overline{H}} \quad . \tag{3.36}$$

However, the amplitudes of the components are the same,

$$f_H = f_{\overline{H}} \quad . \tag{3.37}$$

For the summation in Equation 3.35, if the **H** and $\overline{\textbf{H}}$ terms are separated and the symmetry relationships in Equations 3.35 and 3.36 are included, the atomic distribution simplifies to

$$\rho(\textbf{r}) = 1 + 2 \sum_{\substack{H \neq 0 \\ H \neq \overline{H}}} f_H \cos\left[2\pi\left(P_H - \textbf{H}\cdot\textbf{r}\right)\right] \quad . \tag{3.38}$$

The concept used to reduce the number of terms is comparable to Friedel pairs, which are Bragg reflections related by inversion through the origin. Friedel's Law states that members of a Friedel pair have equal amplitude and opposite phase,

$$\left| F_H \right| = \left| F_{\overline{H}} \right| \tag{3.39}$$

and

$$\varphi_H = -\varphi_{\overline{H}} \quad . \tag{3.40}$$

3.4.2 XSW imaging examples in one-dimension

Back transforming the Fourier coefficients for the normalized atomic distribution creates a direct space reconstruction of the atomic structure. To illustrate how the summation of cosine functions can be used to create an atomic density map in direct space, some examples will be shown for distributions in one

dimension. In the following examples of synthesized atomic distributions, the direct space dimensions are listed in fractional coordinates relative to the lattice parameter a_L. Because the XSW measurements are linked to the **H** reflections from the crystal, it is more appropriate to plot the atomic distributions relative to the fractional unit cell rather than to a specific length scale, such as Å.

In the first example, the atomic distribution along the [111] direction for the diamond cubic crystal structure is examined. The calculated values for f_H and P_H are listed in Table 3.2, and are used to create the curves shown in Figure 3.8. In this example the effects of thermal vibrations on the coherent fraction are not included. The first term is from the (111) reflection and is shown in red. Here there is one peak at $Z = -1/8$ and has one period within the unit cell. Adding the 0th order term (which equals 1) to the 1st order term produces the lower black curve. Subsequent series are offset by 5 on the vertical axis. Because the amplitude of the 2nd order term is zero, it does not alter the shape or magnitude of the distribution. The 3rd order term is shown in green and has three periods in the unit cell. Including the 3rd order term into the summation produces the black curve in the middle of the figure. For the five individual terms shown, the cosine functions all have different phases with respect to one another. When the 4th and 5th order terms are also added into the summation, the distribution function better represents the correct distribution of one atom at $Z=0$ and another atom at $Z=-1/4$; the peaks become sharper and the background flattens out. The resolution of the image increases as the reflections included in the summation extend from the origin further out in reciprocal space.
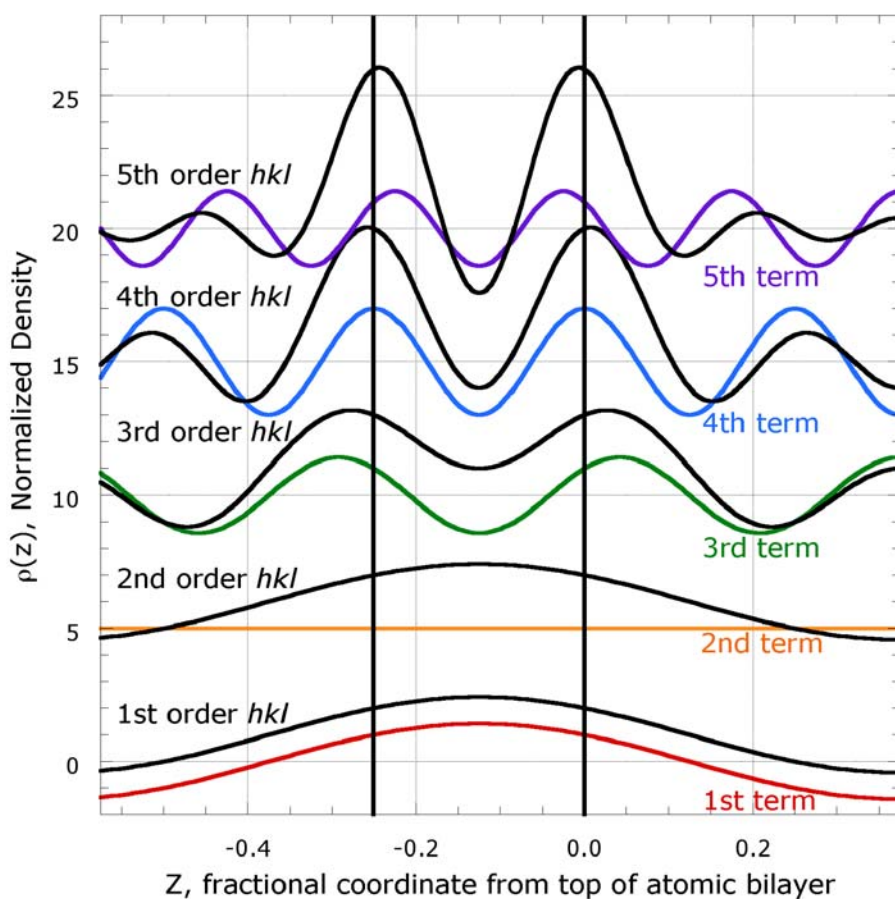
Figure 3.8: A one-dimensional demonstration of the cosine summation listed in Equation 3.38 for the atoms in the diamond cubic crystal structure in the [111] direction. The 0th order term is equal to 1, and the higher order terms (shown in different colors) have the form of cosine functions with modulated amplitude and phase. As the number of terms increases, the distribution (shown in black) approaches the real shape of two atoms separated by 1/4 of the (111) d-spacing and centered about Z=-1/8. Subsequent series are offset by 5 on the vertical scale.
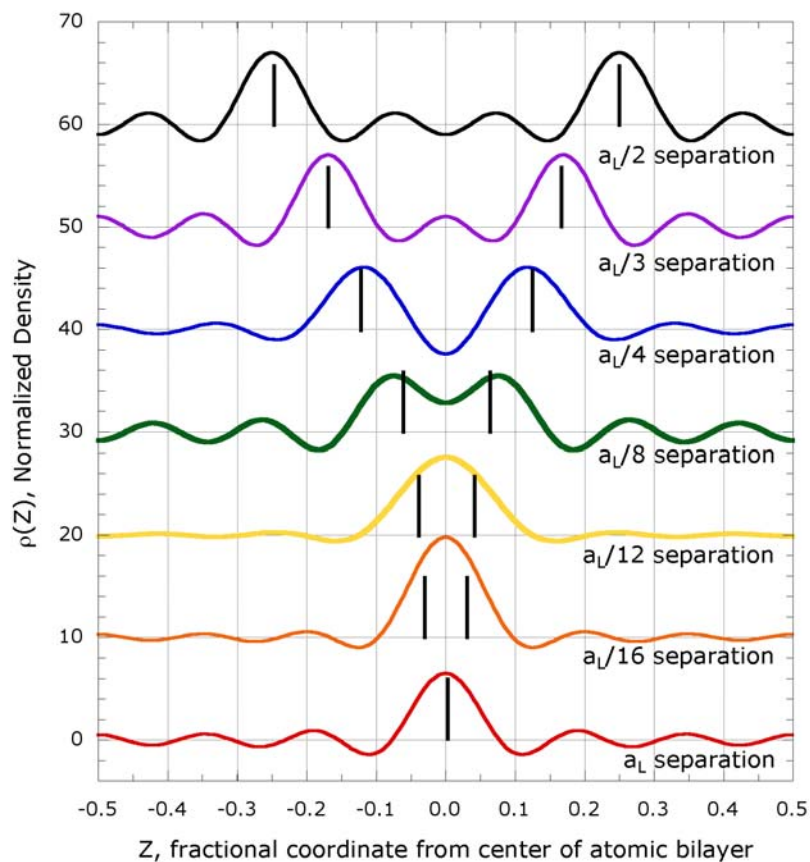
Figure 3.9: Using Equation 3.38, a cosine summation up to the 6th order term, the one-dimensional profile for the atomic distribution is shown for different values of spatial separation. The black, vertical lines represent the atomic positions. Shown in red in the lower part of the figure, there is only one position for atoms in the unit cell. When the atoms are separated by 1/16 of the lattice parameter a_L, the distribution appears as one broader peak because the resolution is below the atomic separation. As the separation in Z increases, the summation better approximates the distribution of the atoms. Subsequent series are offset by 10 on the vertical scale.

Table 3.2:   The values for coherent fraction f_H and coherent position P_H for the atomic distribution of Ge atoms in the [111] direction.   In this calculation, the origin of the unit cell is centered on the top atom of the bilayer.   The value for f_{222} is 0 because of the geometric factor, therefore, a value for P_{222} is not applicable. For this example, C = 1 and D_H = 1.

(hkl) reflection	f_H	P_H
(111)	$1/\sqrt{2}$	-1/8
(222)	0	NA
(333)	$1/\sqrt{2}$	1/8
(444)	1	0
(555)	$1/\sqrt{2}$	-1/8

In another example, the effect of the separation between atoms is illustrated. In Figure 3.9, the summations up to the 6th order term are shown for different interatomic separations.   Black vertical lines are drawn to represent the correct atomic positions.   When the separation between atoms ranges from a_L to a_L /4, the summation creates an image that represents the atom positions well.   If the separation between atoms is at or below a_L /8, the images do not completely represent the correct atom structure.   The peak position may be slightly distorted, as it is for a_L /8, or the peak position are smeared together, as happens for a_L /16. This distortion of the true atomic structure is related to the resolution of the image.

If the summation extended out to higher order terms, the atomic distribution would be better represented.

For a unit cell with two equally occupied sites, the mathematical expression for the resolution along the [hkl] direction can be related to the separation between atoms in the [hkl] direction. The minimum separation Δ_{hkl} is where the phase of the Fourier coefficient changes sign and the amplitude goes to zero. From a practical perspective for the resolution, Δ_{hkl} is the point where it is clear there is more than one occupied site in the unit cell.

A third example demonstrates the effect of the vibrational amplitude on the XSW imaging technique. In Figure 3.10, the distribution of Ge atoms along the [111] direction is calculated using an increasing number of terms and includes the Debye-Waller factor for Ge atoms at 300 K. From Equations 3.25 and 3.28, it can be shown how the vibrational amplitude decreases the coherent fraction and the amplitude of the Fourier coefficient. The positions for the peaks do not change, but the amplitude of the peaks decreases with the inclusion of thermal vibrations. For the summations including up to the 4th order, the intensity is not significantly altered. However, the distributions for summations that include up the 7th and 10th orders are affected.

One final example in one dimension plots a non-centrosymmetric distribution of atoms. Here, there are two positions for the atoms but the occupation ratio is 2:1. In Figure 3.11, the summation includes the 0th through 6th order terms for four different separations between atomic sites. Black vertical lines represent the position and relative amplitudes of the atomic distribution. When the sites are
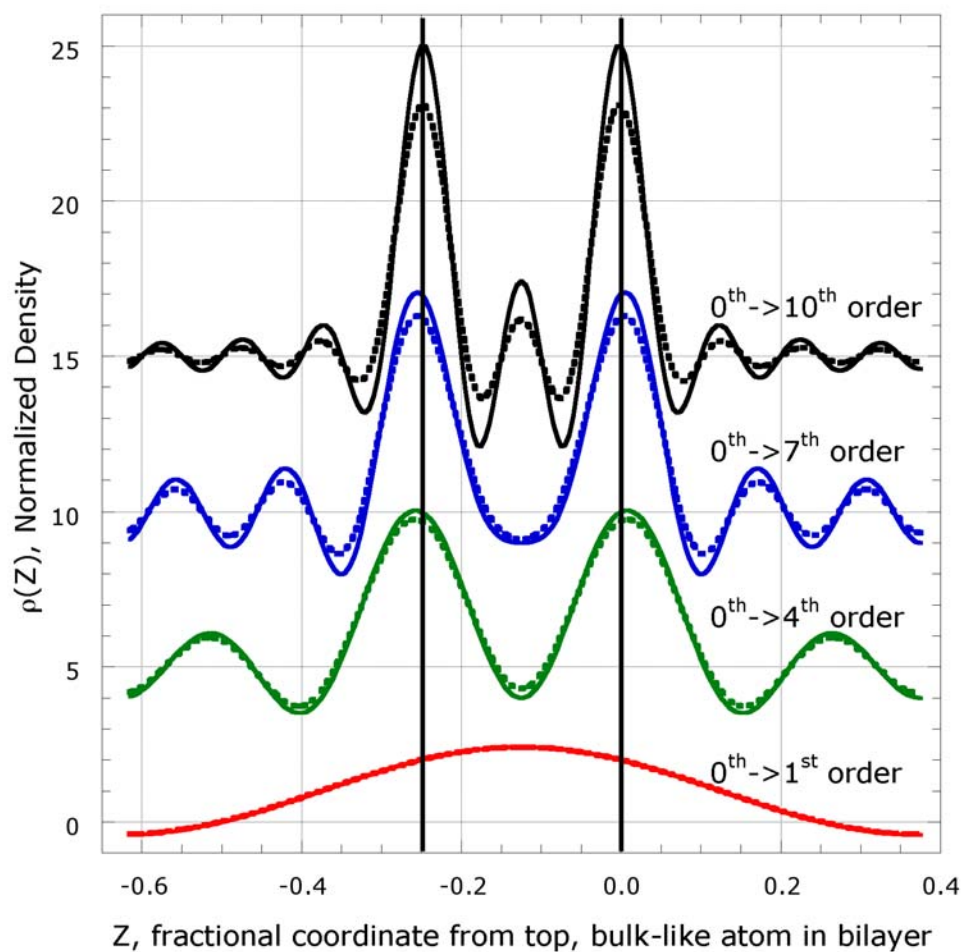
Figure 3.10:   For Ge atoms in a diamond cubic crystal structure in the [111] direction, the effect of increasing the number of cosine terms included in the summation and the vibrational amplitude at room temperature (300 K). Subsequent series are offset by 5 on the vertical scale.
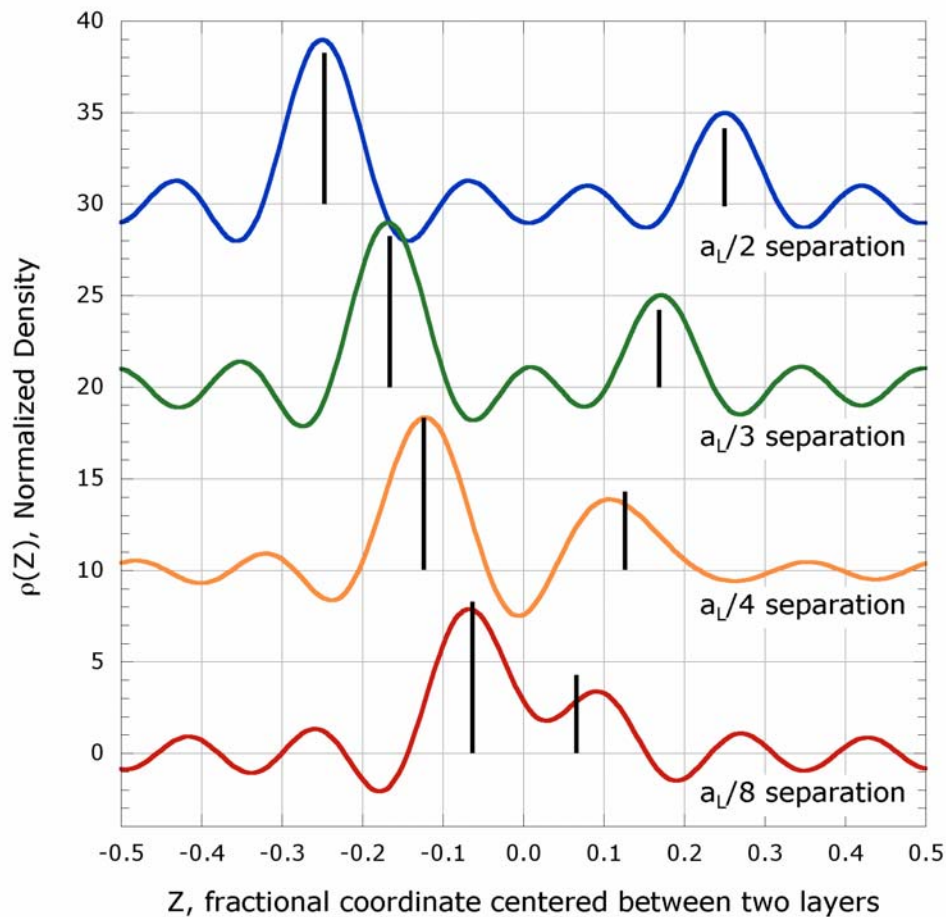
Figure 3.11: The effect of spatial separation between atoms in an asymmetric distribution. Here the atoms occupy a 2:1 ratio for two positions and are represented with black, vertical lines. While the summation (up to the 6th order term) is able to depict two sites, the position for the lower occupation site is distorted from the real position for separations of 1/4 and 1/8 of the lattice parameter a_L. Subsequent series are offset by 10 on the vertical scale.

separated by $a_L/2$ and $a_L/4$, the distributions are well represented with the imaging technique. For separations of $a_L/4$ and $a_L/8$, the position of the lower occupancy site is distorted from its correct position.

From these four examples in one dimension, it can be seen that a map for the atomic distribution can be created from the back transformation of the Fourier coefficients determined from XSW measurements. While the resolution of the image may not fully describe the atomic distribution, the image can be used to create a model to be refined using the XSW values. The method of direct Fourier inversion has recently been demonstrated on a crystal of muscovite to determine the distribution for the host and impurity atoms in the *<00l>* direction using eight XSW measurements in one direction [48].

3.4.3 XSW imaging examples in three-dimensions

The XSW direct space imaging method can also be applied to three dimensional structures. To demonstrate the capability of this technique to create direct space atomic density maps, four cubic crystals are reconstructed from the Fourier coefficients of their atomic distributions. The simple, body-centered (BCC), face-centered (FCC), and diamond cubic crystals were selected because they have different values for their nearest neighbor spacing of a_C, $a_C\sqrt{3}/2$, $a_C/\sqrt{2}$, and $a_C\sqrt{3}/4$, respectively.

Density maps for the cubic crystals are shown in Figures 3.12 through 3.15. In each figure, there are three levels of resolution (A, B, and C) that use an increasing
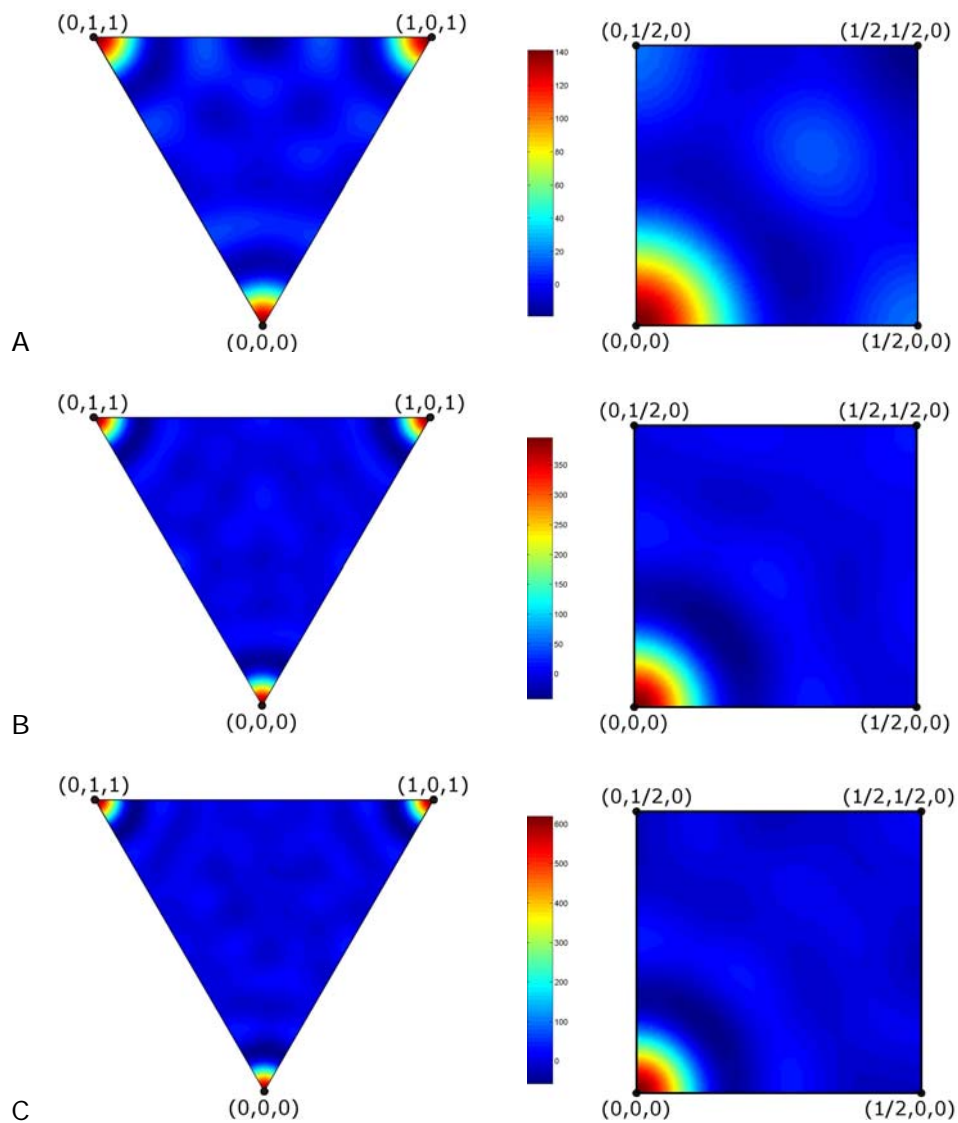
Figure 3.12: The effect of including an increasing number of *hkl* reflections for the XSW imaging technique on a simple cubic unit cell. Two views of the lattice are depicted, a slice of a (111) plane through the cube diagonal and one quadrant of a (001) plane. The summations include reflections from the origin to: A) {310}, B) {331}, and C) {333}.
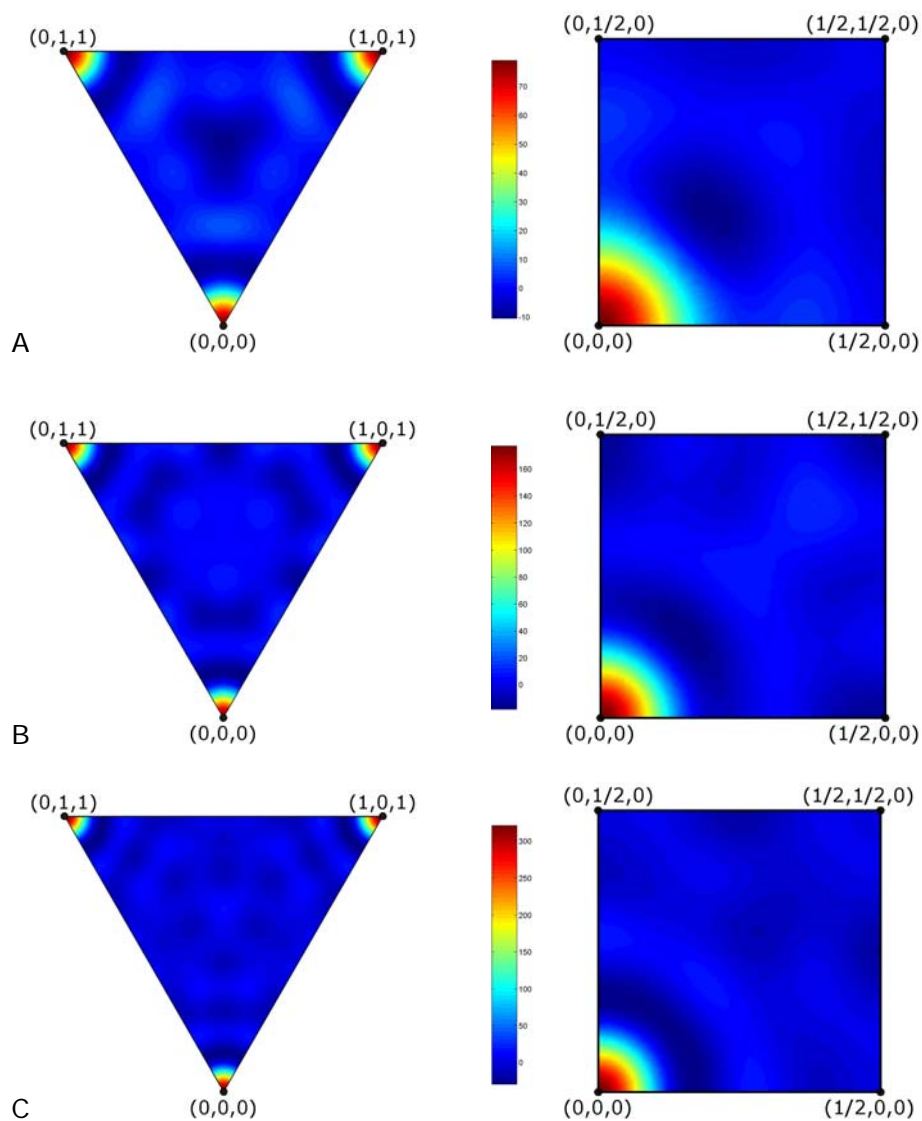
Figure 3.13: The effect of including an increasing number of *hkl* reflections for the XSW imaging technique on a body-centered cubic unit cell. Two views of the lattice are depicted, a slice of a (111) plane through the cube diagonal and one quadrant of a (001) plane. The summations include reflections from the origin to: A) {310}, B) {330}, and C) {431}.
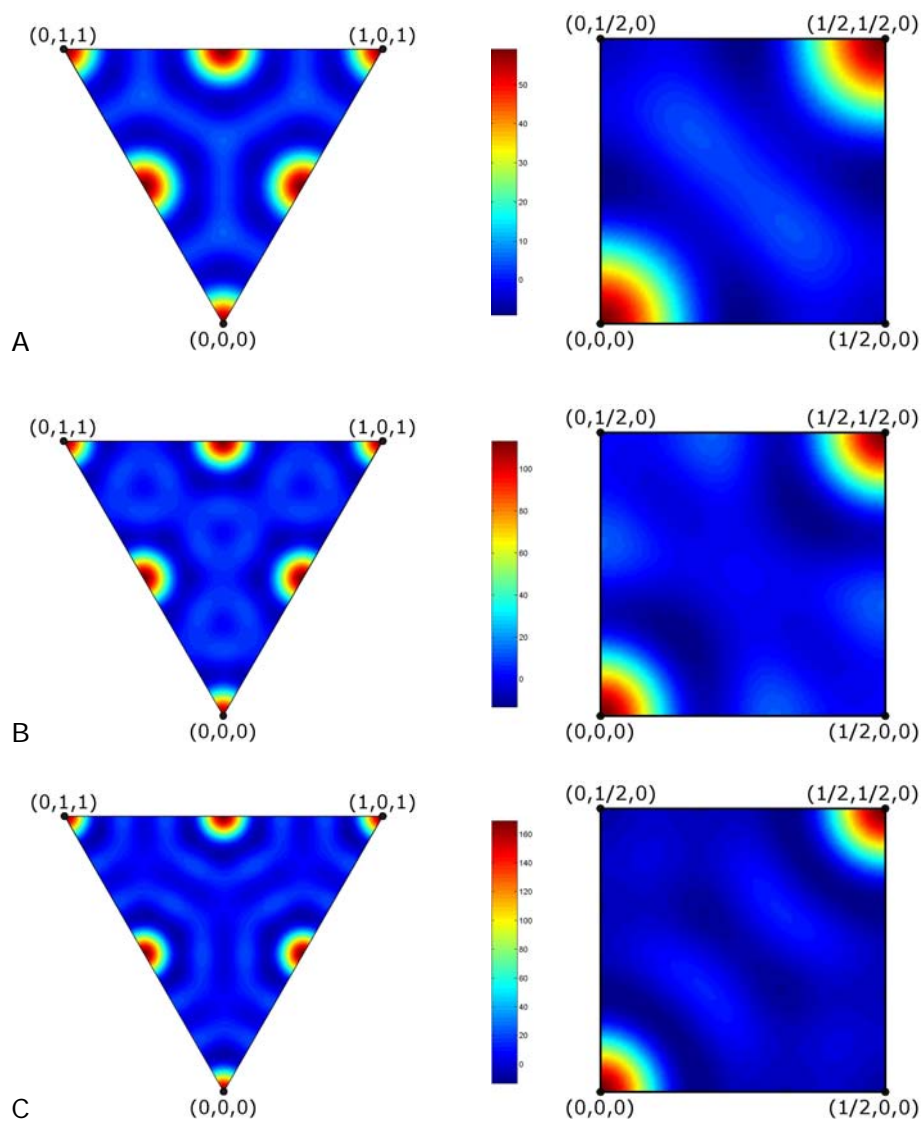
Figure 3.14: The effect of including an increasing number of *hkl* reflections for the XSW imaging technique on a face-centered cubic unit cell. Two views of the lattice are depicted, a slice of a (111) plane through the cube diagonal and one quadrant of a (001) plane. The summations include reflections from the origin to: A) {311}, B) {420}, and C) {333}.
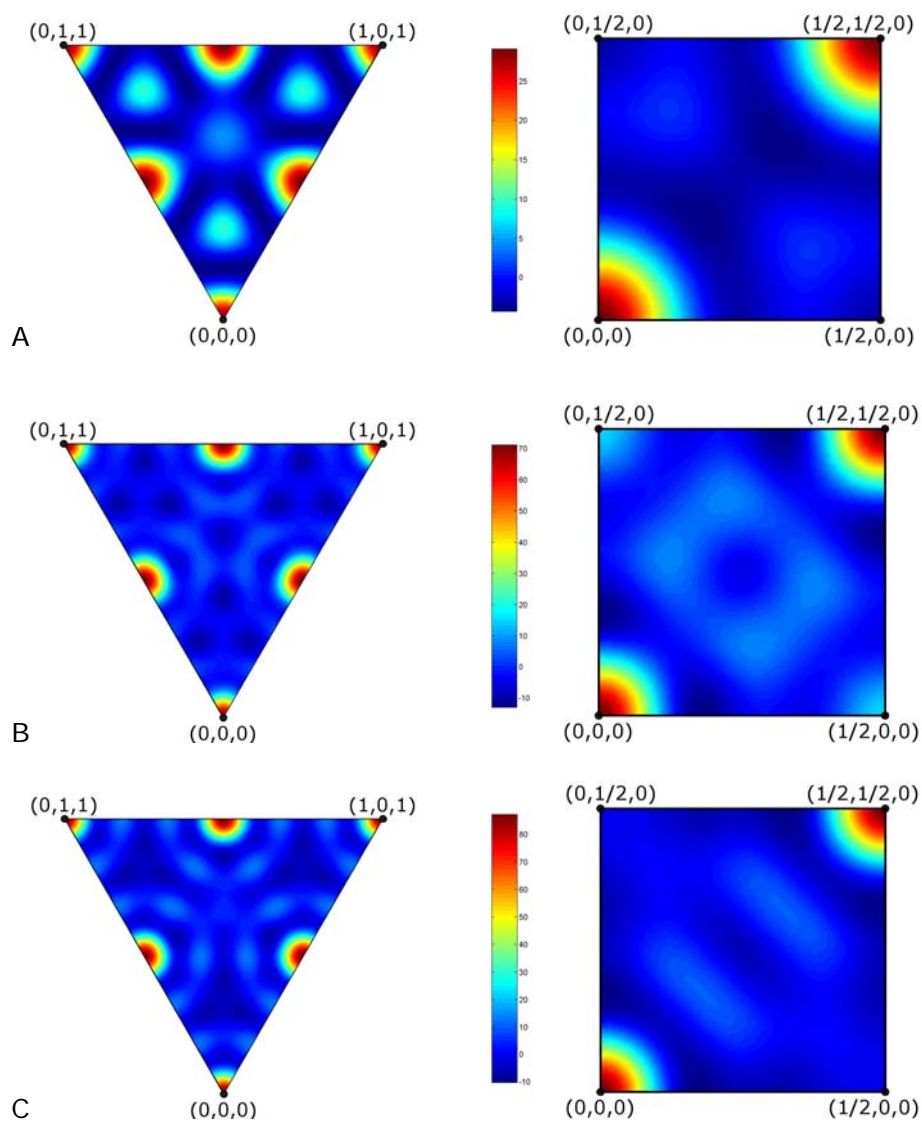
Figure 3.15: The effect of including an increasing number of *hkl* reflections for the XSW imaging technique on a diamond cubic unit cell. Two views of the lattice are depicted, a slice of a (111) plane through the cube diagonal and one quadrant of a (001) plane. The summations include reflections from the origin to: A) {311}, B) {422}, and C) {333}.

number of *hkl* reflections to synthesize the atomic distributions. These levels encompass all of the allowed reflections within spheres (centered on the reciprocal space origin) with radii that extend out to the {311}, {420}, and {333} reflections, respectively.

The triangular-shaped plot is a slice with a surface normal along the $[\bar{1}\,\bar{1}\,1]$ direction of the cube. The sides of the triangle lie along the face diagonals and the vertices are at (0, 0, 0), (0, 1, 1), and (1, 0, 1). The square plot shows one quadrant in the xy-plane with corners at (0, 0, 0), (0, 1/2, 0), (1/2, 1/2, 0), and (1/2, 0, 0). These cross-sections display the shape of the density peaks that should have spherical shapes. The color bar shows the intensity scale. As the number of included Fourier coefficients increases, so does the magnitude of the peaks.

Line profiles for all three resolution levels for each of the four crystal structures are show in Figures 3.16 through 3.19. These curves show how the peak widths decrease with increasing magnitude of the *hkl* reflections included in the summation. Table 3.3 summarizes information from the density maps. One trend apparent in the right-most column is that the ratio of the peak width to minimum d-spacing (from the highest order reflection included in the summation) is approximately 3/4. Using all of the reflections up to the (333) for a Ge crystal, the peaks in the XSW atomic density map would have a fwhm of nearly 0.8 Å.

The images for the simple cubic and BCC structures are similar to each other and have uniform shapes at all three *hkl* levels. The large number of reflections included in the summation are in many different directions and create the spherical symmetry. The FCC structure also appears to be well reproduced; the images

show the atoms at the corners of the cube and at the face centers. The images for diamond cubic structure appear the least symmetric of the four crystals and can be attributed to the relatively low number of reflections included (due to many forbidden reflections) and the smaller interatomic separation between the atoms. The shapes of the peaks in Figure 3.15A and B are slightly distorted from an ideal spherical shape.

In Figure 3.15A, the plot cuts through a $(\bar{1}\bar{1}1)$ atomic plane with three atoms at the corners of the cube and three face-centered atoms. The three green circles also appearing are from the atoms in the adjacent $(\bar{1}\bar{1}1)$ plane that is a distance of $a_C/4\sqrt{3}$ away. Because the summation for this image extends out only to the $\{311\}$ reflections, the expected fwhm for the atomic density peaks is 3/4 of $a_C/\sqrt{11}$ ($=\sim0.30a_C$). These protrusions do not appear Figure 3.15B and C because the peak fwhms are about half of the distance compared to the separation.

For all four crystal structures, the atomic distribution can be well represented by synthesizing the distribution using Fourier coefficients from XSW measurements that extend out to the $\{333\}$ reflections. The spatial resolution is about $0.15a_C$, and the background level fluctuates below $\sim5\%$ of the peak intensity. It should also be noted that this method is not limited to cubic systems, but the number of unique reflections increase as the symmetry is reduced.
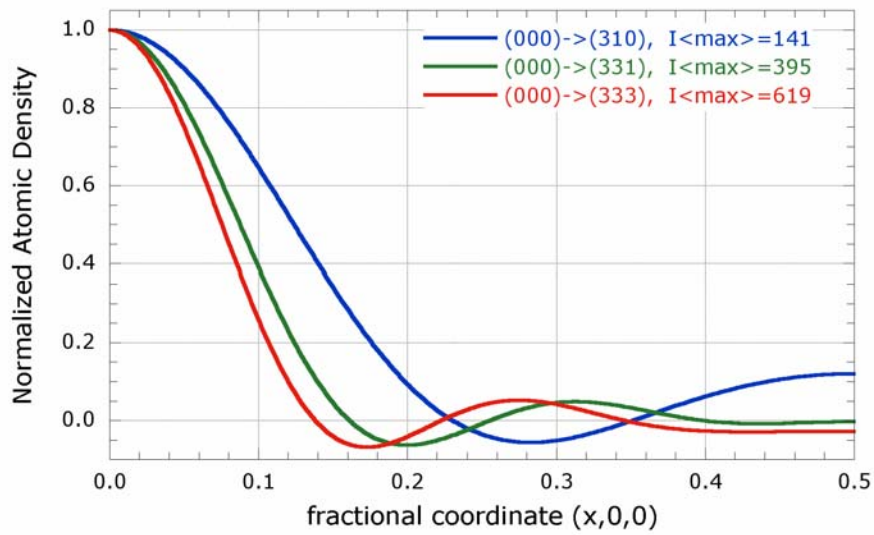
Figure 3.16: Line profiles for simple cubic structure along the x-axis.
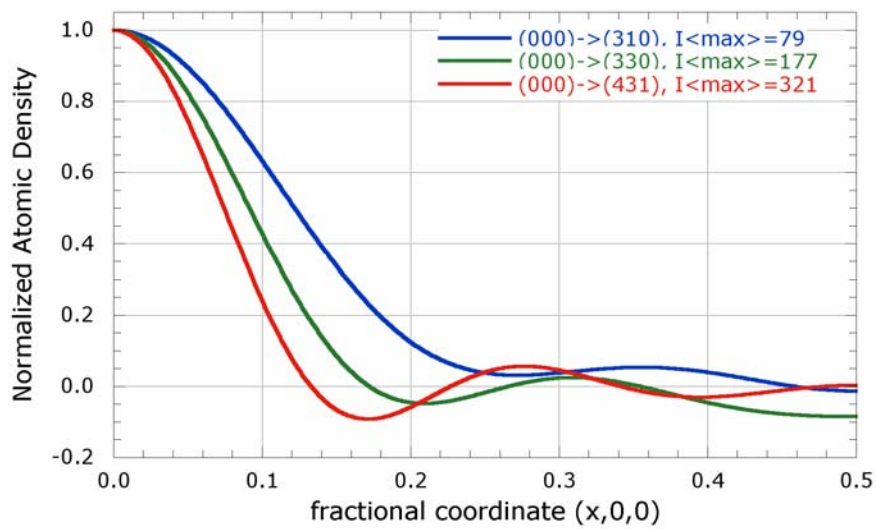
Figure 3.17: Line profiles for body-centered cubic structure along the x-axis.
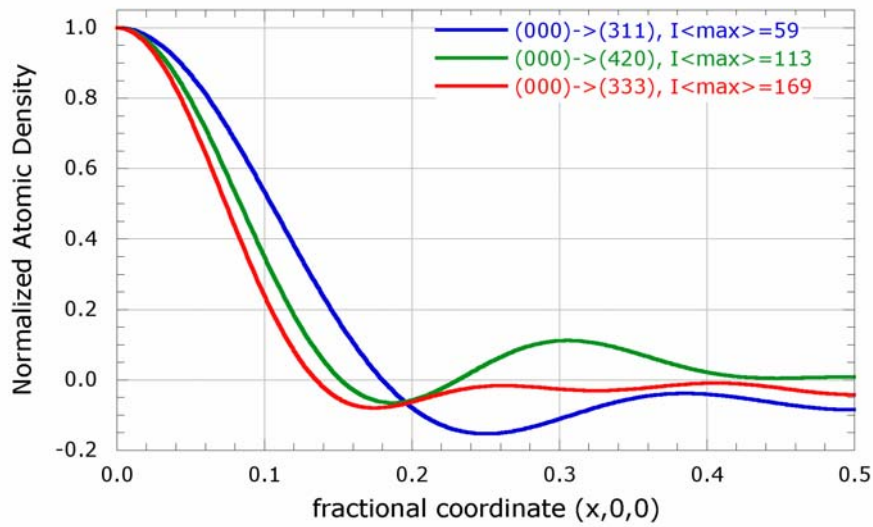
Figure 3.18: Line profiles for face-centered cubic structure along the x-axis.
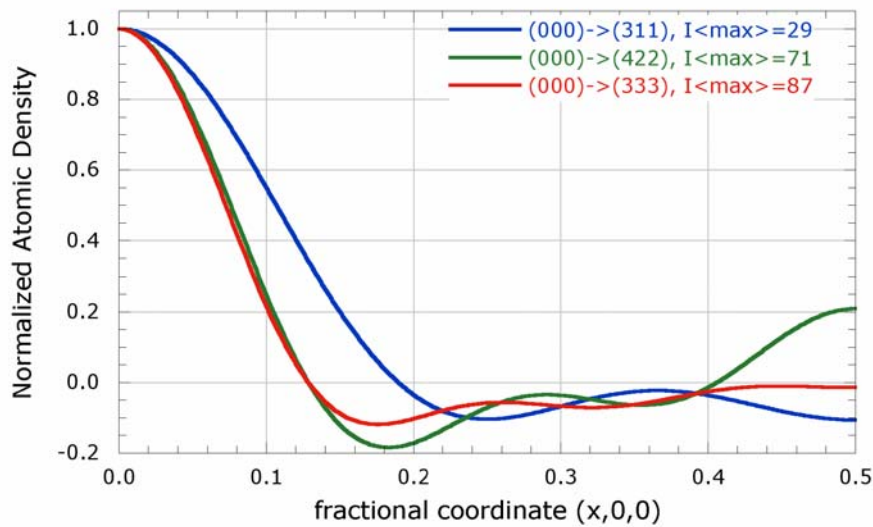
Figure 3.19: Line profiles for diamond cubic structure along the x-axis.

Table 3.3: Summary of the atomic, three-dimensional peak shapes calculated using the XSW imaging method for different bulk crystal structures. These values accompany the images in Figures 3.12 through 3.19.

Simple Cubic

Max. (hkl)	Min. d-spacing	Number of reflections		Max. intensity	Peak width (fwhm)	Peak width min d-spacing
		Total	Unique			
(310)	0.316	146	10	141	0.248	0.785
(331)	0.229	364	20	395	0.175	0.764
(333)	0.192	618	30	619	0.151	0.786

Body-Centered Cubic

Max. (hkl)	Min. d-spacing	Number of reflections		Max. intensity	Peak width (fwhm)	Peak width min d-spacing
		Total	Unique			
(310)	0.316	78	5	79	0.243	0.769
(330)	0.236	176	10	177	0.183	0.775
(431)	0.196	320	15	321	0.149	0.760

Face-Centered Cubic

Max. (hkl)	Min. d-spacing	Number of reflections		Max. intensity	Peak width (fwhm)	Peak width min d-spacing
		Total	Unique			
(311)	0.302	50	4	59	0.210	0.695
(420)	0.224	112	8	113	0.168	0.750
(333)	0.192	168	11	169	0.147	0.766

Diamond Cubic

Max. (hkl)	Min. d-spacing	Number of reflections		Max. intensity	Peak width (fwhm)	Peak width min d-spacing
		Total	Unique			
(311)	0.302	44	5	29	0.210	0.695
(422)	0.204	98	9	71	0.150	0.735
(333)	0.192	130	13	87	0.144	0.750

Chapter 4: Experimental Apparatus

4.1   Introduction

The sample preparations and XSW experiments for the Sn (and Pb) on Ge(111) surface were made at the 5ID-C experimental hutch at the Advanced Photon Source, located onsite at Argonne National Laboratory. The surface preparation and characterization were conducted in a UHV chamber/diffractometer assembly on the undulator beamline of the DuPont-Northwestern-Dow Collaborative Access Team (DND-CAT). The x-ray optics are described in section 4.2. An overview of this UHV equipment is discussed in section 4.3. Additional details for the UHV chamber and the beamline are collected in Appendix A.

Preliminary characterization of the single crystal quality for the Ge substrates were carried out at the Northwestern University (NU) x-ray diffraction facility; a diffractometer was used to measure the rocking curve for the Ge (111) reflection normal to the surface. The Blake diffractometer has a conventional tube source with a Cu target, a high-resolution incident beam 4-bounce, Si(111)

monochromator (λ = 1.5406 Å), and a scannable, high-resolution (~0.5 µrad) theta axis with encoder (Heidenhein URZ166, 0.1 µrad precision).

The incident x-ray beam is conditioned with two pairs of Si (111) channel-cut monochromators that are static and arranged in a dispersive geometry with a "+ − − +" orientation. Two representative scans are shown in Figure 4.1 for the (111) reflection for a Ge(111) single crystal before and after several thermal cycles (115 K < T_{SAMPLE} < 923 K) in the 5ID-C UHV chamber. The measured rocking curve widths from the angle encoder are both approximately 82 µrad and were fit using an appropriate linear combination of σ- and π-polarized incident x-rays. The heating and cooling of the sample appears not to alter the quality of the Ge crystal.

A pair of Si channel-cut monochromators with an *(hhh)* orientation were aligned in the NU x-ray lab and cut at the DND-CAT machine shop using a diamond blade saw. The details for the monochromator design and fabrication are discussed in Appendix B. These channel-cut monochromators are part of the XSW post-monochromator in the 5ID-C station.

Finally, the Al-Cu alloy samples were oriented in the NU x-ray lab using a Mo target x-ray source with a pinhole aperture. The single crystals were then cut and polished before inserting them into the UHV chamber (located in Cook Hall room 1008 at NU). This UHV chamber has been described in the PhD thesis of William Rodrigues [49]. The chamber is equipped with radiative heating from a tungsten filament, an ion sputter gun (with chamber back-filled with argon gas), reverse-view low energy electron diffraction (LEED), and a single-pass cylindrical mirror analyzer.
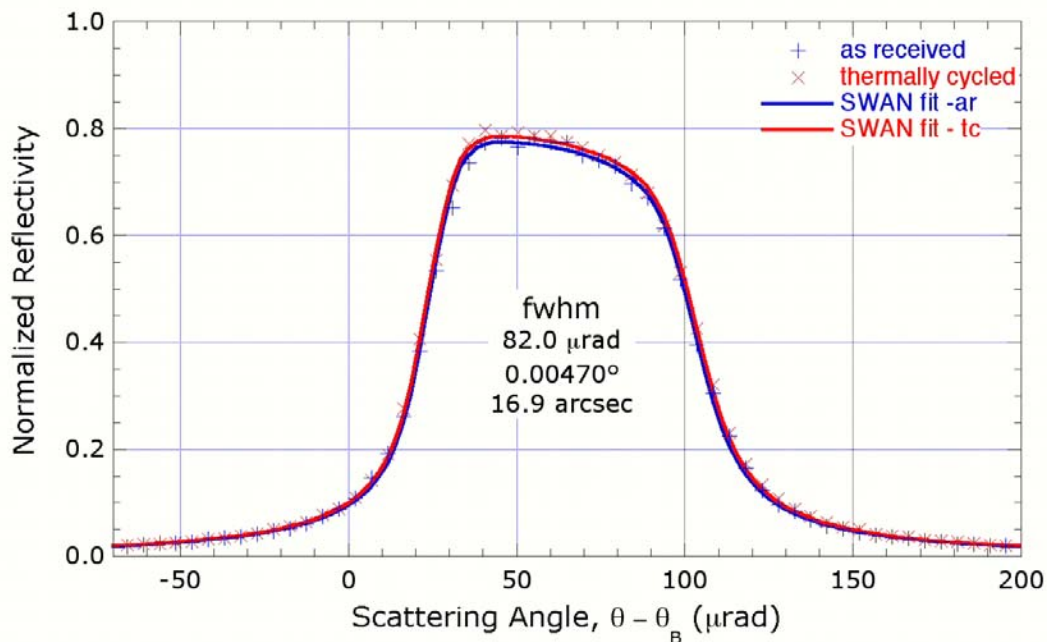
Figure 4.1: Rocking curve measurements for Ge(111) reflection using the Blake diffractometer with incident beam, 4-bounce, Si(111) dispersive monochromator. Two measurements are shown for a substrate, before and after thermal cycling (115 K < T < 923 K) in the 5ID-C UHV chamber. The data are fit using SWAN 2.1b with a linear combination of σ- and π-polarized geometries. The data was measured on an absolute reflectivity scale by normalizing to the incident beam intensity and the experimental range was calibrated by a Heidenhein encoder (URZ166) with 0.1 μrad precision. Using $|b_m|=0.4$, the range was fit to within 2% of theory.

4.2   X-Ray optics at the 5ID beamline at the APS

Referring to Figure 4.2, the x-rays on the 5ID beamline are generated from a 3rd generation synchrotron insertion device (APS Undulator A). The storage ring current typically operates at 100 mA (in top-up mode) but can decrease down as low as 40 mA. In the 5ID-A hutch, the desired x-ray energy is selected using a high-heat-load monochromator (HHL), composed of two Si (111) crystals. Due to the large thermal load on the HHL monochromator, it is cryogenically cooled. The angle of the second crystal has feedback control to maintain a fixed detuning value that adjusts for thermal drift. Two horizontally deflecting mirrors (75 cm in length) reject the higher-order harmonics and can horizontally focus (with 1:1) the x-ray beam. At lower x-ray energies ($E\gamma < 11$ keV), the glass surface is used; for higher energies, either the Pt or Rh stripes are better suited. In Figure 4.2, an overview schematic depicts the main components of the beamline used for XSW measurements. The distances (in meters) are listed for some of these components.

While the undulator produces extremely small angular divergence in the vertical direction (1st harmonic: $2\sigma_y = 13$ µrad at 7.0 keV and 3rd harmonic: 8 µrad at 16.5 keV), additional conditioning is required to reduce the energy distribution of the x-rays. In order to measure the modulation in the XSW yield, the x-ray beam needs to have a smaller angular and energy dispersion compared to the sample. Post monochromator optics are situated on an optical table located at the upstream side of the 5ID-C hutch and are shown in Figure 4.3.

This set-up uses two non-dispersive, two-bounce channel-cut monochromator that are mounted on and positioned with $XZ\theta$-stages. There are actually three
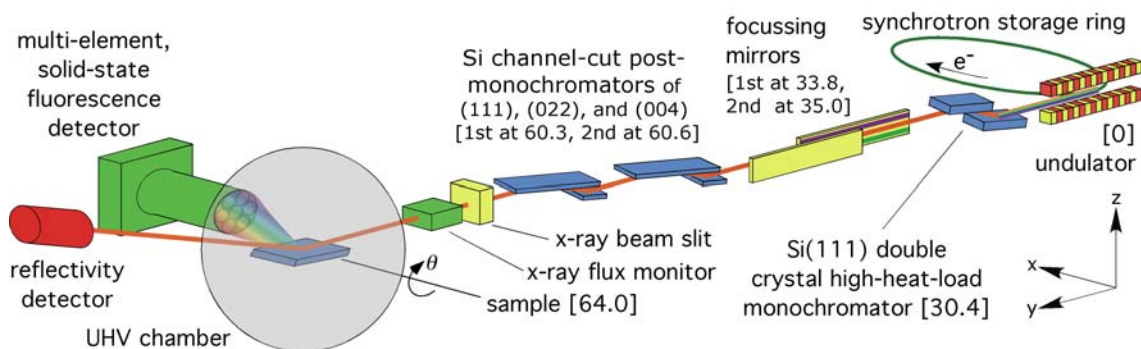
Figure 4.2: Schematic overview of the x-ray optics and equipment used for XSW measurements at the 5ID beamline. A 3rd generation synchrotron undulator source generates the x-rays. In the 5ID-A hutch, a high-heat-load monochromator selects the incident beam energy and a set of mirrors rejects the higher order harmonics and focuses the beam in the horizontal direction. In the 5ID-C hutch, ion chambers measure the x-ray flux, two sets of Si channel-cut monochromators reduce the energy band pass for the x-rays, and slits control the beam size. The sample in the UHV chamber is scanned in angle and the x-ray fluorescence yield and reflectivity are measured. The distances (in meters) from the x-ray source to some of the components are listed in brackets.

A

B

C
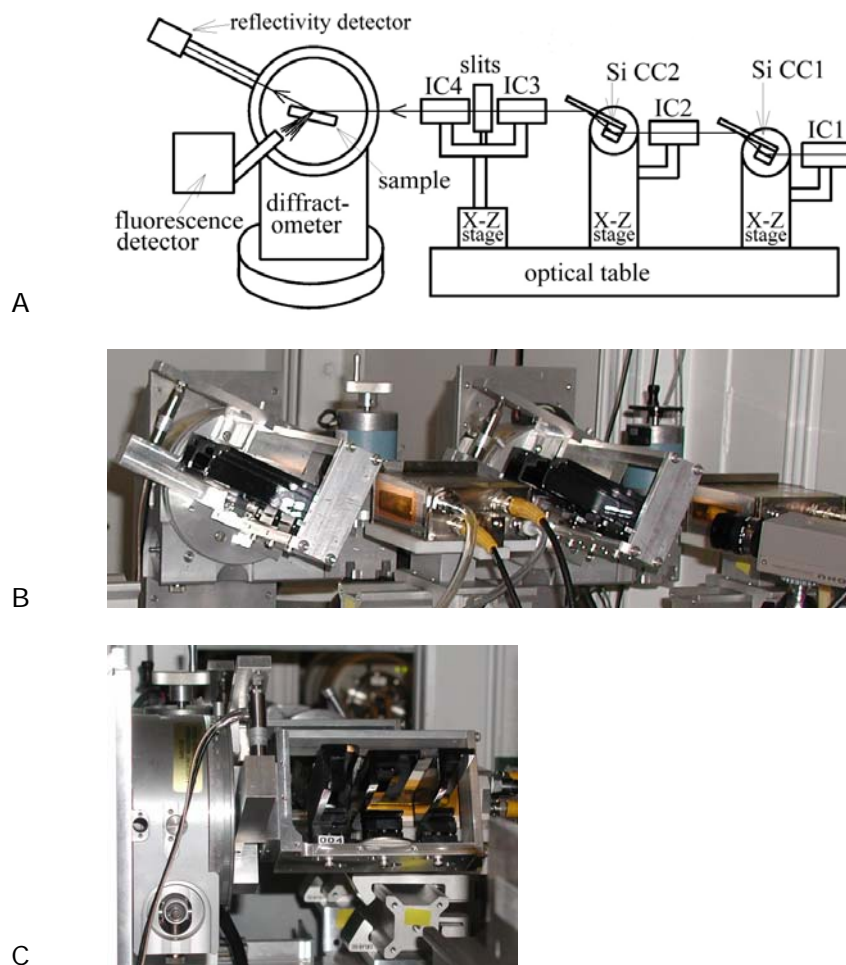
Figure 4.3:   The post monochromator optics in the 5ID-C hutch.   A)   Four ion chambers (IC) monitor the x-ray flux after various components.   Two pairs of Si channel-cut monochromators (Si CC) reduce the energy band pass of the x-ray beam.   Piezo actuators on level arms maintain a fixed detuning value for the two channel-cut monochromators. Figure from reference [51].   B)   An image (perpendicular to x-ray beam direction) of the channel-cut monochromators and the first two ion chambers.   C) Rearview (along upstream direction) of the second set of channel cut monochromators.

orientations of channel-cut monochromators that can be selected to minimize the dispersion with the sample's Bragg reflection: Si(*hhh*), Si(*hh0*), and Si(*h00*). With a piezo actuator on a lever arm, sub-μrad angular resolution can be achieved for these channel-cut monochromators. Using error-integrated feedback control (with analog MOSTAB units), the post-monochromator θ-stages maintain a fixed detune value to follow thermal drift and mechanical motions. The ion chambers shown in Figure 4.3 provide the signal for this feedback control. The slits control the size of the beam onto the sample.

To reduce the energy distribution of the x-rays incident on the sample, the second channel-cut can be detuned (with respect to the first) at the expense of x-ray flux. For Ge single crystals, the first channel-cut monochromator is typically set to be 90% tuned, and the second is set to 50% of the maximum reflectivity value. For Si single crystals, the second post-monochromator is typically set to 25% of the peak intensity. Tuning the channel-cut monochromators to these values produces a strongly modulating XSW in the substrate crystal.

As shown in Figure 4.4, the DuMond diagrams for the output of a Si (111) HHL monochromator and two Si (111) channel-cut monochromators are compared to the Ge (111) reflection using the 1st harmonic of the APS undulator A at Eγ = 7.00 keV. The DuMond diagrams for the (333) reflections are shown in Figure 4.5. In these depictions, the output of the undulator is represented with a yellow, vertical stripe. The slopes of the (*hkl*) reflections are determined from Bragg's Law. The Darwin widths of the Si (111) reflections are 39.4 μrad and 16.0 μrad. Detuning of the monochromators is depicted as an angular offset from the previous one. The
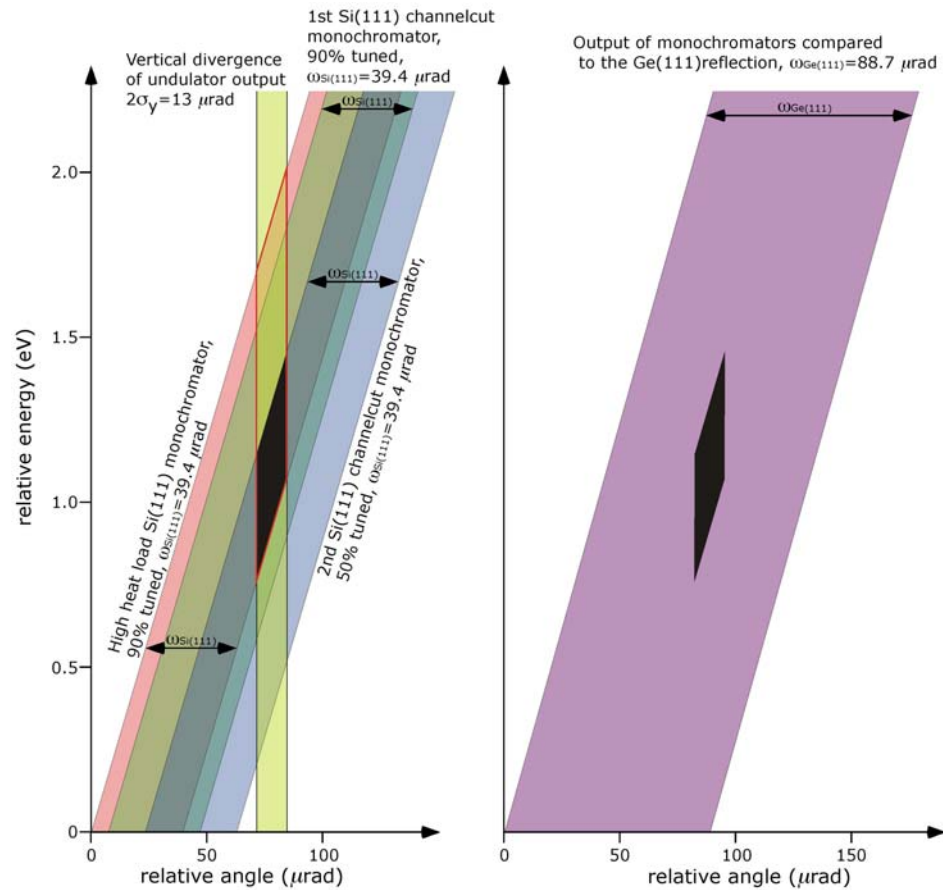
Figure 4.4: DuMond diagram for the Si (111) high-heat-load monochromator (HHLM) and two Si (111) channel-cut monochromators compared to the Ge (111) reflection using the 1st harmonic of the APS undulator A at E_γ = 7.00 keV. The output of the undulator is represented with a yellow, vertical stripe. The widths of the Si (111) reflections are 39.4 μrad. The monochromators (HHL, 1st channel-cut, and 2nd channel-cut) are shown in orange, green and blue, respectively. The output after the HHLM is outlined in red. The final output of the optics is shown in black and compared to the Ge (111) reflection, depicted in purple.
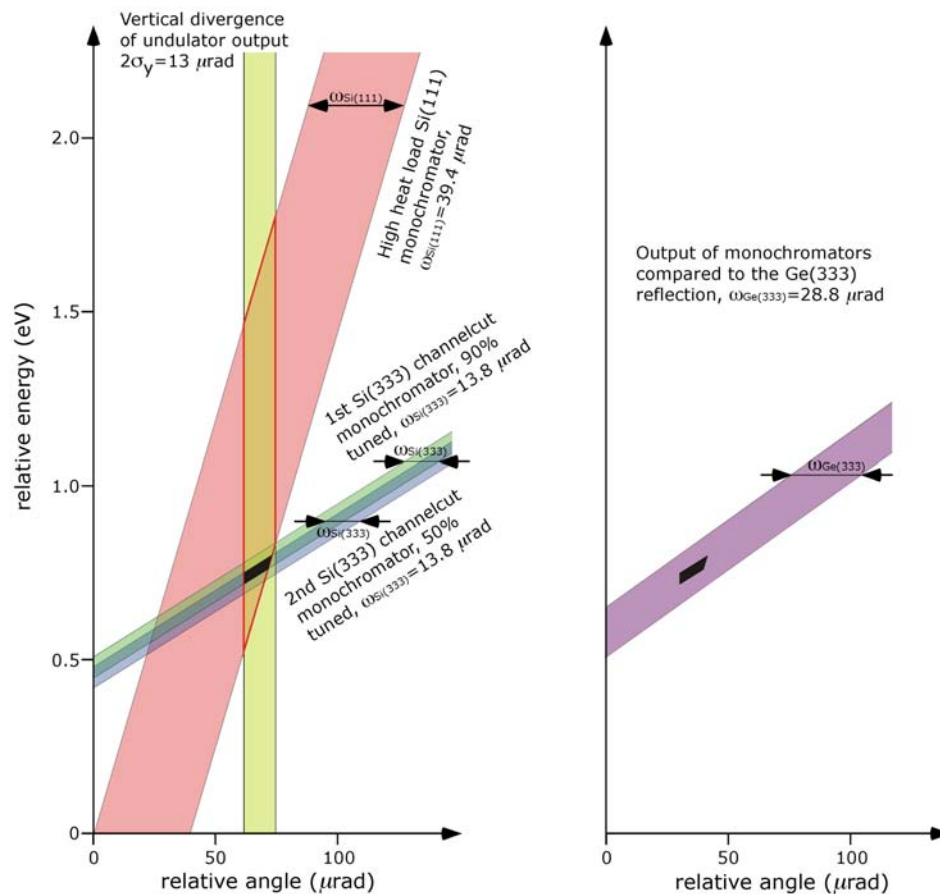
Figure 4.5: DuMond diagram for the Si (111) high-heat-load monochromator (HHLM) and two Si (333) channel-cut monochromators compared to the Ge (333) reflection using the 1st harmonic of the APS undulator A at $E\gamma$ = 7.00 keV. The output of the undulator is represented with a yellow, vertical stripe. The widths of the Si (111) and (333) reflections are 39.4 and 16.0 µrad. The monochromators (HHL, 1st channel-cut, and 2nd channel-cut) are shown in orange, green and blue, respectively. The output after the HHLM is outlined in red. The final optics output is shown in black and compared to the Ge (333) reflection, depicted in purple.

monochromators (HHL, 1st channel-cut, and 2nd channel-cut) are shown in orange, green and blue, respectively. The output after the HHL monochromator is outlined in red. The final outputs of these optics are shown as a black trapezoids and compared to the Ge (111) and (333) reflection, depicted in purple. The bandwidth ($\Delta E/E$) is approximately 1 x 10^{-4} for the (111) reflection at 7.00 keV.

With the storage ring operating in top-up mode (100 mA), the x-ray flux coming into the 5ID-C hutch was typically 8 x 10^{12} photons/sec for a horizontally focused 1.4 mm x 1.4 mm beam. Using a pair of Si(111) channel-cut monochromators (90% and 50% tuned), the incident flux onto the sample was about 2 x 10^{11} photon/sec for a 1.0 mm x 0.8 mm (width x height) x-ray beam. Helium gas flows through the ion chambers (with 400 V bias) in the post-monochromator assembly. The reflectivity is measured with an ion chamber (900 V bias) with atmospheric air inside.

The monochromator optics should also be considered when calculating the reflectivity and yield curves shown in Figure 3.3. Convoluting the monochromator with the sample, the calculated XSW reflectivity and yield curves for the Ge(111) reflection at 7.00 keV with different coherent position values are shown in Figure 4.6. In this figure, the coherent fraction is set to one, and the origin is located on the top atom in the (111) bilayer (corresponding to $P_H=0$). In this figure the Si monochromator is detuned to 50%. The effective-b value for of the monochromator is 0.25. This convolution acts to smear out the x-ray reflectivity and XSW yield.
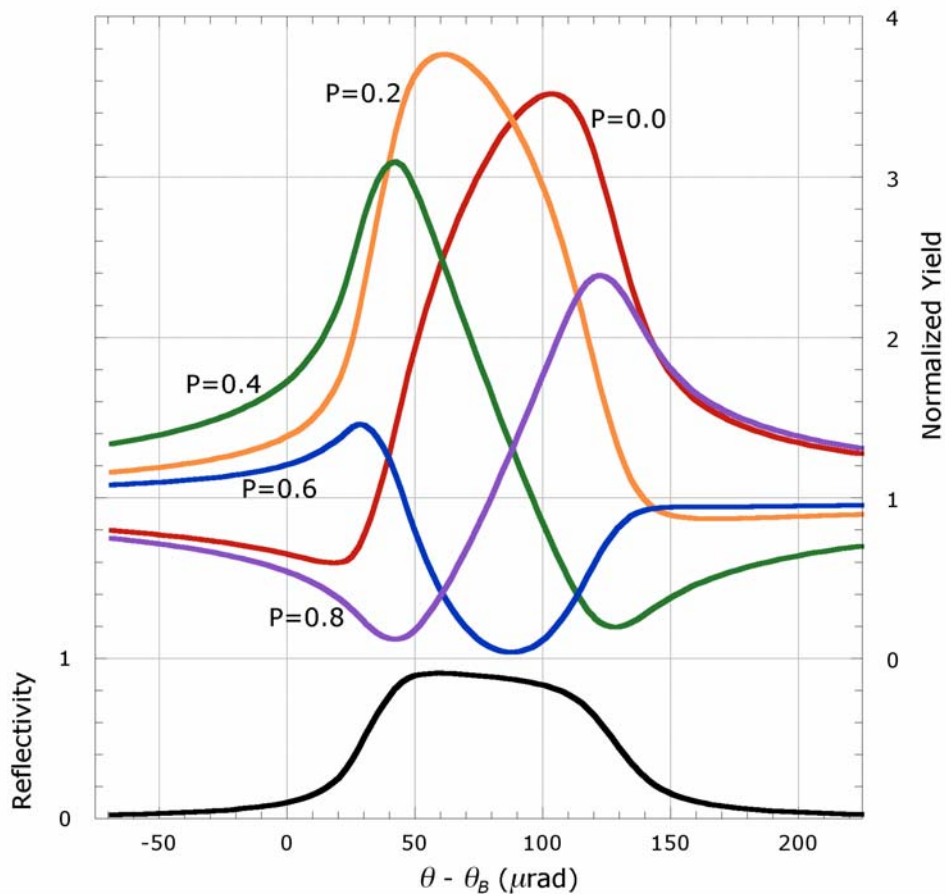
Figure 4.6: The calculated XSW reflectivity and yield curves convoluted with the monochromator for the Ge(111) reflection at 7.00 keV with different coherent position values. This figure is similar to Figure 3.3 except the rocking curve is convoluted with a Si monochromator detuned to 50%. The effective-b value for the monochromator is 0.25. In this figure, the coherent fraction is set to one, and the origin is located on the top atom in the (111) bilayer (corresponding to $P_H=0$).

4.3 UHV Chamber/Diffractometer at 5ID-C Station at the APS

The concept for the design of the UHV chamber/diffractometer was to create an apparatus that combines x-ray scattering techniques with surface science spectroscopy tools [50 - 51]. The entire UHV chamber/diffractometer assembly sits on an APS-designed heavy-duty XZ table to center it in the x-ray beam. The diffractometer can be rapidly and repeatably positioned in and out of the beam path by a 1 m translation on a pair of rails bolted to the floor. A schematic and photographic image are shown in Figure 4.7.

The diffractometer (assembled by Blake Industries from Huber circles) has four rotational axes in a psi-circle configuration, also known as 2S+2D, and is controlled with the psic geometry of SPEC. See Figure 4.7A for a schematic of the geometry. Four of the axes (del, eta, mu, and nu) are high-precision angular stages (Huber Diffraktionstechnik) with 20:1 gear reducers. The eta axis is typically microstepped for high-resolution rocking-curve measurements, which has been confirmed with autocollimator measurements; this motion is coupled to the UHV chamber through a two-stage, differentially pumped rotary feed through (McAllister Technical Services, model DPRF-400). The sample manipulator consists of a XYZ stage (McAllister Technical Services, model MB2002), a long, thick-walled tube, and the remaining two sample axes (model GB16, Thermionics Northwest). The two *in-vacuo* rotation stages, chi and phi, are useful for setting the orientation of the sample's surface normal as needed, e.g., switching between normal and off-normal
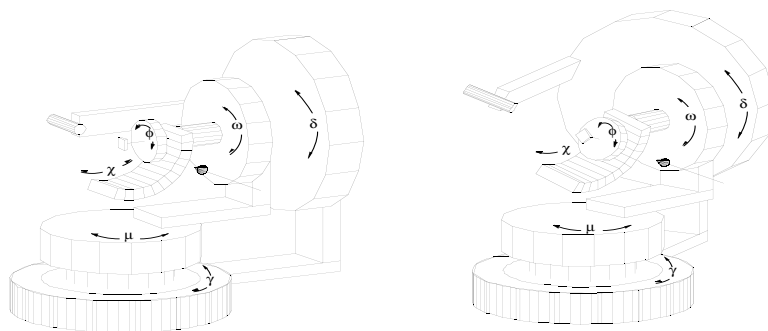
A
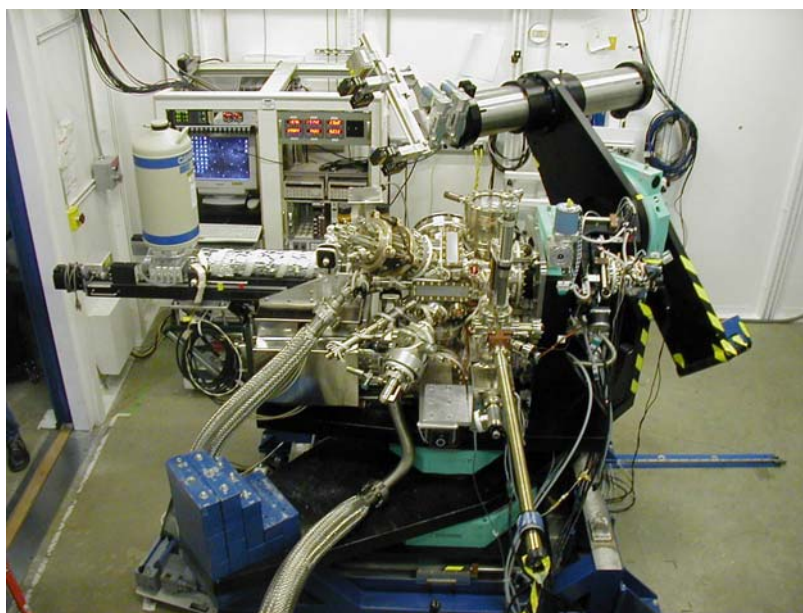
B

Figure 4.7: A) Schematic of the angle motions on the psic diffractometer. Figure taken from reference [50]. B) Image of the UHV chamber/diffractometer at the 5ID-C station at the APS. The diffractometer has four axes for the sample and two axes for the reflectivity detector. The UHV chamber is situated in the center of the diffractometer and has many surface science and spectroscopy tools. In this image the assembly is translated out of the x-ray beam path.

reflections in an XSW measurements or switching polarizations in surface scattering experiments). However, because the chi and phi circles translate on the XYZ stage, phi is not, in general, collinear with eta for chi=0; therefore, chi and phi must remain fixed during a diffraction experiment (typically after the sample surface normal is set parallel to the eta axis). Detector-arm equipment is attached using Newport X48 rails with the additional option of a two-circle analyzer stage. For the XSW experiments, the equipment was operated in a 2-circle mode, where mu=nu=0, eta=θ, and del=2θ.

One key design feature of this compact assembly is that the UHV chamber can translate independent of the diffractometer and sample, thus allowing one chamber position for x-ray scattering studies and a second chamber position for UHV tools that also require a large portion of solid angle. The UHV chamber connects to the diffractometer through large bellows; an air piston system counteracts the vacuum force through a set of pulleys and cables. In the scattering position, the x-ray fluorescence can be measured by an energy dispersive detector with a UHV interface and electron spectroscopy can be measured using a double-pass cylindrical mirror analyzer. A collimator and filter assembly eliminates background fluorescence from the chamber walls and elastic scattering from the Be windows from entering the Ge detector. Large Be windows on Conflat flanges allow x-rays to enter and exit the chamber; a large, semicylindrical Be window is not welded to the chamber, as is traditional for surface diffraction chambers, due to space constraints and concerns of stress on the window due to large UHV attachments nearby [50]. One rectangular Be window allows x-rays to enter the chamber over a wide range of the angle mu. One 10-inch-diameter Be window allows a wide range

of angles for x-rays to exit the chamber, while another, smaller rectangle allows higher-angle scattering at mu and nu ~0°. For XSW experiments, an *in-vacuo* three-grid mesh detector fills in the range of scattering angles not accessible via the Be windows. Samples can be introduced and stored in UHV by transfer to a introduction chamber.

Additional sample preparation and characterization tools include radiative heating with a nude tungsten filament (to 1100 K), liquid nitrogen cooling (to 115 K), a differentially–pumped ion sputtering system (Physical Electronics, A79163 and 179146), molecular beam epitaxy via Knudsen cells (SVT Associates, SVTA-275-16) and electron-beam evaporators (Omicron, EFM T3-100), a reverse-view LEED (Omicron SpectaLEED system, LA SPEC4/P1), a retractable double-pass cylindrical mirror analyzer (Staib Instruments, DESA-100) for Auger and x-ray photoelectron spectroscopy, a residual gas analyzer (Stanford Research Systems, RGA300), a dual-anode soft x-ray source (Omicron, DAR 400), and an electron flood gun (Staib Instruments, EK-300-FG).

With an ion pump (Physical Electronic, SPR10280-1 equipped a titanium sublimation pump and cryoshield) and turbo pump (Varian Vacuum Products, V250; backed by an Alcatel ATH20/40 turbo pump), the base pressure of the chamber is ~1.5×10^{-10} Torr.

A block diagram for the equipment control and data acquisition systems in the 5ID-C hutch is shown in Figure 4.8 [51]. A Linux PC inside of the hutch with several interface and computer cards controls much of the equipment. A Windows PC operates software for some of the surface science equipment (LEED, CMA, and

ion sputter gun). Experiments and beamline operations are controlled with a Linux PC external to the hutch.

A Joerger Enterprises 16-channel scalar is the input source for the scintillator (with SCA output) and ion chambers (with SRS570 current amplifier and a voltage-to-frequency converter). The x-ray fluorescence spectra are collected using a Canberra multi-element UltraLEGe detector with a 25 μm thin Be window and vacuum interface. MESA, a Labview-based software, controls parameters for the amplification of the signal from the energy dispersive detector. Digital pulse-height analysis is performed by X-ray Instrumentation Analysis (XIA) DXP-2X boards into the CAMAC crate. After initializing and calibrating each detector element with MESA, relevant parameters such as gain and shaping time are accessible by SPEC [52]. Because the solid-state detector is very sensitive to noise-pickup originating from the microstep drivers, it is necessary to isolate this signal from the ground loops created by these motor drivers.

SPEC macros (setxswdxp and xswdxp) are used to make XSW scans [52]. At each point of a rocking-curve scan (typically 32 points with 1 s per point), the full spectrum can be collected from every detector element. When each scan is completed, a drift-control routine judges whether the rocking curve is acceptable and adjusts the center for the following scan. If the current scan is accepted, the data are retained and scans are repeated to build up statistics. After a user-specified number of scans, the sum of the data from good scans for each element are written to files (one file per detector element per save set). Data from the different detector elements are written to separate files because they cover
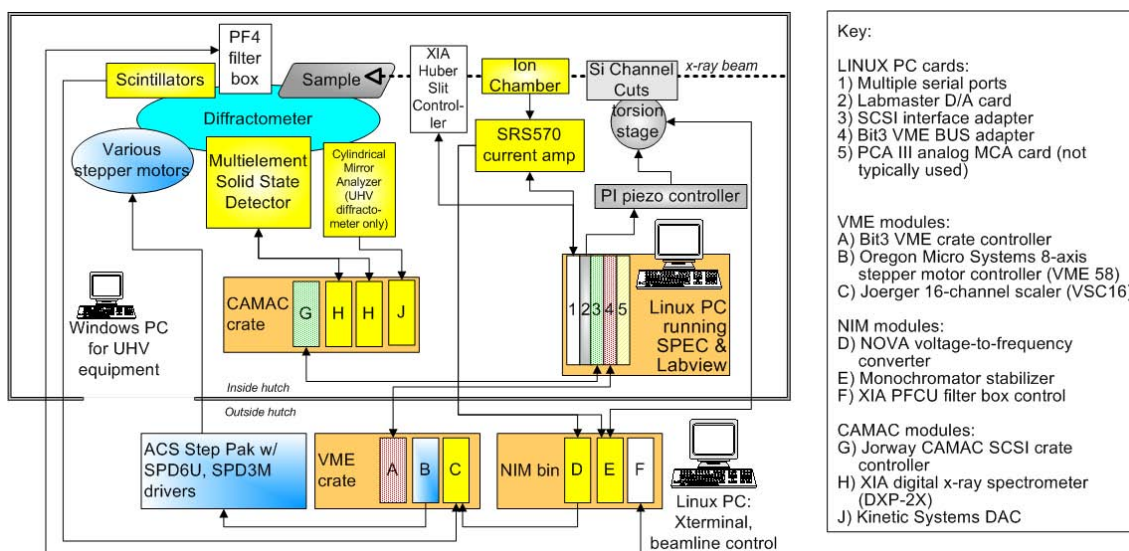
Figure 4.8: Block diagram describing the equipment control and data acquisition systems in the 5ID-C hutch. A Linux PC inside of the hutch with several interface and computer cards controls much of the equipment. A MS Windows PC operates software for some of the surface science equipment (LEED, CMA, and ion sputter gun). Experiments and beamline operations are controlled with a Linux PC external to the hutch. Modified figure from reference [51].

different regions in space, have different take-off angles, and have different deadtimes. The time to collect data for a strong reflection, like the normal (111), was typically 45 minutes. For weaker reflections, like the (333), the collection time could approach 8 hours. To monitor the sample at different stages in the measurement, the data was collected in multiple save sets.

A typical spectrum for Sn/Ge(111) XSW measurements is shown in Figure 4.9. The XSW measurements for Sn/Ge(111) were made with $E_\gamma=7.00$ keV and, therefore, excited the L emission x-ray fluorescence at 1190 eV from the Ge substrate. There is also a broad background starting about 1415 eV below E_γ that can be attributed to Ge L photoelectrons (with a range of energies) emitted from within the sample and decelerated inside of the sample, giving rise to the Bremsstrahlung radiation.

Information is stripped from the data files using SUGO 3.6. The data from different scans is collected and summed together at each XSW scan point. The normalized reflectivity is determined by dividing the total reflectivity counts (refl) by the incident beam monitor counts (ic4) and the straight through beam intensity ratio (STB),

$$R_{NORMALIZED} = \frac{\sum refl}{STB \times \sum ic4} \; \cdot \tag{4.1}$$

Listed in Equation 4.2, the normalized yield is determined by dividing the x-ray fluorescence signal (XRF) by the incident beam monitor counts (ic4) and the live time fraction (LTF).

$$Y_{NORMALIZED} = \frac{\sum XRF}{LTF \times \sum ic4} \quad .$$

(4.2)

The LTF can be determined either with a random pulse generator or with the XIA amplifier signals: fast-filter output count rate (OCR), slow-filter OCR, underflows, and overflows, as listed below. The pulser was primarily used to calculate the live time fraction in this work.

$$LTF = \begin{cases} pulser : \dfrac{\sum pulser\ cts}{(time)(pulser\ count\ rate\ with\ no\ x-rays)} \\[2em] XIA : \dfrac{\sum (slow\ filter\ OCR + underflows + overflows)}{\sum fast\ filter\ OCR} \end{cases}$$

(4.3)

The electron energy spectrum with $E\gamma = 7.00$ keV for 1/3 ML of Sn on the Ge(111) surface is shown in Figure 4.10. The actual data (shown in blue) was collected with the CMA resolution set to a fixed energy (10 eV) mode. The data is converted (shown in red) to simulate the CMA analyzer set to a constant $\Delta E/E$ mode. The Sn MNN Auger lines are near 350 eV and 421 eV. The characteristic Ge LMM Auger electrons are near 930, 1025, 1136, and 1160 eV. The broad spectrum is from secondary electrons and Ge Auger electrons escaping from below the surface and lose energy (from inelastic scattering as they travel to the surface). From this spectrum, it can be seen that the Sn Auger electron signal sits on top of a large background coming from the Ge Auger electrons.
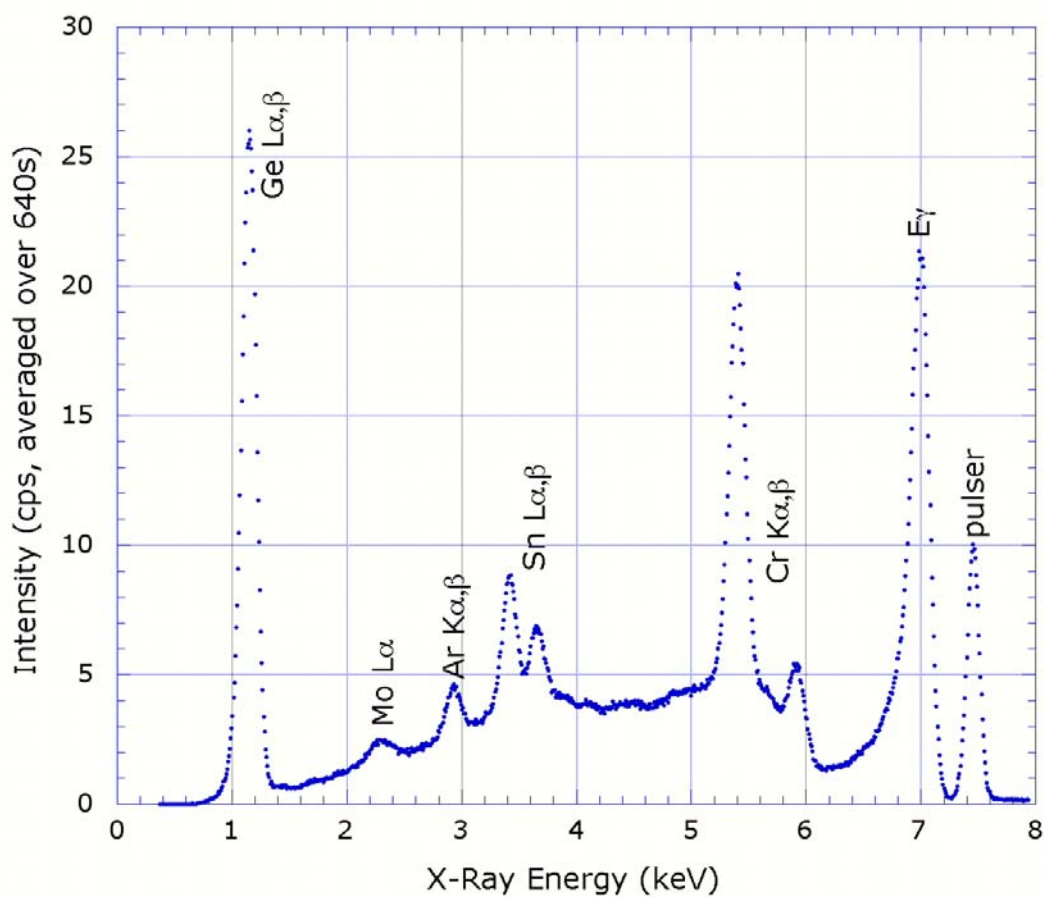
Figure 4.9: Example of the x-ray fluorescence spectrum from 1/3 ML of Sn on the Ge(111) surface with $E\gamma$ = 7.00 keV. This spectrum is summed over the angular range scanned during the normal (111) measurement. The energy dispersive detector is about 95 mm away from the sample and ~10° above the surface plane.
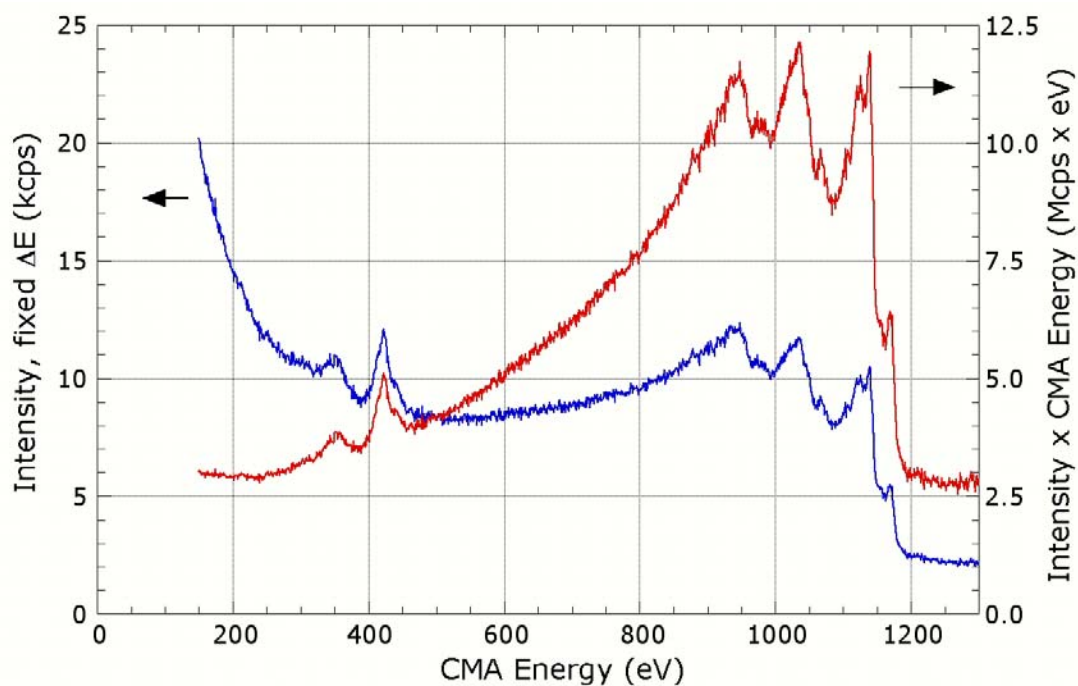
Figure 4.10: Electron energy spectrum for Eγ = 7.00 keV for 1/3 ML of Sn on the Ge(111) surface. The data (shown in blue) was collected with the CMA resolution set in a fixed energy (10 eV) mode. The data is converted (shown in red) to simulate the CMA analyzer set to a constant ΔE/E mode. The Sn MNN lines are near 350 eV and 425 eV. The Ge LMM Auger electron lines are near 930, 1030, 1130, and 1160 eV. The broad spectrum is from Ge Auger electrons escaping from below the surface that lose energy from inelastic scattering as they travel to the surface.

A typical spectrum for Pb/Ge(111) XSW measurements is shown in Figure 4.11. The measurements for Pb/Ge(111) were made with E_γ=16.35 keV and, therefore, excited the K emission at 9870 and 10,2641 eV from the Ge substrate. Because the Ge Kβ emission is extremely strong it dominates the Pb Lα line, therefore, the Pb Lβ line was used as the XSW signal. The signal coming into the detector elements was filtered with a high purity Al window (0.6 mm or 1.2 mm thickness) to preferentially attenuate the lower energy Ge Kα and Kβ x-rays, when compared with the Pb Lβ x-rays. Additionally, the fluorescence from the stainless steel chamber walls is dramatically suppressed. The transmission values for the important emission lines are listed in Table 4.1 for different Al filter thickness.

Table 4.1: X-ray transmission values for important x-ray emission lines for different Al filter thickness.

		Al Attenuator thickness				
element	Energy (keV)	500 μm	750 μm	1000 μm	1250 μm	1500 μm
Cr Kα	5.4	1.8 E-9	7.3 E-14	3.0 E-18	1.3 E-22	5.4 E-24
Fe Kα	6.4	4.4 E-6	9.1 E-8	1.9 E-11	4.0 E-14	8.3 E-17
Ni Kα	7.5	4.2 E-4	8.6 E-6	1.8 E-7	3.6 E-8	7.3 E-11
Ge Kα	9.9	3.2 E-2	5.7 E-3	1.0 E-3	1.8 E-4	3.3 E-5
Pb Lα	10.4	5.1 E-2	1.2 E-2	2.6 E-3	5.9 E-4	1.3 E-4
Ge Kβ	11.0	8.0 E-2	2.3 E-2	6.5 E-3	1.8 E-3	5.2 E-4
Pb Lβ	12.6	1.9 E-1	8.0 E-2	3.4 E-2	1.5 E-2	6.4 E-3
Eγ	16.0	4.4 E-1	2.9 E-1	1.9 E-1	1.3 E-1	8.3 E-2
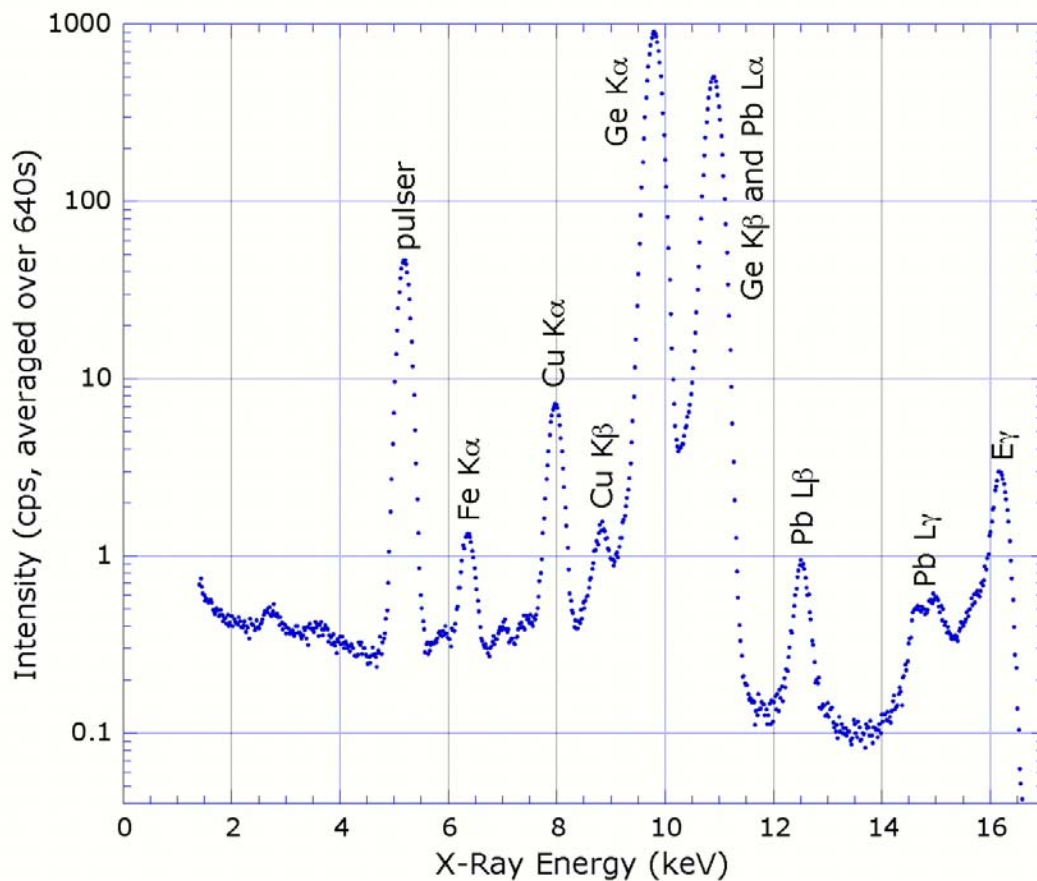
Figure 4.11: Example of the x-ray fluorescence spectrum from 1/3 ML of Pb on the Ge(111) surface with $E_\gamma = 16.35$ keV. The spectrum is summed over the angular range scanned during the normal (111) measurement. The energy dispersive detector is about 90 mm away from the sample and ~6° above the surface plane. The detector has 0.6 mm thick Al filter in front of it.

Chapter 5: Experimental Preparations and

Measurements for 1/3 ML Sn/Ge(111)

5.1   Sample Preparations

The sample preparation and measurements were performed in the UHV
chamber/diffractometer at the 5ID-C experimental station described in section 4.3.
The sample design and polishing is described in Appendix E. Before inserting the
polished samples into the chamber, the samples were cleaned in ultrasonic baths of
acetone and then methanol. Afterwards, the samples were etched with hydrofluoric
acid and transferred to a (deionized, distilled, ultra-filtered) water bath. When the
samples were removed from the water, any water droplets on the surface are
blown off with dry nitrogen gas.

Each sample was mounted on a transferable, molybdenum platen
(Thermionics, model# STLCP-1LR) with a 10 mm square window machined out so

that the rear of the sample was directly exposed to the heater element. Mo foil clips were carefully adjusted so that they held the sample firm but did not apply excessive force. If the clips create too high of a stress, the substrate could be strained and prohibit obtaining ideal rocking curves from the substrate. The "top hat" design for the samples helps reduce stress concentrations in the sample.

After degassing the sample in UHV at 773 K for 4 hours and 953 K for 1 hour, the Ge(111) surface was cleaned using ion sputtering with ultrahigh purity argon as the source gas and a 500 V accelerating potential. With the differentially-pumped sputter gun, the ion current to the samples was 0.5 μA and the chamber pressure was typically 3×10^{-8} Torr. The samples were held at 773 K during a one-hour sputter cycle and then annealed at 953 K for 15 minutes. The chamber pressure during the 953 K anneal was typically below 5×10^{-10} Torr. The total sputtering time required to clean the surface of the sample was typically 6 hours. The sputter gun was oriented normal to the sample surface for the first 3 hours and oriented with a 20° glancing angle for the last 3 hours.

After annealing, a slow cooling rate is required to form a well-ordered c(2 x 8) reconstruction. The heater current was slowly reduced at a rate corresponding to a sample cooling rate of 0.5 K/sec. The quality of (and the ability to acquire) the c(2 x 8) reconstruction is also very sensitive to impurities on the surface. If the cooling rate is too rapid or if there are impurities at the surface, the reconstruction, as measured with LEED, is either blurry or appears as a smeared c(2 x 8) or (2 x 2). Figure 5.1A shows a c(2 x 8) diffraction pattern from a clean Ge(111) surface obtained using LEED with a beam energy of 59 eV. At the center of the image, the origin (0 0) is blocked by the electron gun. Figure 5.1D shows the top-

right corner of the 5.1A image magnified with the intensity inverted. One of the (1 x 1) unit cells (and its diffraction spots) for Ge are highlighted in green. Also shown in purple is the c(2 x 8) surface reconstruction where the unit cell dimensions are equal to 1 and 1/4 of the (1 x 1) unit cell.

Once a sharp c(2 x 8) reconstruction was obtained with LEED, Sn could then be evaporated onto the clean surface at room temperature. After stabilizing the Knudsen cell to 1190 K, the sample surface was oriented normal to the Sn vapor source (at a distance of 50 cm), the shutter was opened, and the sample exposed for 1275 s (corresponding to a deposition rate of 0.016 ML/minute.) After concluding the *in-situ* UHV x-ray experiments, the amount of Sn on the sample surface was measured with *ex-situ* Rutherford backscattering spectroscopy (RBS) [53]. One monolayer on the Ge(111) surface is equal to 7.21×10^{14} atoms/cm^2. An example of an RBS spectrum for Sn on Ge is shown in Figure 5.2. Here the Sn signal is the peak centered at channel 887 and corresponds to 2.3×10^{14} Sn atoms/cm^2. The Ge substrate signal is the broad feature below channel 830. Results for the coverage of Sn on the samples are listed in Table 5.1. The estimated error in the coverage measurement is 10% of the determined value [53].

The LEED pattern for the surface with deposited Sn appeared as (2 x 2) with a diffuse background. To create the √3 phase, the sample was annealed to 473 K for 25 minutes to obtain a sharp √3 LEED pattern (E = 33 eV), as shown in Figure 5.1B. (Attempts to anneal the sample at 423 K did not appear to produce sharp √3 LEED patterns; a diffuse background was present.) The top-right section of this
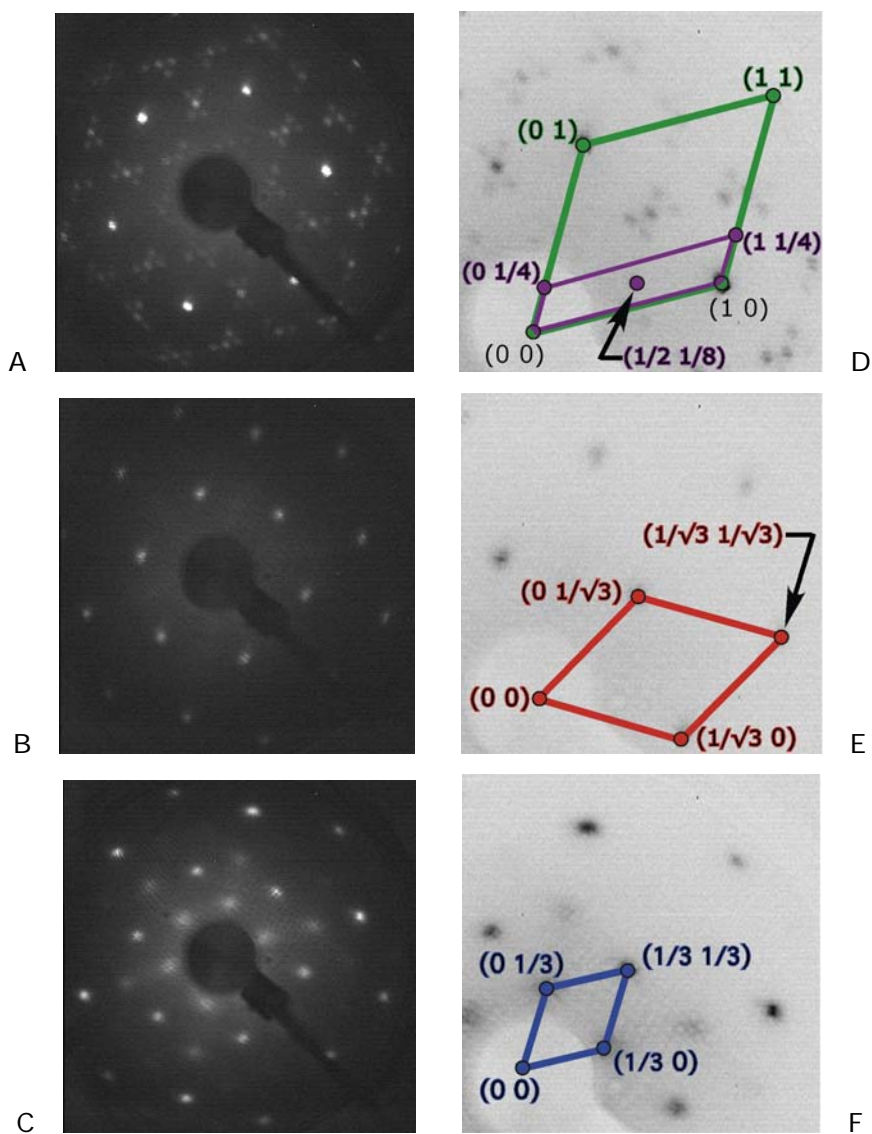
Figure 5.1: A) c(2 x 8) LEED diffraction pattern from a clean Ge(111) surface, E=59 eV. B) √3 LEED pattern for 1/3 ML Sn/Ge(111) at RT, E=33 eV. C) (3 x 3) LEED pattern for 1/3 ML Sn/Ge(111) at LT, E=34 eV. D-F) Top-right corners of A-C images magnified and the intensity inverted. Unit cells for the surface reconstructions are outlined and the diffraction spots are labeled, referring to the (1 x 1) unit cell.
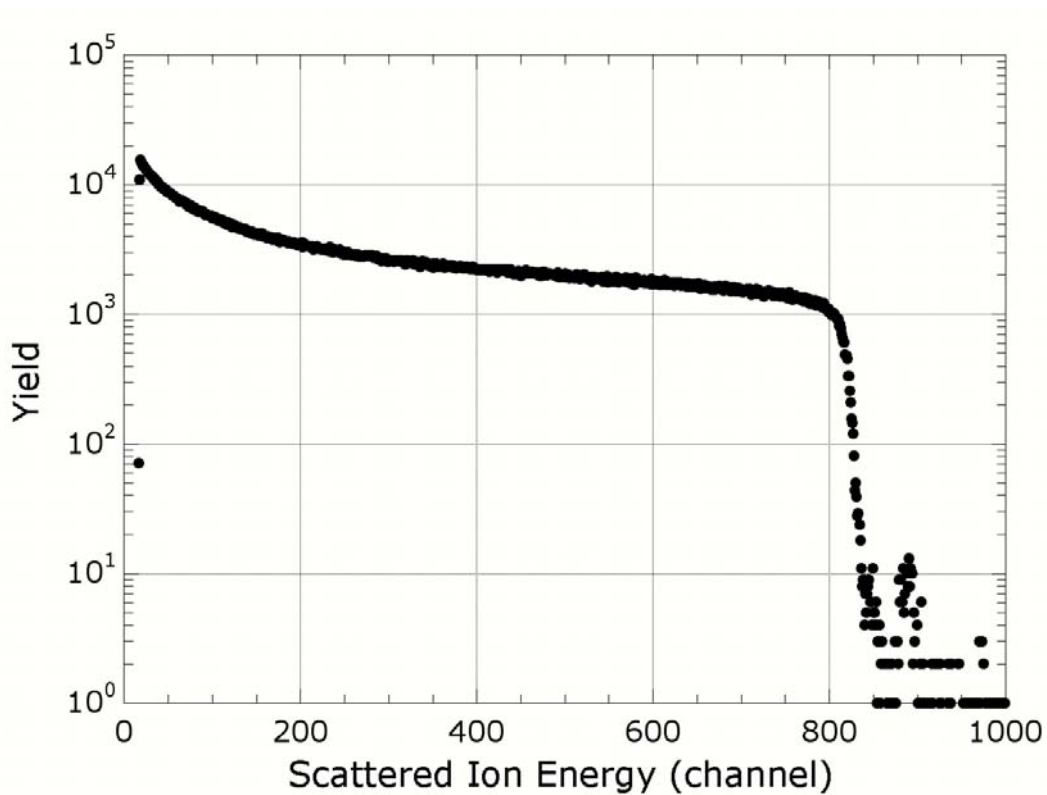
Figure 5.2: RBS (*ex-situ*) spectrum for ~1/3 ML Sn on Ge. The Sn signal is the peak centered at channel 887 and the Ge substrate signal is below channel 830. The quantity of Sn was measured to be 2.3 x 10^{14} Sn atoms/cm^2 and corresponds to 0.32 ML on the Ge(111) surface. This measurement was made by Pete Baldo of the Materials Science Division at Argonne National Laboratory.

image is shown in Figure 5.1E, and the diffraction pattern from √3 unit cell is outlined in red. The LEED images in Figure 5.1 all have the same sample orientation. When compared to the Ge (1 x 1) diffraction pattern, the √3 unit cell is rotated by 30°.

Cooling the sample to 115 K caused the surface to display a (3 x 3) reconstruction, shown in Figure 5.1C (E = 34 eV). The (3 x 3) unit cell, outline in blue in Figure 5.1F, has the same orientation as the Ge (1 x 1) unit cell.

5.2   X-Ray Standing Wave Measurements

There were three different ~1/3 ML Sn/Ge(111) samples prepared and measured (referred to as Sn1, Sn2, and Sn3). The plan was to measure the (111), (333), (11$\overline{1}$), and (33$\overline{3}$) XSW Sn yields at RT and at LT for each sample. A three-dimensional atomic distribution for Sn would be achieved by applying three–fold crystallographic symmetry. However, during a typical, 5-day beam time experiment, all eight XSW measurements per sample were not completed.

During the XSW measurements, the Ge single crystal substrate was scanned in angle through a selected *hkl* Bragg peak, and the induced modulation in the Sn L x-ray fluorescence yield was measured using a multi-element, Ge solid-state detector (Canberra UltraLEGe, either the 3-element or the 7-element model). In the case of sample Sn3, the Auger electron signal was also measured using the CMA. For the XSW measurements on Sn/Ge(111), the incident beam energy was set at Eγ = 7.00 keV. For each *hkl* reflection from the Ge substrate, the corresponding *hkl* reflection was selected for the Si post-monochromators to minimize dispersion. With the

exception of the normal (333) measurements for sample Sn1, two channel-cut monochromators (1st crystal 90% tuned and the 2nd crystal 50% tuned) were used for all of the XSW measurements. For the normal (333) measurements, only one channel-cut monochromator (80% tuned) was used.

The most complete set of *hkl* measurements were made on sample Sn1: two Bragg reflections normal to the surface, (111) and (333), and two off-normal reflections, (11$\bar{1}$) and (33$\bar{3}$), measured at RT and LT, minus the (33$\bar{3}$) at LT. Table 5.1 contains a summary list of the Sn XSW measurements made for the three samples. Plots of the XSW measurements and their fits to theory using Eq. (3.27) are shown in Figures 5.3 – 5.6 for sample Sn1 at RT. The yields and fits for the Ge Lα,β x-ray fluorescence are also shown.

5.3   Results and Discussion for 1/3 ML Sn/Ge(111)

5.3.1 XSW measured values

In this analysis the unit cell origin is centered on the ideal bulk-like Ge site in the top of the bilayer. Therefore, the bulk Ge signal should be P_{111}=-1/8 (or 7/8), as is the case shown in Figure 5.3.   At both 300 K and 115 K, the measured Sn P_{111} values are the same for each sample, within experimental error. The reduction in value of f_H for sample Sn1 at LT is caused by Sn interacting over time with adsorbed gases. During the XSW experiments on sample Sn1, the normal (111) XSW scan was remeasured several times to monitor the decrease of f_{111} (P_{111} and
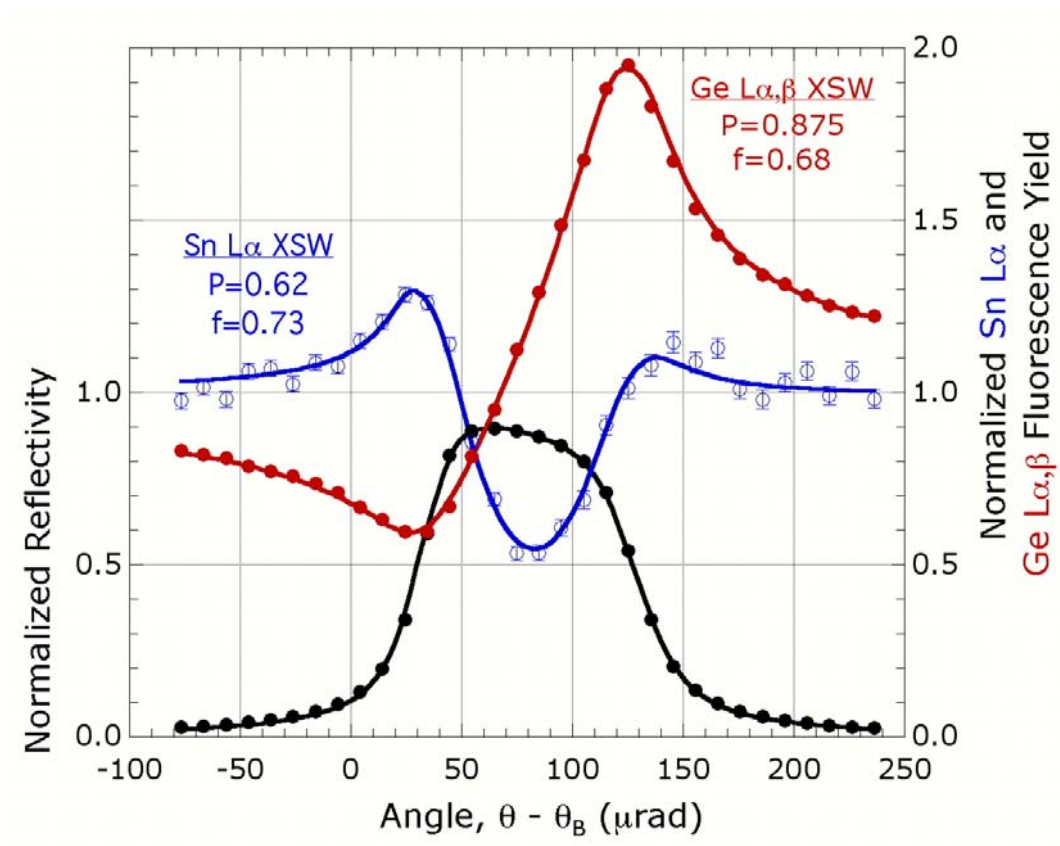
Figure 5.3: RT (111) XSW results showing the angular dependence of the experimental and theoretical curves for reflectivity and fluorescent yields for Sn Lα and Ge Lα,β for sample Sn1.
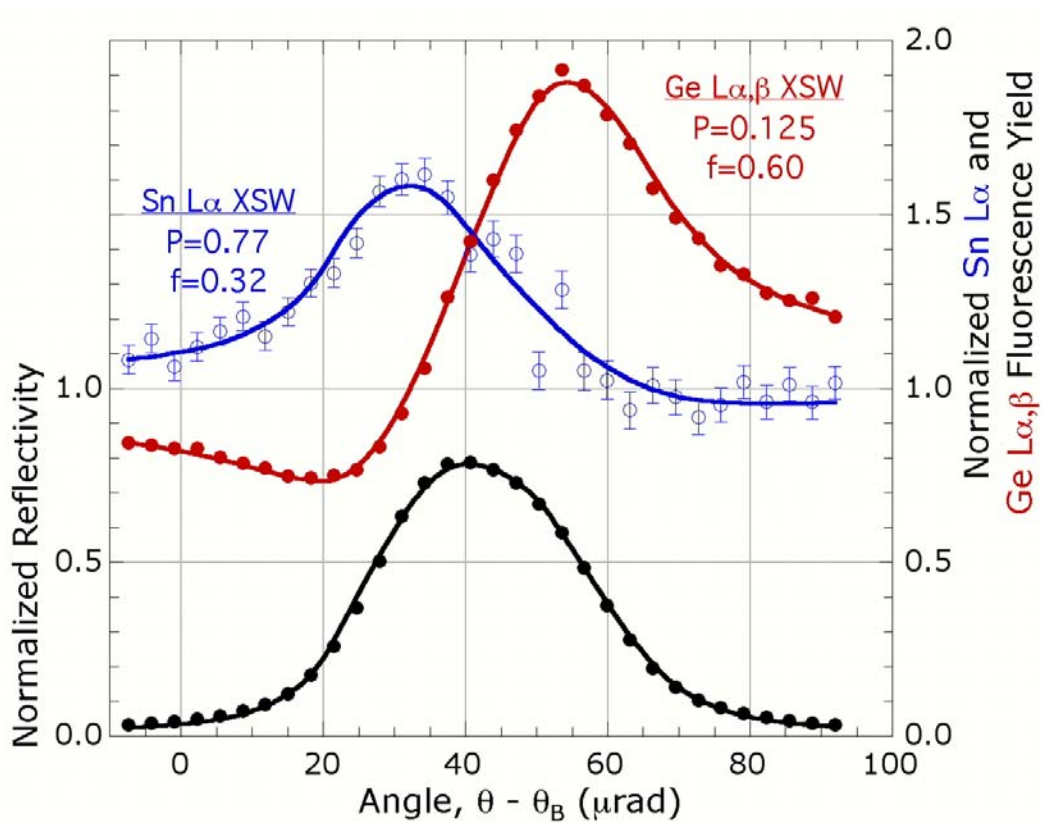
Figure 5.4: RT (333) XSW results showing the angular dependence of the experimental and theoretical curves for reflectivity and fluorescent yields for Sn Lα and Ge Lα,β for sample Sn1.
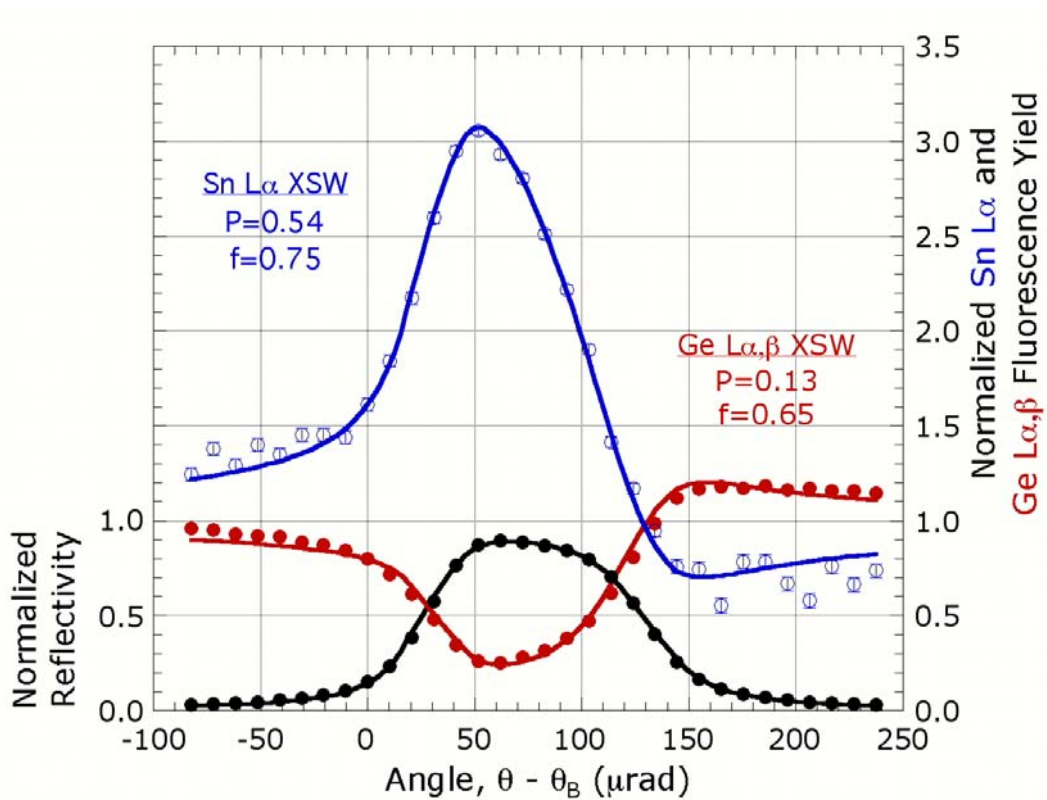
Figure 5.5: RT (11$\bar{1}$) XSW results showing the angular dependence of the experimental and theoretical curves for reflectivity and fluorescent yields for Sn Lα and Ge Lα,β for sample Sn1.
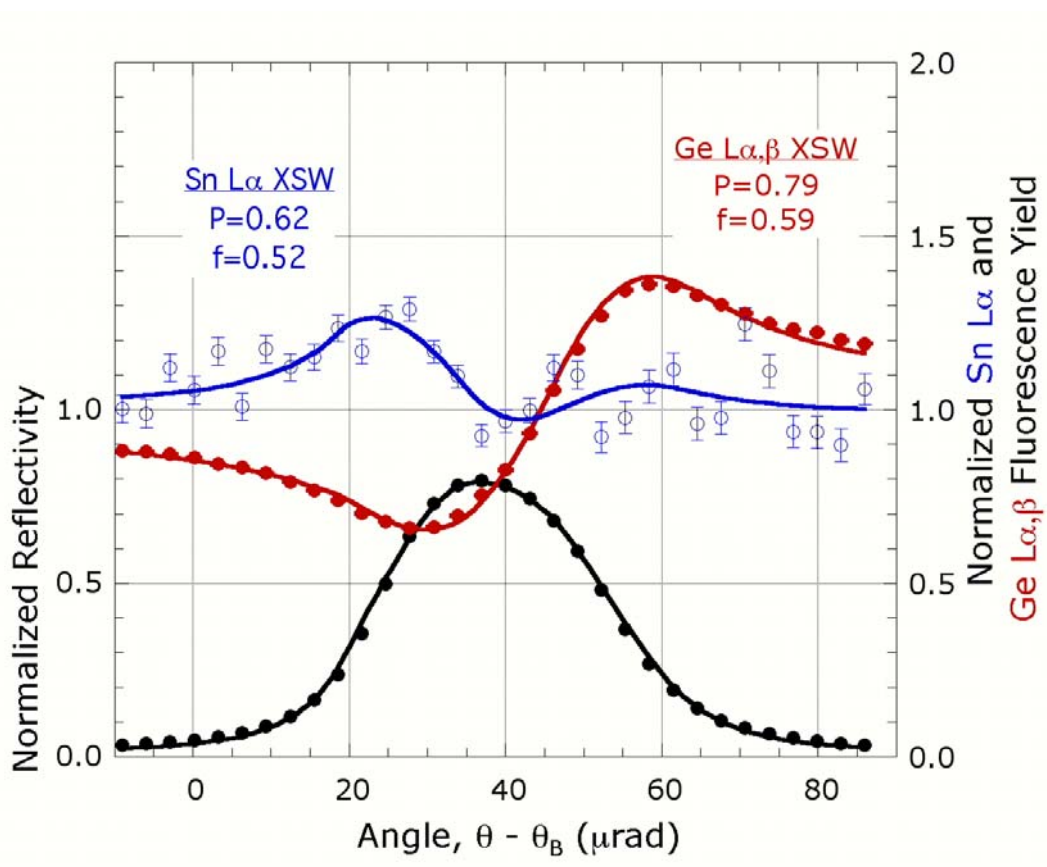
Figure 5.6: RT $(33\bar{3})$ XSW results showing the angular dependence of the experimental and theoretical curves for reflectivity and fluorescent yields for Sn Lα and Ge Lα,β for sample Sn1.

the Sn coverage remained constant). From this time series, it was found that the ordered fraction C decreased by 10% over a 24 hour period. It is important to note that just before and after cooling the sample to 115 K, identical results were obtained for P_{111} and f_{111} at both RT and LT, indicating that the local Sn spatial distribution was unchanged by the phase transition that affects its long-range order.

Table 5.1: Summary of the theoretical fit to the XSW data for Sn/Ge(111). The origin is centered on the top Ge atom in the bulk-like structure. Measurements were made at RT with the sample displaying the √3 reconstruction and at LT with the sample having a (3 x 3) reconstruction. Sample Sn2 had a higher annealing temperature (after Sn deposition). Eγ=7.00 keV.

Sample	T_{ANNEAL}	Θ (ML)	(hkl)	√3 phase, 300 K		(3 x 3) phase, 115 K	
				P_H	f_H	P_H	f_H
Sn1	473 K	0.29(3)	(111)	0.63(1)	0.73(1)	0.64(1)	0.63(1)
			(333)	0.77(2)	0.33(2)	0.82(3)	0.22(3)
			(11$\overline{1}$)	0.54(2)	0.75(2)	0.53(2)	0.64(2)
			(33$\overline{3}$)	0.62(2)	0.52(2)	-	-
Sn2	548 K	0.32(3)	(111)	0.64(1)	0.51(1)	0.64(1)	0.50(1)
			(333)	0.59(2)	0.33(2)	-	-
			(11$\overline{1}$)	0.56(2)	0.50(2)	0.55(2)	0.47(2)
Sn3 (XRF)	473K	~1/3	(111)	0.61(1)	0.57(1)	-	-
Sn3 (AES)			(111)	0.60(2)	0.48(2)	-	-

5.3.2 XSW Direct Space Map for (√3 x √3)*R*30°

Typically, to determine an adsorption site with the XSW technique, the positions of the atoms are triangulated using two measurements, one normal and the other off-normal to the surface. In general, and especially in cases of more than one adsorption site per unit cell, it is desirable to determine the position of atoms without assuming a model prior to the analysis.

As explained in section 3.4, one can create a 3D density map of the Sn atoms by the summation of the measured Fourier components and by taking advantage of the symmetry about the surface normal where domains are equivalent. The Ge(111) surface has three-fold symmetry; the $[11\bar{1}]$, $[1\bar{1}1]$, and $[\bar{1}11]$ directions are equivalent. Key point of the MatLab code are listed in Appendix C.

Inserting the RT XSW-measured Fourier amplitudes and phases for sample Sn1 listed Table 5.1 into equation 3.34 produces the direct space images shown in Figure 5.7. The top view is a cross sectional cut through the 3-D image at 2.0 Å above the surface, and the side view is through the long diagonal of the (1 x 1) unit cell. This diagonal intersects the three high-symmetry (T_1, H_3, and T_4) adsorption sites on the Ge(111) surface. In these images the dark red spots, representing the maximum Sn atomic density, are located in the T_4–adsorption site and are centered 2.0 Å above the top of the bulk-like bilayer. In addition to this evidence from the XSW image, the T_4–adsorption site is confirmed by the XSW measurements obeying the crystallographic symmetry relationship, $P_{11\bar{1}} = (P_{111}+1)/3$. For the T_1-site, $P_{11\bar{1}} = P_{111}/3$; for the H_3-site, $P_{11\bar{1}} = (P_{111}+2)/3$.
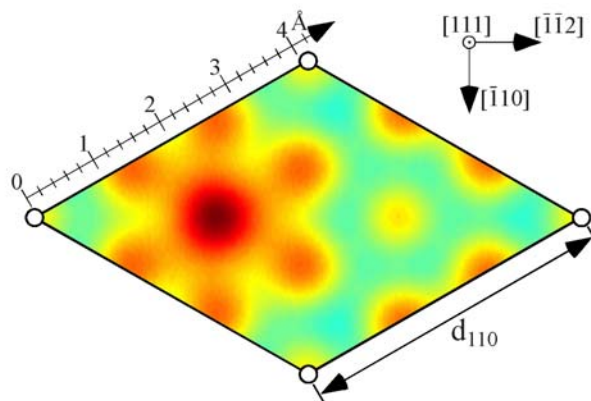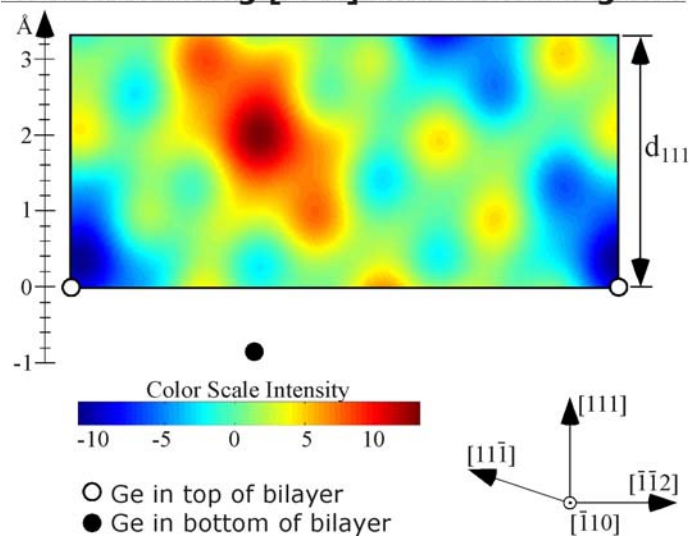
Figure 5.7: XSW direct space atomic density maps for the 1/3 ML Sn/Ge(111) surface at RT for sample Sn1. The XSW measurements project the extended structure into the primitive unit cell of the bulk crystal. The top view corresponds to the (1 x 1) 2D unit cell shown in Figure 2.7 and confirms that the Sn occupies the T_4-site. The black circles are added to the image to represent the bulk-like atoms in the Ge bilayer.

Because the XSW is generated by the allowed reflections from the Ge substrate, the atomic distribution is projected into the primitive unit cell for the Ge crystal. Thus, if there are two distinct heights in the two-dimensional superlattice, their projections will superimpose to form a combined distribution. The resolution of this method along the [111] direction corresponds to one-half of the smallest d-spacing measured, in this case $d_{333}/2 = 0.5$ Å. Within this resolution, the Sn distribution is elongated in the [111] direction, but does not show two distinct positions in the direct space image. Rather, the two positions are smeared together and result in a bottom-heavy ovoid shape in the direction normal to the surface. The density oscillations appearing in the image are the result of unmeasured Fourier coefficients (that are set to zero) that abruptly truncate the summation.

The ability to use rulers of two different periods to measure the vertical distribution is shown in Figure 5.8. The position from the (111) measurement, shown in red on the right side, can be compared to the (333) position on the left side. The coherent positions for the (111) and (333) XSW measurements correspond to different heights. The fact that P_{333} is measured to be less than $3P_{111}$ *modulo-1* (i.e., 0.77 < 0.89), indicates a bottom-heavy, asymmetric distribution that is consistent with "one up and two down". If the height separation is less than $d_{333}/2$ and the time-averaged up:down occupation ratio were even, P_{333} would equal $3P_{111}$ *modulo-1*; if it were 2:1, P_{333} would be greater than $3P_{111}$ *modulo-1*.
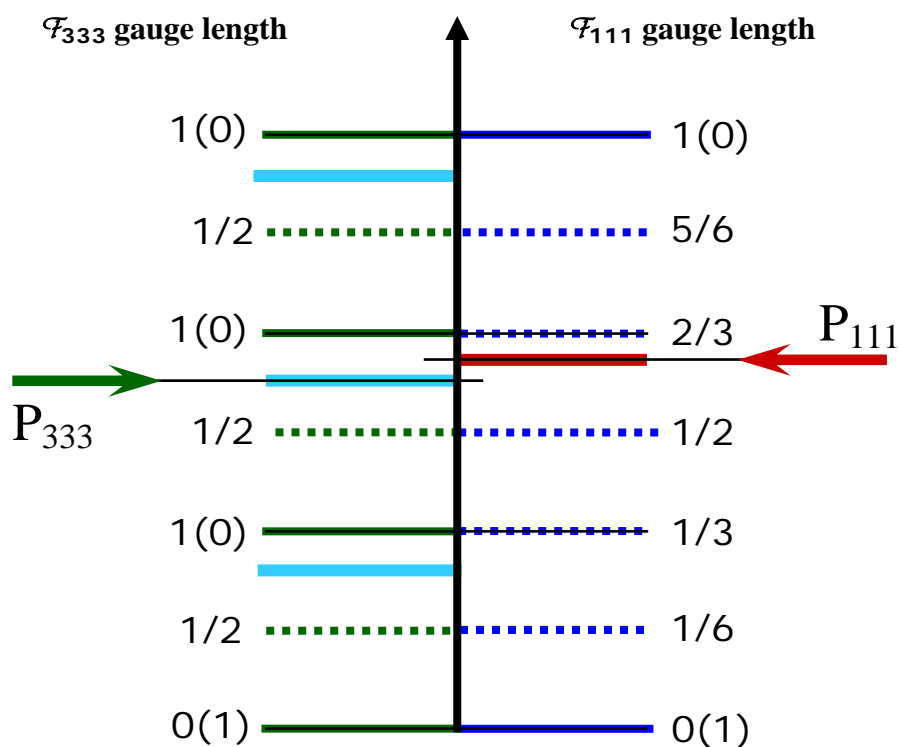
Figure 5.8: The 1-D projection of the Sn distribution is measured with two different rulers, (111) and (333), for sample Sn1. The coherent position from the (111) measurement, shown in red on the right side, can be compared to the (333) position on the left side. The asymmetry of the distribution along the [111] direction leads to the coherent positions for the (111) and (333) XSW measurements to correspond to different heights. The fact that P_{333} is measured to be less than $3P_{111}$ *modulo-1* (i.e., 0.77 < 0.89), indicates a bottom-heavy, asymmetric distribution that is consistent with "one up and two down".

While the XSW direct space imaging technique is useful for determining the position of the adsorbate *a priori*, the XSW results can also be used to precisely determine the positions of the Sn atoms with respect to a model. The XSW direct space image in Figure 5.7 supports the T_4-adsorption site for the Sn atoms. The LT STM images in Figure 2.8 display a 1:2 arrangement for Sn atoms at this site, therefore, a 1/3 and 2/3 weighting is appropriate for modeling the surface structure. Using the normal (111) and (333) XSW measurements, the vertical distribution for the Sn atoms can be determined using a model with the following constraints:

(1)   a fraction C of Sn atoms are at T_4–sites;

(2)   the remaining fraction *(1-C)* are randomly distributed;

(3)   for Sn at the T_4–sites, 1/3 are at height h_A and 2/3 are at height h_B;

(4)   the rms vibrational amplitude $\left\langle u_{111}^2 \right\rangle^{1/2}$ for all Sn atoms is identical.

These model constraints permit a single adsorption height and allow for a "one up and two down" or "two up and one down". A Fourier coefficient in the [111] direction, with its measured amplitude f_H and measured phase P_H, are related to the four parameters of the model as follows:

$$\mathscr{F}_H = f_H \exp(2\pi i P_H)$$

$$= C\left[\frac{1}{3}\exp\left(2\pi im\,\frac{h_A}{d_{111}}\right) + \frac{2}{3}\exp\left(2\pi im\,\frac{h_B}{d_{111}}\right)\right]\exp\left(-2\pi^2 m^2\,\frac{\left\langle u^2 \right\rangle}{d_{111}^2}\right) \qquad . (5.1)$$

For the 111 reflection $m = 1$, and for the 333 reflection $m = 3$. Using the (111) and (333) measured values of P_H and f_H for sample Sn1 listed in Table 5.1, the four unknown model parameters are determined. At RT, the Sn atoms have a "one up and two down" configuration, where $h_A = 2.32(5)$ Å and $h_B = 1.87(5)$ Å. The vibrational amplitude for the Sn atoms was determined to be $\left\langle u_{111}^2 \right\rangle^{1/2} = 0.08(4)$ Å, and the Sn ordered fraction for this sample was $C = 0.82(4)$.

Using a complex-plane representation with polar coordinates (r, ϕ), this model and the XSW measurements for sample Sn1 can be seen in Figure 5.9. The three Sn atoms per (3 x 3) unit cell are each represented by a red arrow with a polar angle in the complex plane determined by

$$\varphi = 2\pi \left(\frac{mh_i}{d_{111}} \right) \quad . \tag{5.2}$$

The lengths of the red arrows are reduced by the Debye-Waller factors, $D_{111}=0.99$ and $D_{333}=0.90$. The measured complex Fourier coefficient (with $f_H = 1$) is drawn with a thin black line from the origin. The XSW-measured Fourier coefficients, based on P_H and f_H are represented with blue lines. The random fraction *(1-C)* from the model is depicted with a green line segment that extends from the end of the blue line to scale the mode (where C=1) to the XSW measurement. The uncertainties in the XSW measurements are represented by the dimensions of the blue rectangles.
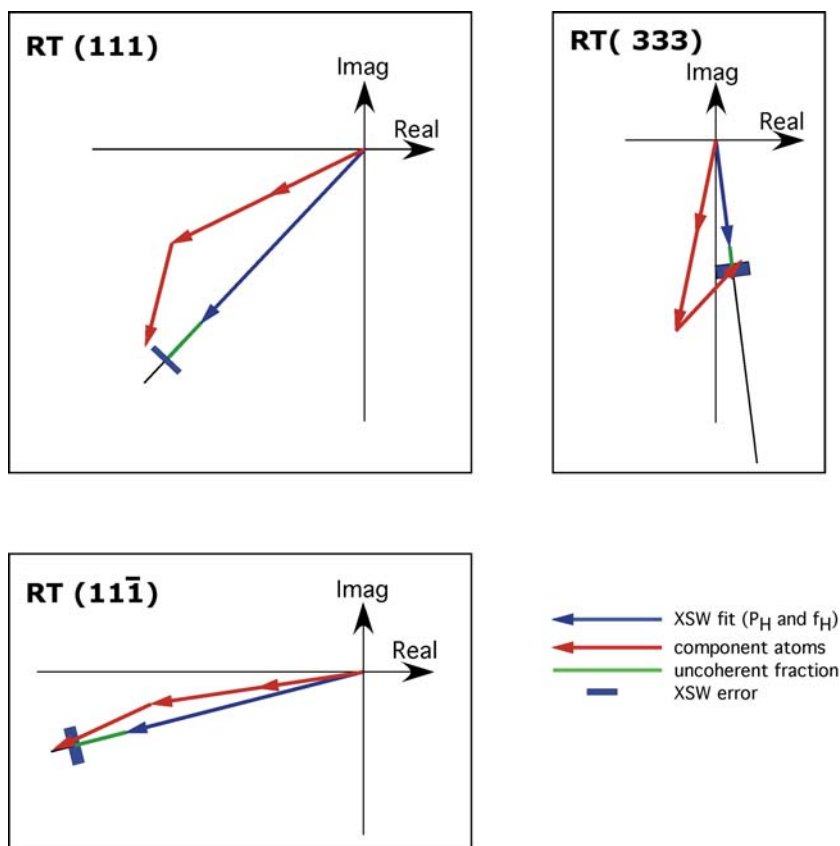
Figure 5.9: Complex-plane representation of the XSW measured Fourier coefficients and the model for sample Sn1. The three Sn atoms per (3 x 3) unit cell are each represented by a red arrow. The lengths of the red arrows are reduced by the rms vibrational amplitude of the Sn atoms. The measured coherent position (with f_H = 1) is drawn with a thin black line from the origin. The measured Fourier coefficients (from P_H and f_H) are represented with blue lines. The random fraction *(1-C)* from the model is depicted with a green line segment that extends from end of the blue line to scale the model to the XSW measurement. The uncertainties in the XSW measurements are represented by the dimensions of the blue rectangles.

5.3.3 XSW results compared with other structural measurements

Although the T_4–site assignment is in agreement with the SXRD results, the XSW-measured vertical distribution of Sn atoms is different and can be seen in Figure 5.10. In this figure the values for coherent position were calculated from the SXRD model and the ordered fraction was set to 82%. At RT Bunk *et al.* [20] determined a single position for the T_4–site Sn atom and refined the height to be 1.84 Å above the surface. While their structure at LT has a similar Sn distribution, "one up and two down", their model has a smaller vertical separation in height, 0.26 Å. It should be noted that the vibrational amplitude for the "up" atom was refined to have an unusually large value (0.41 Å). In their discussion, if the three Sn atoms have the same vibrational amplitude, their vertical separation was ~0.45 Å , which matches the XSW model. The model proposed by Avila *et al.* has a comparable vertical split in height, 0.49 Å, at both RT and LT. However, their distribution showed the opposite asymmetry, "two up and one down" [23].

The XSW-determined model parameters appear most similar to those by Petaccia and Floreano *et al.,* who made photoelectron diffraction (PED) measurements on the (3 x 3) phase and used He diffraction to study the effect of temperature on the local structure of Sn [54 -56]. By analyzing PED from the Sn *4d* core-level, they determined bond information between Sn and the neighboring Ge atoms; they found a "one up and two down" Sn distribution, however, the difference in heights was 0.3 Å. Their temperature studies found an order-disorder behavior near T_C.
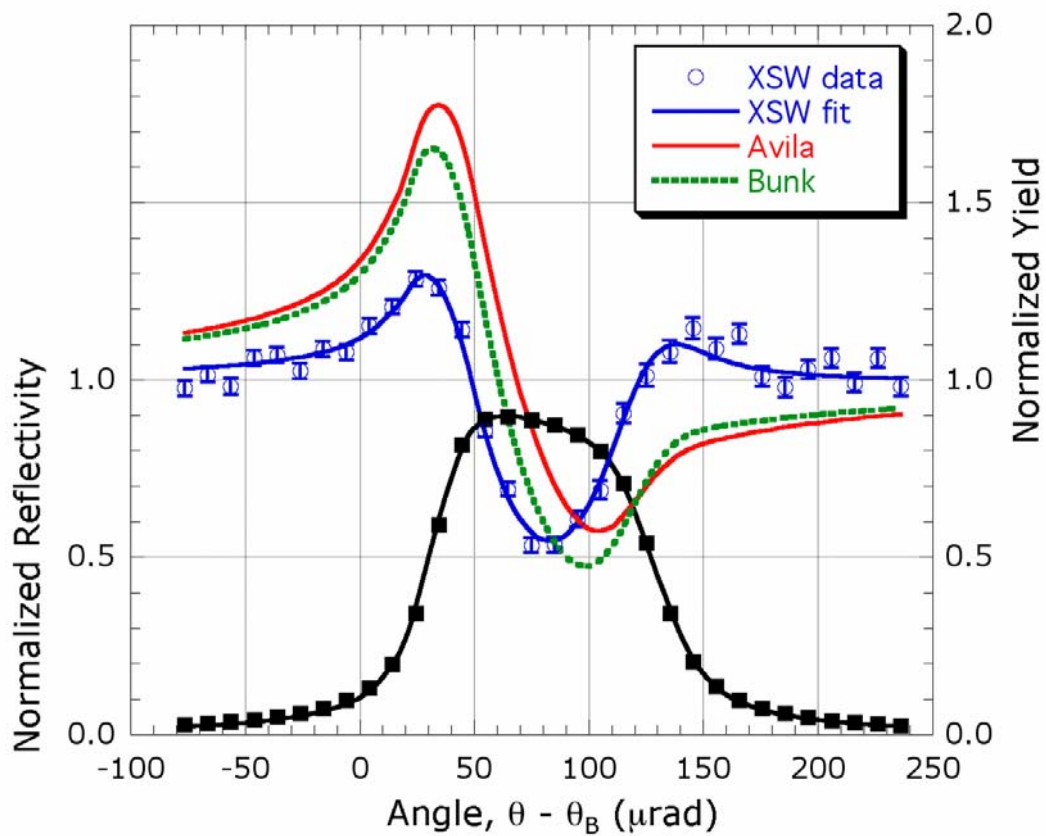
Figure 5.10: RT (111) XSW results showing the angular dependence of the experimental and theoretical curves for reflectivity and fluorescent yields for Sn Lα. For comparison, the predicted yield curves for two SXRD models are also shown.

5.3.4 Phase Transition Determination

Because the XSW is generated by dynamical Bragg diffraction from the bulk Ge crystal, it does not require long-range ordering of Sn atoms to sense their distribution. With measurements at both room temperature and low temperature, the time-averaged distributions for Sn can be compared. The model with displacement of Sn atoms would predict that the XSW results would differ between the RT and LT. If the XSW measurement found an unchanged vertical distribution, it would support an order-disorder transition.

The measured XSW-values for coherent position and fraction were found to be the same for the normal (111) reflection at both RT and 115 K, as expected in an order-disorder phase transition. This is also consistent with the thermal energy being comparable or lower than the barrier height for the transition as shown in Figure 2.11B [57].

5.3.5 Substitution of Sn in Ge bilayer

In the bulk phase diagram for Sn and Ge, shown in Figure 2.3, there are no intermediate phases, and the maximum solubility of Sn in Ge is nearly one atomic percent at 350 °C. Also, in a study on a Ge-0.5at% Sn alloy, Sn was found to segregate to the surface [58]. This relatively low solubility and surface segregation indicates that Sn would have a tendency not to intermix into the bulk Ge structure. In part, it is this mutual low solubility that makes the Sn on Ge attractive for two-dimensional studies. However, when a 1/3 ML Sn/Ge(111) sample was annealed to

higher temperature, some of the Sn appears to have moved below the adlayer and into the Ge bilayer structure. While there are STM reports for Ge atoms appearing as substitutional point defects in the Sn adlayer, there are no direct measurements that conclusively demonstrate that Sn goes to the subsurface.

In the set of XSW measurements on sample Sn2, with a higher anneal temperature (548 K), different values for the Fourier coefficients were found. While the (111) and (11$\bar{1}$) coherent positions for samples Sn1 and Sn2 are similar, the higher temperature anneal sample has reduced coherent fraction values. Additionally, the (333) coherent position for sample Sn2 is substantially lower.

The direct space image shown in Figure 5.11 was created using the XSW measured values for three reflections from sample Sn2 at RT. In this image, the highest density of Sn is shown in red. One deficiency of this image, is that only the (111), (333), and (11$\bar{1}$) reflections were measured; the allotted beam time ended before the (33$\bar{3}$) reflection could be measured. Consequently, the lateral distribution (parallel to the surface plane) has only a single Fourier component. For comparison, Figure 5.12 shows a comparable image for sample Sn1 (with a lower anneal temperature) using the same Fourier coefficients to construct the map.

The Sn distribution for this higher anneal temperature differs from that in Figure 5.7; the Sn appears to be at another location separated by 1 Å (in the vertical direction) from the T_4-site Sn atoms. Based on STM and other considerations, the height of this second location is unlikely to really be higher than the modeled Sn atom height for sample Sn1. Rather, this new position corresponds to a location below the surface. To help visualize the location of this additional site,
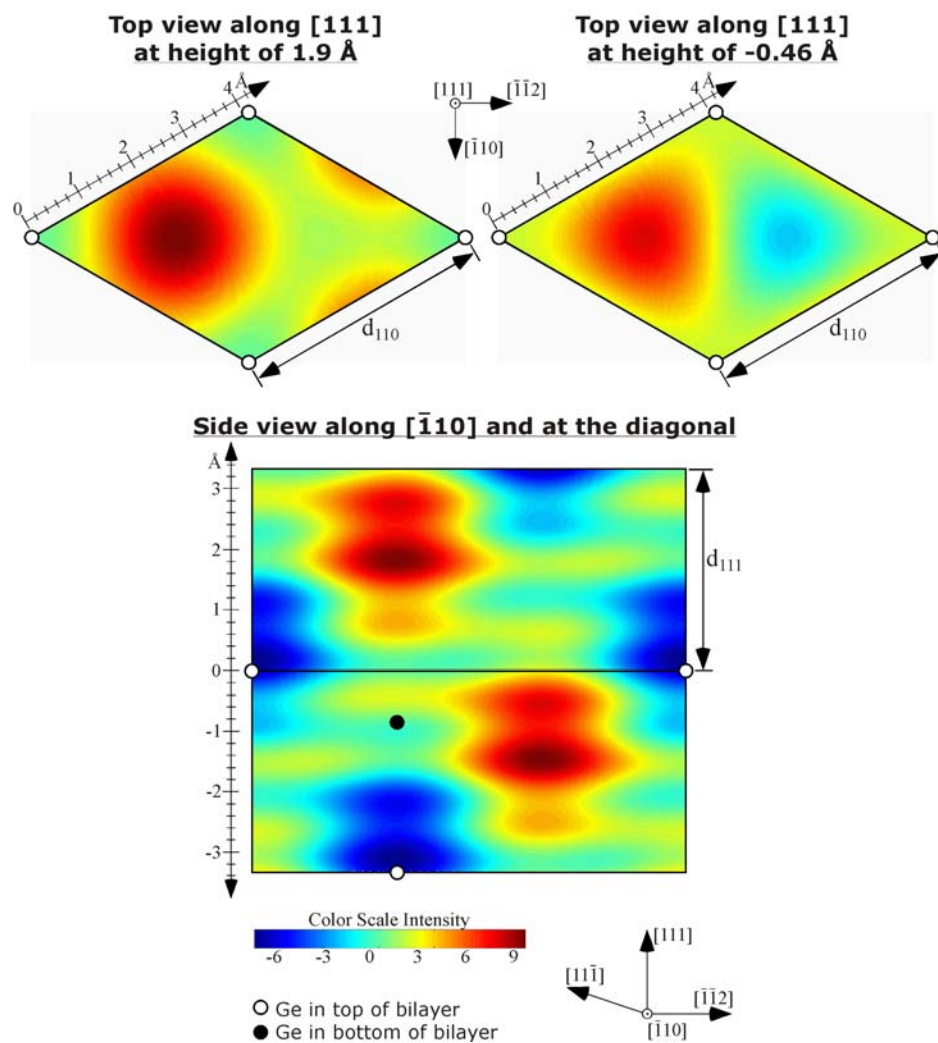
Figure 5.11: XSW direct space atomic density maps for sample Sn2 with a higher annealing temperature (548 K). The lateral distribution has only a single Fourier component. The Sn appears in two location separated by ~1 Å in the vertical direction. The positions of the bulk-like Ge atoms are depicted with black circles. The higher density spot represents Sn in the T_4-site, and second position for Sn corresponds to some of the Sn substituting into the bottom of the Ge bilayer.
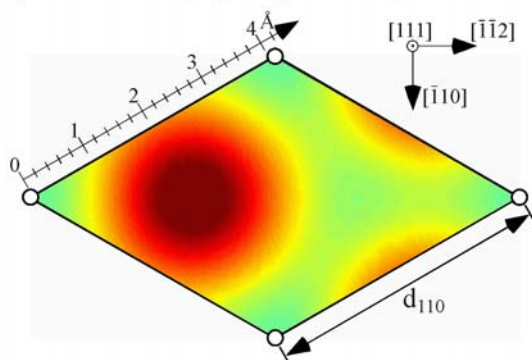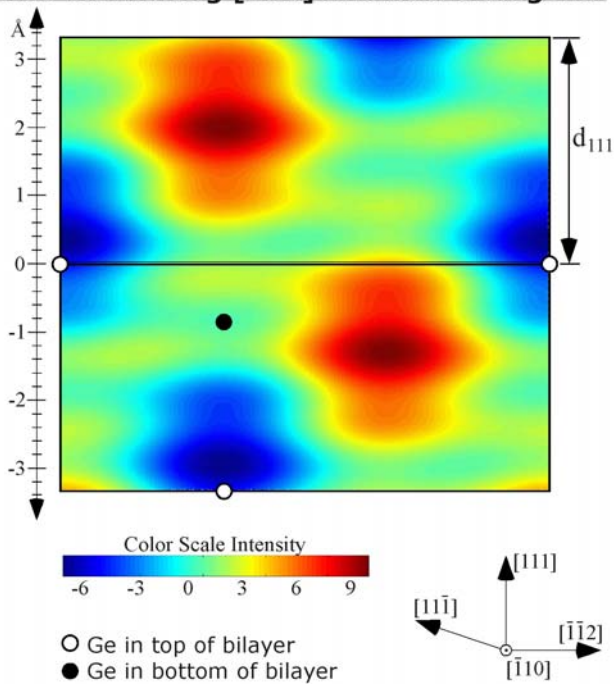
Figure 5.12: XSW direct space atomic density maps for sample Sn1 with a lower annealing temperature (473 K) using only 3 reflections. The lateral distribution has only a single Fourier component. The positions of the bulk-like Ge atoms are depicted with black circles. The high density spot represents Sn in the T_4-site.

two unit cells in the vertical direction are shown in Figure 5.11; the positions of the bulk-like Ge atoms are depicted with black circles.

If the Sn atoms go below the surface, two candidate positions are substituting into the top or bottom of the Ge bilayer. In the XSW image in Figure 5.11, the location of Sn in the lateral direction is dominated by the Sn position with the higher occupation ratio, in this case the T_4-site. In the lower unit cell of the side view, the density of Sn appears to be slightly increased near the Ge site in the bottom of the bilayer. The Sn density is actually negative at the top of the bilayer position.

Because the covalent bond length for Sn-Ge is 7% larger than Ge-Ge (2.45 Å) [59], if Sn substitutes for Ge in the bilayer structure, the expected height for Sn would roughly be 0.2 Å higher than the ideal bulk-like position for Ge. A complex-plane diagram for the RT (111) Fourier coefficient is shown in Figure 5.13. The positions for Sn adatoms determined from model for sample Sn1 are shown with red arrows. In this figure, the estimated positions for Sn substituting into the top and bottom of the bilayer are shown with purple lines starting at the origin. The diagram shows that including 20% of the ordered Sn atoms into the bottom of the bilayer (the short purple line added to the red vector summation) brings the model closer to the XSW measured values.

This additional site for Sn can be included into the model listed in equation 5.1 by including a term with a substituted fraction S_F and substitution height h_S, as shown in equation 5.3.
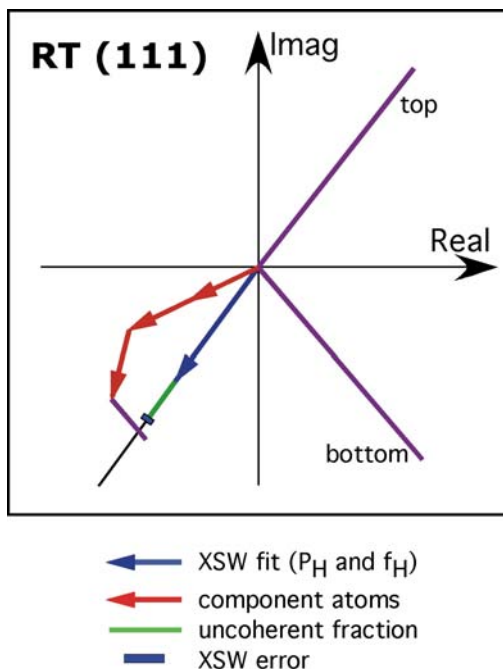
Figure 5.13: Complex-plane representation of the XSW measured Fourier coefficients and the model for sample Sn2. The positions of the three Sn atoms per (3 x 3) unit cell are each represented by a red arrow. The lengths of the red arrows are reduced by the Debye-Waller factors for the Sn atoms. The measured Fourier coefficients (with f_H = 1) is drawn with a thin black line from the origin. The XSW Fourier coefficient for P_H and f_H is represented with a blue line. The ordered fraction C from the model is depicted with a green that extends from end of the blue line to scale the model to the XSW measurement. The uncertainty in the XSW measurements is represented by the dimensions of the blue rectangle. The estimated positions for Sn substituting into the top and bottom of the Ge bilayer are shown with purple lines. 20% of the ordered Sn is located in the bottom of the bilayer improves the fit of the model to the XSW measurements.

$$\mathcal{F}_H = C \exp\left(-2\pi^2 m^2 \frac{\langle u^2 \rangle}{d_{111}^2}\right) \left(\begin{array}{c} [1 - S_F]\left[\frac{1}{3}\exp\left(2\pi i m \frac{h_A}{d_{111}}\right) + \frac{2}{3}\exp\left(2\pi i m \frac{h_B}{d_{111}}\right)\right] \\ + S_F \exp\left(2\pi i m \frac{h_S}{d_{111}}\right) \end{array} \right).$$

(5.3)

To fit the data using equation 5.3, the parameters h_A, h_B, and $\langle u^2 \rangle$ are fixed to their values determined for sample Sn1. Modeling of the data for sample Sn2 yields an ordered fraction C of 0.74 and a third Sn height h_S equal to -0.45 Å (below the ideal surface). This additional position corresponds to Sn substituting for Ge in the bottom of the surface bilayer. This particular 30 minute, 548 K thermally activated interfacial diffusion led to 20% of the Sn migrating to this site (compared to less than 5% in the 473 K anneal experiment described in section 5.3.2). For comparison, the Sn in this third site is 0.37 Å higher than the bulk-like position for Ge in the bottom of the bilayer ($h_{Ge\text{-}bottom} = -d_{111}/4 = -0.82$ Å).

While these XSW measurements are insensitive to the Ge atoms at the surface, the mechanism for Sn atoms substituting into the bottom of the Ge bilayer may involve interchanging a Sn atom with a Ge atom. Observation with STM, always observes some (not less than 2%) Ge substitutional defects at the surface. In this case, the STM only sees the atoms on the top and is complementary to XSW technique which sees Sn below the surface.

Looking at the model from SXRD in Figure 2.10B, the Ge atoms in the top bilayer (labeled 1, 1′, 1″, and 2) are distorted outwards to the surface and deviate from their bulk-like position by 0.17 – 0.26 Å [20]. Because Sn has a larger size, it may relieve some of the stress by substituting for Ge in this surface bilayer. In particular, the atoms labeled 1″ and 2 are the most distorted from their ideal bulk-like positions. In comparison to the Ge atom labeled 2 (h_{Ge2}=-0.47 Å) in the SXRD model, the Sn has nearly the same height (h_S=−0.45 Å).

5.3.6 Sn XSW measurements using Auger electrons

XSW measurements can also be made using the Auger electrons from the sample for the yield signal. In the electron energy spectrum shown in Figure 4.10, there are two peaks from Sn MNN Auger electrons at 350 eV and 421 eV and there are also several peaks from the Ge LMM Auger electrons in the range of 930 to 1160 eV. The Sn peak at 421 eV provides the strongest signal to measure in these conditions. However, the Sn peaks sit atop a high background from a combination of the electron energy loss tail from the Ge Auger electrons (from the right) and the secondary electrons (from the left). This background was subtracted to give the Sn counts. The Ge peak at 1136 eV is a good signal to measure due to its high intensity and the flat region (at higher energy) to determine the background.

From the universal curve for the electron mean free path versus energy, the Sn MNN Auger electrons (421 eV) and the Ge LMM Auger electrons (1136 eV) can be estimated to have an escape depth of 10 Å and 30 Å, respectively. These lengths

correspond to four and ten, respectively, Ge bilayers from the surface. Therefore, the Ge signal would be expected to be dominated by the bulk structure.

To obtain a Ge signal that is more representative of the atoms at the surface, the Ge photoelectrons could be measured. An appropriate incident x-ray beam energy would be 11.203 keV because the binding energy for K $1s$ Ge photoelectrons is 11.103 keV. This value for $E\gamma$ would create 100 eV photoelectrons that have a mean free path of 5 Å.

XSW measurements on the Sn3 sample were made for the normal (111) reflection at RT, and the Ge LMM and Sn MNN Auger electron yields are shown in Figure 5.14. Here the Ge agrees well with the substrate's bulk structure. While the coherent position for Sn Auger electron signal agrees well with Sn x-ray fluorescence value, the coherent fraction values differ, as shown in Figure 5.15. This difference in measured coherent fraction is partly caused by poor extraction of the Sn Auger signal because the Sn peak is at its lowest intensity when the Ge signal is at its highest intensity, as shown in Figure 5.14. As mentioned in section 4.3, the Sn Auger peak is positioned between the electron energy loss tail from Ge LMM Auger electrons and secondary electrons. This location results in a non-uniform background near the Sn MNN Auger peaks.

Another reason for the discrepancy between the two Sn signals can also be attributed to multiple excitation paths for the Sn Auger electron. While the Sn MNN Auger electrons can be stimulated by the photoelectric effect, they can also be excited by the higher energy Ge photoelectrons and Ge LMM Auger electrons. These different routes to creating Sn MNN Auger electrons distorts the yield and can lead to incorrectly measuring the values of the Fourier coefficients.
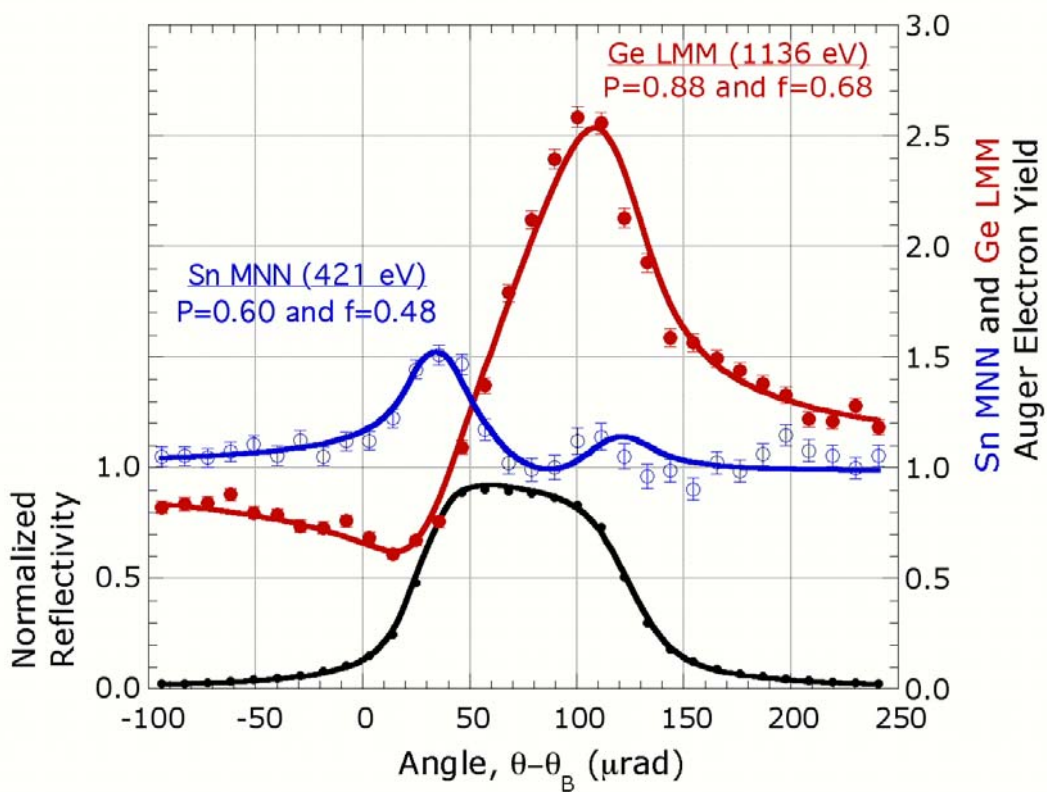
Figure 5.14: RT (111) XSW results showing the angular dependence of the experimental and theoretical curves for reflectivity and Auger electron yields for Sn MNN (at 421 eV) and Ge LMM (at 1136 eV). The electrons for these Sn and Ge Auger emissions have an estimated mean free path of 10 Å and 30 Å, respectively.
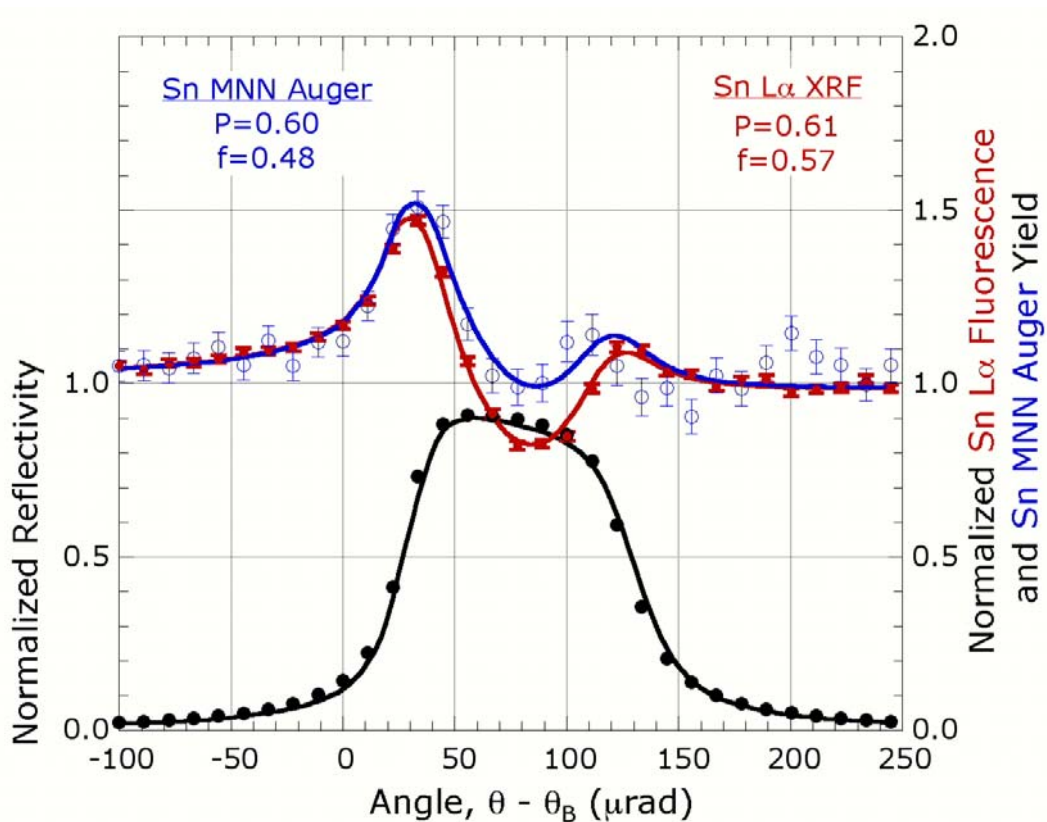
Figure 5.15: RT (111) XSW results showing the angular dependence of the experimental and theoretical curves for reflectivity and Sn yield using Sn MNN Auger electron and Sn Lα x-ray fluorescence for sample Sn3. The different measured coherent fraction may be attributed to multiple excitation routes for the Sn MNN Auger electrons and to improper background subtraction for the Sn peak.

5.4   Summary of Results

Samples for the 1/3 ML Sn/Ge(111) system were characterized using LEED and found to display the RT $\sqrt{3}$ and LT (3 x 3) surface reconstructions. Using the XSW-measured Fourier coefficients for the Sn distribution, direct space images of the Sn 3D distribution maps were made for two of the samples. The direct space image for the sample Sn1 (annealed at 473 K) shows the Sn atoms to occupy the T_4-adsorption site. This determination is made *a priori* and without creating a model for the structure. The image for the sample Sn2 shows that the Sn distribution changes with a higher annealing temperature.

By combining this XSW direct space image of Sn1 with the STM observation of the (3 x 3) phase that the Sn adatoms have an occupation ratio of 2:1, a straight-forward model was used to determine positions for Sn. Using the P_H and f_H values from the (111) and (333) XSW measured Fourier coefficients on sample Sn1, the Sn adatoms were determined to be in a 1 up and 2 down configuration for the RT $\sqrt{3}$ phase and for the LT (3 x 3) phase. The two heights are 1.87 Å and 2.32 Å above the ideal surface (where the origin was chosen to coincide with the Ge atom at the top of the bulk-like Ge bilayer). At higher annealing temperature (548 K), some (20% for sample Sn2) of the Sn atoms move below the adlayer and substitute for Ge atoms in the bottom of the bilayer at a position –0.45 Å below the origin.

While LEED patterns show the reconstruction to change from $\sqrt{3}$ to (3 x 3) when the sample is cooled, XSW measurements on samples at RT and LT show that

the Sn distribution (projected into the Ge primitive unit cell) does not change. The √3 to (3 x 3) phase transition therefore appears to be of the order-disorder type. Furthermore, the STM images see all of the Sn at the same height for the RT √3 surface due to rapid fluctuations between the "up" and "down" position. The XSW measures the time-averaged spatial distribution.

Chapter 6: 1/3 ML Pb/Ge(111)

6.1 Experimental Preparations and Measurements

6.1.1 Sample Preparation

The samples for 1/3 ML Pb/Ge(111) were prepared in a similar method as described for the Sn/Ge(111) experiments in section 5.1.1, with the following differences. The sputter cleaning for the Ge(111) surface began with the use of 2.0 keV Ar$^+$ (with a 10° glancing angle) for the first 1.5 hours, and then the followed by 5 to 6 hours of sputtering with 0.5 to 1.0 keV Ar$^+$. The current to the sample was approximately 0.1 µA (because the lenses in the ion gun were not optimized). (The Pb/Ge(111) experiments were performed prior to the Sn/Ge(111) experiments.)

The LEED images for the c(2 x 8), √3, and (3 x 3) reconstructions were comparable to those observed for the 1/3 ML Sn/Ge(111) sample preparations, shown in Figure 5.1. One difference regarding the (3 x 3) LEED pattern was that it began to appear at higher temperature (near ~250 K) than what was observed for the Sn surface. This is consistent with the higher T_C value reported for the 1/3 ML Pb/Ge(111) surface [14].

The Pb K-cell source was heated to 763 K before exposing the sample to the vapor source. After Pb deposition, the sample was annealed to 450 K for 10 minutes. This post-deposition anneal temperature was chosen, in part, because it falls in the middle of the range that has been reported in the literature (373K - 523 K [14]). The amount of Pb on the surface was determined *in-situ* by comparing the Pb Lβ x-ray fluorescence to a calibrated standard of Pb implanted (8.2×10^{14} Pb atoms/cm^2, with an estimated 300 Å straggling depth) into the surface of a Si crystal. This standard had been measured with RBS prior to its use in the UHV chamber.

6.1.2 X-ray Standing Wave Measurements

The XSW measurements were made using a 16.35 keV x-ray beam. The third harmonic of the undulator was used. The platinum stripe on the mirrors in 5ID-A were used to reject the higher order harmonics.

As discussed in section 4.3, when E_γ = 16.35 keV, the Ge substrate creates a large amount of Kα,β x-ray fluorescence. In order to collect the Pb Lβ x-ray fluorescence, Al filters were placed in front of the SSD to preferentially attenuate the Ge x-ray fluorescence. With the higher intensity for the (111) and (220) reflections, a 1.2 mm thick filter was used. The other (11$\bar{1}$) and (333) reflections were weaker, therefore, a 0.6 mm thick Al filter was used. The choice of filters was determined by the overall count rate entering the detector, where 50 kcps was the upper range used with the XIA digital amplifiers.

6.2 Results and Discussion for 1/3 ML Pb/Ge(111)

The results on four different samples that were prepared and measured with XSW are shown in Table 6.1. The phase of the XSW-measured Fourier coefficient for the (111) reflection was consistently near 0.77. The value for the RT (333) ranged from 0.47 to 0.60 when measured on three separate samples.

Table 6.1: Summary of the theoretical fit to the XSW data for Pb/Ge(111). The origin is centered on the top Ge atom in the bulk-like bilayer structure. Measurements were made at RT with the sample displaying the √3 reconstruction and LT with the sample having the (3 x 3) reconstruction. $E\gamma$=16.35 keV.

sample	Θ (ML)	hkl	RT √3		LT (3 x 3)	
			P_H	f_H	P_H	f_H
Pb1	0.31(3)	(111)	0.80(1)	0.69(2)	-	-
		(11$\bar{1}$)	0.41(2)	0.46(2)	-	-
Pb2	0.27(3)	(111)	0.77(1)	0.67(2)	-	-
		(333)	0.60(2)	0.36(2)	-	-
Pb3	0.42(4)	(111)	0.75(1)	0.70(1)	0.76(1)	0.71(1)
		(333)	0.59(2)	0.45(2)	0.54(2)	0.60(4)
		(11$\bar{1}$)	0.38(2)	0.20(2)	-	-
		(220)	0.14(1)	0.51(2)	0.14(1)	0.50(2)
Pb4	~1/3	(111)	0.77(1)	0.52(1)	0.77(1)	0.50(1)
		(333)	0.47(2)	0.34(2)	-	-
		(11$\bar{1}$)	0.37(2)	0.43(2)	0.37(2)	0.47(2)
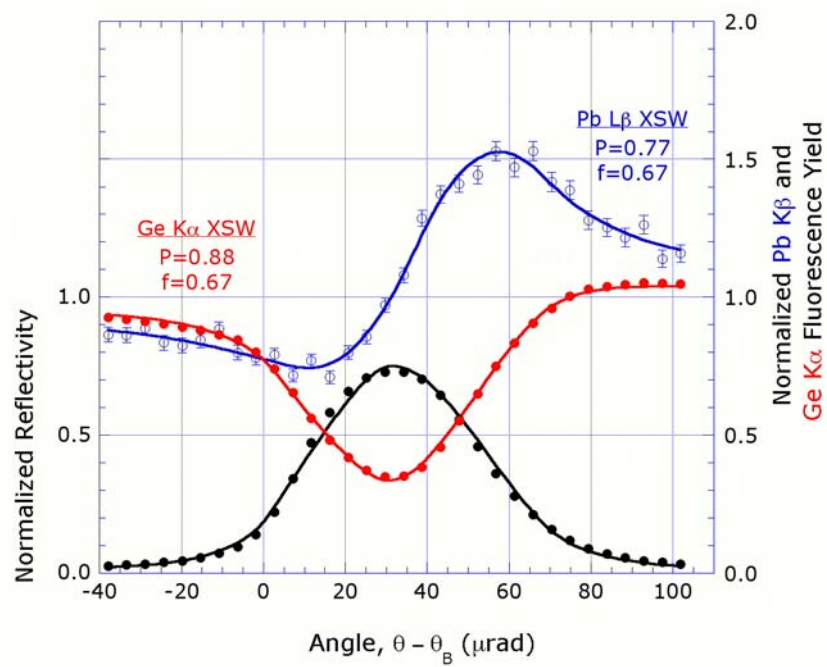
Figure 6.1: RT (111) XSW results showing the angular dependence of the experimental and theoretical curves for reflectivity and fluorescent yields for Pb Kβ and Ge Kα for sample Pb2.
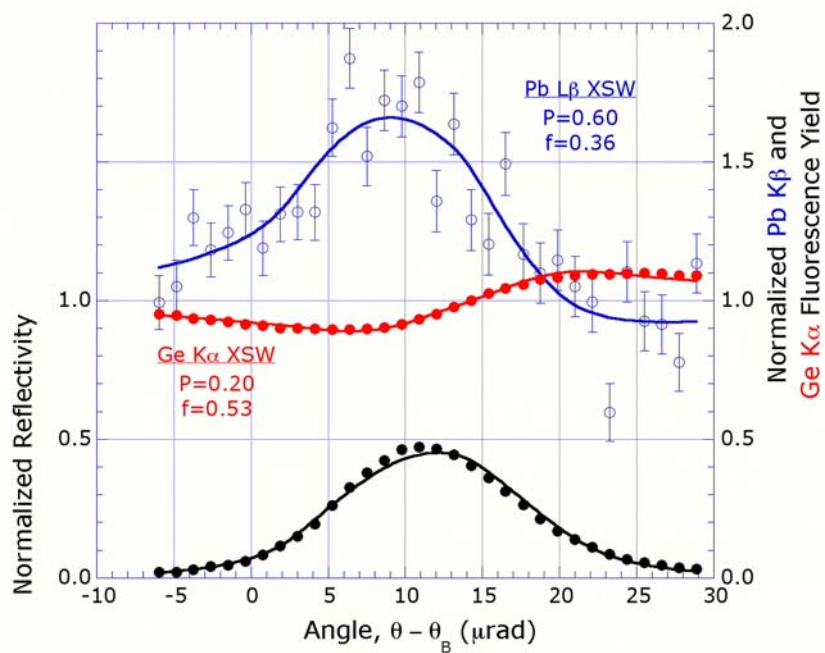
Figure 6.2:   RT (333) XSW results showing the angular dependence of the experimental and theoretical curves for reflectivity and fluorescent yields for Pb Kβ and Ge Kα for sample Pb2.
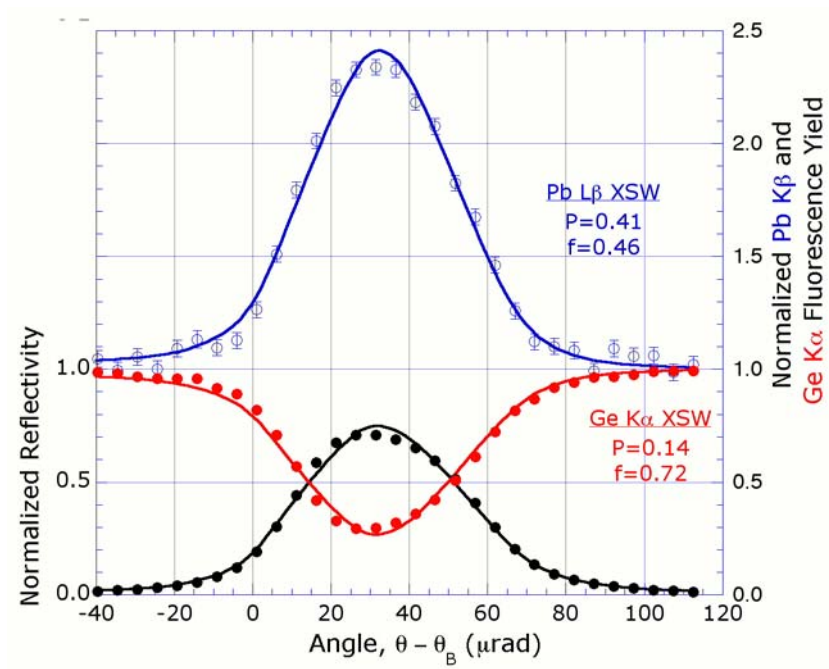
Figure 6.3: RT $(11\bar{1})$ XSW results showing the angular dependence of the experimental and theoretical curves for reflectivity and fluorescent yields for Pb Kβ and Ge Kα for sample Pb1.
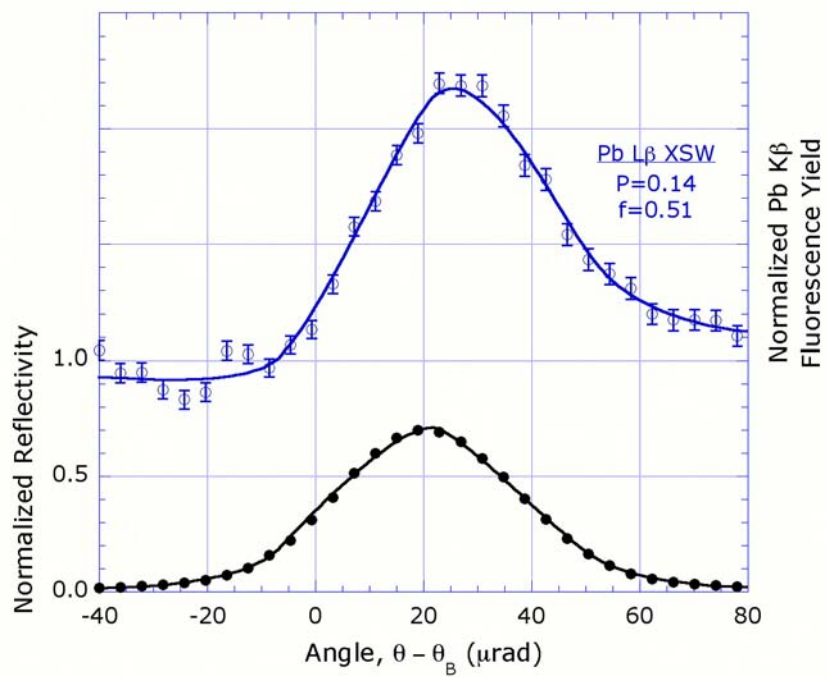
Figure 6.4: RT (220) XSW results showing the angular dependence of the experimental and theoretical curves for reflectivity and fluorescent yields for Pb Kβ for sample Pb3.

6.2.1 Structures for $(\sqrt{3} \times \sqrt{3})R30°$ to (3×3) Phases

As in the case for 1/3ML Sn/Ge(111), the LEED pattern changed from $\sqrt{3}$ to (3 x 3) when the sample was cooled from RT to LT. However, the XSW-measured Fourier distributions for the samples at RT and LT are essentially the same. This finding that the time-averaged distribution for Pb does not change even though the long-range order of the surface does change, supports that this is an order-disorder phase transition for the 1/3 ML Pb/Ge(111).

For adatoms at the T_4-site, the expected relationship between the normal and off-normal distribution, $P_{11\bar{1}} = (P_{111}+1)/3$, does not match this XSW data. Our XSW results for P_{111} and P_{220} are similar to the XSW results for 1/3 ML Pb/Si(111) by Dev *et al.* who measured the normal (111) coherent position to be $P_{111}=0.81$ for Pb deposited on Si(111) at RT (without annealing) and $P_{111}=0.70$ when the Si sample was held at 250 °C during deposition. Combining the distribution normal to the surface with an off-normal (220) measurement, they triangulated the position to be between the T_1- and T_4-sites, which indicated to them a mixture of Pb at T_1- and T_4-sites on Si(111). This finding that Pb is on the T_1-site is not supported by STM and SXRD measurements (which support Pb at the T_4-sites).

From our 1/3 ML Pb/Ge(111) measurements, the vertical position, based on the (111) and (333) coherent positions, indicates that the distributions are asymmetric. However, the asymmetry is in the opposite sense than what was measured for the "one up and two down" structure determined for sample Sn1. Compared to the SXRD results from Avila *et al.*, the XSW-measure coherent

position for the (111) is centered 2.5 Å above the top atom in the bulk-like bilayer structure. This height is 0.5 Å higher than the valued reported for the T_4-site model (average height of 2.0 Å) from SXRD. With all of these inconsistencies, an XSW direct space image can add insight into the distribution for Pb.

6.2.2 XSW image of 1/3ML Pb/Ge(111)

The XSW direct space image in Figure 6.5 was generated using the four Fourier coefficients for the RT Pb3 sample listed in Table 6.1. This image shows that there is clearly another distinct Pb site besides the T_4-site. In fact, a large fraction of the Pb appears in this other site. By comparing this XSW image to the one for Sn/Ge(111) in Figure 5.11, one could speculate that the Pb is in the T1-site or that Pb is substituting for Ge in the bottom of the bilayer. Based on the STM results that Pb is in T_4-sites, one could conclude that the Pb is going below the surface. The partitioning of Pb between these two configurations may be different for each sample due to the slight differences in the sample preparations.

The relative magnitude of the amount of Pb at these two configurations can be estimated by comparing the lateral density profiles through their centers that is shown in Figure 6.6. These profiles are along the [0$\overline{1}$1] direction and cut through the center of the two Pb positions shown on the (111) planes in Figure 6.5. From the ratios of the atomic densities in Figure 6.6, it appears that ~45% of the Pb resides in the T_4-site.
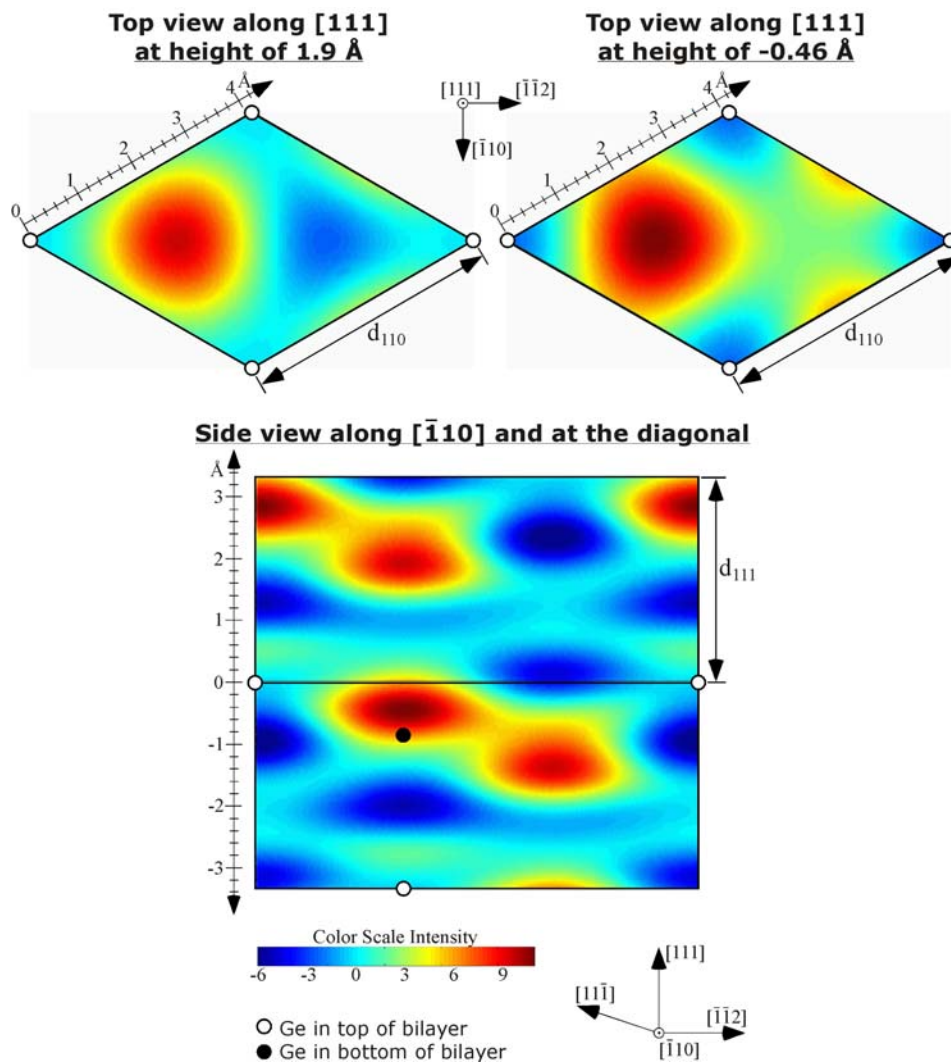
Figure 6.5: XSW direct space atomic density maps for Pb from sample Pb3, where it appears in two locations separated by ~1 Å in the vertical direction. The positions of the bulk-like Ge atoms are depicted with black circles. The top views are slices at 1.9 Å above and −0.46 Å below the ideal surface. The lower density spot represents Pb in the T_4-site, and higher density for Pb corresponds to some of the Pb substituting into the bottom of the Ge bilayer.
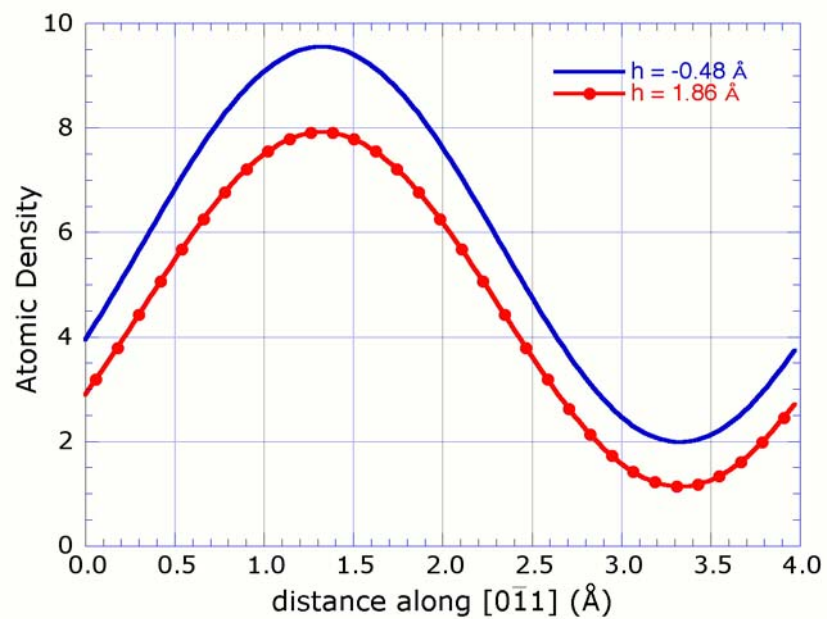
Figure 6.6: The atomic density profiles along the $[0\bar{1}1]$ direction through the center of the two high atomic density (111) planes shown in Figure 6.5. From the magnitude of the atomic density, slightly less than half of the Pb atoms in sample Pb3 are in the T_4-site.

This is a somewhat surprising result, given the fact that the (3 x 3) reconstruction was clearly observed for these samples. Some STM studies have concluded that the presence of a small amount (2 - 5%) of Ge substitutional point defects in the ad-layer can nucleate local patches of (3 x 3) phases. If half of the Pb atoms are not in T_4-sites, this would constitute an important feature to the structure and phase transition.

Using the RT (111) and (333) Fourier coefficients for samples Pb2, Pb3, and Pb4 and equation 6.1, a model was developed to determine the heights of the Pb positions.

$$\mathcal{F}_H = f_H \exp(2\pi i P_H)$$

$$= C \left[(1 - S_F) \left[\frac{1}{3} \exp\left(2\pi i m \frac{h_A}{d_{111}} \right) + \frac{2}{3} \exp\left(2\pi i m \frac{h_B}{d_{111}} \right) \right] \exp\left(-2\pi^2 m^2 \frac{\langle u^2 \rangle}{d_{111}^2} \right) + S_F \exp\left(2\pi i m \frac{h_{BB}}{d_{111}} \right) \right]$$

(6.1)

Here the variables are the ordered fraction C for each sample, the substituted fraction S_F for each sample, the height of the substituted Pb in the bottom of the bilayer h_{BB}, and the height of the Pb atoms at T_4–sites h_A and h_B. To simplify the structural analysis, certain parameters will initially be fixed and later checked for consistency. The rms vibrational amplitude $\langle u^2 \rangle^{1/2}$ was fixed at 0.08 Å, the split of

the T_4-Pb heights was fixed at 0.4 Å, and their occupation ratio (1 up and 2 down). These initial guesses are based on the structure determined from the modeling for sample Sn1 and from the SXRD model for 1/3 ML Pb/Ge(111) [28].

The results for this modeling are listed in Table 6.2. The heights of the T_4-site Pb atoms are 1.90(6) and 2.30(6) Å above the top of the bulk-like Ge bilayer. The Pb substituted in the bottom of the bilayer is −0.52(6) Å below the bulk-like surface. The model values for the Fourier coefficients match well to the XSW-measured values, with the exception of the P_{333} for sample Pb4.

Table 6.2: Summary of the model results from fitting the (111) and (333) Fourier coefficients for samples Pb2, Pb3, and Pb4 using Equation 6.1. The height for the Pb atoms were determined to be: h_A=2.30 Å, h_B=1.90 Å, h_{BB}=-0.52 Å. These model calculated P and f values closely match the measured values shown in Table 6.1, except for The Pb4 P_{333} value which differs by 0.1.

sample	C	S_F	P_{111}	f_{111}	P_{333}	f_{333}
Pb2	0.85(5)	0.63(5)	0.77	0.65	0.57	0.45
Pb3	0.94(4)	0.55(6)	0.75	0.70	0.59	0.44
Pb4	0.66(7)	0.65(5)	0.77	0.51	0.57	0.36

Using a complex-plane representation, the XSW-measured Fourier coefficients for sample Pb3 are compared to the model in Figure 6.7. The convention for representing the atoms is the same as in the previous chapter. The red lines
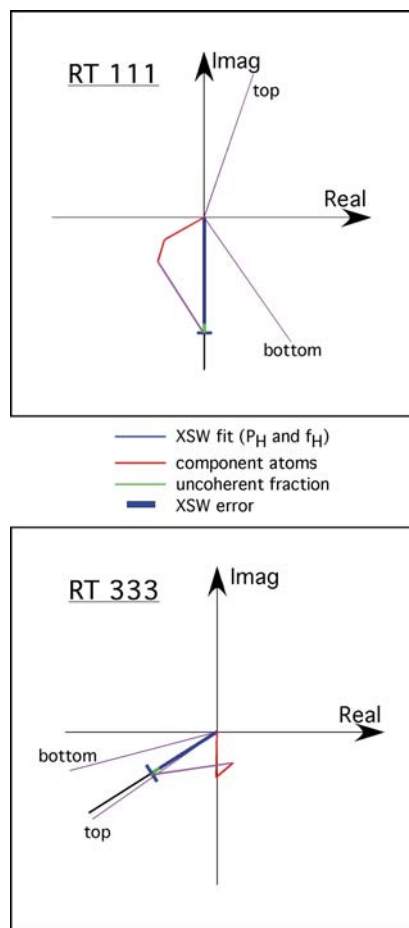
Figure 6.7: Complex-plane representation of the XSW measurements for sample Pb2 and a model for 1/3 ML Pb/Ge(111). The XSW-measured Fourier coefficient is shown with a blue line. The measured Fourier coefficient (with f_H = 1) is drawn with a thin black line. The random fraction *(1-C)* from the model is depicted with a green line segment that extends from the end of the blue line to scale the model to the XSW measurement. The box represents the uncertainty in the measurement. 1/3 of the ordered Pb are in T4-site (shown in red), and 2/3 of the ordered Pb are in the bottom of the bilayer (shown in purple).

represent the Pb atoms at the T4-site, the purple lines from the origin are the estimated position for a larger size Pb atom substituting into the Ge bilayer structure. The XSW-measured Fourier coefficients are shown with a blue line (box represent error), and the green line scales the model to the data.

From this model, heights for the Pb at the T_4-sites is 0.10 Å higher than the SXRD results. The height for the Pb substituted into the bottom of the bilayer, matches the estimated value based on the sum of covalent radii. The Ge-Ge bond length is 2.45 Å , and the length of the Pb-Ge bond is 2.77 Å. Therefore, the Pb can be estimated to be 0.32 Å higher than bulk-like position for Ge ($d_{111}/4$ + 0.3 Å = -0.54 Å).

As a check on the self-consistency of this model, the ($11\bar{1}$) Fourier coefficients for samples Pb3 and Pb4 can be compared between the model and the XSW data. The values from the model are $P_{11\bar{1}}$ =0.40 and $f_{11\bar{1}}$ =0.63 for sample Pb3 and $P_{11\bar{1}}$ =0.36 and $f_{11\bar{1}}$ =0.46 for sample Pb4. These values from the model match the XSW data reasonable well, except the measured coherent fraction value for sample Pb3 is lower.

The position for the Pb atom in the bottom of the bilayer is 0.1 Å further below the surface than the position determined for Sn in section 5.3.5. Because the Pb-Ge bond length is approximately 12% larger than for Ge-Ge (and 5% larger than Sn-Ge), the expected position for Pb substituted in to the bottom of the bilayer would be 0.14 Å higher than Sn (and 0.32 Å higher than Ge). The larger covalent radius of Pb atoms and the observed larger substitutional fraction of Pb into the bottom of the bilayer may indicate that the larger atom is accommodating some strain in the surface region.

6.3 Summary of Results

Samples for the 1/3 ML Pb/Ge(111) system were characterized using LEED and found to display the RT $\sqrt{3}$ and LT (3 x 3) surface reconstructions. Using four XSW-measured Fourier coefficients for sample Pb3, a direct space image of the Pb 3-D distribution map was made. The direct space image for the Pb shows the Pb atoms occupy both the T_4-adsorption site and the bottom position in the bilayer. The image shows a majority of the Pb atoms to be in the bottom of the bilayer.

By using this XSW direct space image of Pb, the occupation ratio was estimated to be 1:1.2 for Pb atoms in the T_4-site and in the bottom of the bilayer. A model was used to determine heights for three Pb positions. Using the P_H and f_H values from the (111) and (333) XSW measured Fourier coefficients on samples Pb2, Pb3, and Pb4, the heights for the two T_4-site Pb are 1.90 and 2.30 Å above the origin and the Pb substituted into the bottom of the bilayer is −0.5 Å below the ideal surface (where the origin was chosen to coincide with the Ge atom at the top of the bulk-like Ge bilayer). The larger size of Pb atoms and an increased fraction of Pb in the bottom of the bilayer may indicate that strain plays a role in Pb occupying the bottom of the bilayer position.

While LEED patterns show the reconstruction to change from $\sqrt{3}$ to (3 x 3) when the sample is cooled, XSW measurements on samples at RT and LT show that the Pb distribution as projected into the Ge primitive unit cell to be unchanged. The $\sqrt{3}$ to (3 x 3) phase transition for 1/3 ML Pb/Ge(111) is also consistent with an order-disorder type.

Chapter 7: Low Index Surfaces for the Al-1.7 at% Cu Dilute Alloy

7.1 Introduction

As feature sizes in integrated circuits decrease, the surface of the material plays an increasing role in the overall properties of the device. In aluminum alloy interconnects, copper is used because it helps the material resist the detrimental effects of electromigration. Understanding the behavior of the Cu atoms at the surface can lead to an increase in the performance of the alloy. Evan though Al-Cu alloys have been widely used for interconnects, there appears to be little published on the structure and composition at the surfaces.

Both experimental and computational studies of the low index faces, (001), (011), and (111), for pure aluminum concluded that these surfaces do not reconstruct but undergo multi-layer relaxation normal to the surfaces [61 - 64]. The (001) and (111) surfaces for Al do not undergo large changes in lattice spacings [63, 65], but the outermost atomic layer for the (011) surface relaxes inward by about eight percent [66]. Alloying aluminum with a dilute amount of Cu

may alter both the equilibrium structure and the composition of the surface because copper has an atomic radius eleven percent smaller than aluminum [67].

In a related material system, Baird *et al.* found an ordered $(\sqrt{3} \times \sqrt{3})R30°$ superlattice forms on the (111) surface of Cu-16at.% Al [68 - 69]. Another similar system, Al-Ag, displays surface segregation, even though the atomic size mismatch is less than one percent [67, 70 - 71]. For the dilute alloy Al-3 at.% Ag, Erbudak *et al.*, found that the (001) and (111) surfaces are enriched with Ag, as high as thirty atomic percent, and report a phase transition at 680 K for the (111) alloy surface [72].

7.2   Experiment

Single crystal samples of Al-1.7 (±0.1) at.% Cu were grown from the melt and cut to the desired low-index faces. (The composition was determined from measuring the lattice parameters of filings from the grown crystal [73].) The sample orientations were determined with x-ray diffraction and then polished to within 0.1° of the desired surface orientations. To obtain flat surfaces with low roughness, the samples were polished with an Al mask and received a final polish with a Syton solution (pH=12) of 0.06 μm colloidal silica [74]. During the ultra-high vacuum (UHV) measurements, the samples were mounted on a molybdenum platen. Before sputter cleaning, the samples were degassed at 723 K for eight hours. A tungsten filament radiatively heated the backside of the sample holder, and the temperature was determined with a pyrometer focused on the sample and a thermocouple located near the sample on the manipulator arm. Due to

limitations in the pyrometer, the temperature of the sample is estimated to within ± 30 K and could only be measured above 623 K. The visible light emitted from the hot filament prohibited LEED measurements at elevated temperatures. The base pressure of the UHV chamber was 4 x 10^{-10} torr.

To initially remove the oxide layer, multiple sputtering and anneal cycles were required. During a cleaning cycle, the chamber was back-filled with argon to 5 x 10^{-5} torr, and the samples were held at 723 K. Sputtering was done with a normal incidence geometry with 2.0 keV argon ions for 1500 s. To restore crystal order after sputtering, the samples were annealed at 723 K for 1800s. The surface was considered clean when the amount of oxygen was less than 0.01 ML (determined from AES measurements of the peak to peak amplitudes of the aluminum and oxygen KLL transition peaks). Sensitivity factors for the elements were taken from literature [75]. Aside from the copper, no other elemental impurities were observed, except for carbon (found in quantities near 0.05 ML).

The Auger data was taken in derivative mode with a normal incidence, 3.0 keV beam and collected with a single pass cylindrical mirror analyzer. The LMM transition peak was used to measure the amount of copper. For AES measurements at different temperatures, the samples were sputtered for 600 s at 723 K and then cooled (or heated) to the desired temperature at a rate of 0.25 K/s and allowed to equilibrate at the desired temperature for at least 1800 s.

LEED measurements were taken in back-scattered geometry with four-grid retarding-field optics. After the samples were cleaned and annealed, they were cooled to room temperature in 1200 s, and LEED measurements were taken. The quality and character of the (001) and (111) images did not appear to change with

cooling rate from the anneal; however, the weak diffraction spots (attributed to faceting in section 7.3.2) on the (011) appeared to be slightly more clear if the sample was slowly cooled (over 7200 s) to room temperature. The maximum cooling rate was 1.5 K/s.

7.3   Results and Discussion

7.3.1 Chemical composition of the (001), (011), and (111) surfaces

The chemical compositions were measured both above and below the bulk solid solution temperature, 773 K [76]; Table 7.1 lists the results obtained at 625 K and 763 K.   Compositions were taken as the average of three consecutive measurements.   The reported error (0.26 at.%) is three times the standard deviation for seven consecutive scans for one composition.   Below the solvus temperature, the (001) surface has the highest concentration of Cu, 5.3 at.%, whereas the (111) surface has the lowest amount of Cu, 2.8 at.%. This trend also holds above the solvus temperature.   For all three surfaces, the Cu composition decreases by a factor of two when the temperature is increased above the solvus. The amount of Cu on the (011) and (111) surfaces changes rapidly by raising the temperature above 710 K. The Cu remained segregated up to 673 K. At 710 K a measurable change in the amount of Cu would occur in less than 300 s. (From the mean free path of the Cu Auger electrons [75], the depth of this signal could be at most in the top 16 Å, although any gradient could be deeper.)

Because Al has a lower heat of sublimation than Cu [77], one might expect Al to preferentially segregate to the surface; however, this experimental data shows Cu segregates to the surface. This suggests that Al-Cu does not behave as an ideal solution. The regular solution parameter Ω can be estimated from the heat of mixing [18], and is calculated to be -18.3 (± 2.3) kJ/mol [19].

$$\Omega = \frac{\Delta H_m}{x_{Cu}^{bulk} x_{Al}^{bulk}} \tag{7.1}$$

Using the regular-solution monolayer approximation shown in Eq. 7.2 [78], the surface concentrations of Cu for the three surfaces are calculated and listed in Table 7.1.

$$\frac{x_{Al}^{surface}}{x_{Cu}^{surface}} = \frac{x_{Al}^{bulk}}{x_{Cu}^{bulk}} \exp\left[\frac{0.16\left(\Delta H_{Cu}^{subl} - \Delta H_{Al}^{subl}\right)}{RT} \right] \exp\left[\frac{\Omega(l+m)}{RT}\left(\left(x_{Al}^{bulk}\right)^2 - \left(x_{Cu}^{bulk}\right)^2 \right) + \frac{\Omega(l)}{RT}\left(\left(x_{Al}^{surface}\right)^2 - \left(x_{Cu}^{surface}\right)^2 \right) \right]$$

$x_{Al}^{surface} \rightarrow$ fraction of Al (Cu) for the surface (bulk)

$\Delta H_{Al}^{subl} \rightarrow$ Heat of sublimation for Al (Cu) $\tag{7.2}$

$\Omega \qquad \rightarrow$ Interaction parameter

$l \qquad \rightarrow$ fraction of nearest neighbors in plane containing atom

$m \qquad \rightarrow$ fraction of nearest neighbors below plane containing atom

$T \qquad \rightarrow$ temperature

$R \qquad \rightarrow$ Gas constant

This simple model adequately calculates the compositions measured at 625 K for the (001) and the (011) surfaces, but it overestimates the concentration for the (111) surface. While this approach does not agree with the concentration of Cu on

the surface at 763 K, it does give the right sense to the temperature effect. However, it predicts more copper at the (111) surface than the (001) surface, which is opposite of the experimental results.

Table 7.1: The measured and calculated amount (atomic percent) of Cu at the surface of an Al-1.7at% Cu alloy sample with different surface normal orientations. The measurement error is estimated to be 0.26 at%. The range for the calculated values is based upon the error in the interaction parameter and composition

surface orientation	measured Cu composition (at%)		calculated Cu composition (at%)	
	625 K	783 K	625 K	783 K
(001)	5.3	2.2	4.6 – 9.1	3.9 – 7.1
(011)	3.9	1.7	2.4 – 4.3	2.2 – 3.7
(111)	2.8	1.2	8.2 - 15.5	6.5 – 11.9

Abraham *et al.* predict surface segregation with a bond and strain energy approach which uses the ratio of the atomic size and bond strengths between Al and Cu [80]. The result from this method predicts segregation and suggests that the increased amount of Cu at the surface is due to the size difference between Al and Cu. [For the Al-Ag system, Ag has a lower heat of sublimation than Al [77], and there is little size difference between the two types of atoms. So the driving force for

segregation is dominated by the strengths of bonds or an interaction between Al and Ag atoms.]

7.3.2 Structure of the (001), (011), and (111) surfaces

The structures for the clean (001) and (111) surfaces match the expected results for pure aluminum [61, 63 - 64, 81]. The diffracted beams are sharp, and the unit cell dimensions agree with the structure for a truncated FCC unit cell. Figures 7.1A – 7.1F show representative LEED images for the (001), (011), and (111) surfaces, respectively. The (011) surface, however, appears to be populated with (111) facets instead of a smoothly truncated face.

In LEED images of surfaces that are simply truncated, the diffraction spots converge towards the center (0 0) beam with increasing energy. When facets are present on the surface, their surface normals are no longer coincident with the surface normal for the average surface. When the LEED pattern is observed for a faceted surface, diffraction spots move towards the surface normals of the facets [75]. For a (011) surface, facets of (111) are oriented 35.3° away from the average surface normal. LEED patterns for the (011) surface are shown in Figures 7.2A – 7.2F. In Figure 7.2A - B, the "facet" diffraction spots in the upper portion of the figure appear as small points that are about to converge on the larger diffraction spot labeled (0 1). Similarly in Figure 7.2C - D, there are diffraction spots moving along the horizontal direction towards the (1 0) spot in the image.
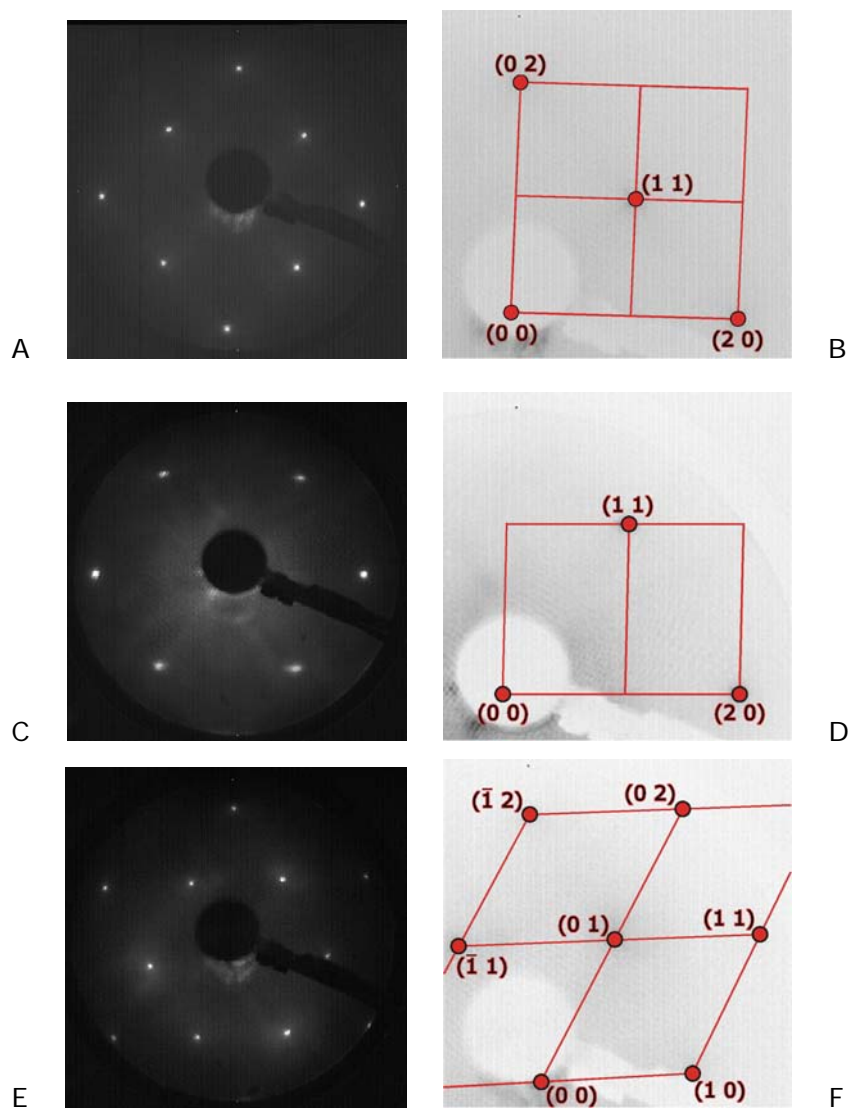
Figure 7.1: LEED images of the low-index surfaces for Al-1.7at% Cu. A) (001) surface at 97.5 eV. B) Magnified and inverse intensity for the upper right corner of (001) image. C) (011) surface at 92.6 eV. D) Magnified and inverse intensity for the upper right corner of (011) image. E) (111) at 141 eV. F) Magnified and inverse intensity for the upper right corner of (111) image.
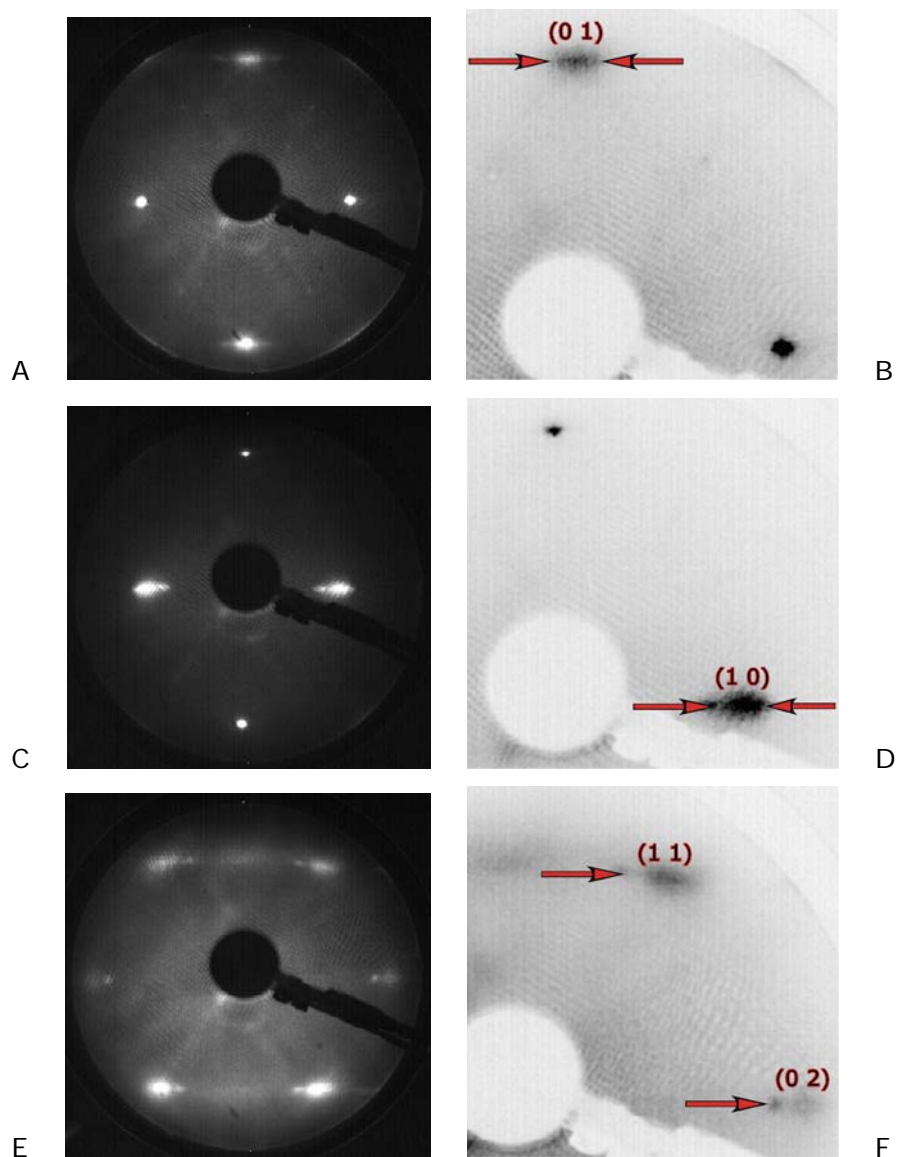
Figure 7.2: LEED images of the (011) surface for Al-1.7at% Cu showing additional diffraction spots attributed to facets on the surface. Red arrows indicate direction of motion for "facet" spots with increasing energy. A) at 46.6 eV. B) Magnified and inverse intensity of image A. C) at 52.2 eV. D) Magnified and inverse intensity of image C. E) at 76.6 eV. F) Magnified and inverse intensity of image E.

While some studies have found faceting due to oxygen absorption [82], the AES results here rule out this as the cause. Also, some reports have expressed concern that the sample preparation may lead to surface defects and faceting [81, 83 - 84]. Because the surface was prepared so that the miscut was less than 0.1°, the spacing between geometrically required steps due to the miscut is on the order of 800 Å. Grepstad *et al.*, found the appearance on all three low index Al surfaces to be similar, 400 μm^2 areas with facet edges formed after sputtering for less than 72,000 s and annealing at 723 K [81]. The sputter conditions appear to be similar to the preparations described here in section 7.2.

Most fcc materials have equilibrium shapes with only (001) and (111) faces, as these surfaces have the lowest surface energies [89], but aluminum also has (011) faces in equilibrium voids [90]. It is possible that a (011) surface is higher in energy than a surface composed of (001) and (111) facets, even though the surface area is increased [91]. For such a case, the overall surface is composed of lower surface energy facets. Investigations [85 - 87] on pure Al show that the (001) and (111) surfaces are stable up to the melting point, but the (011) surface exhibits roughening near $0.67T_{melt}$ [88]; this roughening appears as steps in the <100> and <111> directions on the (011) surface.

The surface for Al-Cu (011) appears to have facets on (111) planes. With an increased concentration of Cu at the surface, it might be expected that Cu (with a smaller size than Al) would help accommodate the inward contraction of the outer layer on the (011) face for Al. However, it may be the smaller size of Cu atoms are strained in the lateral direction and make the (011) surface unstable.

7.4 Conclusions

Samples with (001), (011), and (111) surfaces were prepared for Al-1.7at.% Cu alloy.   After sputter cleaning the samples to remove the oxide layer, the chemical composition was measured using AES.   Cu segregates to the surface for the (001), (011), and (111) faces in an amount that roughly doubles the bulk concentration (1.7 at%).   The Cu concentration at the surface decreases when the temperature exceeds the solvus temperature.   Using LEED to measure the surface structures, the (001) and (111) surfaces are found to be bulk terminated and are similar to pure Al.   The (011) surface contains facets oriented along <111> planes.

Chapter 8: Summary and Outlook

8.1 Thesis Summary

For the research included in this thesis, the primary focus has been using the XSW technique to investigate the structures of the 1/3 ML Sn/Ge(111) and 1/3 ML Pb/Ge(111) surfaces. The interest in these systems has arisen from the reversible phase transition between the room temperature $(\sqrt{3} \times \sqrt{3})R30°$ phase to the low temperature (3 x 3) phase. While STM images show two types of Sn (or Pb) atoms on the low temperature surface, the STM room temperature structure shows the Sn (or Pb) atoms to be equivalent. The nature of this controversial phase transition has been debated for several years. Is it an order-disorder or displacive phase transition?

The XSW technique is well suited to this problem because it directly measures the Fourier coefficients of the atomic distribution. By making (111) and (333) measurements along the surface normal direction on the $(\sqrt{3} \times \sqrt{3})R30°$ phase, the Sn distribution was found to be asymmetric, and inconsistent with a single height for the adatom. A straight-forward model was applied to the XSW-measured

Fourier coefficients for the ($\sqrt{3}$ x $\sqrt{3}$)R30° phase at room temperature. These XSW measurements show that Sn adatoms are at the T_4–site with two-thirds of the Sn at 1.87 Å above the top of the bulk-like Ge bilayer and one-third of the Sn at 2.32 Å, i.e. "one up and two down". Combining the RT and LT XSW measurements, the time-averaged Sn distribution, when projected into the (1 x 1) unit cell, shows no significant change when going through the phase transition. This agrees with an order-disorder transition in which Sn atoms are "frozen in" below the transition temperature and undergo correlated fluctuations above the transition temperature, with little time spent in transition between the two heights. The magnitude (0.45 Å) of the Sn vertical separation from the XSW results agrees with a soft phonon model at room temperature, where the Sn atoms undergo a correlated 0.5 Å switching in their vertical positions. After depositing Sn, annealing the sample to a higher temperature appears to cause some of the Sn to substitute into the bottom of the Ge surface bilayer at a height of –0.45 Å below the bulk-like atom in the top of the bilayer

The XSW direct space imaging procedure has been demonstrated to create an element-specific, subangstrom resolution density map for adsorbate atoms on the Ge(111) surface. By combining the measured XSW Fourier coefficients (amplitude and phase) for a select set of *hkl* Ge Bragg reflections, an image of the Sn atom distribution was produced within the Ge primitive unit cell. This technique produced an image showing Sn atoms to be at the T_4-adsorption site for 1/3 ML Sn/Ge(111) annealed at 473 K. Other sample preparations produced images that show Sn and Pb to occupy another position. Modeling of the structure found the

other position to be consistent with Sn (and Pb) substituting for Ge in the bottom of the bilayer.

Results for chemical composition and surface structure measurements were presented for the (001), (011), and (111) surfaces of an Al-1.7at% Cu alloy. The surfaces have an enrichment of Cu at their surfaces. The (001) and (111) surfaces display the bulk-terminated structure that pure aluminum does. The (011) surface appeared to become facetted along {111} directions.

8.2   Outlook

The investigations of the 1/3 ML Sn/Ge(111) and 1/3 ML Pb/Ge(111) surfaces have obvious corollaries on the Si(111) surface. While no reports in the literature have found the same low temperature phase transition, the Si(111) surface displays many similar features. Density functional theory calculations for the soft phonon model for the 1/3 ML Sn/Ge(111) also showed a similar behavior for the 1/3 ML Sn/Si(111) surface. Another variant experiment is to co-deposit a mixture of Pb and Sn onto the Ge(111) surface with a 1:2 (or 2:1) ratio of Pb to Sn for a total of 1/3 ML. The (3 x 3) phase exhibits long-range ordering in the vertical height distribution for Sn or Pb. While this long-range order is not stable at RT, it may be stable if one of the three atoms in the (3 x 3) unit cell had a larger size (like Pb compared to Sn).

In addition to the Pb-Sn surface alloy, the $Pb_{1-x}Ge_x$/Ge(111) surface displays interesting ordering behavior in two-dimensions. The atoms have a strong preference for short-range ordering in the adlayer. This ordering has been simply

examined using two STM images. More extensive work could be done with either access to an STM or development of a diffraction-based technique that measures the diffuse scattered intensity from the surface. Analyzing the diffuse intensity could produce unique information, such as the static displacements of atoms from their lattice positions and the short-range ordering parameters for the alloy atoms on surfaces.

REFERENCES

[1]   S. Iwanari and K. Takayanagi, Japanese Journal of Applied Physics Part 2-Letters **30**, L1978-L1981 (1991).

[2]   P. G. Evans, O. D. Dubon, J. F. Chervinsky, F. Spaepen, and J. A. Golovchenko, Applied Physics Letters **73**, 3120-3122 (1998).

[3]   D. Vanderbilt, Physical Review B **36**, 6209-6212 (1987).

[4]   P. M. J. Maree, K. Nakagawa, J. F. Vanderveen, and R. M. Tromp, Physical Review B **38**, 1585-1588 (1988).

[5]   R. Feidenhansl, J. S. Pedersen, J. Bohr, M. Nielsen, F. Grey, and R. L. Johnson, Physical Review B **38**, 9715-9720 (1988).

[6]   *Binary Alloy Phase Diagrams*; *Vol. 2*, edited by T. B. Massalski (ASM International, 1990).

[7]   G. Lelay, K. Hricovini, and J. E. Bonnet, Applied Surface Science **41-42**, 25-37 (1989).

[8]   T. Ichikawa and S. Ino, Surface Science **105**, 395-428 (1981).

[9]   M. F. Reedijk, J. Arsic, D. Kaminski, P. Poodt, J. W. M. van Kessel, W. J. Szweryn, H. Knops, and E. Vlieg, Physical Review B **67**, Article Number 165423 (2003).

[10]   J. M. Carpinelli, H. H. Weitering, and E. W. Plummer, Surface Science **401**, L457-L463 (1998).

[11]   J. A. Carlisle, T. Miller, and T. C. Chiang, Physical Review B **47**, 10342-10347 (1993).

[12]   J. S. Pedersen, R. Feidenhans'l, M. Nielsen, F. Grey, and R. L. Johnson, Surf. Sci. **189/190**, 1047-1054 (1987).

[13]   M. Göthelid, M. Hammar, C. Tornevik, U. O. Karlsson, N. G. Nilsson, and S. A. Flodström, Surf. Sci. **271**, L357-L361 (1992).

[14]   J. M. Carpinelli, H. H. Weitering, E. W. Plummer, and R. Stumpf, Nature **381,** 398-400 (1996).

[15]   J. M. Carpinelli, H. H. Weitering, M. Bartkowiak, R. Stumpf, and E. W. Plummer, Physical Review Letters **79**, 2859-2862 (1997).

[16]   A. P. Baddorf, V. Jahns, J. D. Zhang, J. M. Carpinelli, and E. W. Plummer, Physical Review B **57**, 4579-4583 (1998).

[17]   R. I. G. Uhrberg and T. Balasubramanian, Physical Review Letters **81**, 2108-2111 (1998).

[18]   G. Le Lay, V. Y. Aristov, O. Boström, J. M. Layet, M. C. Asensio, J. Avila, Y. Huttel, and A. Cricenti, Applied Surface Science **123**, 440-444 (1998).

[19]   J. Avila, A. Mascaraque, E. G. Michel, M. C. Asensio, G. LeLay, J. Ortega, R. Pérez, and F. Flores, Physical Review Letters **82**, 442-445 (1999).

[20]   O. Bunk, J. H. Zeysing, G. Falkenberg, R. L. Johnson, M. Nielsen, M. M. Nielsen, and R. Feidenhans'l, Physical Review Letters **83**, 2226-2229 (1999).

[21]   J. D. Zhang, Ismail, P. J. Rous, A. P. Baddorf, and E. W. Plummer, Physical Review B **60**, 2860-2863 (1999).

[22]   T. E. Kidd, T. Miller, M. Y. Chou, and T. C. Chiang, Physical Review Letters **85**, 3684-3687 (2000).

[23]   J. Avila, A. Mascaraque, G. LeLay, E. G. Michel, M. Gothelid, H. Ascolani, J. Alvarez, S. Ferrer, and M. C. Asensio, http://arXiv.org/abs/cond-mat/0104259 (2001).

[24]   R. Pérez, J. Ortega, and F. Flores, Physical Review Letters **86**, 4891-4894 (2001).

[25]   G. Ballabio, G. Profeta, S. de Gironcoli, S. Scandolo, G. E. Santoro, and E. Tosatti, Physical Review Letters **89**, 126803 (2002).

[26] L. Petersen, Ismail, and E. W. Plummer, Progress in Surface Science **71**, 1-29 (2002).

[27] M. Göthelid, M. Björkqvist, T. M. Grehk, G. Lelay, and U. O. Karlsson, Physical Review B **52**, 14352-14355 (1995).

[28] A. Mascaraque, J. Avila, J. Alvarez, M. C. Asensio, S. Ferrer, and E. G. Michel, Physical Review Letters **82**, 2524-2527 (1999).

[29] H. H. Weitering, J. M. Carpinelli, A. V. Melechko, J. Zhang, M. Bartkowiak, and E. W. Plummer, Science **285**, 2107 - 2110 (1999).

[30] A. V. Melechko, M. V. Simkin, N. F. Samatova, J. Braun, and E. W. Plummer, Physical Review B **64**, 235424 (2001).

[31] A. V. Melechko, J. Braun, H. H. Weitering, and E. W. Plummer, Physical Review Letters **83**, 999-1002 (1999).

[32] B. E. Warren, *X-ray Diffraction* (Dover Publications, New York, 1969).

[33] B. W. Batterman, Physical Review **133**, A759-A764 (1964).

[34] B. W. Batterman, Physical Review Letters **22**, 703-705 (1969).

[35] P. L. Cowan, J. A. Golovchenko, and M. F. Robbins, Physical Review Letters **44**, 1680-1683 (1980).

[36] J. A. Golovchenko, J. R. Patel, D. R. Kaplan, P. L. Cowan, and M. J. Bedzyk, Physical Review Letters **49**, 560-563 (1982).

[37] A. M. Afanas'ev and V. G. Kohn, Zhurnal Eksperimentalnoi I Teoreticheskoi Fiziki **74**, 300-313 (1978).

[38] T. Takahashi and S. Kikuta, Journal of the Physical Society of Japan **46**, 1608-1615 (1979).

[39] N. Hertel, G. Materlik, and J. Zegenhagen, Zeitschrift fur Physik B-Condensed Matter **58**, 199-204 (1985).

[40] M. J. Bedzyk and G. Materlik, Physical Review B **32**, 6456-6463 (1985).

[41] J. Zegenhagen, Surface Science Reports **18**, 199-271 (1993).

[42] M. Bedzyk and L. Cheng, Reviews in Mineralogy and Geochemistry **49**, 221-266 (2002).

[43]   M. Laue, *Roentgenstrahl-Interfernzen* (Akademische-Verlagsgeslellschaft, Frankfurt, 1960).

[44]   B. W. Batterman and H. Cole, Review of Modern Physics **36**, 681-717 (1964).

[45]   A. Authier, *Dynamical Theory of X-Ray Diffraction* (Oxford University Press, New York, 2001).

[46]   Reflectivity curves are calculated using SWAN (version 2.1 b2).   The monochromator effective-b value is set to 0.25, and the sample effective-b value is set to -1.

[47]   H. A. Bethe and R. W. Jackiw, *Intermediate Quantuum Mechanics* (Benjamin, New York, 1968).

[48]   L. Cheng, P. Fenter, M. J. Bedzyk, and N. C. Sturchio, Physical Review Letters **90**, Article Number 255503 (2003).

[49]   W. Rodrigues, Growth and Characterization of Si/Ge Heterostructures on Si(001) and Ge Nano-Dots on Patterned Si(001) Surface, (Department of Physics and Astronomy, Northwestern University, Evanston, Illinois, 2000).

[50]   P. F. Lyman, D. T. Keane, and M. J. Bedzyk, American Institute of Physics Conference Proceedings **417**, 10-14 (1997).

[51]   D. A. Walko, O. Sakata, P. F. Lyman, T.-L. Lee, B. P. Tinkham, J. S. Okasinski, Z. Zhang, and M. J. Bedzyk, American Institute of Physics Conference Proceedings, Synchrotron Radiation Instrumentation 2003 (in press).

[52]   Z. Zhang, Probing Atomic Scale Structure of Rutile (110)-Aqueous Interface with High Brilliance X-rays, (Department of Materials Science and Engineering, Northwestern University, Evanston, Illinois, 2004).

[53]   The RBS measurements and analysis were completed by Pete Baldo of the Materials Science Division at Argonne National Laboratory. Pete Baldo estimates that for these submonolayer coverages for Sn and Pb, the error in the measured value is 10% of that value, i.e. 0.32 (±0.03) ML.

[54]   L. Petaccia, L. Floreano, A. Goldoni, D. Cvetko, A. Morgante, L. Grill, A. Verdini, G. Comelli, G. Paolucci, and S. Modesti, Physical Review B **64**, Article Number 193410 (2001).

[55]   L. Floreano, D. Cvetko, G. Bavdek, M. Benes, and A. Morgante, Physical Review B **64**, Article Number 075405 (2001).

[56] L. Petaccia, L. Floreano, M. Benes, D. Cvetko, A. Goldoni, L. Grill, A. Morgante, A. Verdini, and S. Modesti, Physical Review B **63**, Article Number 115406 (2001).

[57] L. Petersen, Ismail, and E. W. Plummer, Progress in Surface Science **71**, 1-29 (2002).

[58] A. Rouabah, J. Bernardini, and A. Rolland, Surface Science **315**, 119-126 (1994).

[59] Bond lengths for Ge-Ge is 2.45 Å and Sn-Sn is 2.81 Å. Bond length for Sn-Ge = (2.81 Å + 2.45 Å)/2 = 2.63 Å.

[60] J. S. Pedersen, R. Feidenhansl, M. Nielsen, F. Grey, and R. L. Johnson, Physical Review B **38**, 13210-13221 (1988).

[61] F. Jona, Journal of Physics and Chemistry of Solids **28**, 2155-2160 (1967).

[62] G. E. Laramore and C. B. Duke, Physical Review B **5**, 267-285 (1972).

[63] D. W. Jepsen, P. M. Marcus, and F. Jona, Physical Review B **6**, 3684-3690 (1972).

[64] M. R. Martin and G. A. Somorjai, Physical Review B **7**, 3607-3615 (1973).

[65] J. R. Noonan, H. L. Davis, W. Erley, Surface Science **152**, 142- (1985).

[66] H. B. Nielsen, J. N. Andersen, L. Petersen, D. L. Adams, Journal of Physics **15**, L1113-L1117 (1982).

[67] W. B. Pearson, A Handbook on Lattice Spacings and Structures of Metals and Alloys (Pergamon Press, New York, 1967), vol. 2.

[68] R. J. Baird, D. F. Ogletree, M. A. v. Hove, and G. A. Somorjai, Surface Science **165**, 345-354 (1986).

[69] R. J. Baird and W. Eberhardt, Journal of Vacuum Science Technology **18**, 538-540 (1981).

[70] E. Wetli, M. Erbudak, and T. Schulthess, Physical Review B **49**, 14628-14631 (1994).

[71] E. Wetli, M. Erbudak, and D. D. Vvedensky, Surface Science **317**, 235-240 (1994).

[72] M. Erbudak, M. Hochstrasser, and E. Wetli, Journal of Electron Spectroscopy and Related Phenomena **76**, 529-534 (1995).

[73]   E. Matsubara and J. B. Cohen, Acta Metallurgia **31**, 2129-2135 (1983).

[74]   H. Dosch, Critical Phenomena at Surfaces and Interfaces, Springer Tracts in Modern Physics (Springer-Verlag, Berlin, 1992), vol. 126.

[75]   G. Ertl and J. Küppers, Low Energy Electrons and Surface Chemistry (Weinheim, Germany, ed. 2nd, 1985).

[76]   J. L. Murray, in *Binary Alloy Phase Diagram* T. B. Massalski, H. Okamoto, P. R. Subramanian, and L. Kacprzak, Eds. (William W. Scott, USA, 1985), vol. 1, 141-143.

[77]   B. C. Allen, Transactions of the Metalographic Society, AIME **227**, 1175 (1963).

[78]   G. A. Somorjai, in *Introduction to Surface Chemistry and Catalysis*, (John Wiley & Sons, Inc., 1994) 282-291.

[79]   ASM, in *Selected Values of the Thermodynamic Properties of binary Alloys*, (American Society for Metals, USA, 1973) 152.

[80]   F. F. Abraham, N.-H. Tsai, and G. M. Pound, Surface Science **83**, 406-422 (1979).

[81]   J. K. Grepstad, P. O. Gartland, and B. J. Slagsvold, Surface Science **57**, 348-362 (1976).

[82]   S. M. Bedair and J. H. P. Smith, Journal of Applied Physics **42**, 3616-3618 (1971).

[83]   F. Jona, J. J. A. Strozier , and C. Wong, Surface Science **30**, 225-231 (1972).

[84]   C. W. B. Martinson, S. A. Flodstrom, J. Rundgren, and P. Westrin, Surface Science **89**, 102-113 (1979).

[85]   H. Dosch, T. Höfer, J. Peisl, and R. L. Johnson, Europhysics Letters **15**, 527-533 (1991).

[86]   A. W. D. van der Gon, R. J. Smith, J. M. Gay, D. J. O'Connor, and J. F. van der Veen, Surface Science **227**, 143-149 (1990).

[87]   A. M. Molenbroek and J. W. M. Frenken, Physical Review B **50**, 11132-11141 (1994).

[88]   P. v. Blanckenhagen, Berichte der Bunsen Gesellschaft für Physikalische Chemie **98**, 312-321 (1994).

[89] D. A. Porter and K. E. Easterling, Phase Transformations in Metals and Alloys (Chapman & Hall, Padstow, Cornwall, ed. Second, 1992).

[90] R. S. Nelson, D. J. Mazey, and R. S. Barnes, Philosophical Magazine **11**, 91-97 (1965).

[91] C. Herring, Physical Review **82**, 87-93 (1951).

APPENDICES

Appendix A: Details of the APS 5ID-C Station

A.1 High-heat-load monochromator at 5ID-A

When the storage ring is refilled after a dump/trip, it is advisable to reset the undulator gap, scan the high-heat-load (HHL) monochromator energy, and reset the monochromator tuning. While not a typical problem, the storage ring orbit may become misaligned with the undulator, causing a decrease in performance. The result from scanning the monochromator energy (mono_ev) is shown in Figure A.1. The band pass (ΔE/E) for the undulator (Eγ=7.00 keV using the first harmonic) was measured to be 3.9% and agrees with the expected value from the APS design handbook.

After setting the HHL monochromator to the desired energy, the second crystal of the monochromator (monocoil) should be scanned. The monocoil position should be moved to left side of the peak at a position corresponding to 90% of the peak intensity, as shown in Figure A.2. Using the program "piezo_servo_C", the HHL monochromator can follow the thermal drift in the system.
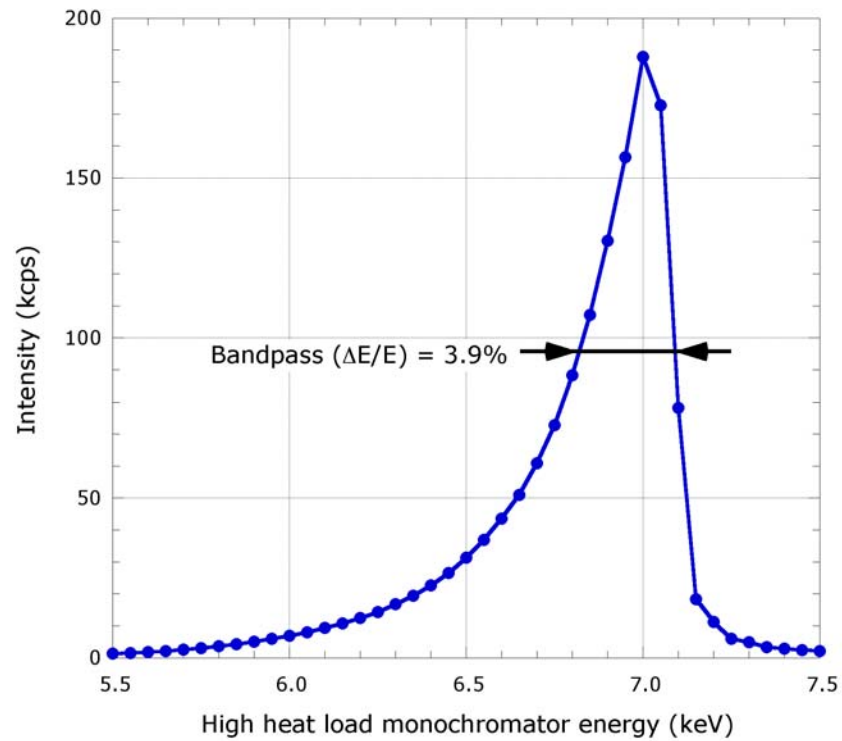
Figure A.1: A band pass value of 4% can be determined by scanning of the high-heat-load monochromator energy. The undulator gap is set for 7.00 keV. The detector used here is an ion chamber in the 5ID-B station. If the value for the band pass is too high (such as 8%), it may indicate an alignment problem the electron orbit of the storage ring and the undulator.
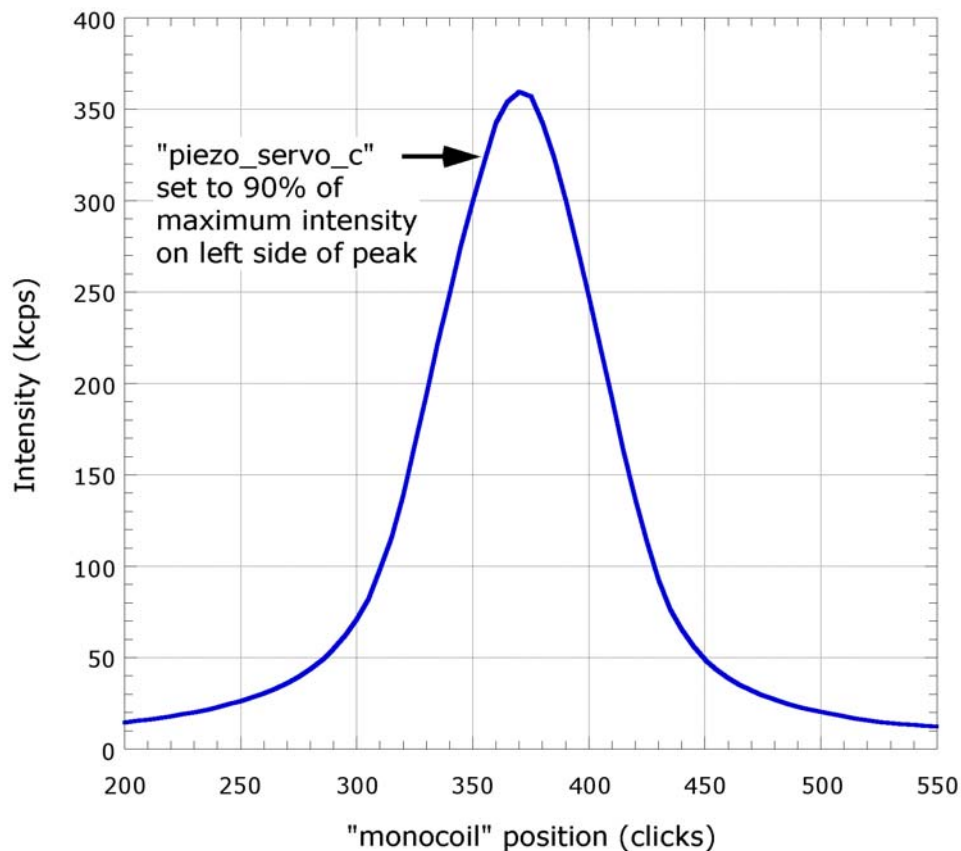
Figure A.2: A scan of the "monocoil" position shows the second crystal in the high-heat-load monochromator assembly passing through the Si(111) reflection at 7.0 keV. The "piezo_servo_C" program uses feedback control to maintain the monochromator locked onto the reflection; it maintains a fixed value of the ratio of the ion chamber counts to the electron ring current. (Transient thermal loads on the monochromator will cause it to drift.) The tuning of the second crystal is typically set to 90% of the peak reflectivity value and on the left side. This value is chosen primarily to pass most the x-rays and provide the program a reasonable value of slope to measure the response of the "monocoil" position.

A.2 Operating the UHV chamber at 5ID-C

A.2.1 UHV chamber positions and port assignments

Table A.1: Encoder readings from the Linear Variable Differential Transformer (LVDT) units for the linear translation stages and the eta values for important operations in the UHV chamber at 5ID-C. The positions are listed in mm.

operation	Xsamp	Ysamp	Zsamp	lincham	Xtab	eta (°)
XSW	-1.14	2.52	8.50	157.5	-12.11	θ_B
LEED	-0.06	4.57	20.2	292.06	N/A	2°
sputter	-2.38	3.64	23.8	170.2	N/A	35°
CMA-XSW	-3.00	8.84	18.8.0	170	-3.7	θ_B
MBE	-7.17	2.12	38.00	292.15	N/A	-130

Table A.2: Sputtering gun parameters for Ar^+ with a 500 V potential. When using the picoammeter to measure the ion current to the sample, detach the permanent thermal couple to achieve an accurate reading.

parameter	Value
accelerating potential	500 V
condenser lens	72.3% (363 V)
objective lens	73.4 % (367 V)
extractor pressure	20 mPa
chamber pressure	3.3×10^{-8} Torr
current to sample	0.49 μA

Table A.3: Assignments, port positions, and orientations, and for the UHV chamber in the 5ID-C hutch. The Port # refers to the layout in Figure A.3.

Port #	level	Flange	tube OD	focal pt. (") X	Y	Z	dist. to Focus	azimu.. angle (φ)	polar ang. (θ)	intended use
A1	base	1000-800T	6"	0	0	0 (CL)	N/A	0 (N/A)	180	goniometer
B1	lower	600-400	4″	0	0	4.25	8.25	319.5	90	VP
B2	lower	133-075	0.75"	0	0	1.75	6.5	342.5	90	unassigned
B3	lower	133-075	0.75"	0	0	1.75	6.5	0.0	90	unassigned
B4	lower	275-175T	1.75″	0	0	4.39	6.0	0.0	90	load lock
B5	lower	275-175	1.75"	0	0	2.10	7.0	29.5	90	
B6	lower	275-175	1.75	0	0	6.68	7.0	29.5	90	
B7	lower	133-075	0.75″	0	0	7.31	6.5	51.0	90	pin diode actuator
B8	lower	800-600	6″	0	0	4.25	6.0	87.7	90	LEED
B9	lower	133-075	0.75"	0	0	1.50	6.5	125.5	90	LEED shutter
B10	lower	450-250	2.5"	0	0	3.17	8	144.8	90	VP
B11	lower	275-175T	1.75"	0	0	4.25	7.5	180.0	110	VP 4 pyro
B12	lower	275-175T	1.75"	0	0	4.70	7.0	180.0	90	VP
B13	lower	133-075	0.75	0	0	1.75	6.5	200.5	90	RGA
B14	lower	800-600	6″	0	0	4.94	8.5	228.6	90	MBE
B15	lower	275-175	1.75	0	0	2.38	7.0	270.0	90	(up-to-air)
B16	lower	275-175T	1.75	0	0	5.57	7.0	277.6	90	nude gauge
C1	upper	133-075	0.75	0	0	8.25	6.5	306.2	90	VP (XRD spot)
C2	upper	275-175T	1.75"	0	0	9.25	7.0	331.3	95	
C3	upper	450-250	2.5"	0	0	9.25	8.0	325.7	65	ion gun
C4	upper	2.938 × 8.75	rectnglr	0	0	11.16	5.7	0.0	90	x-ray in
C5A	upper	133-075	0.75	0	0	9.25	6.5	22.0	90	VP (XSW)
C5B	upper	133-075	0.75	0	0	11.0	6.5	22.0	90	shutter 4 ?
C6	upper	2.938 × 7.0 (H)	rectnglr	0	0	9.85	5.7	63.2	90	x-ray out 2/ e⁻ flood gun
C7	upper	600-400T	4"	0	0.40	9.25	8.2	43.6	41.3	C7N for CMA
C7N	upper	from Staib	<4"	0	0.40	9.25	11.6	43.6	41.3	CMA
C7TN	upper	600-400		0	0.10	9.25	11.6	45.9	42.5	tilted CMA
C8	upper	1000-800T	8"	0	0	10.71	6.1	159.0	90	x-ray out 1
C9	upper	275-175T	1.75"	0	0	10.71	7.0	222.0	90	pin diode
C10	upper	800-600	6"	0	0	11.04	8.5	270.0	90	pumping
D1	dished top	600-400	4"	0	0	9.25	7.2	0 (N/A)	0	fluorescence SSD
D2	top	275-175	1.75	0	0	8.25	9.0	100.0	35	laser align 1
D3	top	275-175	1.75	0	0	8.25	9.0	225.0	35	k-cell in-situ
D4	top	275-175	1.75	0	0	8.25	9.0	280.0	35	laser align 2
D5	top	275-175	1.75	0	0	8.25	9.0	315.0	35	k-cell in-situ
D6	top	133-075	0.75	-3.73	1.44	9.25	6.75	N/A	0	shutter for x-ray out
D7	top	133-075	0.75	4.0	0.0	9.25	6.75	N/A	0	shutter for k-cell
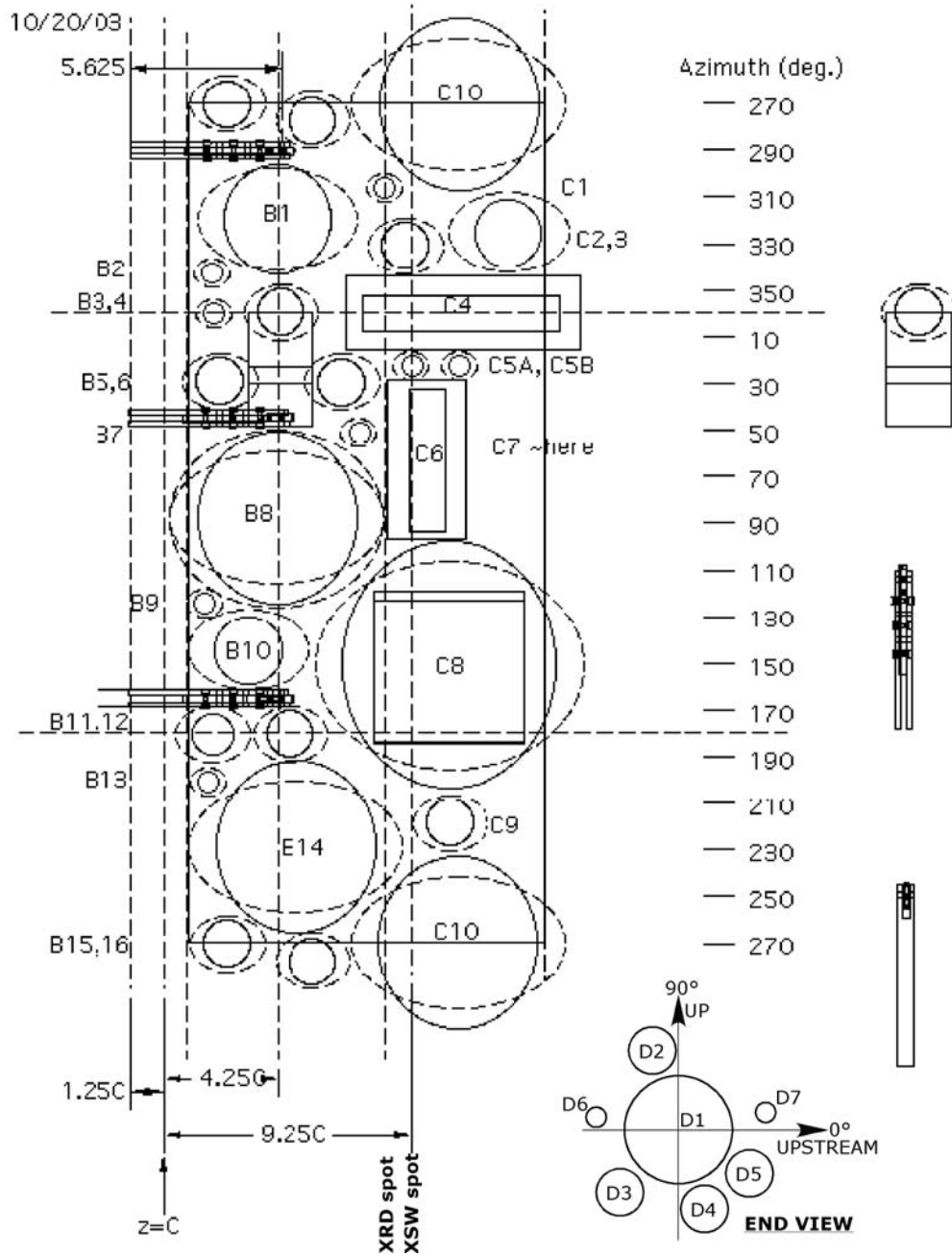
Figure A.3: Diagram of the "unrolled" chamber at 5ID-C. The port designations and positions are listed in Table A.3.

A.2.2 Baking-out the UHV chamber

Baking out the UHV chamber in the 5ID-C hutch is more difficult than typical chambers because it is attached to a diffractometer, it has numerous tools attached, and it is composed of three sub-chambers. In regards to baking the chamber, the total system can be considered to have three sections that are separated with gate valves: the main chamber, the introduction chamber, and the solid-state detector assembly. Regulating the bake-out temperature of the main chamber is aided by a network of K-type thermal couples attached to the components of the chamber. Due to a temperature restriction for the Viton O-rings in the gate valves, the bake-out temperature for the main chamber and introduction chamber is 150 °C. The Canberra solid state detectors have a temperature limitation of 80 °C at the bellows for extended bake-out time. An example of the typical bake-out schedule is listed in Table A.4. Photographs for the heat tape distribution and wrapping the main chamber and the sample manipulator are shown in Figure A.4.

A.2.3 Sample heating and cooling

The sample manipulator is equipped with both heating and cooling capabilities. The sample is radiatively heated from behind using a nude tungsten filament. An image of a large, heated sample can be seen in Figure A.5. Based on pyrometer readings and the visible light from the sample, the heating is not uniform over the entire area of the Thermionics LR sample platen. This is partially caused by the

Table A.4: Record for typical bake-out for main UHV chamber at 5ID-C.

Chamber pressure (x10-7 Torr)

bake-out time (hours)	0	2	2.5	3.3	4.5	16	19	44	56	62
nude gauge	1.7	14	23	47	36	9.3	6.5	3.9	3.6	0.2
ion pump	1.5	12	18	35	26	4.5	3.1	1.6	1.3	0.1

Thermal couple reading (°C)

1	sample	RT	50	89	166	201	231	232	367	338	113
2	LEED	RT	49	58	90	117	139	134	144	144	68
3	CMA bellows	RT	73	88	130	171	175	153	147	52	56
4	CMA / chamber	RT	58	72	101	137	164	149	148	152	58
5	sputter gun	RT	84	97	143	174	152	145	151	153	51
6	MBE – base	RT	77	89	130	154	160	154	151	148	62
7	MBE – tail	RT	73	83	123	139	127	132	136	133	48
8	chamber – downstream	RT	74	91	132	160	168	154	149	141	58
9	chamber – upstream	RT	82	99	138	170	171	161	161	154	52
10	chamber – outboard	RT	69	84	118	147	167	160	164	157	63
11	chamber – inboard	RT	72	89	125	161	177	168	173	165	62
12	chamber / cross	RT	66	78	112	138	169	162	164	159	67
13	cross / base	RT	65	76	117	133	152	151	152	146	62
14	bellows flange	RT	56	62	91	104	101	111	107	107	63
15	chamber bellows	RT	115	127	185	195	153	144	137	138	64
16	manipulator / bellows	RT	58	64	98	106	108	125	NR	124	56
17	manipulator	RT	74	88	123	146	146	145	142	154	68
18	ion pump gate valve	RT	68	76	114	128	138	146	142	142	63
19	turbo pump gate valve	RT	70	81	121	134	136	147	144	153	60
20	Pb K-cell (crucible)	RT	73	114	165	187	182	179	181	179	96
21	Sn K-cell (crucible)	RT	72	136	217	255	146	222	276	273	66
22	ion pump	RT	NR	NR	NR	NR	NR	152	148	NR	61

Heating: heat tape power (%) and filament current

1	turbo pump gate valve	20	40	60	60	57	62	61	62	62	0
2	ion pump gate valve	20	40	60	60	57	62	61	62	62	0
3	chamber - inboard	20	40	60	60	46	46	44	44	44	0
4	chamber - outboard	20	40	60	60	53	53	52	54	54	0
5	chamber – downstream	20	40	60	60	51	51	51	54	54	0
6	chamber - upstream	20	40	60	60	46	46	44	44	44	0
7	LEED	20	40	70	70	60	62	66	80	80	0
8	MBE	20	40	60	60	60	60	51	51	51	0
9	bellows / chamber	20	40	60	60	43	43	44	47	47	0
10	bellows / eta stage	20	40	70	70	67	76	85	92	92	0
11	cross – front / back	20	40	60	60	55	55	55	55	55	0
12	cross – top / bottom	20	40	60	60	55	55	55	55	55	0
13	manipulator	20	40	60	60	53	53	52	54	54	0
14	manipulator bellows	20	40	70	70	67	76	85	92	92	0
15	sputter gun	20	40	60	60	44	44	42	42	42	0
16	CMA	20	40	60	60	44	44	42	42	42	0
17	ion pump outer flange	20	40	60	60	43	43	44	47	47	0
18	sample (I)	0.5	1.0	2.0	2.0	2.0	2.0	2.5	3.0	3.0	0
19	Pb K-cell (I)	0.5	1.0	1.5	1.5	1.2	1.2	1.2	1.2	1.2	0
20	Sn K-cell (I)	0.5	1.0	1.5	1.5	1.5	1.5	1.5	1.5	1.5	0
21	TSP (I in filament #4)	10A	10A	12A	12A	12A	12A	12A	12A	12A	0
22	Ion Pump	20	50	82	82	77	77	77	77	77	0
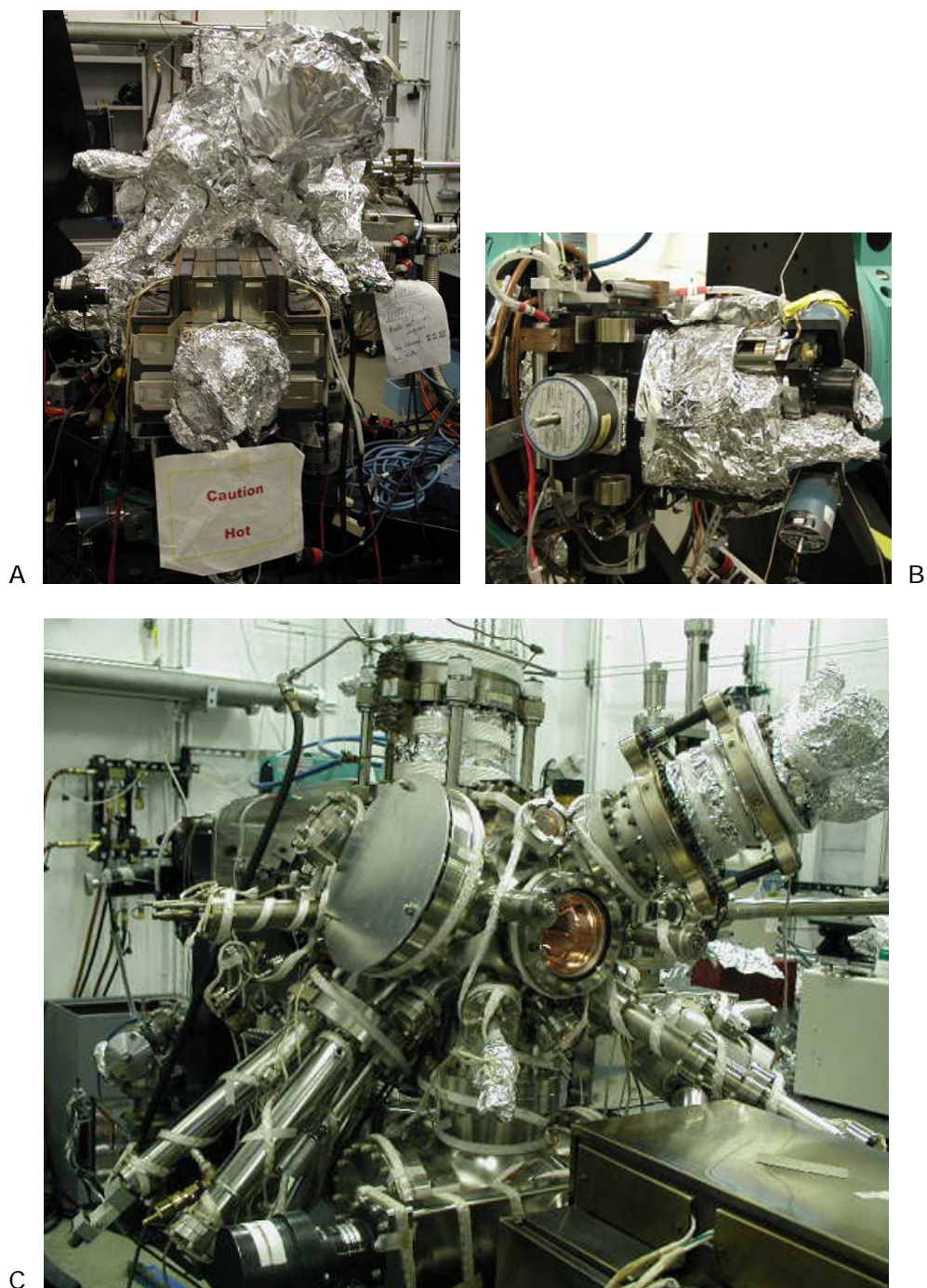
Figure A.4: A) Main UHV chamber wrapped for bake-out. B) Sample manipulator wrapped for bake-out. C) Distribution of the heat tape on the main UHV chamber.

1 cm^2 window in the center of the sample platen. The heating is fairly uniform in the region of the platen window; the temperature variation here is ~30 K. The temperature calibration for a typical XSW sample (see Figure E.1) and the permanent thermal couple are plotted in Figure A.6. The actual sample temperature is lower than the permanent thermal couple.

The sample can also be cooled with using liquid nitrogen. Typically, the lowest achievable temperature for the sample is 115 K after a period of 2.5 to 3 hours, as shown in Figure A.7. After cooling for more than 2 hours, the sample is about 45 K colder than the permanent thermal couple. It is important to use an insulated and short supply line from the liquid nitrogen dewar to the sample manipulator. Also, the pressure inside of the dewar should be at 90 - 100 psi. If the dewar pressure is not high enough, the cooling performance can be considerably diminished.
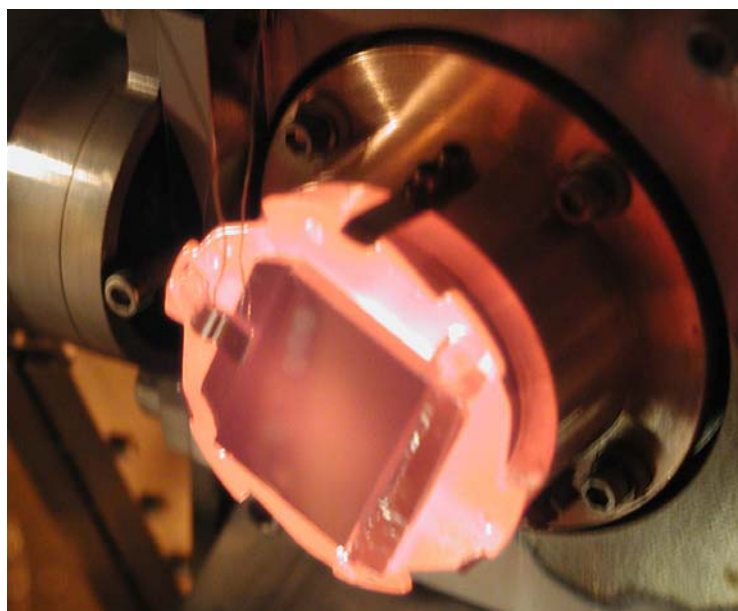
Figure A.5: Large area Ge sample heated on Thermionics LR platen with window.
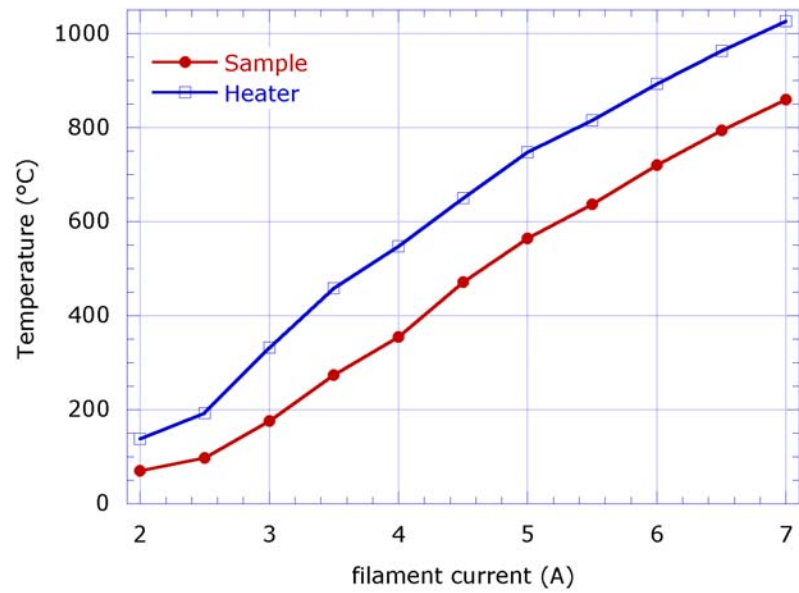
Figure A.6: Calibration for sample heating for Thermionics LR platen with window.
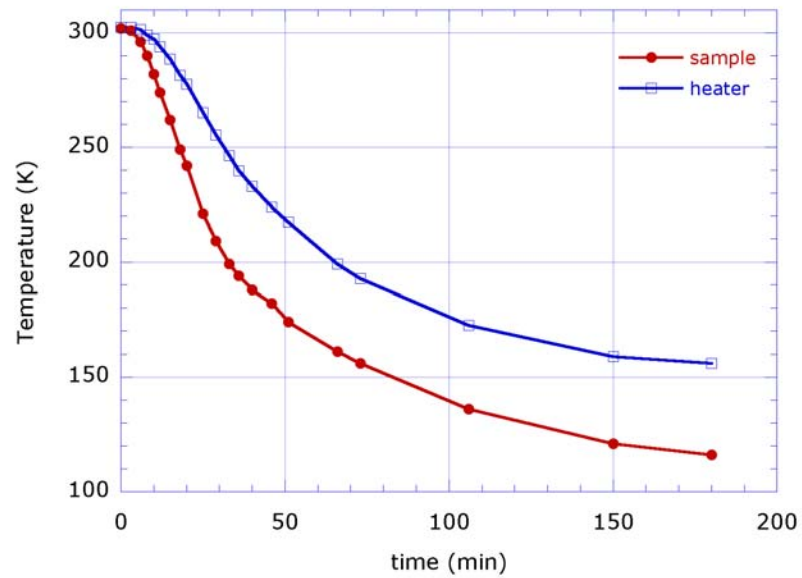
Figure A.7: Calibration for sample cooling for Thermionics LR platen with window.

A.2.4 Moving "lincham" with piston/pulley assist

The 10″ diameter bellows between the main chamber and the eta-stage creates a large vacuum force (~550 lb) that pulls the main chamber in towards the eta stage. A piston/pulley system counteracts this force to minimize the torque applied to the chamber and to permit linear translation of the chamber. Three pneumatic pistons actuate the motion of three steel cables; each cable is guided through seven pulleys to counteract the vacuum force on the main chamber. The geometry of the set-up doubles the stroke length of the piston and reduces by half the force on the cable. The component parts are listed in Table A.5.

The pulleys were modified by machining a 0.18″ hole through the center and pressing a bronze bearing into it. Because some of the bronze bearings have failed (cracked and fallen apart) under the loads in the piston/pulley system, 6061 Al "bearings" were machined to replace them.

A.2.5 Accessing the sample manipulator

If the internal components to the sample manipulator need to be accessed, the main chamber can be disconnected from the large 10″ bellows. First, the main ion pump must be removed. It is advisable to first vent both the main chamber and ion pump with dry nitrogen. Figure A.8 shows some of the steps in separating the bellows from the chamber. An overhead crane lifts the ion pump by four eye-bolts and straps. Three aluminum brackets hold the bellows and flange in place when the flange is unbolted from the chamber. The main chamber can then be translated away from the Huber stage using the lincham motion.

Table A.5: Parts for the piston/pulley system

Manufacturer	Part #	Description
Flodyne, Inc.	Q974227 (custom)	Air pistons: 2.5″ ID and 4″ stroke
McMaster-Carr	3458T76	302 stainless steel wire rope, 3/32″, 7x19 strand core, 920 lb break strength, (expect 0.5% strain for 440 lb load)
	3755T14	stainless steel sleeves
	8914T22	304 stainless steel thin pattern thimble
	3632T14	single groove crimp tool for 3/32″ wire
W M Berg, Inc.	PG-1	1″ grooved stainless steel pulley for 3/32″ cable, 1/8″ ID
	PG-2	0.5″ grooved stainless steel pulley for 3/32″ cable, 1/8″ ID
	PZ-11-3	shoulder screw, 0.187 dia., 0.50″ long
	PZ-12-3	shoulder screw, 0.187 dia., 0.626″ long
	B7-7	oil-less bronze bearing, 0.314″ OD, 0.188″ ID, 0.25 long
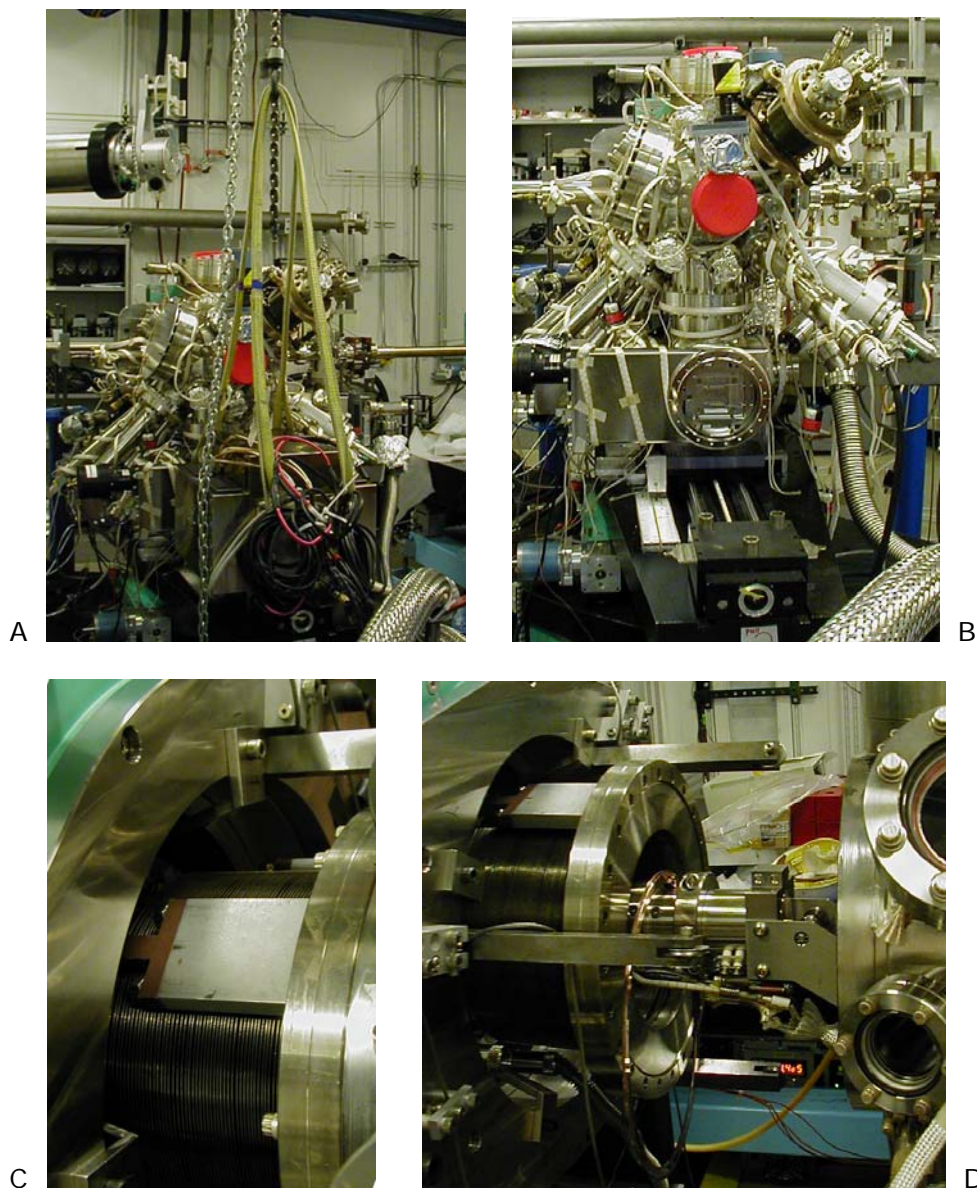
Figure A.8: To access the sample manipulator, the main ion pump must be removed. A) Overhead crane connected to the ion pump using eye-bolt and straps. B) Main chamber without ion pump. C) Three brackets hold the bellows and flange in place. D) The main chamber translated away from the Huber stage.

A.2.6 Storing samples in the introduction chamber

The upstream side of the main chamber is connected to the introduction chamber. Up to four samples can be stored at UHV conditions (P = 10^{-10} Torr) inside of the introduction chamber. In Figure A.9, a transparent TiO_2 sample and a Ge sample are shown mounted on the carousel before they are sealed inside the introduction chamber. Care should be given to ensure that the sample transfer fork can properly engage the sample platen without interference from the sample clips.
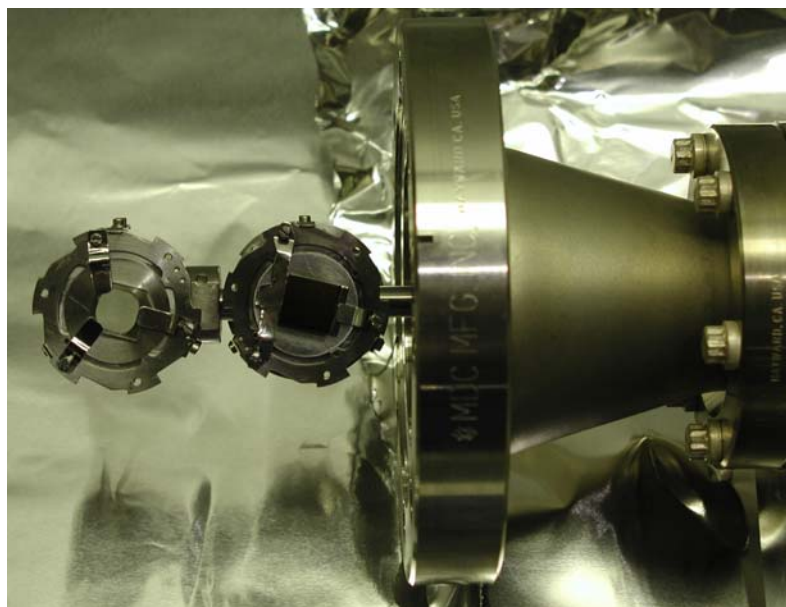
Figure A.9: Two samples mounted on the carousel of the introduction chamber.

A.2.7 Differential-pumping system for the vacuum compatible SSD

The design of the differential pumping system for the Canberra x-ray detector with a vacuum-compatible interface is shown in Figure A.10. The design for the two custom pieces, reducer nipple and cross, are shown in Figure A.11 and A.12.
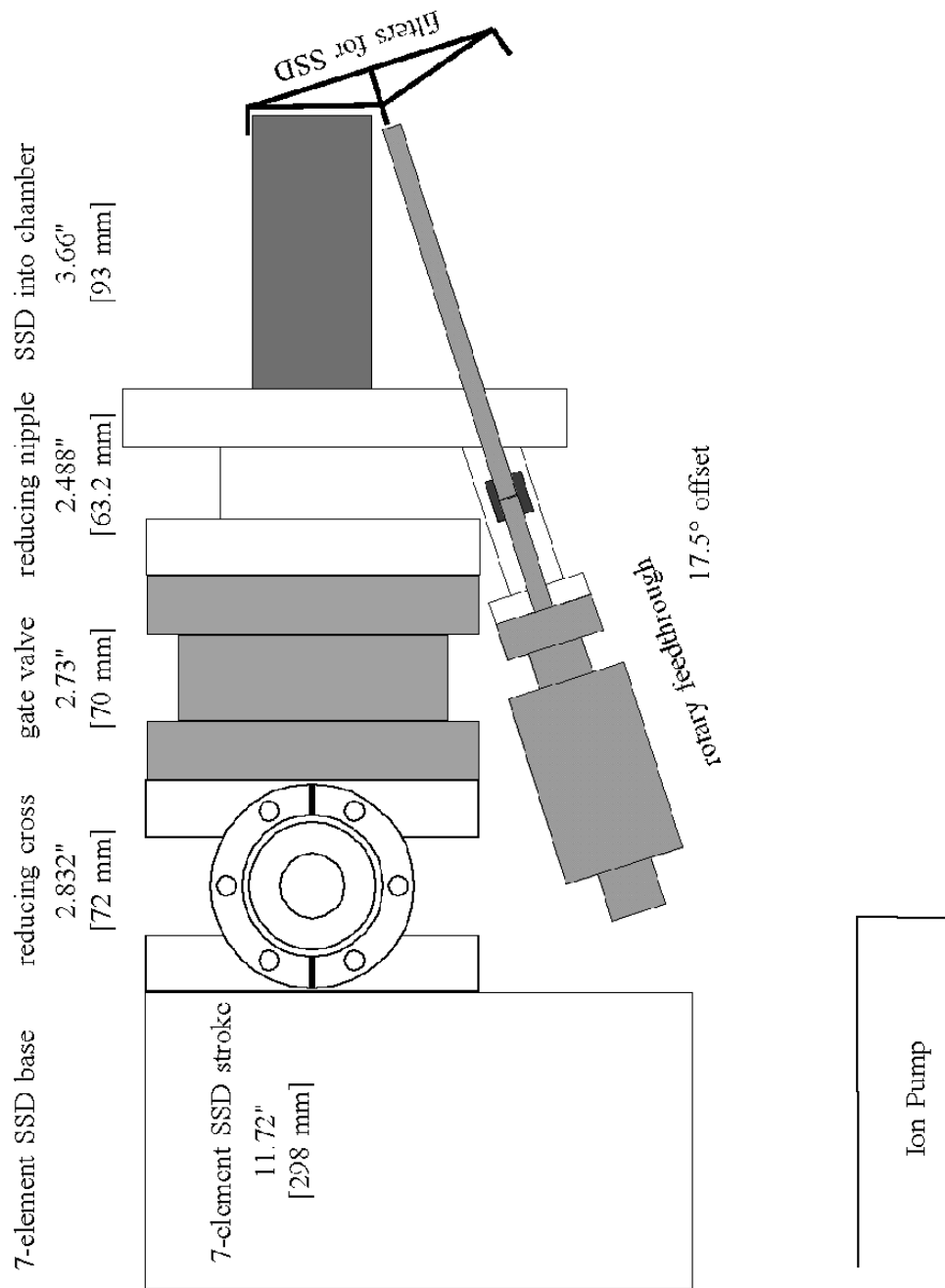
Figure A.10: Design for differential pumping and filter/collar assembly for the Canberra detector with vacuum interface.
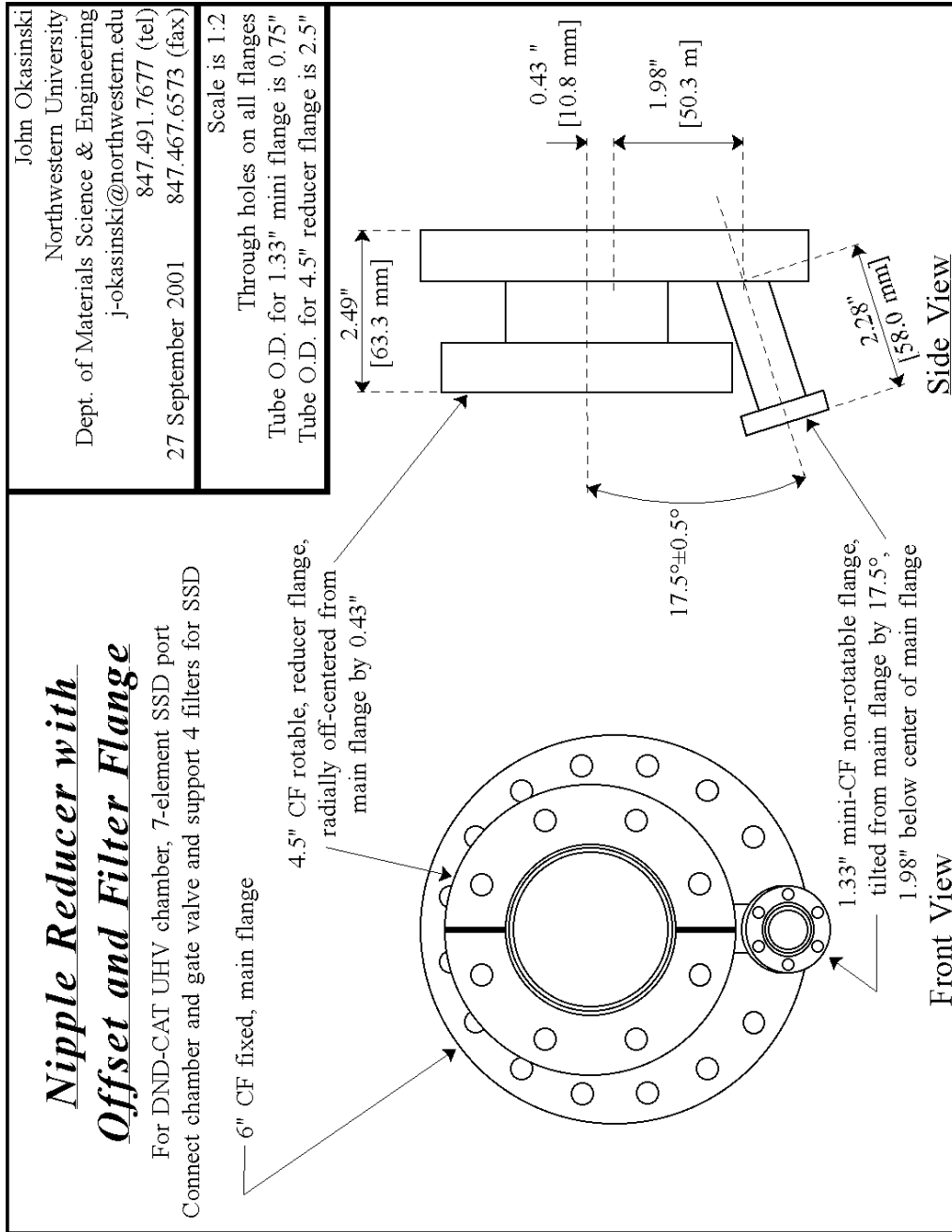
Figure A.11: Design for offset nipple reducer with port for filter rotary feedthrough.
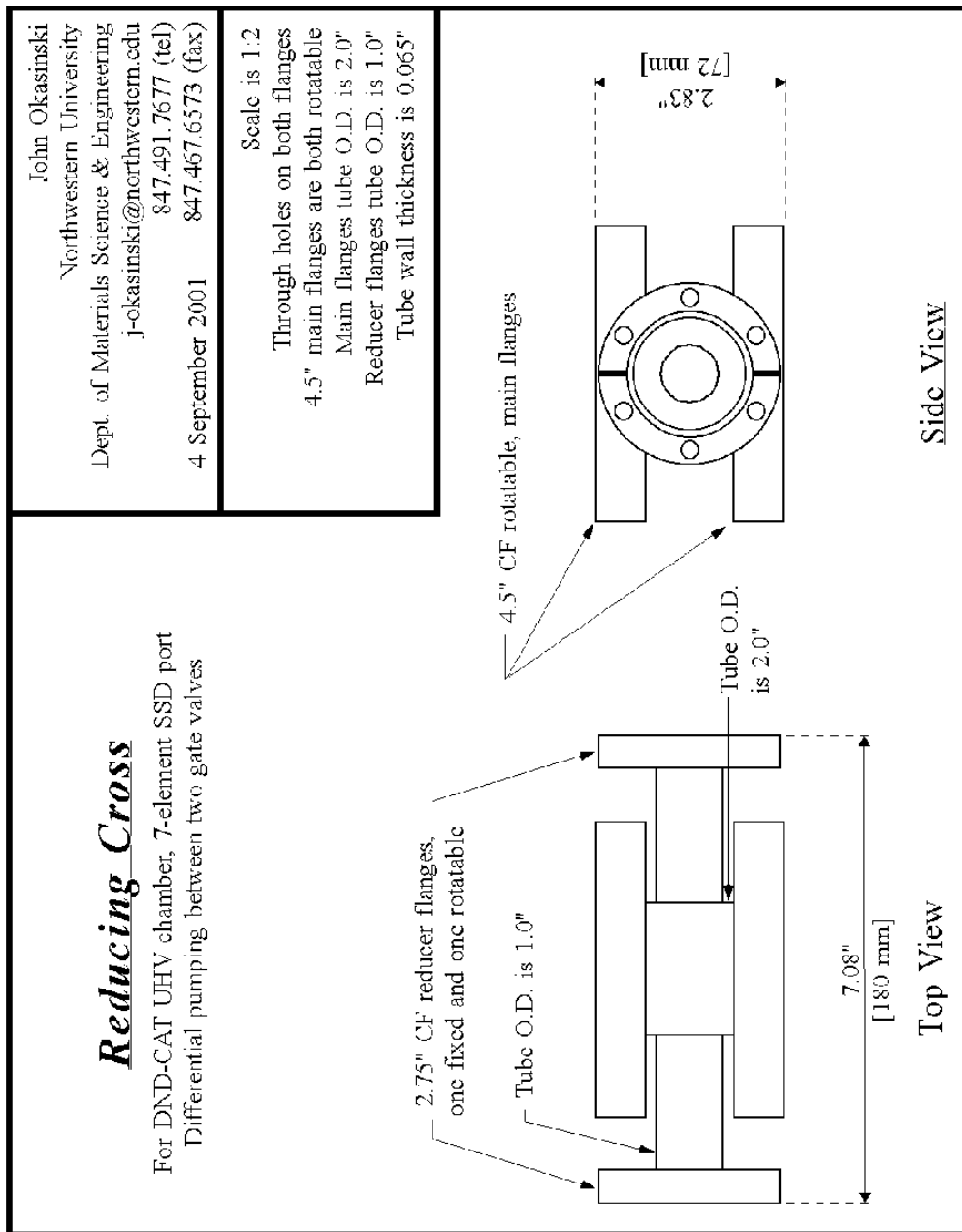
Figure A.12: Design for minimum-length cross for differential pumping on UHV compatible SSD.

Appendix B: Fabricating Si Channel-Cut Monochromators

B.1 Design and dimensions of the Si channel cut monochromators

B.1.1 Channel-cut monochromator designed for use at synchrotrons

A series of Si channel cut monochromators with *(00h), (0hh), and (hhh)* orientations were designed for use at synchrotrons, where the x-ray energy is tunable over a broad range. At the 5ID undulator beamline, the high-heat-load monochromator is tunable between 4 keV and 18 keV. These channel-cut monochromators have a 20 mm long face for the first-bounce and an 80 mm long second face that is offset (from the first diffraction surface) at two different distances. Full-scale drawing for these monochromators are shown in Figure B.1. The overall lengths are 100 mm. The diffraction faces are at least 10 mm in height.

The actual gap dimensions and their associated energy ranges are listed in Table B.1. The paths for x-rays with the minimum allowed energy are shown in red, and the paths for the maximum energy x-rays are shown in blue. These values are conservative estimates and were determined for the x-ray beam striking at least 5 mm from the edge.

Table B.1: Actual gap dimensions for the Si channel-cut monochromators and the corresponding minimum and maximum x-ray energies for the *(hkl)* reflections.

(hkl)	gap (mm)		$E_{minimum}$ (keV)		$E_{maximum}$ (keV)	
	small	large	small	large	small	Large
(004)A	10.2	14.6	7.1	5.3	35.0	24.4
(004)B	10.8	15.6	7.1	5.3	35.0	24.4
(022)	6.9	12.0	4.4	3.7	39.9	23.1
(111)	6.2	12.3	3.6	2.3	26.4	79.1
(333)	6.2	12.3	10.8	6.8	13.4	40.2
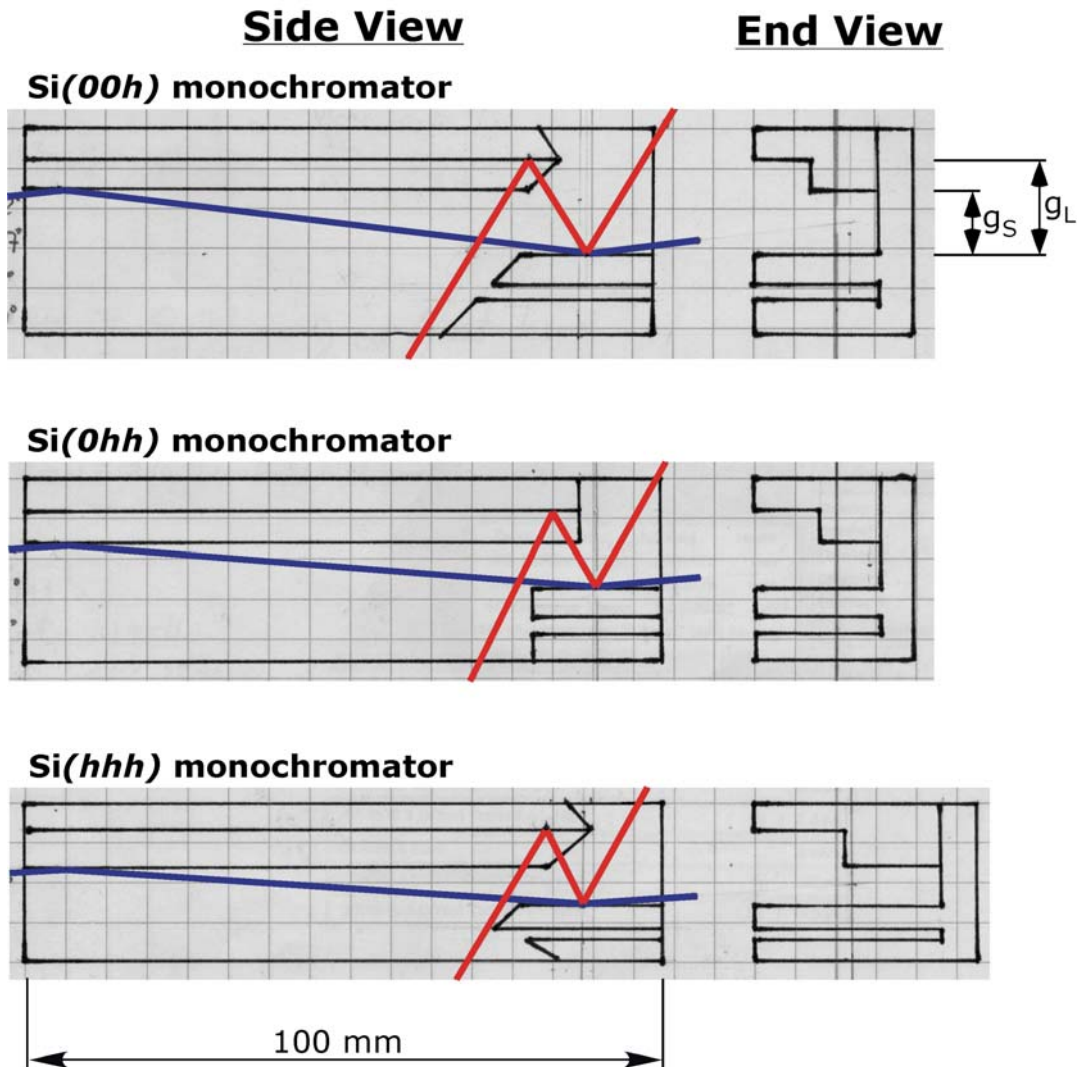
Figure B.1: Scaled drawing for the Si channel cut monochromators with *(00h)*, *(0hh)*, and *(hhh)* orientations for use at the Advanced Photon Source. These values were measured from the actual monochromators and reflect the average values between the pairs. The *(0hh)* and *(hhh)* have little deviations in their dimensions. The *(00h)* pair have somewhat higher deviations between each other.

B.1.2 Channel-cut monochromator for conventional x-ray sources

For laboratory x-ray sources, it is desired to have monochromatic x-rays beam for high resolution measurements. A series of 2–bounce channel-cut monochromators with *(00h), (0hh), and (hhh)* orientations were designed for use with the Kα or Kβ x-ray emission for Cr, Cu, and Mo targets. Some of the crystals can also operate as 4-bouce monochromators. The designs are shown in Figures B.2 – B.4. These monochromators are interchangable and require little time to switch between them. It should be noted that in order to accommodate a range of x-ray energies, the monochromators have both a left– and right–hand sense to them. In order to minimize dispersion in the diffraction geometry, the choice of the sense will depend on if it functions as an incident or diffracted beam monochromator.

B.2 Fabrication of the Si channel-cut monochromators

The three sets of Si channel-cut monochromators designed for use at the APS were made by different people. David Marasco made the *(00h)* monochromators. John Okasinski made the *(hhh)* monochromators. The APS optics shop made the *(0hh)* monochromators. The APS optics shop also made the Si(111) and (333) channel-cut monochromators for use in the NU x-ray lab (and will make the (022) and (004) monochromators).

B.2.1 Determining the surface normal direction and orienting to the *(hkl)* direction for a Si boule

The orientation of a Si boule can be quickly determined (or verified) by taking a Laue photograph of the surface. Depending on the desired orientation, (001), (011), or (111), the symmetry of the zone axes can easily be seen to be 4–, 2–, or 3–fold, respectively. In addition to the normal reflection for the *(00h), (0hh), and (hhh)* channel-cut monochromators, they are designed to also accommodate asymmetric reflections. For this reason, it was important to properly orient the off-normal directions for the Si crystals before cutting them. Figure B.5A show the how the Laue camera can be used to orient the crystallographic directions within 1°. The outline of the blocks, from which the monochromators are cut, is drawn on the slice of Si shown in Figure B.5B.

The barrel alignment tool enables crystals to be oriented and cut to a desired crystallographic direction to within 0.1°; the components are shown in Figure B.6. After the crystal is bonded to the mount, the crystallographic direction can be aligned using the rotary stage and x-ray point source shown in Figure B.7. A Mo target tube is connected to a 1 mm pinhole at a distance of 700 mm.

Since the x-ray tube spectrum is polychromatic, the Mo Kα and Kβ diffraction peaks will both be observed. The angle for the desired reflection is measured using four different azimuthal angles (0°, 90°, 180°, and 270°). The rotary stage is then set to the average θ peak position for Mo Kα. The three screws on the barrel are adjusted so that the crystal undergoes Bragg diffraction for the reflection over the full range of the azimuthal angle. The intensity deviation should typically range from 10% to 50%, depending on the crystal size and geometry.

The design of these two channel cut monos have the same side profile with a 4.0 ±0.1 mm gap and diffracting wall thickness of 3.0 ±0.2 mm (for a total width=10.0 ±0.4 mm). The diffracting wall height is 15 ±1 mm. The center height is 4.0 ±0.5 mm, and the strain relief groove is 2.0 ±0.5 mm, and the base is 2.0 ±0.5 mm (for a total height=23 ±2 mm). The individual lengths are listed for each mono. Align to (004) ±0.1 °. The lengths of the diffracting wall corner to be removed are listed and are ±0.3 mm. Drawn to 2:1 scale
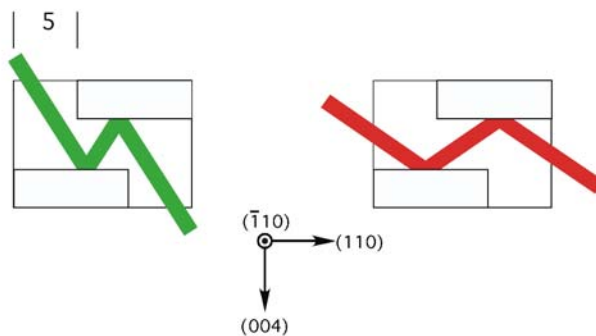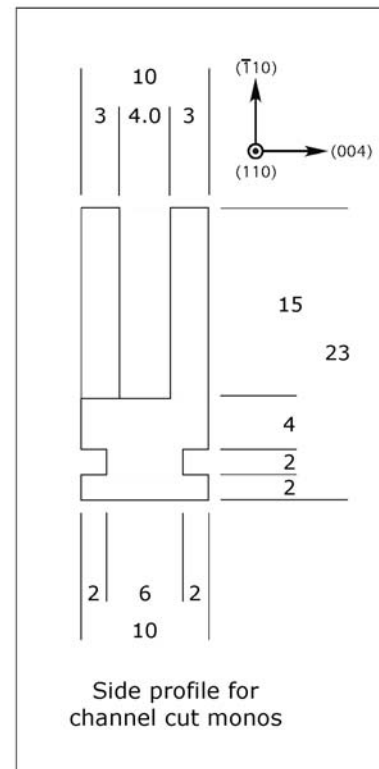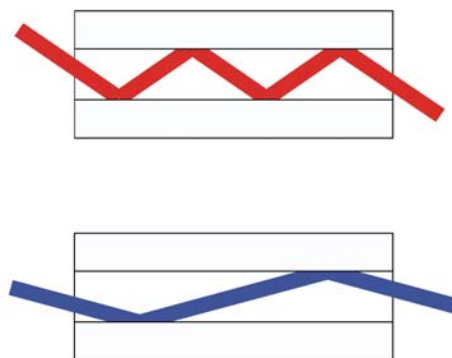
Figure B.2: Si(004) monochromators for Cr, Cu, and Mo target x-ray sources.

The design of these two channel cut monos all have the same side profile with a 3.5 ±0.1 mm gap and diffracting wall thickness of 3.0 ±0.2 mm (for a total width=9.5 ±0.4 mm). The diffracting wall height is 15 ±1 mm. The center height is 4.0 ±0.5 mm, and the strain relief groove is 2.0 ±0.5 mm, and the base is 2.0 ±0.5 mm (for a total height=23 ±2 mm). The individual lengths are listed for each mono. Align to (220) ±0.1 °. The lengths of the diffracting wall corner to be removed are listed and are ±0.3 mm. Drawn to 2:1 scale.
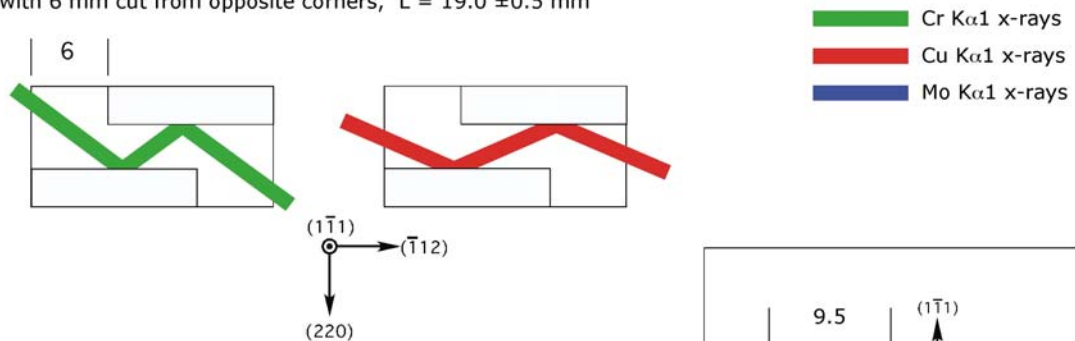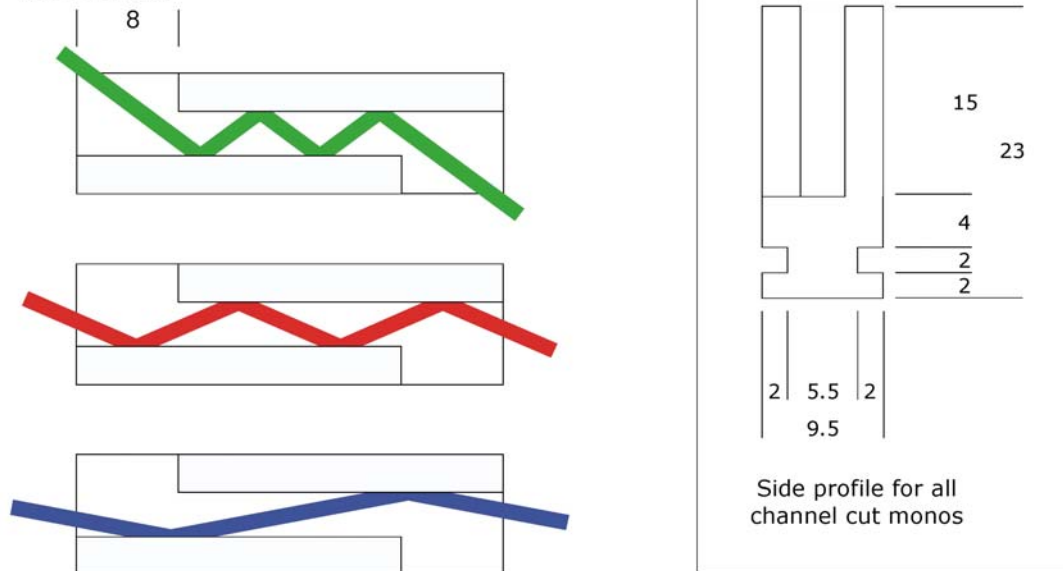
Figure B.3: Si(220) monochromators for Cr, Cu, and Mo target x-ray sources.

The design of these four channel cut monos all have the same side profile with a 3.0 ±0.1 mm gap and diffracting wall thickness of 3.0 ±0.2 mm (for a total width=9.0 ±0.4 mm). The diffracting wall height is 15 ±1 mm. The base height is 4.0 ±0.5 mm, and the strain relief groove is 2.0 ±0.5 mm, and the base is 2.0 ±0.5 mm (for a total height=23 ±2 mm). The individual lengths are listed for each mono. Align to (111) ±0.1 °. The lengths of the diffracting wall corner to be removed are listed and are ±0.3 mm.
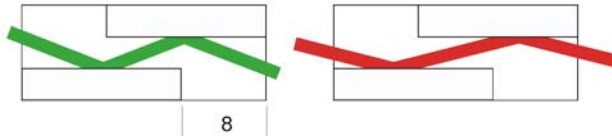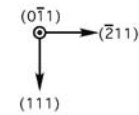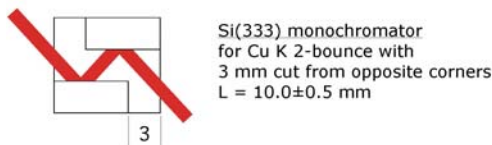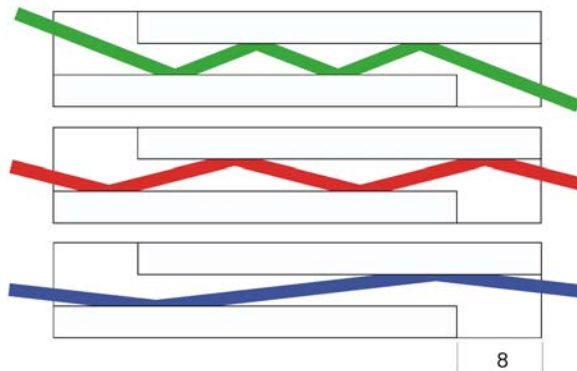
Figure B.4: Si(111) and (333) monochromators for use with Cr, Cu, and Mo target x-ray sources.

A   B
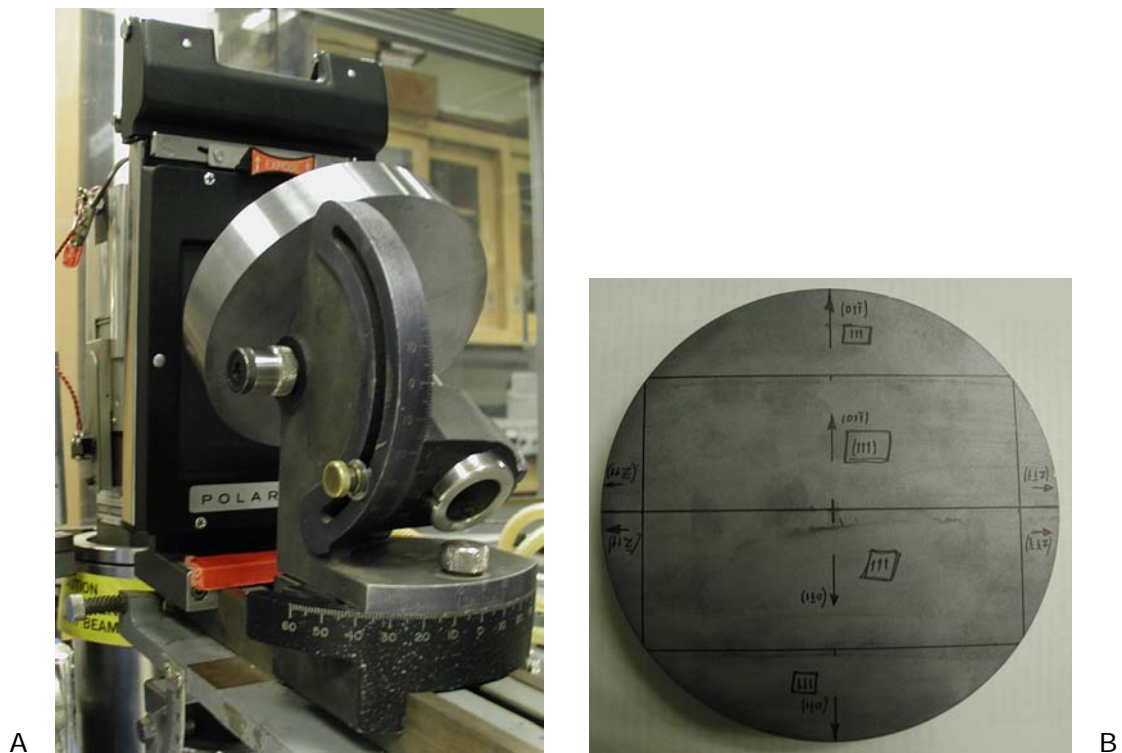
Figure B.5: A) The Laue camera can be used to quickly determine the orientation of a large piece of Si crystal. In this case, the off-normal (011) direction is determined for a slice of Si with a (111) surface normal. B) The blocks, from which the *(hhh)* monochromators are to be cut from the Si boule, are outlined on the crystal.
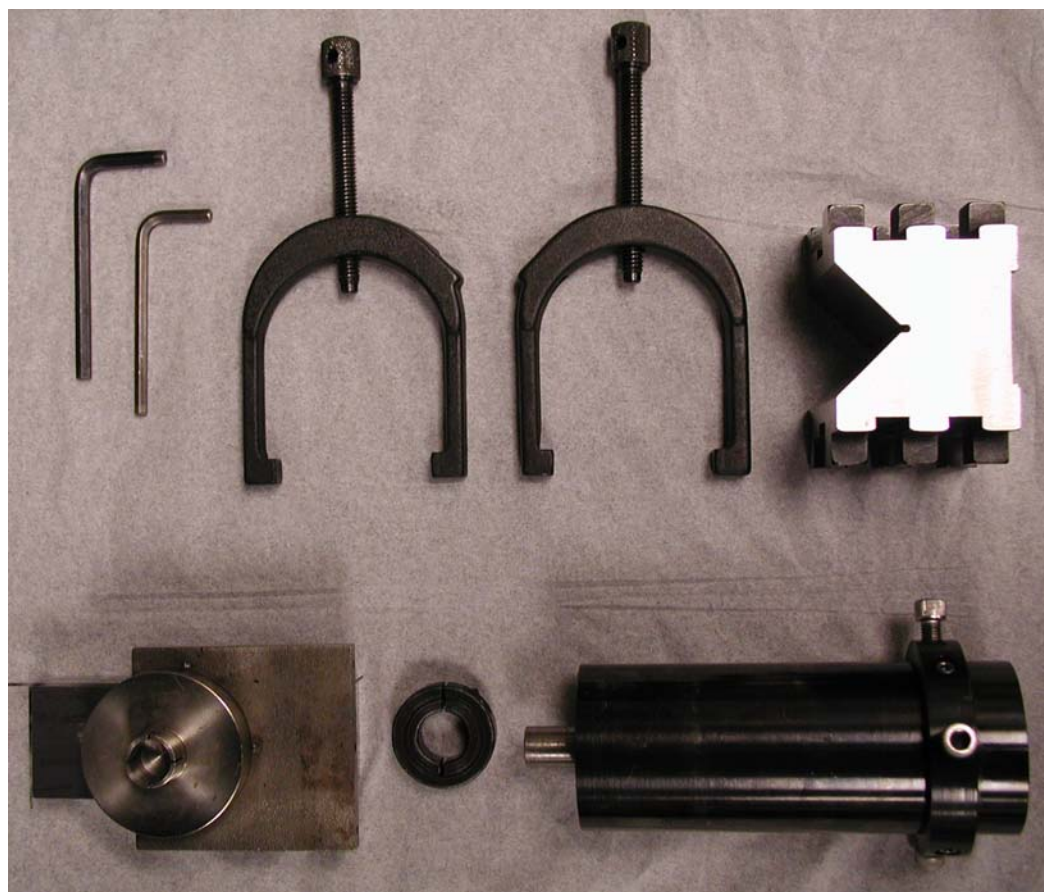
Figure B.6: Components for barrel alignment tool: barrel, collar clamp, sample mount, allen wrenches, clamps, and V-block. (Tools on loan from DND-CAT.)
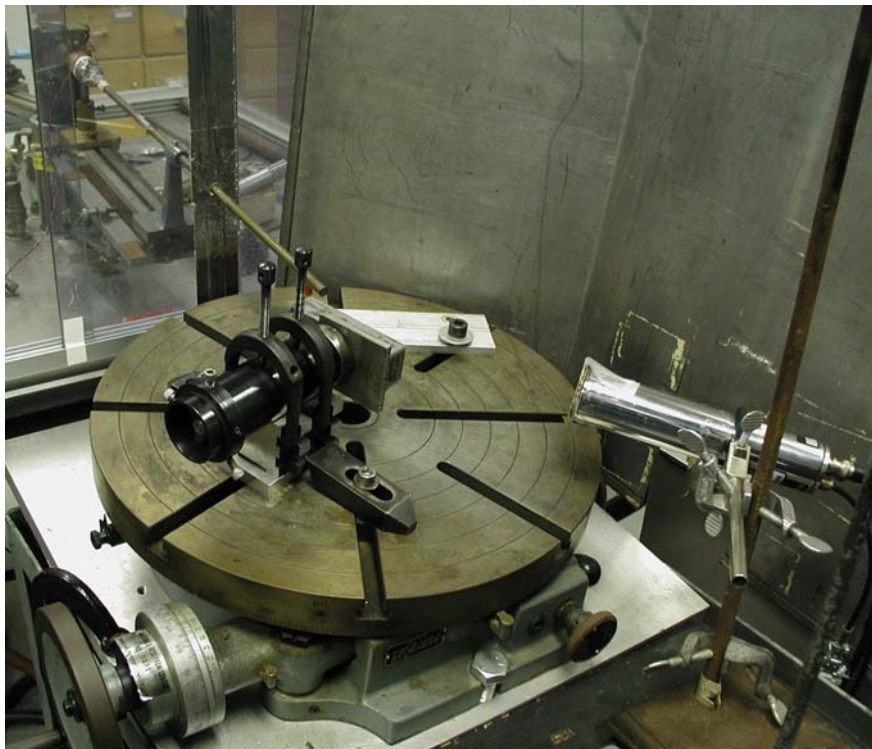
Figure B.7: The single-axis rotary stage and x-ray point source set-up used to precisely align the surface orientation for the Si*(hhh)* channel-cut monochromator. Using Mo Kα x-rays, the Si(333) reflection was used to orient the surface normal.

B.2.2 Cutting Si crystal with diamond blade saw

After precisely orienting ($\phi < 0.1°$) the crystallographic direction to be parallel to the barrel axis, the components were taken to the diamond blade saw (surface grinder manufactured by Harig Bridgeport) to make the critical cuts. The V-block was held in place on the table via a magnetic mount. After carefully aligning the V-block axes to be perpendicular to the cut plane, the block of Si was cut with the saw using an extremely slow transverse speed (~0.1 mm/s). Several adjacent parallel cuts were made to open up the gap to the desired value. To protect the Si crystal from chipping and damage during cutting, the external surfaces exposed to the saw blade were protected with 1/8″ of glass. When cutting the gaps, the dimensions should account for both the saw blade cut width and the 0.1 mm removed from each surface from etching.

Figure B.8: Cutting the channel-cut monochromator with the diamond blade saw in the machine shop at DND-CAT. The Si block is mounted on the barrel-aligner and held with the V-block while the critical cuts are made with the saw. The external surfaces of Si crystal were bonded to 1/8″ thick glass to prevent chipping and the cut was made in a single pass with an extremely slow transverse speed (~0.1 mm/s). The cutting fluid was shut off during this photograph.

B.2.3 Etching of Si crystals

To remove the saw damage and stresses in the surfaces of the Si single crystals, the damaged material needs to be removed. Before etching the crystals, round off the sharp corners with a grinding stone or fine grit (≤ 600) abrasive paper. Remove organic materials with a sulfuric acid bath (overnight soak at RT). A simple method to etch Si is to use a chilled solution of 10% (by volume) hydrofluoric acid and 90% nitric acid. (For Ge crystals, use 5% hydrofluoric acid and 95% nitric acid.) Because the Si etching is exothermic, a nest of ice should be used to chill the container (made of HDPE) that holds the etch solution. A 2 L etch bath was used for each of the large channel monochromators. Unless severe damage has been caused, it is sufficient to remove the outer 100 μm of material. The total etch time is ~20 minutes. While etching the crystal, it should be cradled in a HDPE mesh and gently agitated in the solution to ensure uniform etching.

NOTE: Whenever you are working with hydrofluoric acid, adhere to the MSDS guidelines, work in a fume hood, and wear the proper safety protection: gloves (more than the typical thin latex type), face shield, and chemically resistant apron with sleeves. Also, have non-expired calcium gluconate gel nearby, in case you are exposed to the hydrofluoric acid.

B.3 X-ray lab Si channel-cut monochromator performance

On the 18 kW rotating (Mo target) anode with an Osmic multilayer optic in the NU x-ray lab, the Si(333) channel-cut monochromator was placed as an incident beam monochromator and tuned to the Mo Kα_1 x-ray radiation. The output flux was estimated to be 1.5 x10^6 cps for a 0.1 mm x 5.0 mm (width x height) beam size. Using a 17° asymmetricly-cut Si(333) crystal with an oblique incident angle as a sample (to reduce the angular acceptance to the crystal), the Si (333) rocking curve FWHM was measured to be 4.5 µrad wide. The theory predicted a FWHM = 3.6 µrad. The Si(333) sample was scanned in angle using either a stepping motor or a torsion-bearing stage with a piezo actuator; the results are shown in Figure B.9. On a 30 ms time scale, the vibration in the experimental set–up created an estimated 1.5 µrad angular motion.
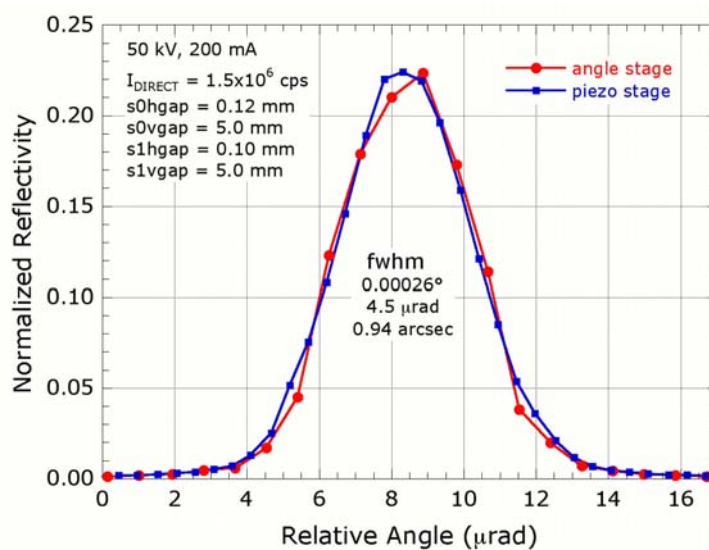
Figure B.9: Rocking curve using the Si(333) channel-cut monochromator made for use with Mo Kα radiation. The rocking curve FWHM is measured to be 4.5 µrad.

Appendix C: Transformation Matrices and MATLAB Code for XSW Imaging

C.1 Transformation matrices

When considering the (111) surface of the diamond cubic structure, it is convenient to use a hexagonal unit cell with the surface normal along the $(00l)_{hex}$ direction. Converting the (hkl) reflections from a cubic crystal structure basis to a hexagonal surface unit cell basis can be accomplished using a linear combination of the vectors listed below. Examples of the equivalent (hkl) reflections in the cubic and hexagonal bases are listed in Table C.1.

$$a_1 = \frac{3}{2}\begin{bmatrix} 1 & 0 & \bar{1} \end{bmatrix} \tag{C.1}$$

$$a_2 = \frac{3}{2}\begin{bmatrix} \bar{1} & 1 & 0 \end{bmatrix} \tag{C.2}$$

$$a_3 = \begin{bmatrix} 1 & 1 & 1 \end{bmatrix} \tag{C.3}$$

By combining these vectors into a matrix, cubic *(hkl)* reflections can be converted to a hexagonal basis with the following matrix,

$$
\begin{pmatrix}
\dfrac{3}{2} & 0 & -\dfrac{3}{2} \\
-\dfrac{3}{2} & \dfrac{3}{2} & 0 \\
1 & 1 & 1
\end{pmatrix} . \tag{C.4}
$$

In a similar method, the hexagonal *(hkl)* reflections can be converted to a cubic basis using the matrix below,

$$
\begin{pmatrix}
\dfrac{2}{9} & -\dfrac{2}{9} & \dfrac{1}{3} \\
\dfrac{2}{9} & \dfrac{4}{9} & \dfrac{1}{3} \\
-\dfrac{4}{9} & -\dfrac{2}{9} & \dfrac{1}{3}
\end{pmatrix} . \tag{C.5}
$$

Table C.1: *(hkl)* reflections in the cubic and hexagonal bases.

cubic	hexagonal
(111)	(003)
(333)	(009)
(11$\bar{1}$)	(301)
(33$\bar{3}$)	(903)
(220)	(304)

C.2 Selected parts of MATLAB code for XSW imaging

The program MATLAB version 6.5 was used to compute and plot the atomic density maps for the XSW imaging technique. The "bftSN.m" file was used to calculate the atomic density in 3D, and the "aplot.m" file plotted the results. For the (111) surface of the diamond crystal structure, all of the computations were performed using hexagonal coordinates. Portions of the code from these two files are listed in sections C.2.1 and C.2.2.

C.2.1 Calculation of atomic density with "bftSN.m" function

Select lines of code are listed below. For the hexagonal unit cell, the xH coordinate is introduced to shift the atomic density image from cubic to hexagonal. The xH period is half of the step size of the x, y, and z coordinates. The lengths of the hexagonal lattice parameters are 3X larger than the primitive unit cell for diamond cubic.

```
%  x, xH, y, z ranges for the a single primitive unit cell
x=0:interv/2:0.34;
xH=-0.17:interv/2:0.34;
y=0:interv:0.34;
z=0.0:interv:0.34;
```

The lines of code that cycle through 3D space to calculate the summation of the atomic density are listed next.

```
for ind0=1:size(pin,2)
        fin(:,ind0)=fin(:,ind0)/max(fin(:,ind0));
        ad=zeros(size(X));
        pl_adHEX=zeros(size(XH));
        size(pl_adHEX)
            for ind1=1:length(y)
          for ind2=length(xH)-length(x)+1:length(xH)
            for ind3=1:length(z)
%              back transformation, 0th order = 1
            tmp=1;
                r=[X(ind1,ind2,ind3);Y(ind1,ind2,ind3);Z(ind1,ind2,ind3)];
             for ind4=1:size(pin,1)
%                The calculation is based on:  2*f*exp(2*pi*P)*exp(-2*pi*(Q.r));
%                The center of symmetry yields a factor of 2 comes because (1 1 1)
%                 and (-1 -1 -1) have same coherent fraction but opposite sign
%                  for coherent position( although actually the same position).
              tmp=tmp+2*fin(ind4,ind0)*cos(2*pi*pin(ind4,ind0)-2*pi*(q(ind4,:)*r));
              end
              ad(ind1,ind2,ind3)=tmp;
            end
          end
        end    % end for ind1=...

%   Try to switch to hexagonal coordinates that are projected onto orthogonal axes
%   cycle through z in the mesh
      for indZ=1:length(z)
%       cycle through y in the mesh
        for indY=1:length(y)
          for indX=length(xH)-length(x)+1:length(xH)
              indXH=indX-indY+1;
              pl_adHEX(indY,indXH,indZ)=ad(indY,indX,indZ);
          end
        end
      end
```

C.2.2 Plotting atomic density with "aplotSUC.m" function

The lines of code that pertain to plotting the atomic density on planes parallel to the surface and through the unit cell diagonal (when viewed from the top) are listed below.

```
% for the 3x3 unit cell
   hsp = surf(linspace(-0.4,0.52,500),linspace(-0.35,0.68,500),zeros(500));
   rotate(hsp,[-0.5,0.3333,0],-90,[0.3333,0,0]);
% OR for single unit cell;
   % hsp = surf(linspace(-0.26,0.52,300),linspace(-0.02,0.68,300),zeros(300));
   % rotate(hsp,[-0.5,0.3333,0],90,[0.5,0.3333,0]);
  % slice(pl_X,pl_Y,pl_Z,pl_adHEX,xd,yd,zd);
% rotate the plane "hsp"
  % vector1 is the axis direction for rotation (with starting point at 0,0,0)
  % rotation angle… 0 does not seem to work!?
  % vector2 is the origin for the rotation axis
  % rotate(hsp,[-0.5,0.3333,0],-90,[0.3333,0,0]);
  xd = get(hsp,'XData');
  yd = get(hsp,'YData');
  zd = get(hsp,'ZData');
  delete(hsp);
% you can specify additional (orthogonal) planes easily
  %slice(pl_X,pl_Y,pl_Z,pl_adHEX,[],[],[]); % Draw no planes
  slice(pl_X,pl_Y,pl_Z,pl_adHEX,[],[],0.203); % Draw some plane at z=something
  hold on;
% this draws the hsp plane slice
  %slice(pl_X,pl_Y,pl_Z,pl_adHEX,xd,yd,zd);
  hold off;
end
%adjust aspect ratio so that xHEX=yHEX (=4.0006 A) and zHEX (=3.266 A) match
daspect([0.866,1,1.0606]);
```

Appendix D: Origins for Diamond Cubic Structure

There are four high-symmetry choices for the origin in the diamond cubic crystal structure. In this work, the origin is located at the atom in the top of the bilayer and labeled "1" in the Figure D.1. The fractional coordinates of the eight atoms for the different origins, shown in the figure below, are listed in Table D.1.
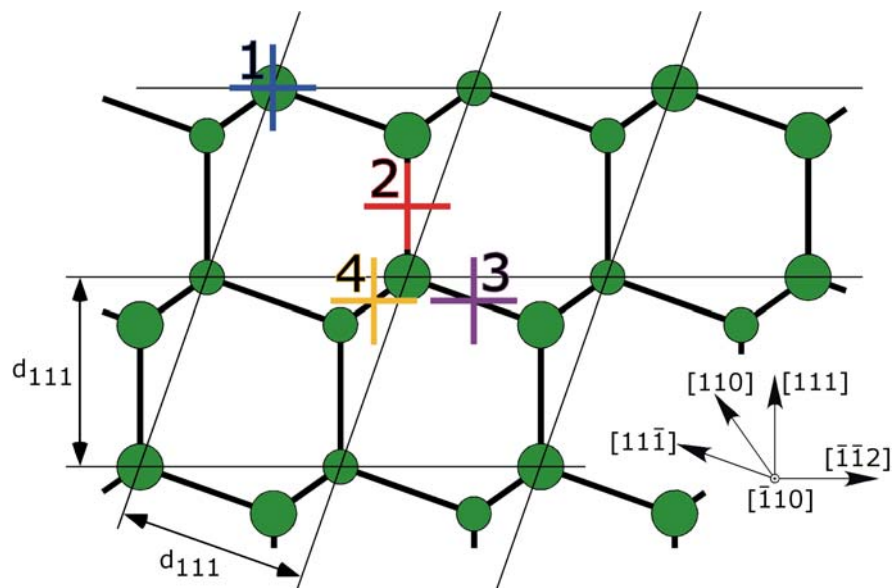
Figure D.1: Four high-symmetry origins for diamond cubic crystal structure.

Table D1: Fractional coordinates for four high-symmetry origins in the diamond cubic crystal structure shown in Figure D.1.

Component Atoms		Origins			
		1	2	3	4
Atom 1	x	0	7/8	1/8	7/8
	y	0	7/8	1/8	1/8
	z	0	7/8	7/8	1/8
Atom 2	x	1/2	3/8	5/8	3/8
	y	1/2	3/8	5/8	5/8
	z	0	7/8	7/8	1/8
Atom 3	x	1/2	3/8	5/8	3/8
	y	0	7/8	1/8	1/8
	z	1/2	3/8	3/8	5/8
Atom 4	x	0	7/8	1/8	7/8
	y	1/2	3/8	5/8	5/8
	z	1/2	3/8	3/8	5/8
Atom 5	x	1/4	1/8	3/8	1/8
	y	1/4	1/8	3/8	3/8
	z	1/4	1/8	1/8	3/8
Atom 6	x	3/4	5/8	7/8	5/8
	y	3/4	5/8	7/8	7/8
	z	1/4	1/8	1/8	3/8
Atom 7	x	3/4	5/8	7/8	5/8
	y	1/4	1/8	3/8	3/8
	z	3/4	5/8	5/8	7/8
Atom 8	x	1/4	1/8	3/8	1/8
	y	3/4	5/8	7/8	7/8
	z	3/4	5/8	5/8	7/8

Appendix E: Ge(111) Sample Preparations

The Ge(111) samples were cut from two different Ge boules. The samples for the Pb/Ge(111) experiments are from a CZ grown boule with an etch pit density < 1500 / cm^2 and was N-type (with a resistivity < 10 Ω-cm). The samples for the Sn/Ge(111) experiments were cut from a boule with nearly zero defect density. (The APS Optics Shop obtained the second boule and the details are not completely known.)

All of the XSW samples were cut into a "top hat" or "winged" shape, as shown in Figure E.1. The strain-relief tabs provide a place to hold the sample without blocking the surface for the x-rays.

After the samples were cut by the APS Optics Shop, the sharp corners were removed using 600 grit SiC abrasive paper. The saw damage was removed by etching in a solution of 5% hydrofluoric acid and 95% nitric acid. The top surfaces of the samples were then ground flat using wet 600 grit SiC abrasive paper.

A mirror surface was obtained by polishing the surface with a Syton solution (Nalco 2360 colloidal silica mixed with 5% hydrogen peroxide) on Politex Supreme cloth pads. After polishing, the colloidal silica residue was removed by immediately transferring the samples (while keeping the surfaces continuously immersed in water) to an ultrasonic water bath. The samples were then transferred to an ultrasonic methanol bath.

The surface roughness for this polishing treatment achieved an RMS value of < 2 Å. The result for an AFM scan on a polished sample is shown in Figure E.2. In part A, a 5 x 5 μm region is shown. The curvature is attributed to the equipment and not the sample. The roughness was determined from AFM line profiles, as shown in part B.
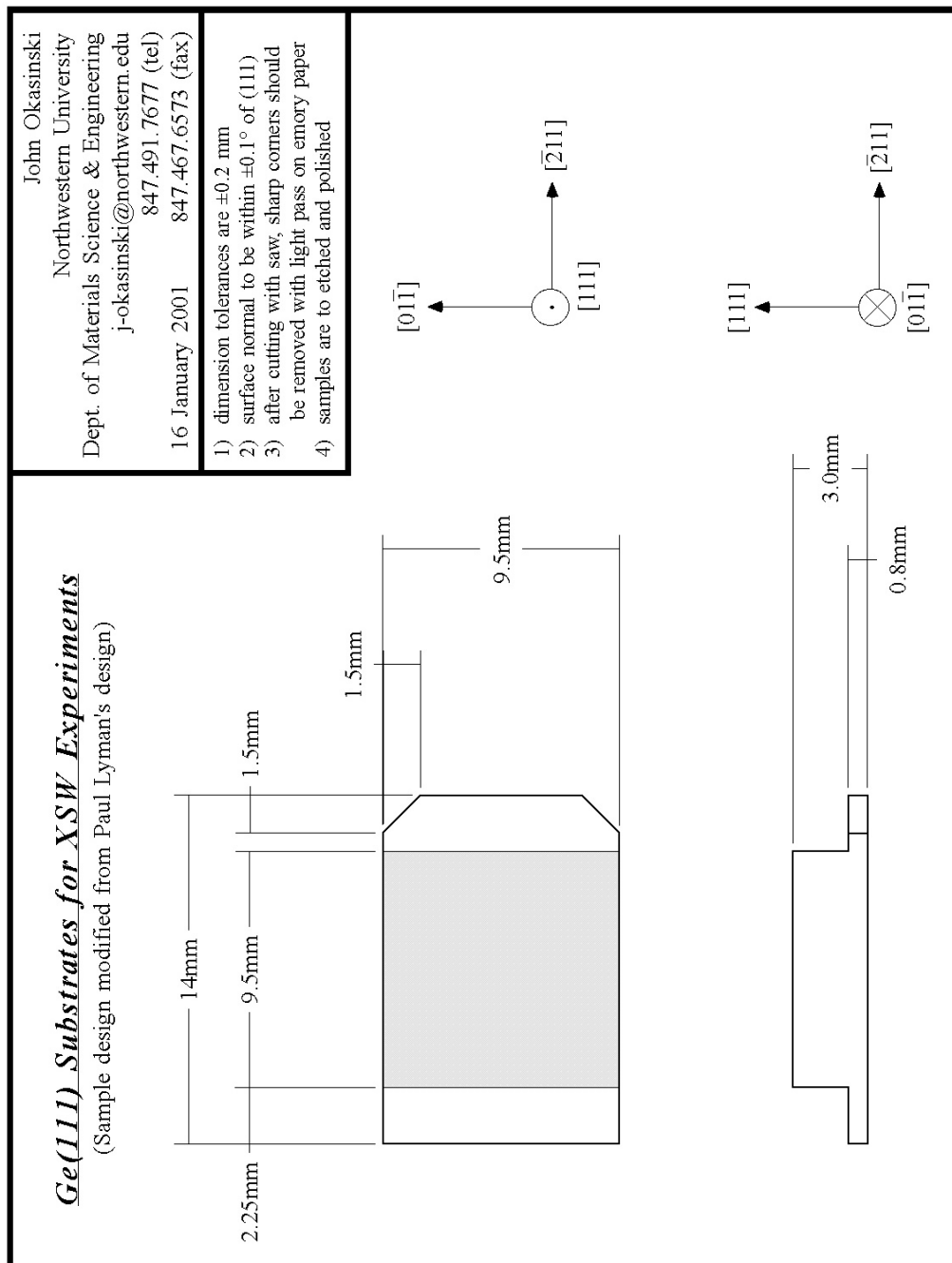
Figure E.1: Design for the Ge(111) samples for XSW experiments. The recessed tabs provide a region to hold the sample without creating strain in the crystal.

A

B
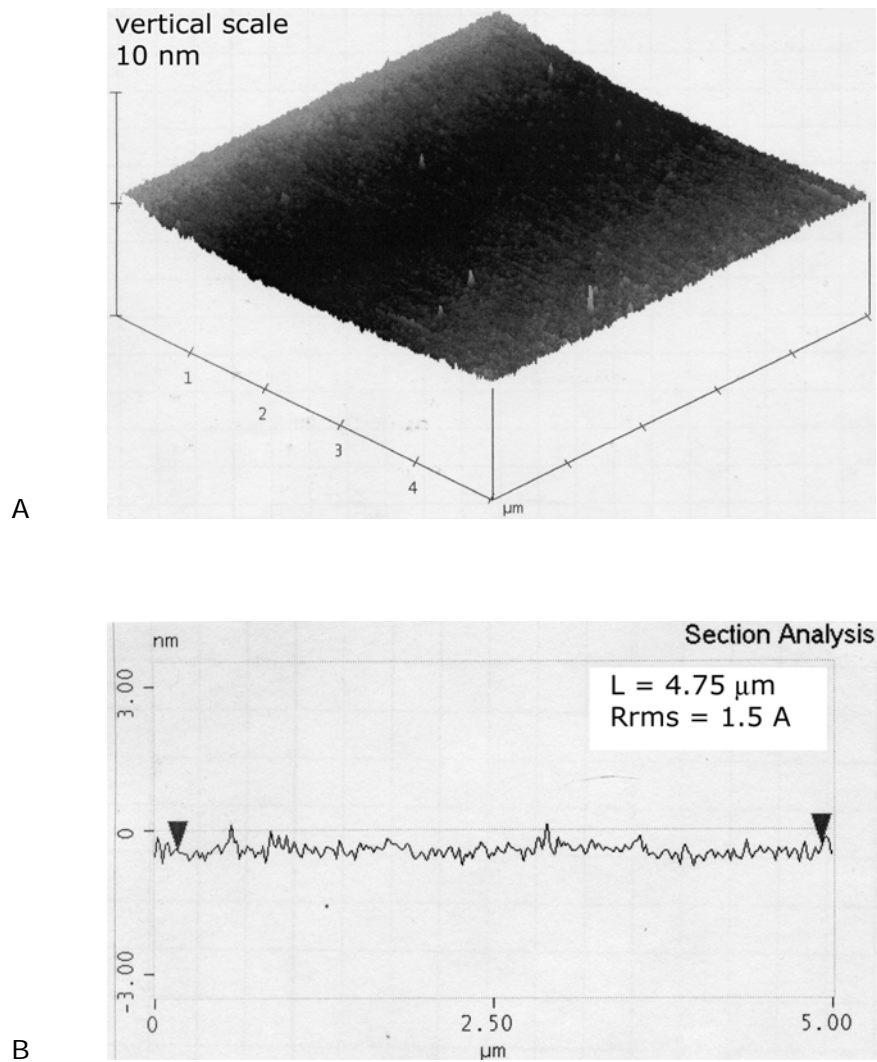
Figure E.2: Results from an AFM scan on a polished Ge(111) sample. A) The 2D

map of the height profile for a 5 x 5 μm region. B) The 1D line scan indicates that

the RMS roughness about 1.5 Å. (AFM scans obtained by Jennifer Mott.)

VITA

JOHN SCOTT OKASINSKI

BORN

January 15, 1972, Dearborn, Michigan

EDUCATION

Northwestern University, Evanston, Illinois
Ph. D. in Materials Science and Engineering
June 2004

University of Michigan, Ann Arbor, Michigan
B. S. E. in Materials Science and Engineering
Cum laude
May 1995

PUBLICATIONS

"X-ray standing wave imaging of the 1/3 monolayer Sn/Ge(111) surface", JS Okasinski, C-Y Kim, DA Walko, and MJ Bedzyk, Physical Review B **69**, 041401(R) (2004).

"Surface and interface studies at the APS endstation 5ID-C", DA Walko , O Sakata, PF Lyman, T-L Lee, BP Tinkham, JS Okasinski, Z Zhang, and MJ Bedzyk, American Institute of Physics Conference Proceedings, Synchrotron Radiation Instrumentation 2003, (in press).

"Defect and electronic structures of calcium-doped lanthanum cuprate", J Okasinski, JB Cohen, J Hwang, TO Mason, ZO Ding, O Warschkow, and DE Ellis, Journal of the American Ceramic Society **82**, 2451-2459 (1999).

ORAL PRESENTATIONS

"Low-Temperature Phase Transition Study for 1/3 ML Sn on Ge(111)", JS Okasinski, DA Walko, C-Y Kim, and MJ Bedzyk, American Physical Society, Annual APS March Meeting, 2002.

"Study of the Low-Temperature Phase Transition for 1/3 ML of Pb on Ge(111)", JS Okasinski, DA Walko, C-Y Kim, and MJ Bedzyk, American Physical Society, Annual APS March Meeting, 2001.

"Near edge and EXAFS study of point defects in Superconducting $La_{2-x}Ca_xCuO_{4-y}$", J Okasinski, J–H Hwang, P Georgopoulos, TO Mason, and JB Cohen, Engineering Foundation Conferences, Nonstoichiometric Ceramics and Intermetallics, April 1999.